Universidade of São Paulo
Instituto de Física

Espectro de elétrons provenientes de hádrons que contêm quarks pesados em colisões de proton-chumbo a $\sqrt{s_{NN}} = 5.02$ TeV usando os detetores TPC e EMCAL do ALICE no LHC

Cristiane Jahnke

Orientador: Prof. Dr. Marcelo Gameiro Munhoz

Tese submetida ao Instituto de Física da
Universidade de São Paulo para a obtenção do
título de Doutor em Ciências

Banca examinadora:
Prof. Dr. Marcelo Gameiro Munhoz - IFUSP (Orientador)
Prof. Dr. Airton Deppman - IFUSP
Prof. Dr. Fernando Silveira Navarra - IFUSP
Prof. Dr. Eduardo Souza Fraga - UFRJ
Prof. Dr. Wei-Liang Qian - EEL/USP

São Paulo
2016

FICHA CATALOGRÁFICA
Preparada pelo Serviço de Biblioteca e Informação do Instituto de Física da Universidade de São Paulo

Jahnke, Cristiane

Espectro de elétrons provenientes de hádrons que contêm quarks pesados em colisões de próton-chumbo a $\sqrt{s_{NN}} = 5.02$ TeV usando os detetores TPC e EMCAL do ALICE no LHC. São Paulo, 2016.

Tese (Doutorado) – Universidade de São Paulo. Instituto de Física. Depto. de Física Nuclear.

Orientador: Prof. Dr. Marcelo Gameiro Munhoz.

Área de Concentração: Física de Alta Energia.

Unitermos: 1. Colisões de íons pesados relativísticos; 2. Quarks; 3. Elétrons.

USP/IF/SBI-025/2016

University of Sao Paulo
Institute of Physics

Measurement of electrons from heavy-flavour hadron decays in p-Pb collisions at $\sqrt{s_{NN}} = 5.02$ TeV using TPC and EMCal detectors with ALICE at LHC

Cristiane Jahnke

Supervisor: Prof. Dr. Marcelo Gameiro Munhoz

Thesis submitted to the Institute of Physics
of the University of Sao Paulo to obtain
the degree of PhD of science

Thesis committee:
Prof. Dr. Marcelo Gameiro Munhoz - IFUSP (Supervisor)
Prof. Dr. Airton Deppman - IFUSP
Prof. Dr. Fernando Silveira Navarra - IFUSP
Prof. Dr. Eduardo Souza Fraga - UFRJ
Prof. Dr. Wei-Liang Qian - EEL/USP

Sao Paulo
2016

Resumo

Colisões de íons pesados relativísticos é uma ferramenta poderosa para se estudar o plasma de quarks e glúons (QGP). Quarks pesados (*charm* e *beauty*) são produzidos nos estágios iniciais da colisão e participam da evolução completa do sistema. Medidas de elétrons provenientes de quarks pesados é uma das possíveis formas de se estudar a interação destas partículas com o QGP. Utilizando o detetor ALICE do LHC, elétrons podem ser identificados com alta eficiência e boa pureza. Uma forte supressão de elétrons provenientes de quarks pesados foi observada em alto p_{T} em colisões de Pb-Pb a 2.76 TeV. Medidas do mesmo observável em colisões p-Pb são cruciais para se entender os efeitos da matéria nuclear fria na produção de tais partículas. O espectro de elétrons provenientes de hádrons que contêm *charm* ou *beauty* foi medido em colisões p-Pb a $\sqrt{s_{NN}} = 5.02$ TeV. Os elétrons foram identificados utilizando o *Time Projection Chamber* (TPC) e o *Electromagnetic Calorimeter* (EMCal) do detetor ALICE, no intervalo de momento transversal de $2 < p_{\mathrm{T}} < 20$ GeV/c. As medidas foram realizadas utilizando dois diferentes conjunto de dados: colisões de mínima tendenciosidade (*minimum bias (MB)*) e colisões tomadas utilizando o trigger do EMCal. Os elétrons de fundo foram removidos utilizando um método de massa invariante. Os resultados são compatíveis com a unidade ($R_{\mathrm{pPb}} \approx 1$) e os efeitos da matéria nuclear fria são pequenos para elétrons provenientes de quarks pesados.

Abstract

Heavy-ion collisions are a powerful tool to study hot and dense QCD matter, the so-called Quark Gluon Plasma (QGP). Since heavy quarks (charm and beauty) are dominantly produced in the early stages of the collision, they experience the complete evolution of the system. Measurements of electrons from heavy-flavour hadron decay is one possible way to study the interaction of these particles with the QGP. With ALICE at LHC, electrons can be identified with high efficiency and purity. A strong suppression of heavy-flavour decay electrons has been observed at high p_{T} in Pb-Pb collisions at 2.76 TeV. Measurements in p-Pb collisions are crucial to understand cold nuclear matter effects on heavy-flavour production in heavy-ion collisions. The spectrum of electrons from the decays of hadrons containing charm and beauty was measured in p-Pb collisions at $\sqrt{s_{NN}} = 5.02$ TeV. The heavy flavour decay electrons were measured by using the Time Projection Chamber (TPC) and the Electromagnetic Calorimeter (EMCal) detectors from ALICE in the transverse-momentum range $2 < p_{\mathrm{T}} < 20$ GeV/c. The measurements were done in two different data set: minimum bias collisions and data using the EMCal trigger. The non-heavy flavour electron background was removed using an invariant mass method. The results are compatible with one ($R_{\mathrm{pPb}} \approx 1$) and the cold nuclear matter effects in p-Pb collisions are small for the electrons from heavy-flavour hadron decays.

Acknowledgements

First and above all, I thank God for providing me this opportunity and granting me the capability and persistence to proceed successfully with this work.

I would like to express my deepest appreciation to my supervisor Prof. Dr. Marcelo Gameiro Munhoz, for the continuous support of my Ph.D. study, for his patience, motivation, and immense knowledge. Without his guidance and persistent help this thesis would not have been possible. His guidance was essential during the research time and when writing this thesis. I am very greatfull for all the discussions and specially that he always understood me as a student. I could not have imagined a better supervisor.

Besides my supervisor, I would like to thank the rest of my thesis committee: Prof. Dr. Airton Deppman, Prof. Dr. Fernando Navarra, Prof. Dr. Eduardo Fraga and Prof. Dr. Wei-Liang Qian, for all their corrections, insightful comments, and questions that helped to improve this thesis.

It gives me great pleasure in acknowledging the support given by Dr. Shingo Sakai. He was an incredible mentor for the analysis performed in this thesis and also became a good friend.

I consider it an honor the mutual collaboration with the ALICE GSI group. My sincere thanks to Dr. Silvia Masciocchi, Dr. Ralf Averbeck, Dr. Raphaelle Bailhache, Dr. Yvonne Chiara Pachmayer and Jan Wagner, for receiving me in their group, for all the comments and encouragement, and specially for the hard questions which improved our research in various aspects.

I am gratefull to my colleagues from Griper/HEPIC: Camila, Caio Eduardo, Caio Laganá, Caio Prado, Elienos, Renato, Júlia, Henrique, Diógenes, Antônio, Hermann, Mauro, Hugo, Marcel, Sudipan and Alexis, for all being always very encouraging and ready for any help. I also thank the friendship of all. A special thanks to Camila for being a very good friend these last four years. I own a special gratitude to Elienos, who helped me a lot in the beginning of my analysis, was always encouraging and an example of dedication. I am also greatfull to Marcel and Sudipan, who helped me with the analysis using the EMCal trigger. I also want to express my gratitude to Marcel for the help with Aliroot during my firsts steps in the analysis when I initiated the Ph.D. It is with immense gratitude that I acknowledge the support of the professors of my group, Dr. Alexandre Suaide, Dr. Nelson Carlin, Dr. Marco Bregant and Dr. Alejandro Szanto de Toledo (*in memoriam*), for all their help, insightful comments and encouragement that helped to improve this work.

I also thank my friends from IFUSP, specially Cely, Josi, Tati and Graciella for all the chats, laughs, coffees and pizzas together.

Last but not least, I would like to thank my family for all the support and love. I cannot find words to express my gratitude to my husband Tiago Fiorini da Silva, for all his help

along this work, helping me to learn how to deal with the ”stressful situations” that always happens in the Ph.D period and for always making me smile. I am very grateful for his love, patience, encouragement and specially for being an outstanding example of academic person. I also thank his family for the friendship and incentive. My sincere thanks to my mother Gilda Timóteo Leite, for all the love and support in my entire life: without her incentive and dedication I would not be the person I am today. I also thank my brothers Max Reinhold Jahnke and Viktor Jahnke, for the friendship, encouragement and for being an inspiration for me. Special thanks to Viktor for all the discussions and help with the theoretical aspects of this thesis and for being an example of dedication. I also thank my father Horst Reinhold Jahnke for all love and incentive. A special thanks goes to Joyce Ribeiro Jahnke, my sister-in-law and my nephew Pedro Ribeiro Jahnke, that always make weekends happier. I also thank Adèle Ribeiro for the friendship. A special thanks to all my family for understanding that some times I simply could not be present due to the required work in the Ph.D.

Finally, I would like to thank FAPESP and CAPES for the financial support of this work.

To my love

Tiago Fiorini da Silva

Contents

List of Figures

List of Tables

Chapter 1

Introduction

One of the main goals of modern nuclear physics is to investigate and understand the strongly interacting matter under extreme conditions of temperature and energy density: the so-called Quark-Gluon Plasma (QGP) [1, 2]. The conditions to create this medium can be attained in heavy-ion collisions, like Pb-Pb at LHC and Au-Au at RHIC.

One available probe to study the QGP is the open-heavy flavour, which are particles carrying single charm or single beauty [3]. Since they have large masses, they are produced in the early moments of the collisions and, once formed, they can live much longer than the duration of the QGP, thus they can experience the full evolution of the medium. Additionally, measurements of these particles may serve as a crucial test for the perturbative Quantum Chromodynamics (pQCD).

In heavy-ion collisions, there are also cold nuclear matter (CNM) effects together with effects due to the formation of the QGP. To assess this effects, baseline collisions, like pp and p-Pb collisions are needed. In pp collisions, the heavy-flavour production can be described by perturbative QCD. On the other hand, in p-Pb collisions, due to the presence of the Pb nucleus, cold nuclear matter effects can be present, while the formation of an extended QGP is not expected. Then, comparing results of the particle production in p-Pb and pp, the CNM effects can be measured, then a comparison of the results of Pb-Pb with p-Pb and pp, the effects due to the formation of the QGP can be assessed.

Additionally, the better understanding of the nuclear effects that interfere in hadronic observables in p-Pb collisions has its importance by its own, since these measurements can be used to elucidate the understanding of the parton distribution function, the multiparton interaction and possible energy losses in the cold nuclear matter.

In this thesis, the first measurement of open-heavy flavour production through its semi-electronic decay channel in p-Pb collision at $\sqrt{s_{NN}} = 5.02$ TeV in the intermediate and high transverse momentum (range up to 20 GeV/c) is presented.

The analysis was performed using the combination of the Time Projection Chamber (TPC) and the Electromagnetic Chamber (EMCal) for particle identification. Two data set were used: a minimum bias (MB) data and a sample using the EMCal trigger. Using the MB data, the spectrum of electrons from heavy-flavour hadron decays was measured in the transverse momentum range from 2 to 12 GeV/c and the nuclear modification factor (R_{pPb}) was calculated using an interpolation of pp measurements at 7 and 2.76 TeV. This data was combined with a spectrum obtained from 0.5 to 6 GeV/c using a different particle identification strategy and the results were published in Physics Letter B [4]. For the sample using the EMCal trigger, two thresholds of energy were used: one at 7 GeV and other at 11 GeV. The spectrum of electrons from heavy-flavour hadron decays was measured from 8 to 16 GeV/c using the 7 GeV threshold and from 12 to 20 GeV/c using the 11 GeV threshold. The nuclear modification factor was obtained using the ATLAS pp measurements at 7 TeV, scaled to 5.02 TeV using FONLL predictions. The results obtained from 12 to 20 GeV/c were presented in the conference *Quark Matter 2015*.

In Chap. 2 we give a theoretical introduction about the role of heavy-ion collisions in the study of the Quark-Gluon Plasma and the possible observables used for its study. In Chap. 3 we discuss the production of heavy-quarks and some of the available models for its interaction with cold and hot nuclear medium. In Chap. 4 we present the experimental setup, where the ALICE detector is described and the offline computation of the ALICE data is introduced. The Chaps. 5 and 6 are dedicated to the results obtained in this thesis: in Chap. 5 we present the details of the electrons analysis performed in the MB data and in Chap. 6 we present the analysis using the EMCal triggered data, where a spectrum in high transverse momentum was measured, extending the MB results. The Chap. 7 is dedicated to a discussion about the implications of our results, together with other results from ALICE, to our understanding of the QGP properties and the cold nuclear matter effects. Finally, in Chap. 8 we present the conclusions of this work.

Chapter 2

The study of the Quark-Gluon Plasma by means of open heavy-flavour

In the present chapter we discuss the role of heavy-ion collisions in the study of the Quark-Gluon Plasma, and how the Large Hadron Collider data, in particular the data obtained with the ALICE detector, can bring new insights to a better understanding of this state of matter initiating a new era in the investigation of the standard model. We also discuss some of the possible observables used to study the QGP with ALICE data and the possible decay channels to study the heavy-flavour particles interactions with the plasma medium. The motivation for the choice of channel and observable to be studied in this thesis is also given.

2.1 The Quark-Gluon Plasma state

In very high-energy or very high-density conditions (or even when both conditions happens simultaneously), the quarks and gluons that form the hadrons are found in a deconfined state, forming the Quark-Gluon Plasma (QGP) [1, 2]. This is a high-density and highly-energetic state of strongly-interacting matter where the deconfinement occurs over a volume much larger than typical hadron sizes. It is believed that, up to the first tens of microseconds after the big bang, the entire universe was in a QGP state. When the universe started to cool down, the formation of hadrons occurred. The QGP formation is a direct consequence of the *asymptotic freedom* [5–9], as will be explained later.

Basically, the Standard Model (SM) is the theory that describes the fundamental forces and the composition of the matter. There are three fundamental interactions described in the SM: electromagnetic force, weak force and strong force. Each of these interactions respect a gauge symmetry and is mediated by a field whose quanta are particles called gauge bosons. For the electromagnetic field, the force is mediated by the photons, which are massless and do not carry charge. The mediation by a single particle originates from the fact that the

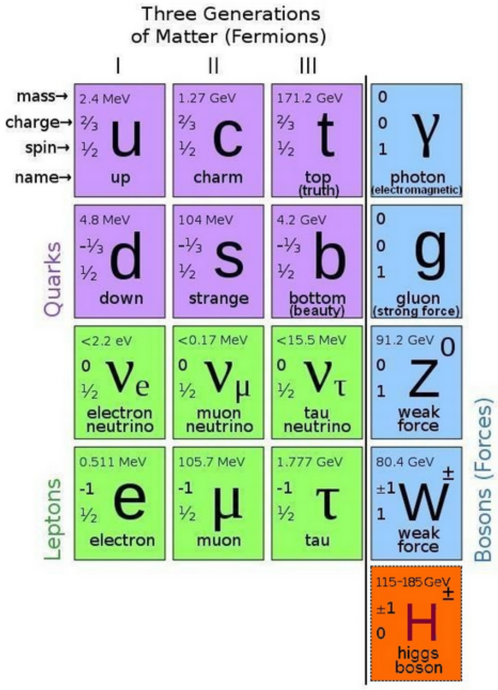

Figure 2.1: Elementary particles included in the Standard Model: quarks, leptons and bosons. Fig. from [10].

symmetry group of the electromagnetic field is the unitary transformation U(1)[1], which has a single generator[2]. For the weak force, the gauge group is the SU(2)[3], which has three generators that are related to the gauge bosons W^+, W^- and Z. The gauge group of the strong force is SU(3), which has eight generators that give rise to eight gluons that mediates the interactions between the quarks. Fig. 2.1 shows the quarks and leptons separated in three generations and the mass, charge and spin for each quark, lepton and boson.

Quarks and gluons have a colour charge and they interact by strong force. Thus, their interaction is described by a gauge field theory called Quantum Chromodynamics (QCD). The Lagrangian of the QCD is given by Eq. 2.1 [12, 13].

$$L = \overline{\psi_q^i}(i\gamma^\rho)(D_\rho)_{ij}\psi_q^j - m_q\overline{\psi_q^i}\psi_{qi} - \frac{1}{4}F^a_{\rho\nu}F^{a\rho\nu} \tag{2.1}$$

where ψ_q^i denotes the quark field with colour index i (i = red, green or blue), γ^ρ is a Dirac matrix where ρ is the Lorentz vector index, m_q is the quark mass, $F^a_{\rho\nu}$ is the gluon field strength tensor for a gluon with colour charge index a (a is a combination of a colour and an anticolor and have 8 possibilities) and D_ρ is the covariant derivative in QCD, given by Eq.

---

[1] U(N), and U(1) in particular, represents a *Unitarity group*, which is a Lie group [11].

[2] The number of gauge bosons corresponding to each field is equal to number of generators of the symmetry group. As the group U(N) has N^2 generators, the group U(1) has only one generator.

[3] SU(N) express the *Special Unitary group*. The number of generators of SU(N) is N^2-1.

2.2 [12, 13].

$$(D_\rho)_{ij} = \delta_{ij}\partial_\rho - ig_s t^a_{ij} A^a_\rho \tag{2.2}$$

where g_s is the strong coupling, related to α_s (coupling constant, defined later in Eq. 2.3) by $g_s^2 = 4\pi\alpha_s$, A^a_ρ is the gluon field with colour index a, and the t^a_{ij} is proportional to the Gell-Mann matrices (λ^a): $t^a_{ij} = \lambda^a_{ij}/2$ [12, 13].

Since leptons do not carry colour charge, they are neutral to the strong force and their interactions are described by the electroweak theory, which includes the Quantum Electrodynamics (QED) and the weak force, which is mediated by Z and W bosons while the electromagnetic force is mediated by photons exchange.

Back to the QCD, coloured free particles are not allowed to exist, thus quarks and gluons are confined in space, forming the colourless particles which are the hadrons. The meson particles are bound states of a quark and an antiquark, and the baryon particles are bound states of three quarks.

The interaction strength between quarks, and consequently the strength of the confinement, is given by the coupling constant, α_s, which is shown to be, in pQCD, as in Eq. 2.3 (only valid for high Q^2)[4].

$$\alpha_s(Q^2) = \frac{12\pi}{(33 - 2n_f)ln(Q^2/\Lambda^2_{QCD})} \tag{2.3}$$

where Q is the momentum transferred in a collision, n_f is the number of flavours and Λ_{QCD} is the QCD scale. The strength of the strong interaction decreases at small distances or high energies. The energy dependence of α_s is shown in Fig. 2.2.

Analysing Eq. 2.3, when $\Lambda_{QCD} << Q^2$, $\alpha_s \rightarrow 0$ and the deconfinement occurs. This is the feature of the QCD called *asymptotic freedom*. This theory was discovered by Frank Wilczek, David Gross, and independently by David Politzer in 1973, and their discovery led to the Nobel Prize in physics in 2004.

Quantitative lattice QCD (l-QCD) calculations [15] agrees with asymptotic freedom theory predictions that matter goes through a transition from a hadronic gas to a QGP. This phase transition happens in a temperature (T) around 160 MeV which corresponds to an energy density (ϵ) of around 1 GeV/fm^3. Fig. 2.3 shows a theoretical phase diagram of the QCD, where it can be seen regions of temperature and baryonic chemical potential in which the QGP occurs and the transition region for the hadronic phase.

Fig. 2.4 shows the energy density (normalised by the T^4) as a function of the temperature (normalised by T_c, the critical temperature necessary for the QGP formation). It is possible to see that the phase transition is actually a crossover around the critical temperature. The

---

[4] In case of processes at low Q^2, α_s is not analytically calculable.

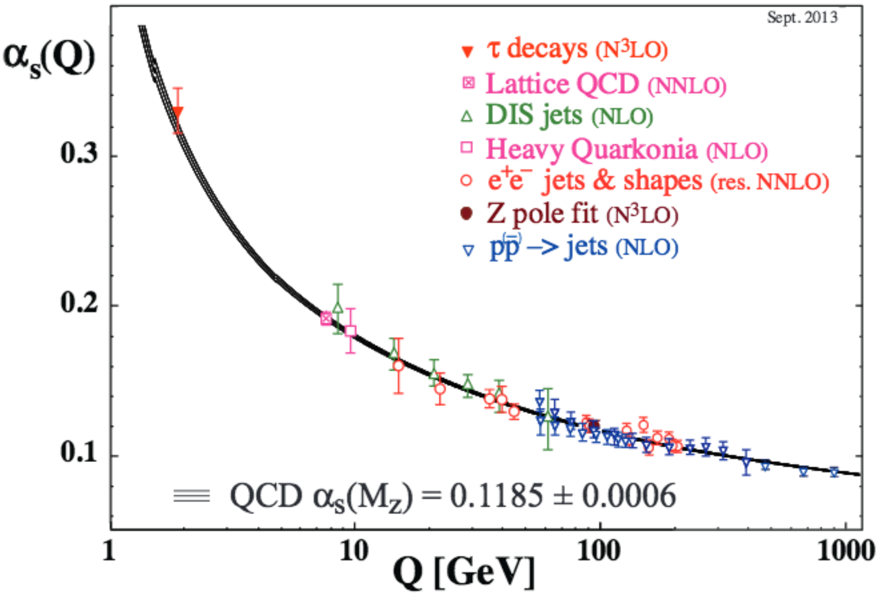

Figure 2.2: Measurements of α_s as a function of the respective energy scale Q. Fig. from [14].

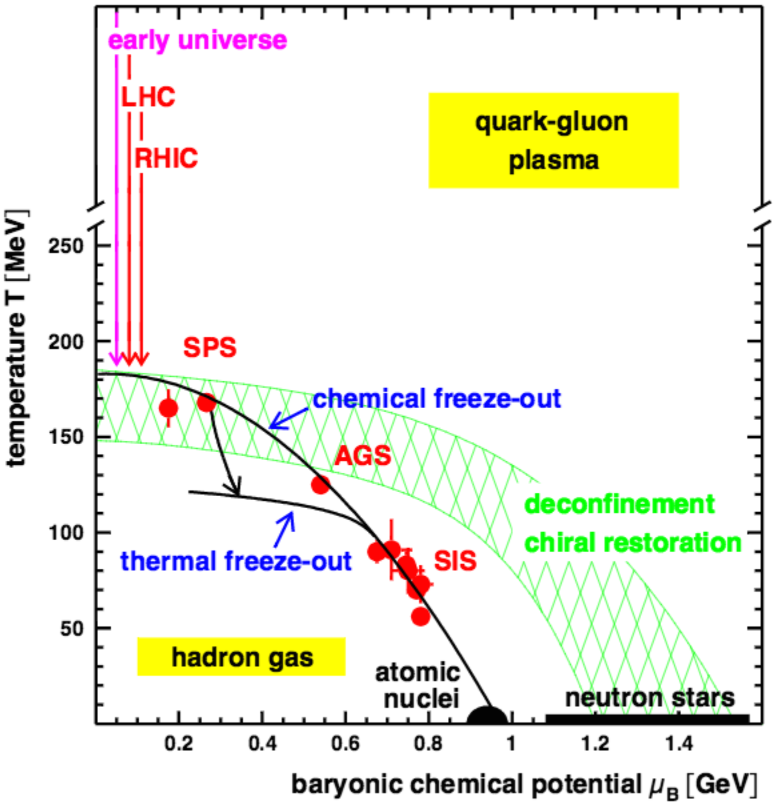

Figure 2.3: Phase diagram of the QCD depicting the expected QGP phase transition. Fig. from [16].

results are shown for 2 and 3 light flavours, and for 2 light and 1 heavy-flavour with all the cases presenting similar behaviour. Fig. 2.5 shows the pressure as a function of temperature, normalised by the T^4 (left) and by p_{SB}, which is the pressure of an ideal gas (right).

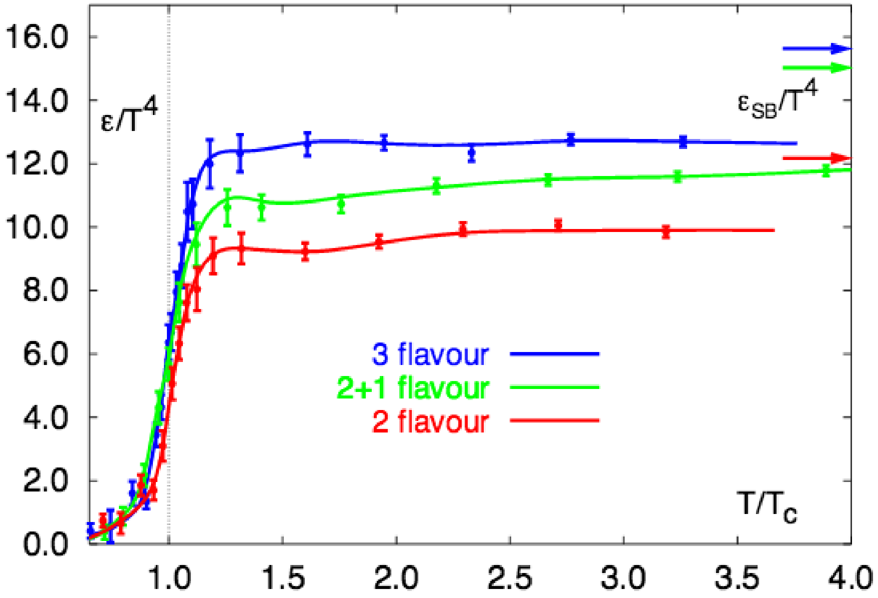

Figure 2.4: Energy density as a function of temperature calculated by lattice QCD. The results are shown for 2 or 3 light flavours or 2 light and 1 heavy flavour. Fig. from [17].

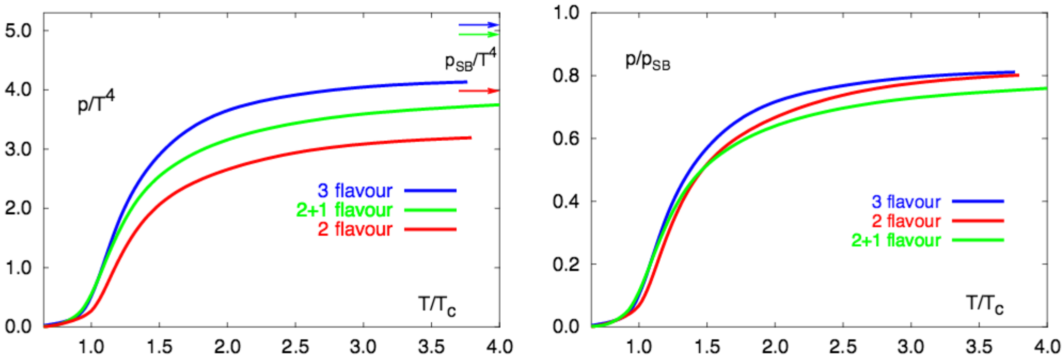

Figure 2.5: Pressure as a function of temperature calculated by lattice QCD. p_{SB} is the pressure of an ideal gas. The results are shown for 2 or 3 light flavours or 2 light and 1 heavy flavour. Fig. from [18].

With all that exposed, the study of the QGP state is of fundamental interest in the context of understanding the QCD phase diagram and the crossover between the hadronic phase and the strongly-interacting matter. So that, ways to experimentally explore and assess the QGP properties are highly desired, and the question that shall be discussed in the next section is: How to experimentally reproduce the conditions for the formation of the QGP?

2.2 Probing the QGP state: heavy-ion collisions

In Fig. 2.3 it is possible to notice how extreme are the conditions for the QGP formation and for the hadronic phase transition. The controlled reproduction of this state can only be achieved under very specific and stringent experimental conditions, where equivalent energy density can be obtained.

The high temperatures, typically achieved in heavy-ion collisions, make this process well suited for the study of the QGP, and this is the only way the human being has found to reproduce under controlled situation the same conditions of the early times of the universe. In Fig. 2.6 is shown a schematic view of a heavy-ion collision.

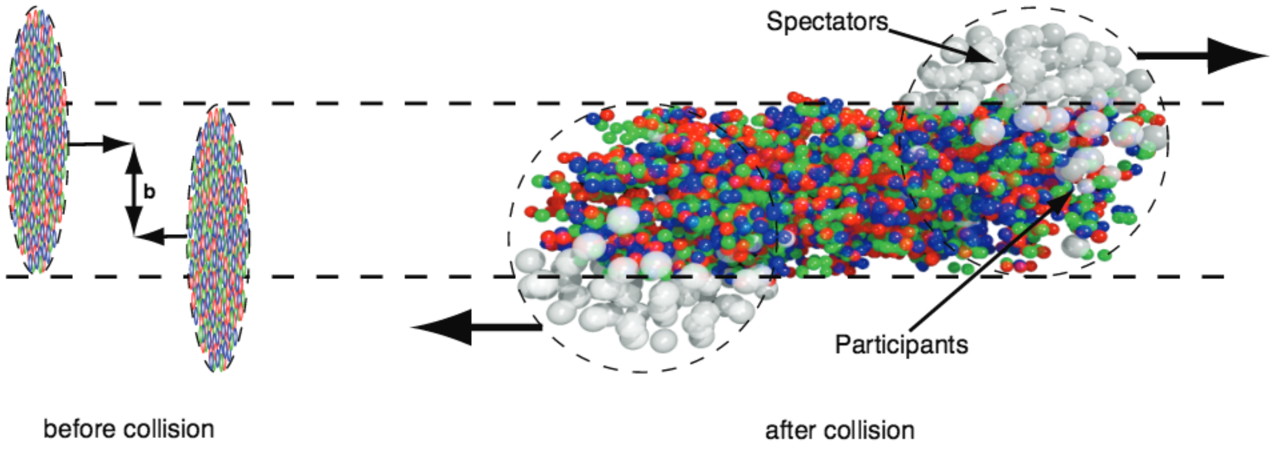

Figure 2.6: Schematic view of a heavy-ion collision with impact parameter b. Fig. from [19].

Fig. 2.7 shows a schematic view of the evolution of a heavy-ions collision. The abscissa z is the beam direction and the ordinate t is the time. The stages of the evolution are [20]:

- Pre-equilibrium: Right after the heavy-ion collision, many quarks and gluons are created by inelastic collisions. At this moment, the matter is in a pre-equilibrium stage, where the created partons interact with themselves. Due to the increase of density, more and more quark-antiquark ($q\bar{q}$) pairs are created.

- Formation of the QGP: When this partonic matter reaches the equilibrium, we have the state of matter called QGP.

- Hadronic matter: The pressure in the QGP is very high and the medium expands due to the gradient of pressure. With the expansion, the density starts to decrease and the hadronization starts.

- Free hadrons: The system expands until it is cold enough to elastic collisions between particles stop to occur. In this stage the hadrons momenta are fixed.

Much effort has been directed to assess the QGP properties by means of heavy-ion collisions. The most recent (and largest) experiment is the Large Hadron Collider (LHC). Studies of heavy-ion collisions are an integral part of the LHC physics program. The first Pb-Pb collision in the LHC was performed in the end of 2010. Three detectors participate in the

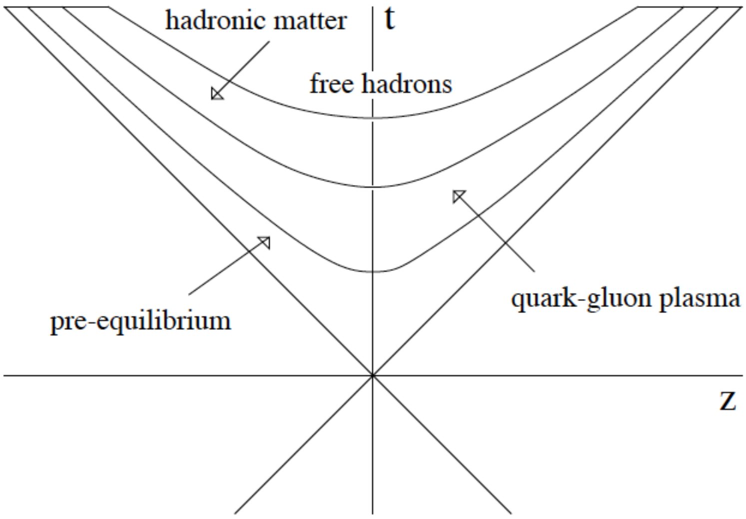

Figure 2.7: Evolution of a heavy-ion collisions. After the collision, there is a pre-equilibrium phase, followed by the formation of the QGP. When the QGP expands, it starts to cool down and the density starts to decrease, leading to hadrons formation. This is the hadronic matter. The next phase is the free hadrons that will be measured (directly or indirectly) by the detectors. Fig. from [21].

LHC heavy-ion program: ALICE (A Large Ion Collider Experiment), ATLAS (A Toroidal LHC ApparatuS) and CMS (Compact Muon Spectrometer). ALICE detector is the only one fully dedicated to the QGP studies. The fourth detector in LHC is the LHCb, dedicated to studies of beauty production. This detector did not take data in the first Pb-Pb run due to occupancy limitation, but the LHCb has measurements in pp and p-Pb collisions.

The LHC is the highest-energy particle accelerator ever constructed, and it has provided Pb-Pb collisions at $\sqrt{s_{NN}}$ = 2.76 TeV, exceeding the RHIC (Relativistic Heavy Ion Collider) collisions energies ($\sqrt{s_{NN}}$= 0.2 TeV) by more than one order of magnitude. In 2015 the LHC started its run-2, taking data in Pb-Pb collisions at $\sqrt{s_{NN}}$= 5.02 TeV and pp collisions at $\sqrt{s}$ = 13 TeV, establishing by far new energy records.

The history of heavy-ion collisions at CERN started with SPS (Super Proton Synchrotron). The SPS started its operation in 1976 and in 1994, started the heavy ions collisions (Pb-Pb). Possible evidences of the production of QGP were observed in the SPS [22]: The enhancement of the production of strange and multi-strange baryons when compared to pp collisions [23, 24] and suppression of the production of J/ψ meson [25]. Both of this effects were previously predicted by the theory [26, 27]. Today SPS is used as the final injector for the LHC.

The LHC accelerator schematic view is shown in Fig. 2.8. The ions are created in the ion source, which provides ^{128}Pb isotopic beam, that is guided to a spectrometer to select only the 29+ charge state. The selected ions are injected into a linear accelerator and accelerated to 4.2 MeV/n. Then, the beam is stripped to Pb^{54+} by a carbon foil (of 0.3 μm) and the

Pb^{54+} are selected by another spectrometer. The selected ions are injected into the CERN Low Energy Ion Ring (LEIR). The LEIR is used to transform the low intensity pulses of ions into shorter bunches of ions with high intensity. The bunches from LEIR are then injected into CERN PS (Proton Syncrotron), where they are accelerated to 5.9 GeV/n and stripped to Pb^{82+} using an aluminium foil of 0.8 mm. These ions are inserted to SPS where they are accelerated to 177 GeV/n. After reaching this energy they are injected into LHC [28].

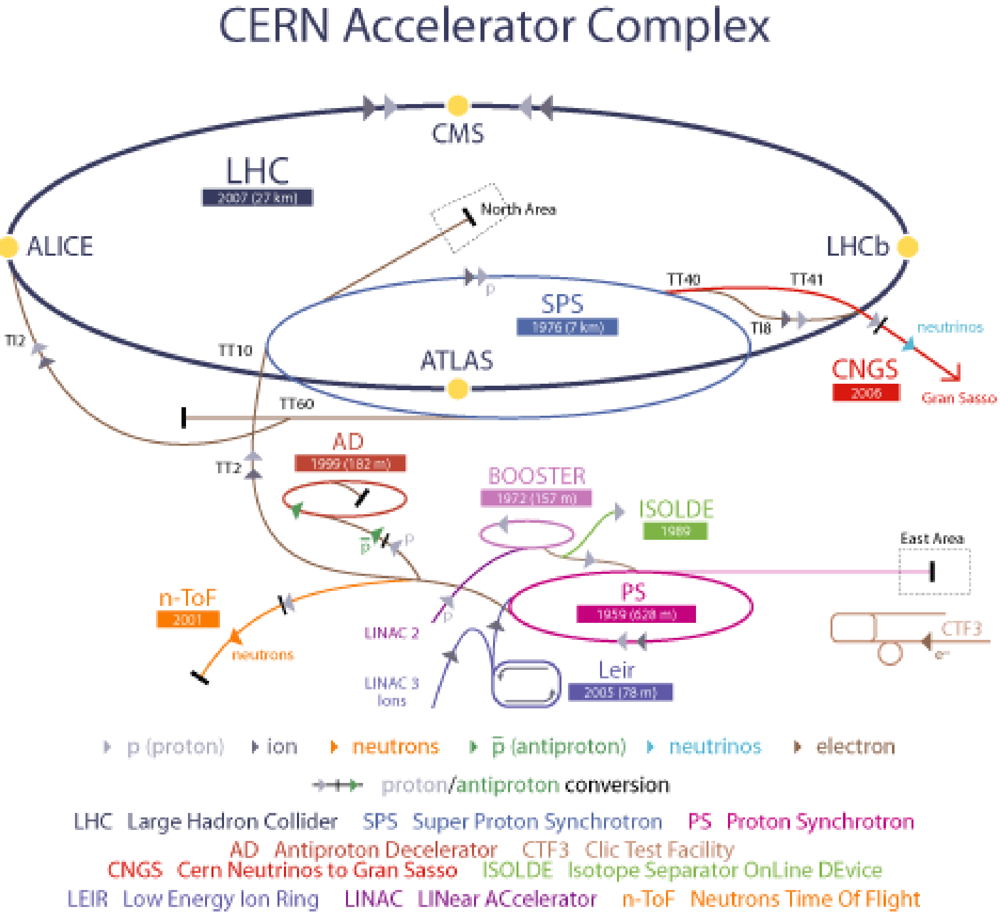

Figure 2.8: Schematic view of LHC injector [29].

In the LHC run-1, two heavy-ions runs and one p-Pb run were performed. The runs are listed below in chronological order:

- November-December 2010, Pb-Pb collision: It had 120 colliding bunches in each ring, with a centre of mass energy of $\sqrt{s_{NN}} = 2.76$ TeV per nucleon pair, integrated luminosity of 7 μb^{-1}.
- November-December 2011, Pb-Pb collision: It had 360 colliding bunches in each ring, also with a centre of mass energy of $\sqrt{s_{NN}} = 2.76$ teV per nucleon pair and the integrated luminosity was 150 μb^{-1}
- January-February 2013, p-Pb collision: Provided proton-lead collision at $\sqrt{s_{NN}} = 5.02$ TeV per nucleon in the centre of mass. The integrated luminosity in this case was around 32 nb^{-1}.

The LHC also provides pp collisions, used for heavy-ion studies as a reference for normalisations (we will come back to this later). The energies of pp collisions provided in the LHC run-1 were measured at $\sqrt{s} = 0.9$, 2.76, 7 and 8 TeV in the centre of mass energies.

These collisions were analysed by ALICE, ATLAS and CMS and they have complementary results. ALICE has a very good hadron identification, while ATLAS and CMS can make precise measurements of probes in high transverse momentum (p_{T}).

Initially, the results from LHC confirmed what was established by RHIC: a hot and dense medium that flows with a viscosity to shear-entropy ratio close to the predicted lower bound was created [30, 31].

In this thesis we use the ALICE detector data to study the QGP by means of measuring heavy-flavour particles. Heavy quarks, mainly charm and beauty, play a crucial role when probing the QGP since they are not constituents of the bulk part of the plasma, once they are created in initial hard parton scatterings. Therefore, heavy-flavour observables can bring insights of the properties of the QGP, as will be discussed in the next section.

2.3 Open heavy-flavour production in heavy-ion collisions

One of the available probes to study the QGP is the open-heavy flavour hadrons, which are particles carrying single charm or single beauty, as for instance: B meson, D meson, Λ_c and the Λ_b. Open heavy-flavour production are experimentally accessible through the reconstruction of their hadronic decays via invariant mass method, or through the measurements of their decay products. In the ALICE detector, the possible ways to study open heavy-flavour production are:

- Hadronic decay channel: when D mesons are reconstructed via their hadronic decays. The possible D-meson hadronic decays are listed in Tab. 2.1:

Decay channel	Branching ratio (%)
$D^+ \to K^-\pi^+\pi^+$	9.13
$D^0 \to K^-\pi^+$	3.88
$D^{*+} \to D^0\pi^+$	67.7
$D_s^+ \to \Phi\pi^{\to} K^+K^-\pi^+$	2.28

Table 2.1: Hadronic decays of D-meson species and their branching ratio.

- Semi-leptonic decay channel: B, D $\to l+X$ with branching ration of around 10%, where l can be either electrons or muons.

- Separation of electrons generated by beauty and charm decays: Since beauty quarks lives longer than charm quarks, their decay to electrons occurs later and this information can be used to separate both sources.

Studies of the interaction of heavy quarks with the QGP are of particular interest in heavy-ion physics. This is because heavy quark masses[5] exceed the QCD scale parameter $\Lambda_{QCD} \simeq 0.2$ GeV, and their production occurs mainly on initial hard partonic scatterings (in the heavy-ion collision process itself). Once formed, heavy quarks can live much longer ($\sim 10^{-11}$ sec) than the duration of the QGP ($\sim 10^{-23}$ sec) [33]. Therefore, they can experience the whole evolution of the system. Additionally, they can be treated by perturbative QCD even at low transverse momentum [34], in contrast with gluon and light quarks which can be treated perturbatively only at high transverse momentum. And finally, charm and bottom do not occur as valence flavour in the beam particle as ligth quarks (u, d and s). This implies that differently from light quarks, identified heavy flavour hadrons do not carry ambiguous information on its interaction with the QGP [3].

Therefore, the QCD can describe the production of the heavy-flavour, and measurements of these particles in pp collisions provide a crucial test of the perturbative QCD. Differently than in pp collisions, in heavy-ion collisions there are cold nuclear matter (CNM) effects (this effects will be discussed in Sec. 3.2) together with effects due to the formation of the QGP. In this situation, the QCD can only describe the initial production of heavy-flavour but not the observed spectrum after interacting with the QGP. Then, since the measurements in pp collisions is well described by the perturbative QCD, it can be used as the reference for the heavy-ion collisions, and the effects due to the interaction with the QGP or the CNM effects can be measured.

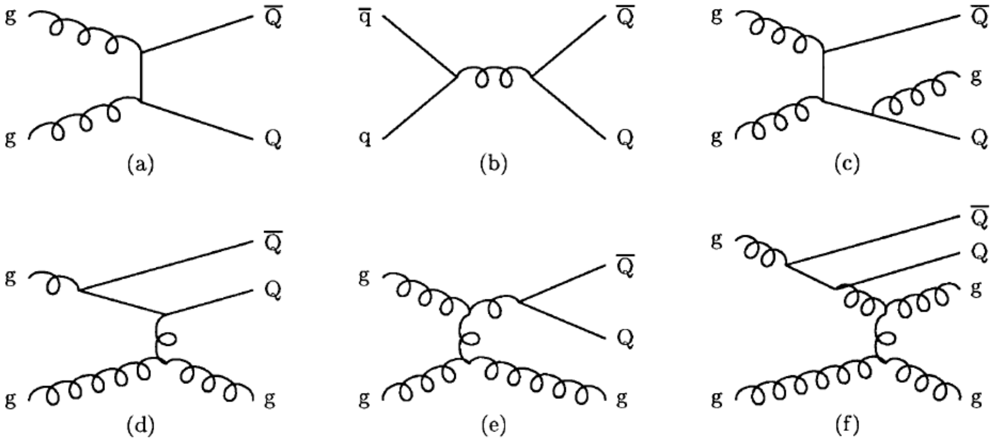

Figure 2.9: Fig. from ref. [3] Fig. 1a–f. Examples of heavy-flavor production diagrams. a,b. Leading order. c. Pair creation (with gluon emission). d. Flavor excitation. e. Gluon splitting. f. Events classified as gluon splitting but of flavor-excitation character. Fig. from [3].

The heavy-flavour production can be divided in three classes:

- Pair creation: In this case, the hard subprocess is one of the two Leading Order (LO) process, and are represented in Fig. 2.9a, 2.9b and 2.9c. In the case of Fig. 2.9a it is

---

[5] $m_c = 1.29^{+0.05}_{-0.11}$ and $m_b = 4.19^{+0.18}_{-0.06}$ GeV [32]

shown the process gg → $Q\bar{Q}$, where Q means a heavy quark. In Fig.2.9b it is shown the process $q\bar{q}$ → $Q\bar{Q}$ and in Fig. 2.9c it has the addition of a shower of a gluon. The shower do not modify production cross section but changes kinematics. For example, in case of 2.9a or b, the Q and $\bar{Q}$ have to emerge back-to-back in order to not violate the momentum conservation. On the other hand, in case of 2.9c the parton shower allows a net recoil by other partons [3].

- Flavour excitation: It is the process shown in Fig.2.9d, where a heavy flavour is generated in the parton distribution function from one of the incident particle (Q is on the mass shell of the particle) and scatter against a parton in the other beam particle. When Q is not a valence flavour it has to come from gluon splitting g → $Q\bar{Q}$ inside the incident particle previously the scattering [3].
- Gluon spliting: That is the case where there is no heavy-flavour in the hard scattering as shown in Fig.2.9e. In this process the branching $Q\bar{Q}$ can occur in the initial or final state shower [3].

Figure 2.9f is an event considered as gluon splitting but it has flavour-excitation characteristics. In that process a gluon first branches to $Q\bar{Q}$ and one of the Q later emits another gluon. The gluon is the one that participates in the hard scattering [3].

In the pQCD approach, the production process of a hadron composed by a heavy-flavour can be factorized in the following components [34]:

- The initial conditions: parametrized as Parton Distribution Function (PDF).
- The partonic scattering cross section: calculated using pQCD for the processes of the heavy-quark production shown in Fig. 2.9.
- Fragmentation of heavy-quarks into heavy-flavour hadrons: open heavy-flavour (like B or D meson) or hidden heavy-flavour (quarkonium states, like J/ψ) can be formed.

2.4 Experimental observables

There are several observables that can be used to study the QGP, such as particle yields, particle momentum distributions, multiplicity dependence of particle production, two particle correlations, jets spectrum, azimuthal anisotropy and nuclear modification factor.

Here, we only discuss the azimuthal anisotropy and the nuclear modification factor measurements. This thesis consists in the measurements of the nuclear modification factor of electrons from heavy-flavour decay in p-Pb collisions. These measurements are used to understand the energy losses in the QGP formed in Pb-Pb collisions, then in the following sections, we give an introduction for the nuclear modification factor in p-Pb and in Pb-Pb collisions. The concept of the elliptic flow is also given, since these measurements, together with the nuclear modification factor establishes constraints for energy loss models that try to explain the interaction of heavy-flavour hadrons with the QGP.

Due the interaction with the QGP, the momentum of particles will be decreased, what makes they thermalize and participate in collective flow dynamics [35]. This interaction can be studied experimentally via elliptic flow and nuclear modification factor. The elliptic flow is an anisotropic flow caused by the initial asymmetries in the geometry of the system due to a non-central collision, and the initial spatial anisotropy of the created particles is converted in momentum anisotropy due to the pressure gradients of the medium. Since thermalised particles will flow with the medium, this quantity is used to determine the thermalisation level of the medium, as will be explained in Sec. 2.4.1. On the other hand, the nuclear modification factor is a quantity to measure the energy loss of the particles in the medium, by comparing the results of the produced particles in heavy-ion collisions with those in pp collisions, as will be explained in Sec. 2.4.2.

2.4.1 Azimuthal anisotropy

As mentioned before, the anisotropic flow is caused by the initial asymmetries in the geometry of the system produced in a non-central collision, as pictorially shown in Fig. 2.10. The matter in the overlapped area of the two colliding nuclei gets compressed and heated, creating the QGP. The initial spatial anisotropy of the created particles is converted in momentum anisotropy due to the pressure gradients of the medium.

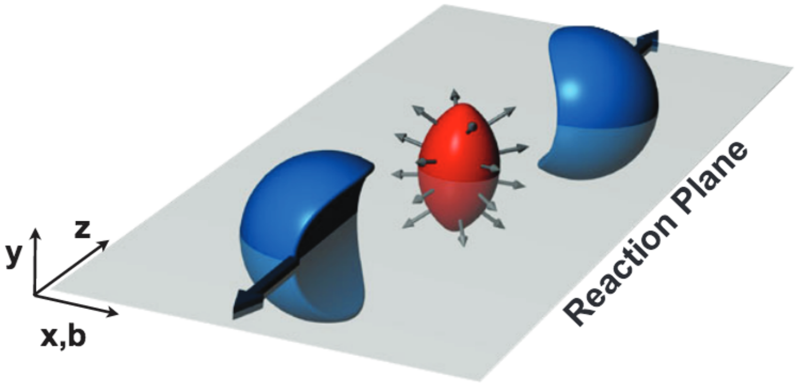

Figure 2.10: Schematic view of a non-central collision of two nuclei and the definition of the reaction plane. The initial spatial anisotropy of the created particles, with respect to the reaction plane, is converted in momentum anisotropy due to the pressure gradients of the medium. Fig. from [19].

The yield of the produced particles as a function of the transverse momentum can be described by a Fourier series, as in Eq. 2.4.

$$E\frac{d^3N}{dp_T^3} = \frac{d^3N}{p_T d\phi dp_T dy}\sum_{n=0}^{\infty} 2v_n cos[n(\phi - \Phi_R)] \tag{2.4}$$

where ϕ is the azimuthal emission angle of the particles with respect to the orientation of the reaction plane Φ_R, which is defined as a plane formed by the beam direction (z) and the impact parameter direction (b) (see Fig. 2.10).

The harmonic coefficients (v_n) quantify the strength of the anisotropy, and the specific case of the second harmonic, which is known as elliptic flow, is given by:

$$v_2 =< cos[2(\phi - \Phi_R)] > \tag{2.5}$$

The flow is caused by multiple interactions of the constituents of the created medium. The laws of ideal or viscous relativistic hydrodynamics predicts the azimuthal asymmetry in the momentum space of an expanding medium [36, 37].

It is expected that more interactions imply in higher values of the anisotropic flow as well as a higher degree of thermalization of the medium. Thus, the magnitude of the flow is a probe of the level of thermalization of the medium [19] and v_2 is expected to be sensitive to the early dynamics of the collision. The higher order components v_n are related to fluctuations of the initial state geometry.

Comparisons of the v_2 measurements with hydrodynamic predictions indicates that the produced medium expands collectively almost like a perfect fluid, with a small shear viscosity to entropy density ratio, η/s. The values found are close to the lower bound of $\eta/s = 1/4\pi$ [38].

2.4.2 The nuclear modification factor

The medium formed in heavy-ion collisions are very dense, what implies that quarks and gluons created in the initial state of the collision (in initial partonic hard scattering process) lose their energy as they propagate through the created plasma.

In order to quantify the energy losses in the medium, the nuclear modification factor (R_{AA}) is used. It is defined as the yield of given produced particles in heavy-ion collisions divided by the yield of the same particle produced in pp collisions, after a normalisation considering a superposition of independent binary nucleon-nucleon collisions. The expression for R_{AA} is given by Eq. 2.6.

$$R_{\mathrm{AA}} = \frac{1}{< N_{\mathrm{coll}} >} \frac{\mathrm{d}N^{\mathrm{AA}}/\mathrm{d}p_{\mathrm{T}}}{\mathrm{d}N^{\mathrm{pp}}/\mathrm{d}p_{\mathrm{T}}} = \frac{1}{< T_{\mathrm{AA}} >} \frac{\mathrm{d}N^{\mathrm{AA}}/\mathrm{d}p_{\mathrm{T}}}{\mathrm{d}\sigma^{\mathrm{pp}}/\mathrm{d}p_{\mathrm{T}}} \tag{2.6}$$

where $\mathrm{d}N^{AA}/\mathrm{d}p_{\mathrm{T}}$ is the p_{T}-differential invariant yield measured in AA collision, $\mathrm{d}N^{\mathrm{pp}}/\mathrm{d}p_{\mathrm{T}}$ is the p_{T}-differential invariant yield measured in pp collision at the same energy in the centre of mass reference frame, and $< N_{\mathrm{coll}} >$ is the number of binary collisions calculated based on Glauber Model [39]. R_{AA} can be also defined using the cross section in pp collisions, $\mathrm{d}\sigma^{\mathrm{pp}}/\mathrm{d}p_{\mathrm{T}}$ and the $< T_{\mathrm{AA}} >$, which is the nuclear overlap function [40], also obtained via

Glauber model, and it is related to the number of nucleon-nucleon collisions and to the inelastic nucleon-nucleon cross section, $\sigma_{\mathrm{NN}}^{inel}$, as the following:

$$N_{\mathrm{coll}} = \sigma_{\mathrm{NN}}^{inel} T_{AA} \tag{2.7}$$

If there is no medium effects, the R_{AA} is expected to be equal to one. In case of suppression of the particles, the R_{AA} will be smaller than one in both intermediate and high transverse momentum. Effects due to the medium formed is also called *final state effects*. In heavy-ion collisions, the R_{AA} measurements are sensitive to the energy loss in the medium and also to Cold Nuclear Matter (CNM) effects. The CNM effects are present in the collisions due to the fact that the protons are bounded inside the nucleus. These effects are also called *initial state effects* and are the following:

- Parton density shadowing or saturation: These modifications can be described using modified nuclear Parton Distribution Function (nPDF) [41] or using Color Glass Condensate (CGC) theory [42].
- Momentum broadening: also known as Cronin enhancement [43], which can be explained as consequence of multiple scatterings [44, 45].
- Energy loss in the initial or final states [45].

In order to separate the CNM effects from the effects due to the medium (QGP), it is used p-A collisions. The R_{pA} is defined as the following:

$$R_{\mathrm{pA}} = \frac{1}{< T_{\mathrm{pA}} >} \frac{\mathrm{d}N^{\mathrm{pA}}/\mathrm{d}p_{\mathrm{T}}}{\mathrm{d}\sigma^{\mathrm{pp}}/\mathrm{d}p_{\mathrm{T}}} \tag{2.8}$$

where $\mathrm{d}N^{pA}/\mathrm{d}p_{\mathrm{T}}$ is the p_{T}-differential invariant yield measured in p-A collisions. If there is no CNM effects, the R_{pA} is expected to be one. The CNM effects are discussed with more details in Sec. 3.2.

2.5 Final considerations of this chapter

In this thesis we measured the nuclear modification factor of electrons from heavy-flavour hadron decays in p-Pb collisions at $\sqrt{s_{NN}} = 5.02$ TeV. The electrons measured are from B and D mesons decays. As explained in section 2.3, B and D mesons are produced in the initial state of the collisions and they can experience the full evolution of the system. Thus, they are key probes to study the properties of the QGP.

The B and D mesons semi-electronic decay have a branching ratio of around 10% and the produced electrons can be identified with a good purity by the ALICE detector. The measurements in p-Pb collisions is important to understand the results obtained in Pb-Pb collisions, separating initial and final states effects. As explained in section 2.4.2, in A-A collisions take place both the initial state cold nuclear matter effects and final state effects. The latter can also modify the final state observables. On the other hand, in p-Pb collisions, it is not established an extended medium, and only the cold nuclear matter effects are expected.

In Pb-Pb collisions, a suppression of the yield of electrons from heavy-flavour hadron decays (HFE) relative to a binary scaled pp reference was observed in the transverse momentum range $3 < p_{\rm T} < 18$ GeV/c in the most central collisions [46]. Fig. 2.11 shows the nuclear modification factor of HFE in Pb-Pb collisions at $\sqrt{s_{NN}} = 2.76$ TeV. This suppression can be interpreted in terms of parton energy loss in the plasma[6]. However, CNM effects can also be present in heavy-ion collisions, and by studying the p-Pb collisions, it is possible to correct for its contribution.

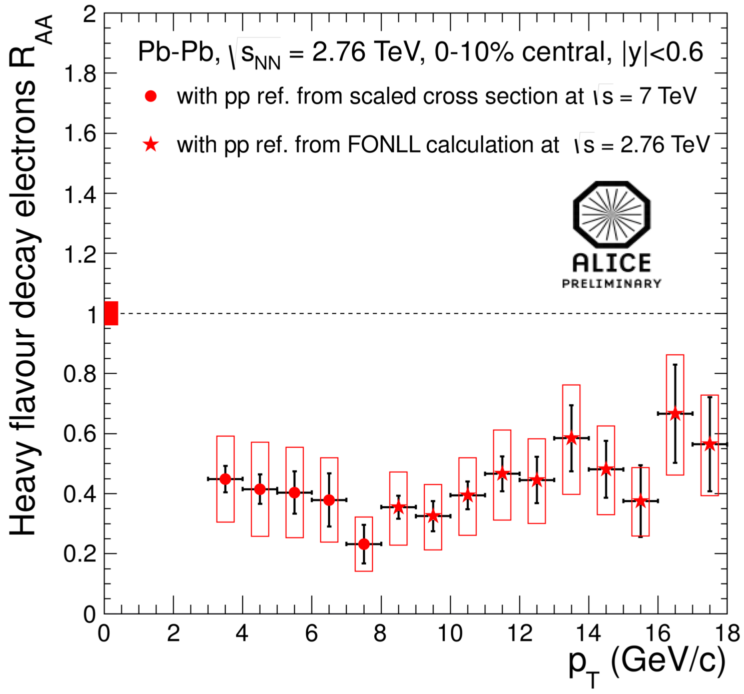

ALI-PREL-31917

Figure 2.11: Nuclear modification factor of electrons from heavy-flavour hadron decays in Pb-Pb collisions at $\sqrt{s_{NN}} = 2.76$ TeV [46].

Measurements of pp and p-Pb collisions can provide a solid baseline for the studies of the QGP properties in Pb-Pb collisions. Additionally, the understanding of the nuclear effects that interfere in hadronic observables in p-Pb collisions has its importance by its own, since this measurements can be used to elucidate the QCD dynamics of the multi parton interactions, the transport properties of the CNM, the structure of the nucleus and multi-parton correlations [45].

This is the first measurement of electrons from heavy-flavour hadron decays in p-Pb collisions at $\sqrt{s_{NN}} = 5.02$ TeV in the intermediate and high transverse momentum (range up to 20 GeV/c).

---

[6] Indeed, several energy loss models can explain, at least qualitatively, the suppression observed in Pb-Pb collisions for HFE $R_{\rm AA}$.

Chapter 3

Heavy Quarks production and its interaction with Cold and Hot medium

In this chapter we present some models for the production of heavy-quarks and the mechanisms of its interactions with cold and hot nuclear matter. For Cold Nuclear Matter (CNM) we consider the matter present within a nucleus, and for hot nuclear matter we consider a medium consisting of a QGP state.

To understand the properties of the cold or hot medium, we use theoretical calculations, with certain assumptions for the particles interactions with the medium, and the models are compared to the experimental data. The comparison between experimental data and theoretical models give us insights about the physics of the studied medium, since we can corroborate or not some of the proposed theoretical hypothesis. In this chapter, we discuss some of the theoretical assumptions for the cold nuclear matter that can give possible explanations to the measured particles production in p-A collisions. On the other hand, in A-A collisions, it is expected a combination of cold nuclear matter effects and QGP effects. Then, models including both effects can be used to understand the interaction of the produced particles with the medium. Furthermore, the measurement in p-A collisions is used to quantify the CNM effects and provide a reference for A-A collisions, in order to separate the effects from CNM and those from the QGP.

Thus, the effects of this two different media in the production and propagation of heavy flavour are different, and this chapter will present the main features of each of these topics. Additionally, it is also important to describe the heavy-flavour production itself, outside the nuclear medium, which is presented in Sec. 3.1, where a brief review of the heavy-flavour production in pp collisions is given. The review presented for pp collisions is based on a more complete review, published in [34]. In Sec. 3.2 we present the CNM effects and in the Sec. 3.3 we present models for the interaction of heavy-flavour particles with the QGP.

3.1 Heavy-quarks production

In this section we present some theoretical approaches to calculate the hadronic cross-section of heavy-flavour in pp collisions and how this models can describe the experimental data. We start giving a brief introduction about the FONLL, the GM-VFNS and the k_{T}-factorization approaches to calculate the production of heavy-flavour. Then, we show some experimental results and its comparison with these approaches.

3.1.1 FONLL

The FONLL [47, 48] is a framework that uses next-to-leading order (NLO) QCD with all-order resummation of next-to-leading log (NLL) to calculate hadronic cross sections. The NLO calculation of the hadronic cross section can be given by:

$$\frac{d\sigma}{dp_T^2} = A(m)\alpha_s^2 + B(m)\alpha_s^3 + \mathcal{O}(\alpha_s^4) \tag{3.1}$$

where the coupling constant is related to the renormalisation μ_R and factorization μ_F scale as $\alpha_s = \alpha(\mu)$ and m is the heavy-quark mass. In case of the NLL resumed calculation, we have the following expression:

$$\frac{d\sigma}{dp_T^2} = \alpha_s^2 \sum_{i=0}^{\infty} a_i \left(\alpha_s \log \mu/m\right)^i + \alpha_s^3 \sum_{i=0}^{\infty} b_i \left(\alpha_s \log \mu/m\right)^i + \\ \mathcal{O}\left(\alpha_s^4 \left(\alpha_s \log \mu/m\right)^i\right) + \mathcal{O}\left(\alpha_s^2 \times PST\right) \tag{3.2}$$

where PST stands for the suppressed terms. The FONLL framework combines both results:

$$\frac{d\sigma}{dp_T^2} = A(m)\alpha_s^2 + B(m)\alpha_S^3 + \left(\alpha_s^2 \sum_{i=0}^{\infty} a_i \left(\alpha_s \log \mu/m\right)^i + \alpha_s^3 \sum_{i=0}^{\infty} b_i \left(\alpha_s \log \mu/m\right)^i\right) \times G(m, p_T) + \\ \mathcal{O}\left(\alpha_s^4 \left(\alpha_s \log \mu/m\right)^i\right) + \mathcal{O}\left(\alpha_s^4 \times PST\right) \tag{3.3}$$

where the function $G(m, p_{\mathrm{T}})$ is a function that has to approach 1 when $m/p_{\mathrm{T}} \to 0$.

This combination of NLO and NLL allows calculations of single inclusive distribution of heavy-quarks in transverse momentum, rapidity and pseudorapidity.

As an example, the production of a lepton l can be obtained in the FONLL framework as a numerical convolution of a perturbative cross section $d\sigma_Q^{FONLL}$ with a non-perturbative fragmentation function $D_{Q\to H_Q}$ and a decay function $g_{H_Q\to l}$ of the heavy-flavour hadron H_Q to the lepton, as the following:

$$d\sigma_l^{FONLL} = d\sigma_Q^{FONLL} \otimes D_{Q\to H_Q} \otimes g_{H_Q\to l} \tag{3.4}$$

where the parameters for $D_{Q\to H_Q}$ and $g_{H_Q\to l}$ are extracted from experimental data.

The renormalisation and factorization scales are set equal to the transverse mass $\mu_{R,F} = \mu_0 = \sqrt{p_{\rm T}^2 + m^2}$, where $p_{\rm T}$ and m are the transverse momentum and mass of the heavy quark, respectively. The uncertainties of the calculations are determined performing variations in the scales and mass of the heavy quarks and also includes the uncertainties of the parton distribution function (a discussion about parton distribution function is done in Sec. 3.2.1).

3.1.2 GM-VFNS

Another framework to calculate hadronic cross sections is the general-mass variable-flavour-number scheme (GM-VFNS) [49, 50].

For the calculation where $p_{\rm T} \leq m$, the approach fixed-flavour number scheme (FFNS) can be used assuming that gluons and light partons (u, d, s) are the only active partons, and the heavy-quarks emerge in the final state from hard scattering processes. For the case where $p_{\rm T} \gg m$, the formalism zero-mass variable flavour number scheme (ZM-VFNS) is used assuming that the heavy-quark is massless and comes as incoming partons or via fragmentation of light partons.

The GM-VFNS combines the FFNS and the ZM-VFNS, considering m not negligible and the large logarithms $ln(p_{\rm T}/m)$ are incorporated in the parton distribution and fragmentation functions.

The fragmentation functions are determined based on fits on experimental data and the theoretical uncertainties are determined varying the renormalisation and factorization scales and taking into account the parton distribution function uncertainties.

3.1.3 $k_{\rm T}$-factorization

$k_{\rm T}$-factorization [51] is also an approach to calculate hadronic cross section. The authors of [51] argue that the FONLL and GM-VFNS are approaches that cannot be used when the transverse momenta of charm quark and antiquark are not equal. In the $k_{\rm T}$-factorization framework, unintegrated gluon distributions in the proton are used. They are functions of the longitudinal momentum fractions of the nucleon that the gluon can carry.

The inclusive distribution of charmed mesons can be obtained by the convolution of the inclusive distribution of charm quarks and the fragmentation function, where it is used the Peterson Model.

3.1.4 Pre-RHIC measurements

In this section we present some of the heavy-flavour measurements before the RHIC and LHC era. The first open-charm particle was observed in the SLAC SPEAR[1] [52, 53] storage

---

[1] SPEAR stands for Stanford Positron Electron Accelerating Ring and SLAC is the Stanford Linear Accelerator Center

ring in 1976, while the first evidence of the open-beauty production was obtained by Cornell Electron Storage Ring[2] with CLEO [54] and CUSB [55] detectors in 1981. The open-charm particles were observed via measurements of hadronic decays and the open-beauty particles via electrons from semi-leptonic B-meson decays [34].

In that era, the heavy-flavour studies were handled mainly on fixed target experiments at $\sqrt{s} < 50$ GeV with pions and protons beams in the SPS at CERN, at the FNAL, and at DESY [34]. Most of the experiments used nuclear targets as Be, Al, Cu, and W [34]. A concise review of the results can be found in [56].

The Fig. 3.1 (left) shows the D meson production cross section in pp collisions as a function of $\sqrt{s}$ and in Fig. 3.1 (right) it is shown the corresponding total charm-anticharm ($c\bar{c}$) cross-sections, measured by different experiments. Both figures also show the PYTHIA [57] calculations (event generator including QCD at leading order (LO)) of the D meson production applying different parton distribution functions. Since higher order calculations are not included in PYTHIA, the calculations were scaled by an empirical factor. For the charm cross section production, the factor is between 2.5 and 4.5 and for the beauty, this factor is around 2 [34].

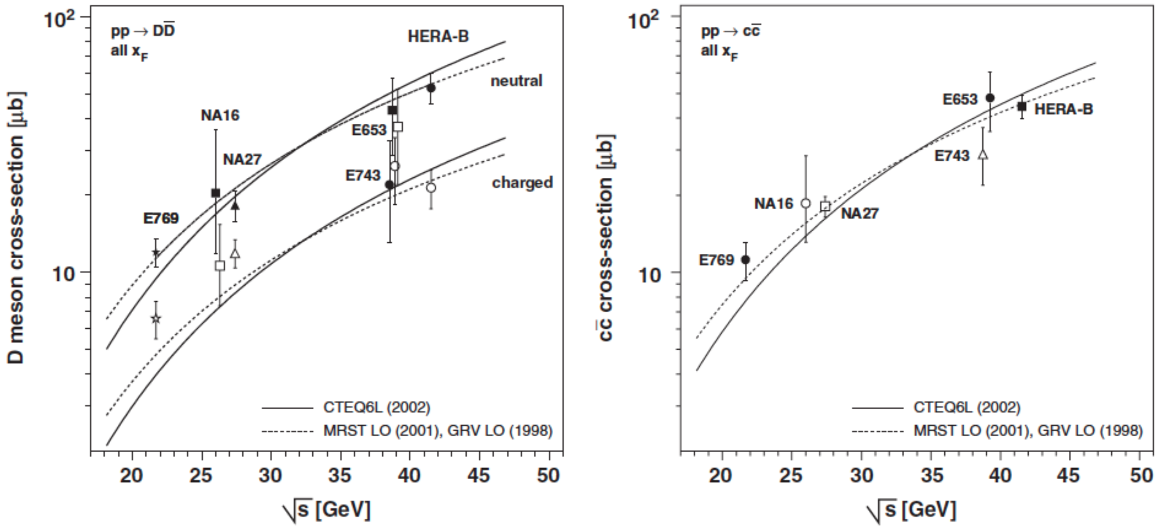

Figure 3.1: Cross-sections of neutral (closed symbols) and charged (open symbols) D meson (left) and corresponding total $c\bar{c}$ cross-section (right), as a function of $\sqrt{s}$, compared to PYTHIA LO pQCD calculations with three different parton distribution functions. Fig. from [56].

Fig. 3.2 shows bottom production cross section measured by different experiments, which is smaller than the charm production cross section by more than 2 orders of magnitude in the energy range of the measurements [34].

In the SPS at CERN, the production of open heavy flavour was studied indirectly, via the

---

[2] The Cornell Electron Storage Ring is an electron-positron collider

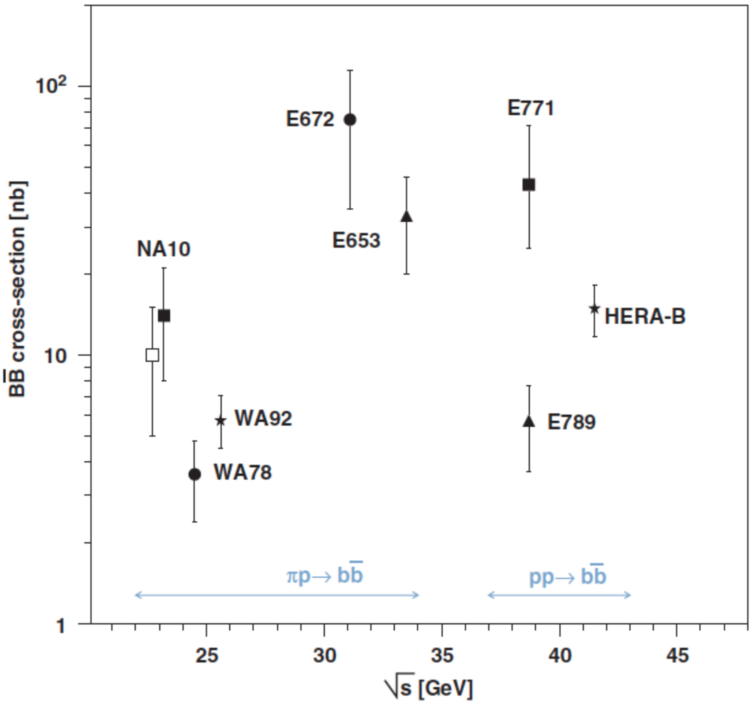

Figure 3.2: Cross-sections of B meson from fixed target πp and pp collisions. Fig. from [56].

measurements of simultaneous semimuonic decays of correlated D$\bar{\mathrm{D}}$ pairs to dimuon. Initially, the SPS was not able to separate the prompt and non-prompt (secondary vertices, proper for open charm decays) dimuons. The separation was possible only in the NA50[3], where it was also possible to derive the total charm cross section in pp collisions using PYTHIA [58]. It was assumed that in p-A collisions the total open charm cross section scales with mass number of the nuclear target [34].

The first open heavy flavour hadron-production measurement at a collider was done in the Intersecting Storage Ring (ISR) at CERN. Since ISR was a collider, the energy achieved was much higher than in previous fixed target experiments. In the beginning of the 1970's decade, the first measurement of electrons from semileptonic charm hadron decays was obtained by ISR in pp collisions at $\sqrt{s}$= 52.7 GeV [59]. At that time, since the charm was not discovered yet, the origin of the single electrons was not known [34].

Beauty production at colliders was first measured in the end of the 1980's in the Super Proton-Antiproton Synchrotron (Sp$\bar{\mathrm{p}}$S) at CERN [34]. The UA1 experiment measured the beauty production in p$\bar{\mathrm{p}}$ collisions at $\sqrt{s}$= 546 GeV and $\sqrt{s}$= 630 GeV. The UA1 experiment also measured the $D^{\star +}$ meson reconstructing its hadronic decay. It was the only charmed meson that could be reconstructed with the UA experiment [34]. A review of the measurements of heavy-quark production at the CERN Sp$\bar{\mathrm{p}}$S can be found in [60].

The Tevatron at Fermilab started its operation in 1980's decade and the measurements of open heavy-flavour production was performed in 1990's decade with the CDF and D0 ex-

---

[3] NA50 was one of the fixed target experiments that used the proton and lead beams of the SPS at CERN

periments[4] in p$\bar{\text{p}}$ collisions at $\sqrt{s}$= 1.8 TeV (run-1) and $\sqrt{s}$= 1.96 TeV (run-2). The results of open bottom hadron production from run-2 at the Tevatron are consistent with FONLL pQCD calculations [61]. The charm measurements were only accessed in Tevatron run-2 by the CDF experiment. In the charmed meson case, the FONLL calculation is systematically lower than the measurements, but still consistent within experimental and theoretical uncertainties [62].

The open heavy flavour hadron production measurements in pp and p$\bar{\text{p}}$ collisions can be described by pQCD, as the results obtained by fixed target experiments.

Despite observed in the pre-RHIC era, it was only with the start of high energy nucleus-nucleus colliders (RHIC and LHC) that open heavy flavour hadrons started to have their role as unique probes for hot QCD matter [34]. In the next section we present the RHIC results for open heavy-flavour hadrons decays in pp collisions, followed by a section of LHC pp measurements.

3.1.5 RHIC pp measurements

PHENIX and STAR experiments at RHIC have studied the open heavy-flavour hadrons since 2000. In this section we present results in pp collisions.

In the PHENIX detector, the open heavy-flavour hadrons are studied via the measurements of the leptons (electrons and muons) from heavy-flavour measurements decays. PHENIX can provide studies of the rapidity dependence of open heavy-flavour production measuring electrons at midrapidity and muons at forward rapidity. Moreover, with the STAR detector the heavy-flavour hadrons can be fully reconstructed via their hadronic decay products and can be also studied via the heavy-flavour hadron decays to electrons.

In pp collisions at $\sqrt{s_{NN}} = 200$ GeV, STAR has measured the c$\bar{\text{c}}$ production cross section, using the measured D^0 and $D^{\star +}$ cross section applying the fragmentation ratios of c $\rightarrow D^0$ and c $\rightarrow D^{\star +}$ [63]. The result is shown in Fig. 3.3, where it is also compared to FONLL pQCD calculations. The upper limit of the calculation is consistent with the experimental results.

The heavy-flavour hadron decay to electrons were measured by STAR and PHENIX. The layout of both experiments was optimized to reduce the background, which is formed by electrons from photon conversion in the detector material and electrons from light meson Dalitz decays. Fig. 3.4 shows the cross section measured by PHENIX [64] and Fig. 3.5 shows the cross section measured by STAR [65]. For the STAR case, two measurements are shown: Including SVT[5] detector (the detector was installed, but not being used in the data taking), in the range $1.2 < p_T < 10$ GeV/c and without the SVT detector in the range $3 < p_T < 10$

---

[4] CDF and D0 are the two experiments at Tevatron collider. CDF stands for Collider Detector at Fermilab and D0 was named for its location on the accelerator ring.

[5] SVT stands for Silicon Vertex Tracker, which is a detector installed to improve the vertex determination of the collisions.

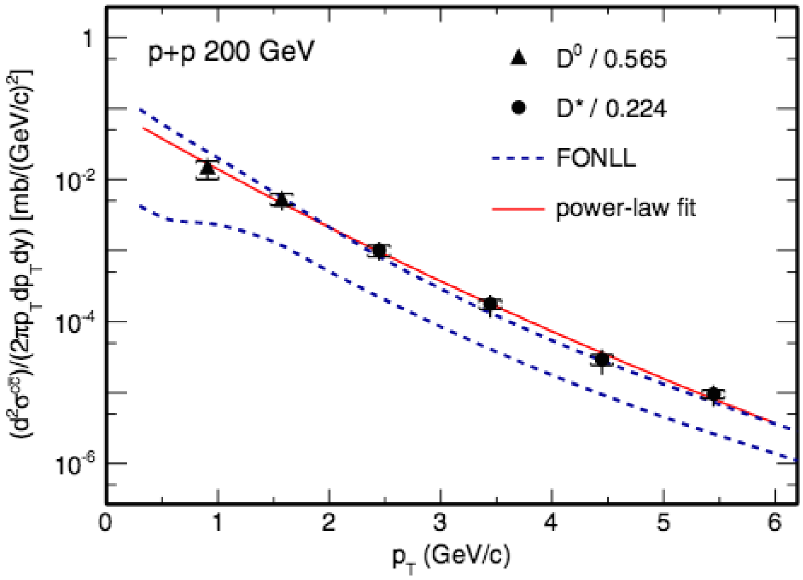

Figure 3.3: $c\bar{c}$ production cross section obtained by STAR using the D^0 and $D^{\star +}$ cross sections measurements in pp collisions at $\sqrt{s_{NN}}$ = 200 GeV, compared to FONLL calculations. Fig. from [63].

GeV/c, where the precision of the data was improved[6].

As can be noticed in Fig. 3.4 and Fig. 3.5, the pQCD calculations are in agreement with the measured data. Although the experimental points are close to the upper limit of the theoretical predictions, the results are still consistent with the measurement of D-meson performed by STAR, shown in Fig. 3.3.

Another important measurement performed by RHIC was the separation of charm and beauty decay contributions to electrons, in order to test the FONLL pQCD predictions. This measurement is also important to provide individual references for the electron decay spectra from the two heavy quark species in heavy-ion collisions. The separation in STAR and PHENIX was based on electron-hadron correlation measurements. PHENIX has measured the invariant mass distribution of electron-hadron pairs and has compared to charm and bottom decay distributions obtained by PYTHIA and EVTGEN simulations [66]. This distributions were fitted to the data, to extract the relative contributions. In the STAR, the azimuthal angle between electrons from heavy-flavour decays and hadrons were measured and PYTHIA simulations were used to extract the relative contributions from charm and beauty decays.

Fig. 3.6 and Fig. 3.8 show the results of the relative contributions from charm and beauty decays for PHENIX and STAR, respectively. The electron production cross section from charm and beauty separately is also shown in Fig. 3.7 for PHENIX and Fig. 3.9 for STAR. For both experiments, the results are compared with the expectation from FONLL pQCD calculations, and the results are in good agreement.

---

[6] SVT detector increases the background, due to its thickness in terms of radiation length.

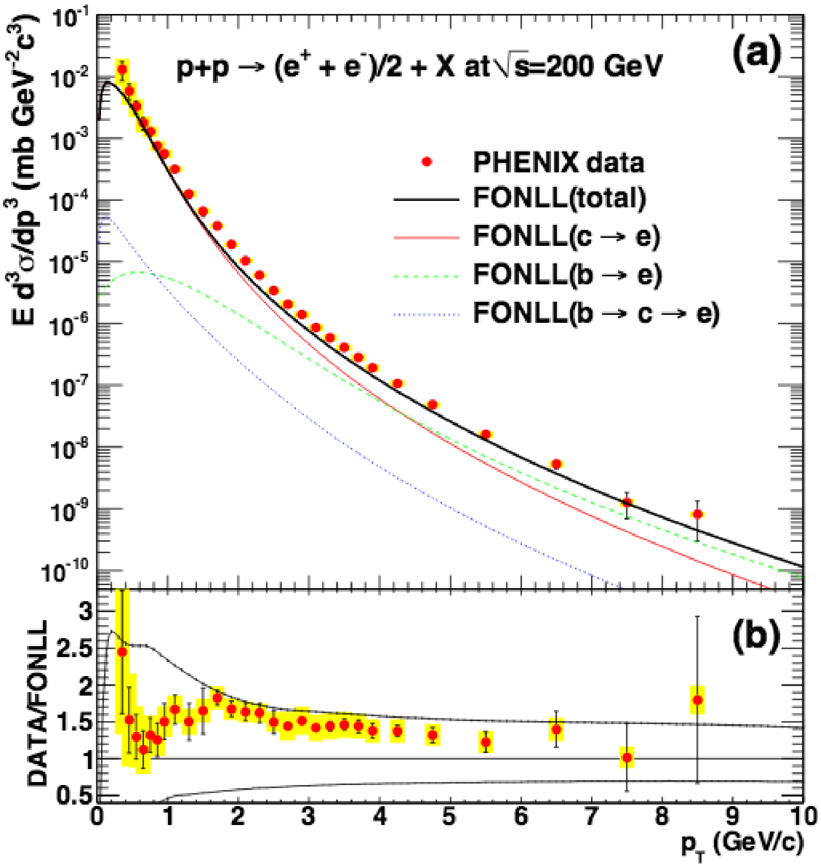

Figure 3.4: Invariant cross section of electrons from heavy-flavour hadron decays as a function of p_T measured by PHENIX in pp collisions at $\sqrt{s_{NN}} = 200$ GeV compared to FONLL pQCD calculations (upper panel). The lower panel shows the ratio of the data and the calculation. Fig. from [64].

In the Fig. 3.10 it is shown the results of charm production cross section as a function of rapidity measured by PHENIX in pp collisions at $\sqrt{s} = 200$ GeV via measurements of open heavy-flavour hadron decay to electrons at mid rapidity and to muons at forward rapidity [69]. The FONLL pQCD prediction is shown in the figure and the experimental data are closer to the upper limit of the calculations. However, the shape of the rapidity distribution cannot be discussed due to the large experimental and theoretical uncertainties.

3.1.6 LHC pp measurements

The ALICE has studied the open heavy-flavour production, in pp collisions, via semi-leptonic decays (electrons and muons) and hadronic decays (B and D meson decays to hadrons).

In the hadronic channel, the open charm is studied via the reconstruction of D mesons. Fig. 3.11 shows the production cross section of D^0, D^+ and D^{*+} measured by ALICE in pp collisions at $\sqrt{s} = 7$ TeV [70]. The data is compared to FONLL and GM-VFNS[7] [71] calculations and the results are compatible within the uncertainties.

---

[7] GM-VFNS is the General-Mass Variable-Flavor-Numbering Scheme, explained in Sec. 3.1.2

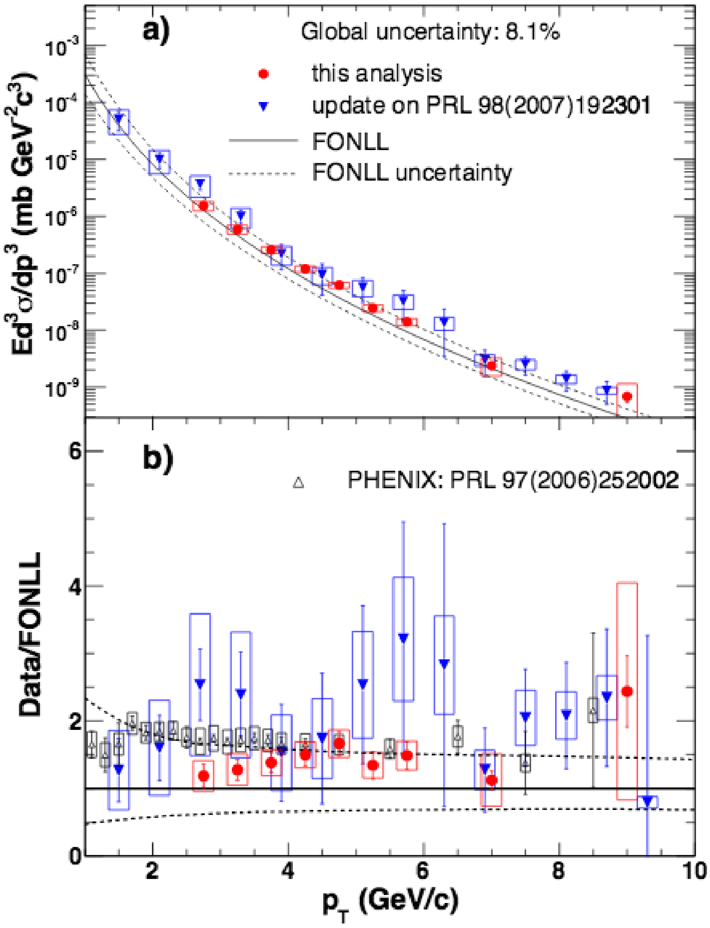

Figure 3.5: Invariant cross section of electrons from heavy-flavour hadron decays as a function of p_T measured by STAR in pp collisions at $\sqrt{s_{NN}} = 200$ GeV, in two different configurations, compared to FONLL pQCD calculations (upper panel). The lower panel shows the ratio of the data and the calculation. Fig. from [65].

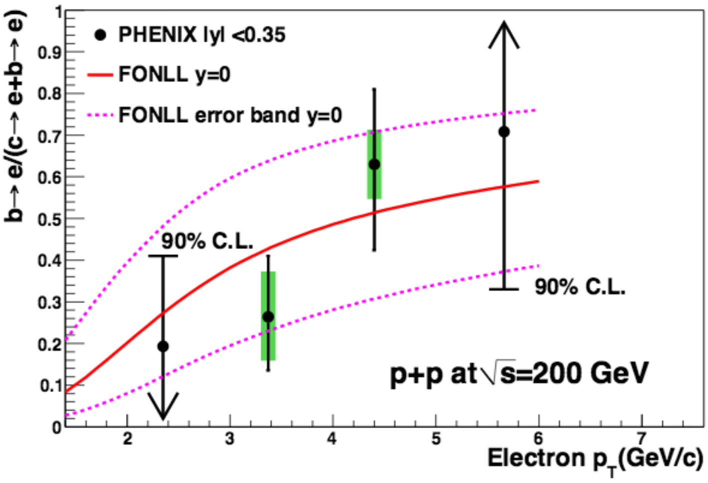

Figure 3.6: Relative contributions from beauty decays to the total production of electrons from heavy-flavour decays measured by PHENIX as a function of p_T and its comparison with FONLL pQCD calculations. Fig. from [67].

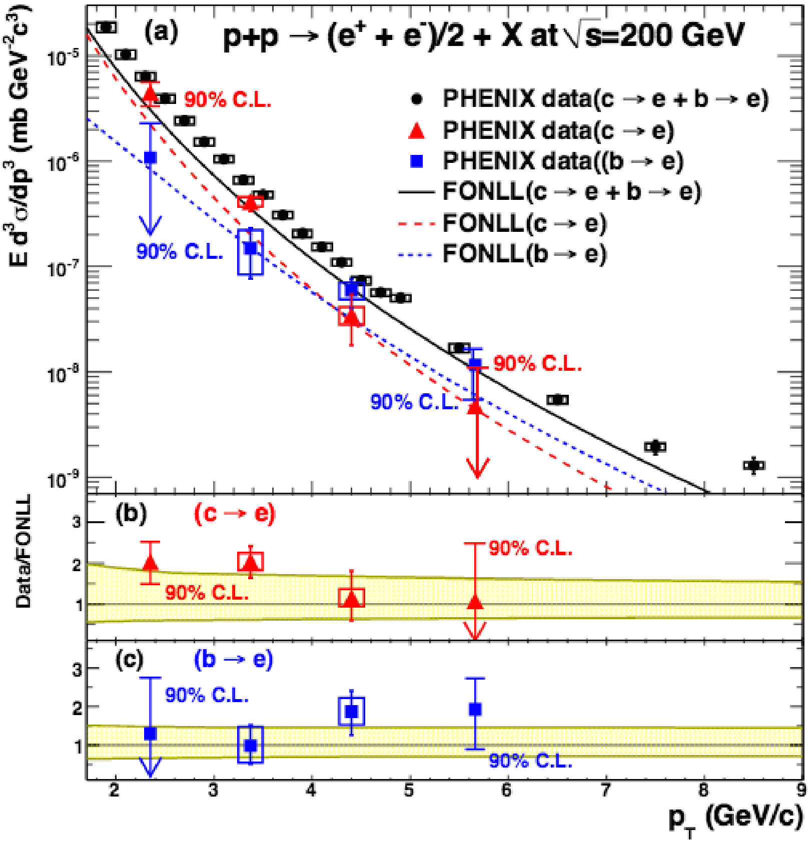

Figure 3.7: Invariant production cross section of charm and beauty measured by PHENIX as a function of p_T. The data are compared to FONLL pQCD calculations and the lower panel shows the ratio of data to FONLL. Fig. from [67].

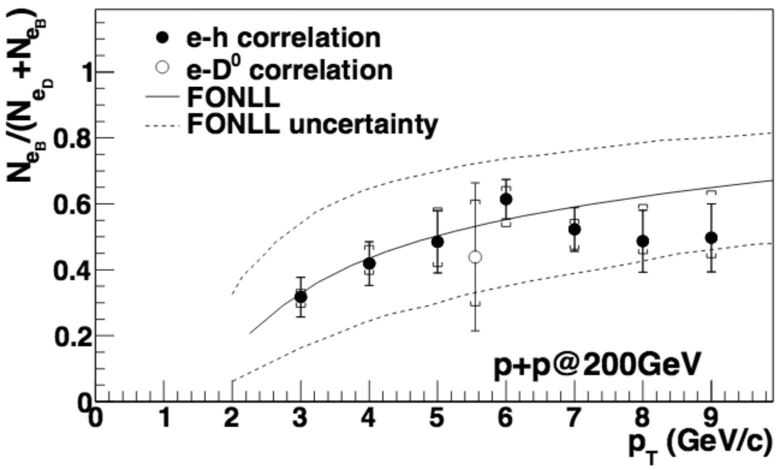

Figure 3.8: Relative contributions from beauty decays to the total production of electrons from heavy-flavour decays measured by STAR as a function of p_T and its comparison with FONLL pQCD calculations. Fig. from [68].

CMS also have studies of open heavy flavour using the hadronic heavy-flavour decays channel in pp at $\sqrt{s} = 7$ TeV. Fig. 3.12, Fig. 3.13 and Fig. 3.14 show the results for

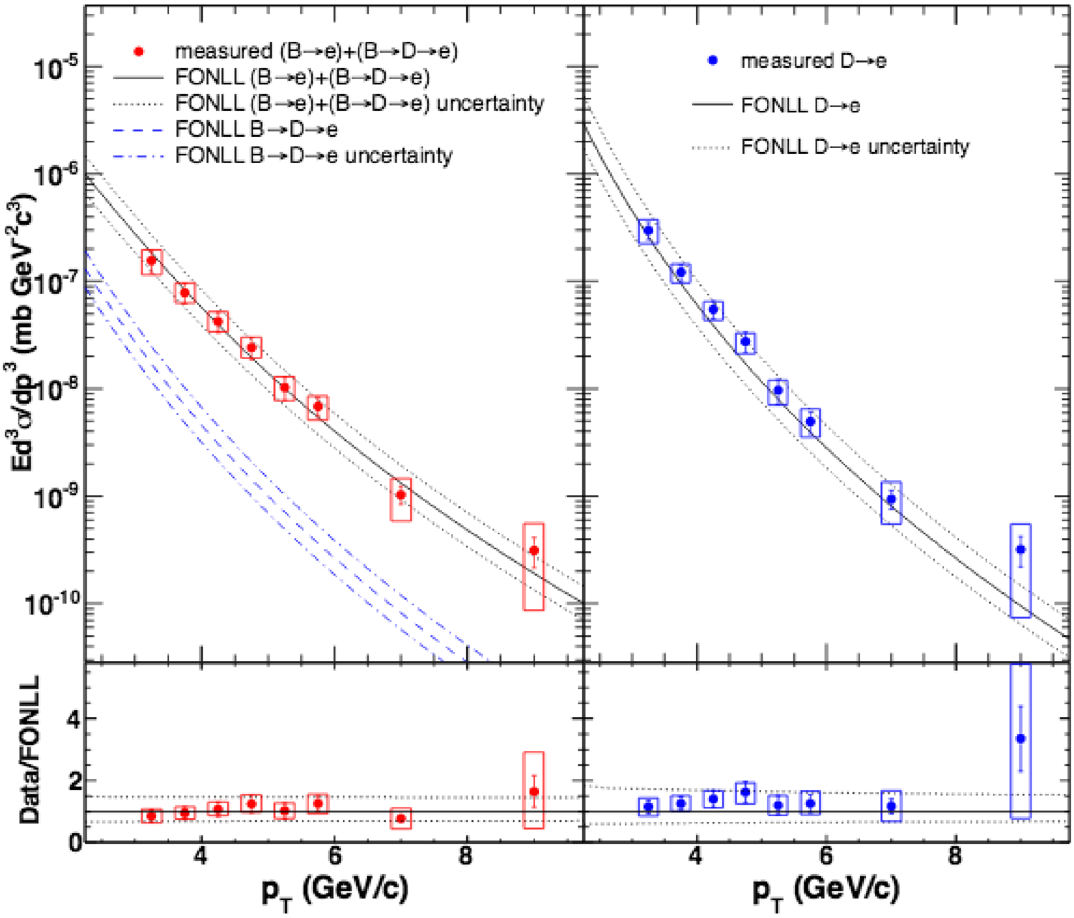

Figure 3.9: Invariant production cross section of charm and beauty measured by STAR as a function of p_T. The data are compared to FONLL pQCD calculations and the lower panel shows the ratio of data to FONLL. Fig. from [65].

production cross section as a function of momentum (left) and rapidity (right) for B^0, B^+ and B_s, respectively. Theoretical predictions from MC@NLO [72, 73], which is a higher-order pQCD model, are in agreement with the data within experimental and theoretical systematic uncertainties. The production cross section of B^0 meson decays is reconstructed in the exclusive final state $J/\psi K_s^0$, with the subsequent decays $J/\psi \to \mu^+\mu^-$ and $K_s^0 \to \pi^+\pi^-$. B^+ is reconstructed via the state $J/\psi K^+$ and B_s^0 is reconstructed using its decay to $J/\psi\phi$ with $\phi \to K^+K^-$.

The LHCb experiment has also studied the $B^\pm$ production in pp collisions $\sqrt{s_{NN}} = 7$ TeV and the results are shown in Fig. 3.15. The reconstruction is based on the decay $B^\pm \to J/\psi K^\pm$ [77] and the cross sections are in good agreement with FONLL pQCD calculations.

ALICE, ATLAS and CMS have studied the bottom hadron production via the measurement of non-prompt J/ψ mesons. Non-prompt J/ψ mesons comes from the decay $B \to J/\psi$ while prompt J/ψ comes directly from the collision. Non-prompt J/ψ can be identified via the displaced decay vertices [78]. Fig. 3.16 (upper left) show the fraction f_B which is the relative contribution of bottom hadron decays to the inclusive J/ψ yield obtained by ALICE,

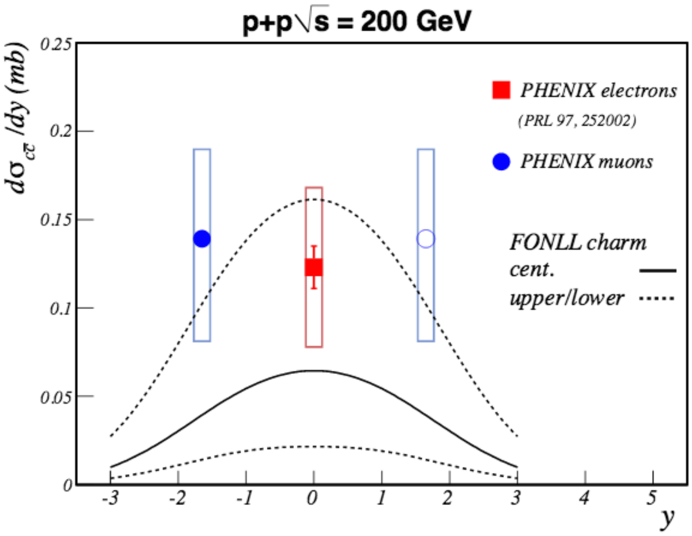

Figure 3.10: $c\bar{c}$ cross section as a function of rapidity measured via semileptonic decay to electrons (mid rapidity) and muons (forward rapidity). The negative rapidity was reflected to positive rapidity. The FONLL pQCD prediction is shown in the figure. Fig. from [69].

ATLAS and CMS in pp collisions at $\sqrt{s_{NN}} = 7$ TeV. The f_B increases from 10% at low p_{T} to more than 60% at high p_{T}. Fig. 3.16 (upper right) shows the non-prompt J/ψ cross section as a function of p_{T} and Fig. 3.16 (bottom) shows the rapidity-differential production cross section of non-prompt J/ψ measured with ALICE, ATLAS and CMS in pp collisions at $\sqrt{s_{NN}} = 7$ TeV. The measured rapidity dependence of non-prompt J/ψ is reproduced by FONLL pQCD whithin experimental and theoretical uncertainties, as can be seen in Fig. 3.16 (bottom).

ALICE has measured the heavy-flavour decay electrons in pp at $\sqrt{s_{NN}} = 7$ TeV [79] and $\sqrt{s_{NN}} = 2.76$ TeV [80] and the results of the production cross section as a function of p_{T} is shown in Fig. 3.17 (left) and Fig. 3.17 (right), respectively. ATLAS also measured the heavy flavour decay electrons and the result is shown in Fig. 3.17 (left), as an extension of the ALICE measurements in high-p_{T}. The results are compared to FONLL predictions (left) and to FONLL, GM-VFNS and k_{T}-factorization (right), and they are compatible within the systematic uncertainties.

ALICE also measured the contribution of electrons from beauty decays and the results are shown in Fig. 3.18 (left) for $\sqrt{s_{NN}} = 7$ TeV [81] and Fig. 3.18 (right) for $\sqrt{s_{NN}} = 2.76$ TeV [82]. The results are compared to FONLL, GM-VFNS and k_{T}-factorization, and they are compatible within the systematic uncertainties.

ALICE has also measured the heavy-flavour hadron decay muons at forward rapidity in pp at $\sqrt{s_{NN}} = 7$ TeV [83] and at $\sqrt{s_{NN}} = 2.76$ TeV [84]. Fig. 3.19 shows the results of production cross section as a function of p_{T} (left) and rapidity (right) at $\sqrt{s_{NN}} = 7$ TeV and Fig. 3.20 shows the results of production cross section as a function of p_{T} at $\sqrt{s_{NN}} =$ 2.76 TeV. The results are compared to FONLL pQCD calculations and they are compatible

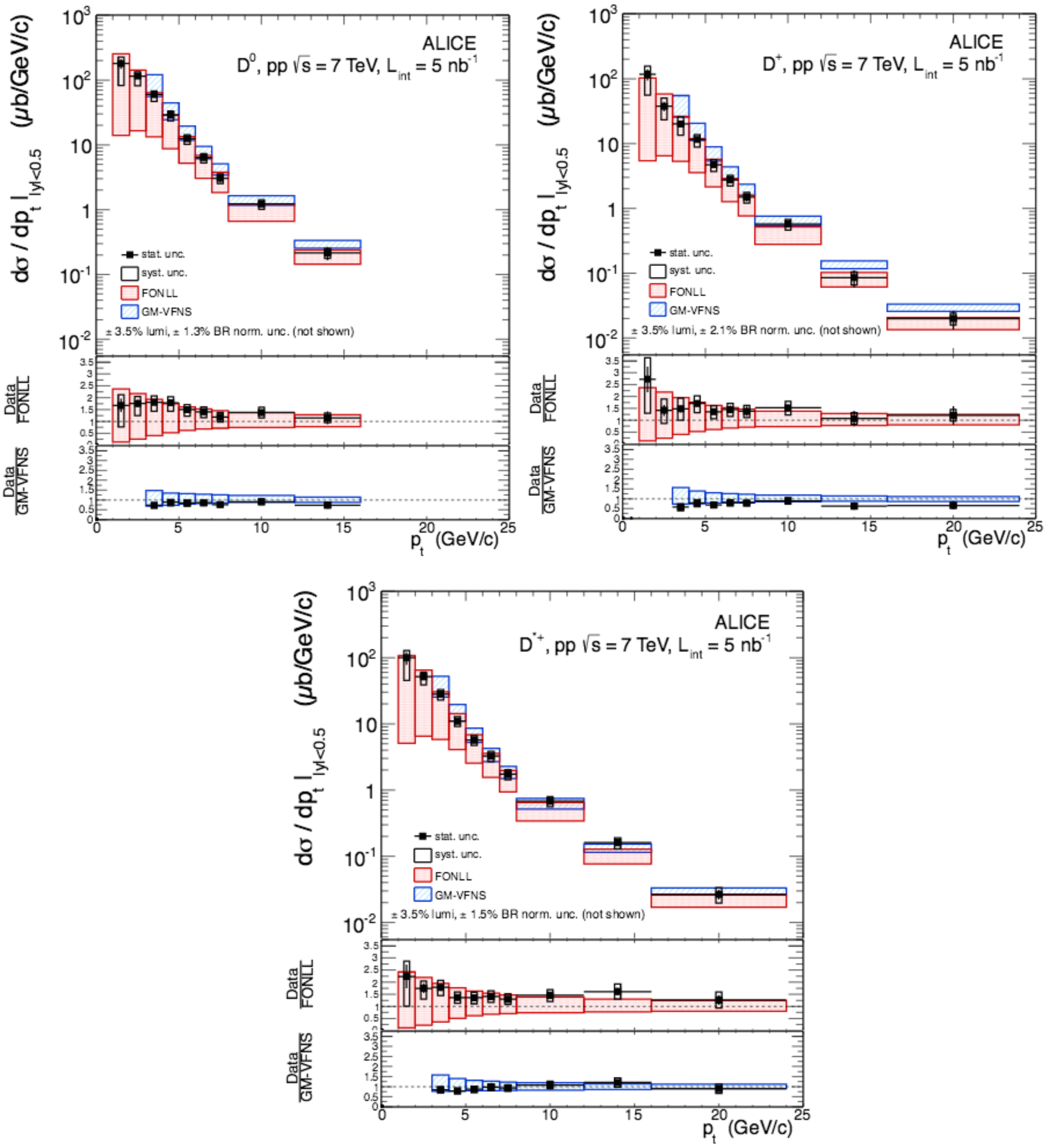

Figure 3.11: Production cross section of D^0, D^+ and D^{*+} measured by ALICE in pp collisions at $\sqrt{s}$ = 7 TeV. The data is compared to FONLL and GM-VFNS calculations. Fig. from [70]

within systematic uncertainties.

Muons measured by ATLAS are shown in Fig. 3.21 [85] . The results are compared to FONLL with NLO+NLL and only NLO and the former describes the data better in such a high-p_T range measured by ATLAS. This shows that although the FONLL NLO calculations can describe most of the LHC data in pp, in high-p_T measurements higher order of the calculations are necessary to describe the data.

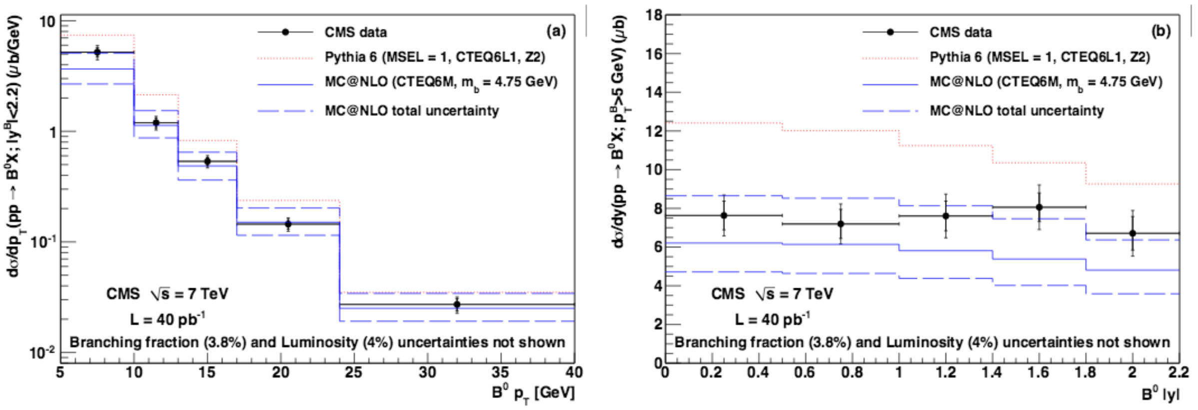

Figure 3.12: The production cross section of B^0 meson decays as a function of momentum (left) and rapidity (right) measured with CMS in pp collisions at $\sqrt{s_{NN}} = 7$ TeV. Theoretical predictions from MC@NLO are compared to data. Fig. from [74].

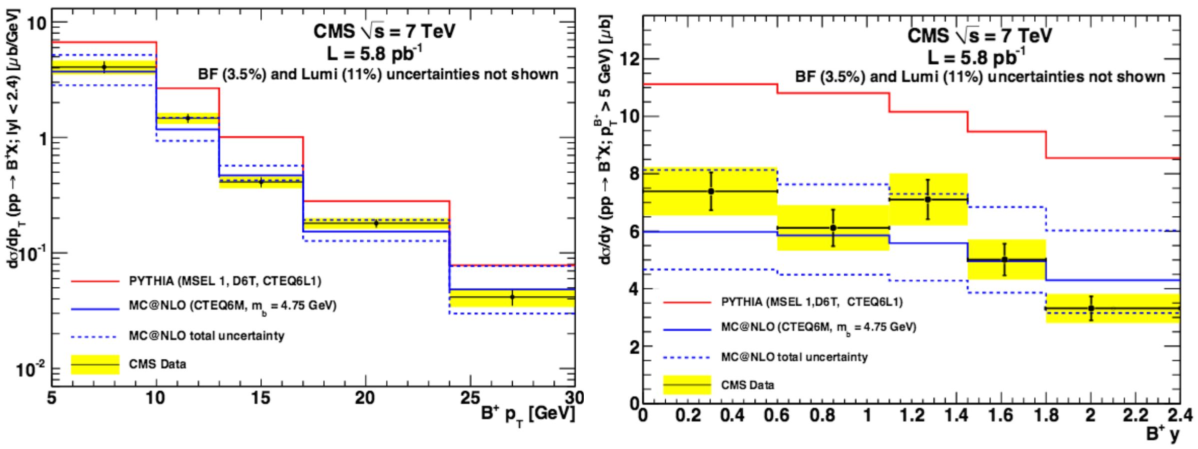

Figure 3.13: The production cross section of B^+ meson decays as a function of momentum (left) and rapidity (right) measured with CMS in pp collisions at $\sqrt{s_{NN}} = 7$ TeV. Theoretical predictions from MC@NLO are compared to data. Fig. from [75]

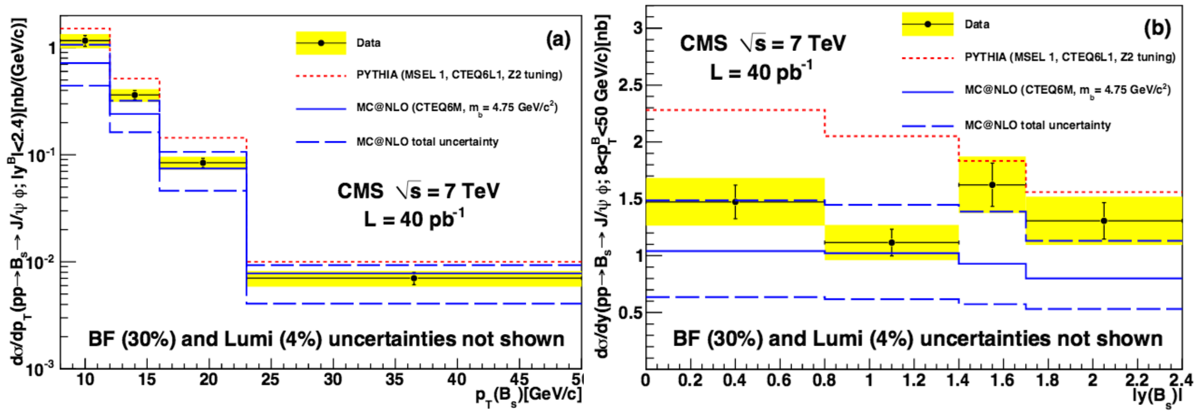

Figure 3.14: The production cross section of B_s meson decays as a function of momentum (left) and rapidity (right) measured with CMS in pp collisions at $\sqrt{s_{NN}} = 7$ TeV. Theoretical predictions from MC@NLO are compared to data. Fig. from [76].

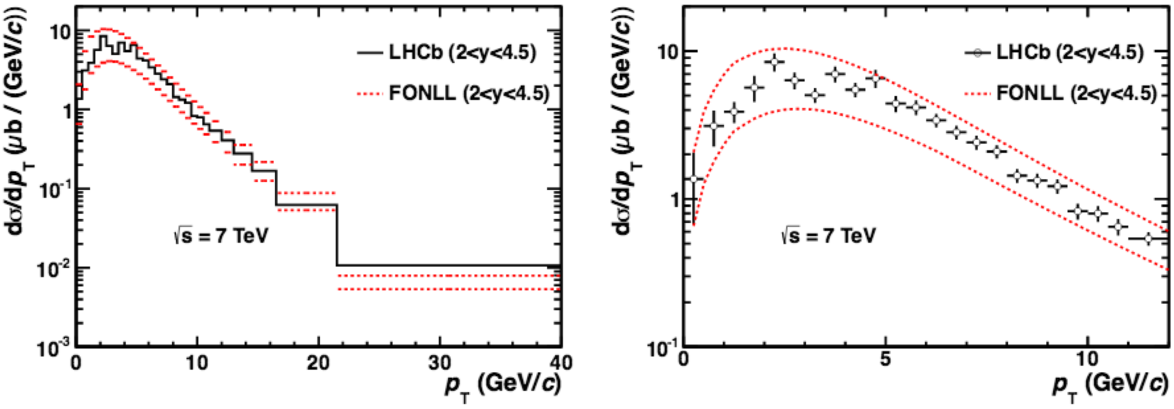

Figure 3.15: $B^{\pm}$ cross section production in pp collisions $\sqrt{s_{NN}} = 7$ TeV measured by LHCb (left) and a zoom in the low p_{T} range (right). Fig. from [77].

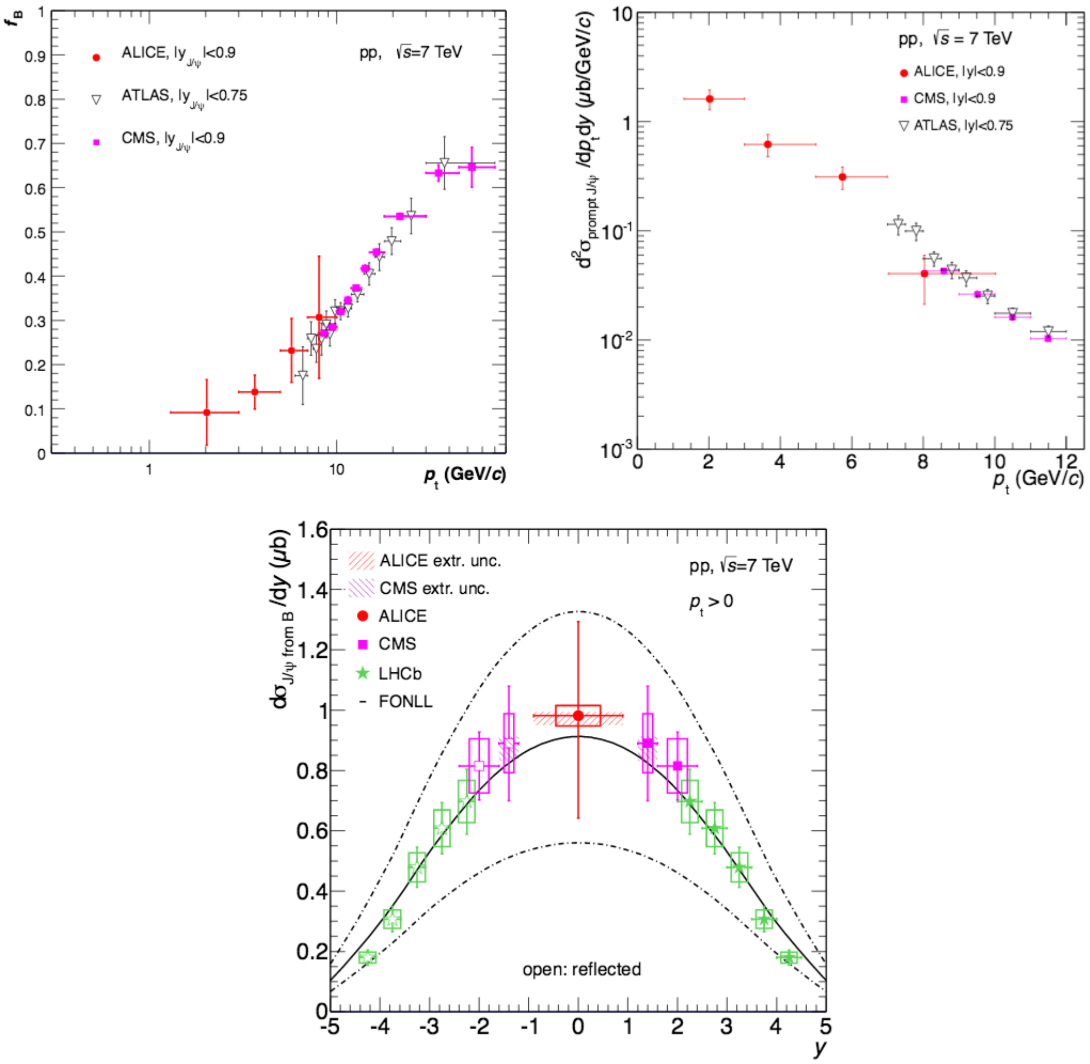

Figure 3.16: Top left: Relative contribution of bottom hadron decays to the inclusive J/ψ yield obtained by ALICE, ATLAS and CMS in pp collisions at $\sqrt{s_{NN}} = 7$ TeV. Top right: Non-prompt J/ψ cross section as a function of p_{T} measured by ALICE, ATLAS and CMS in pp collisions at $\sqrt{s_{NN}} = 7$ TeV. Bottom: Rapidity-differential production cross section of non-prompt J/ψ measured with ALICE, ATLAS and CMS in pp collisions at $\sqrt{s_{NN}} =$ 7 TeV. The results are compared with FONLL pQCD calculations and they are consistent whithin experimental and theoretical uncertainties. Fig. from [78].

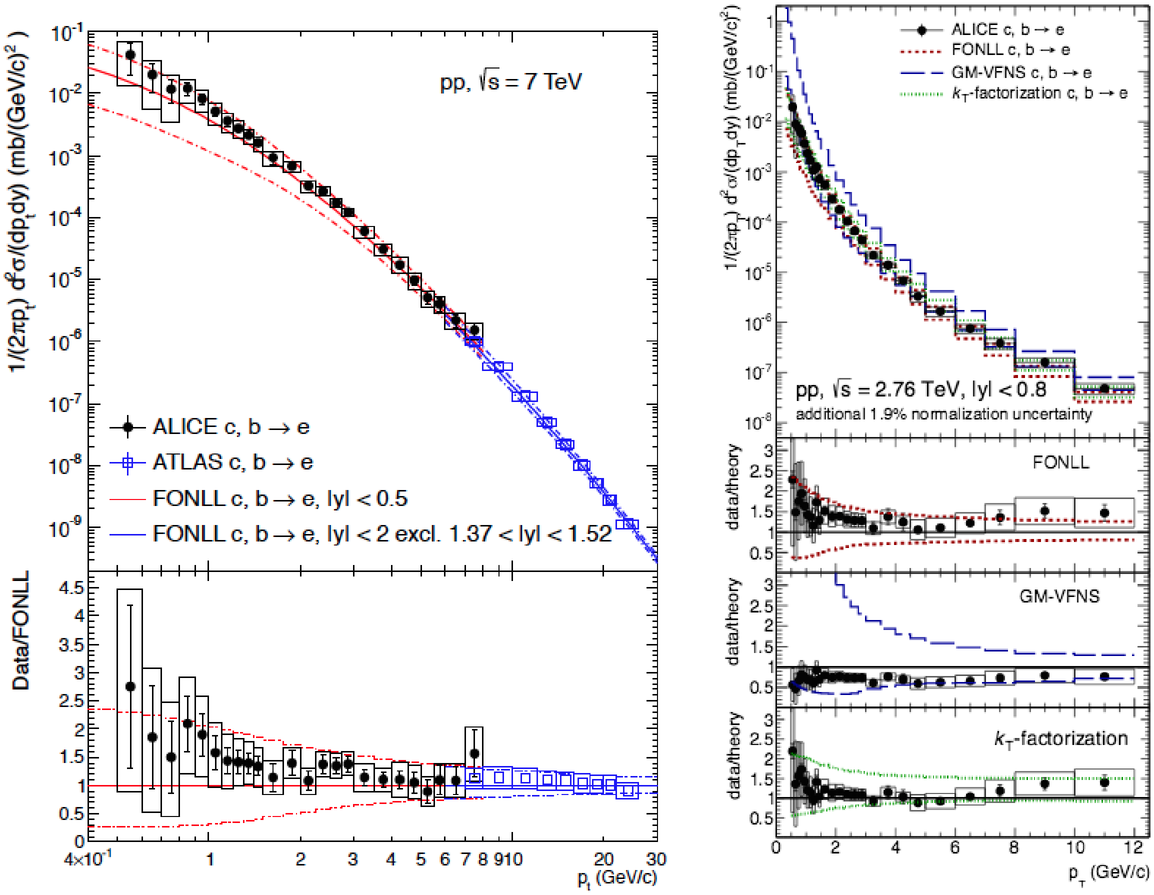

Figure 3.17: Production cross section as a function of p_{T} of heavy-flavour decay electrons in pp at $\sqrt{s_{NN}}$ = 7 TeV (left) and $\sqrt{s_{NN}}$ = 2.76 TeV (right) measured by ALICE. The cross action is compared with ATLAS results at $\sqrt{s_{NN}}$ = 7 TeV (left). The results are compared to FONLL predictions (left) and to FONLL, GM-VFNS and k_{T}-factorization (right). Figs. from [79] and [80].

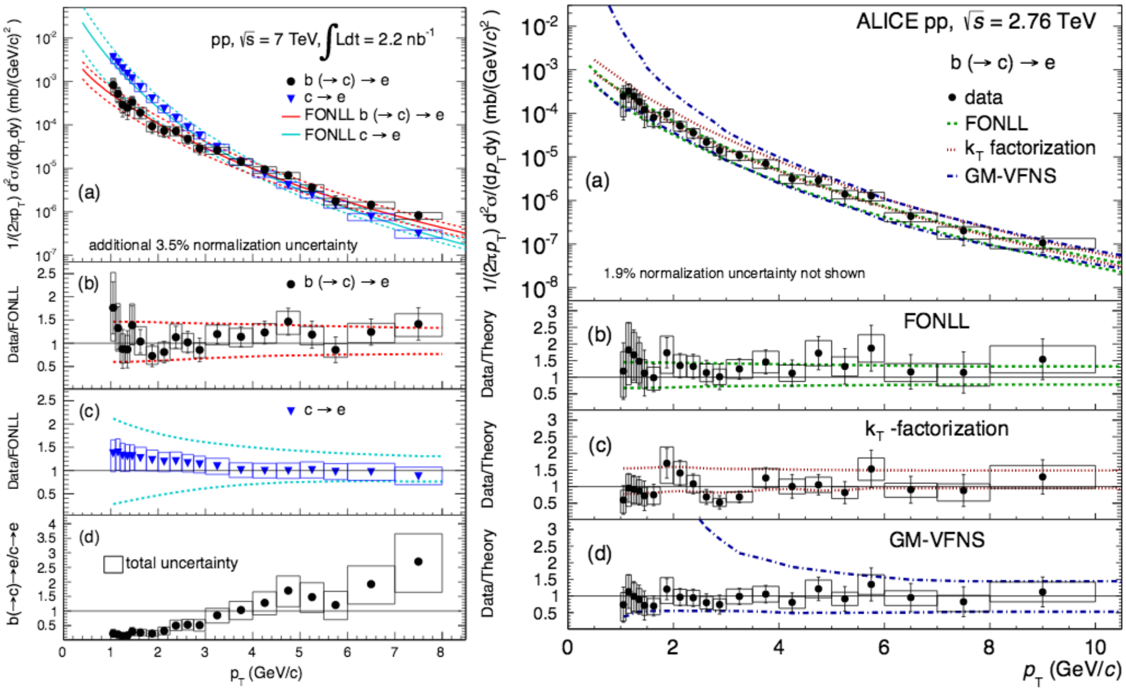

Figure 3.18: Production cross section as a function of p_{T} of electrons from beauty decay in pp at $\sqrt{s_{NN}} = 7$ TeV (left) and $\sqrt{s_{NN}} = 2.76$ TeV (right) measured by ALICE. The results are compared to FONLL, GM-VFNS and k_{T}-factorization, and they are compatible within the systematic uncertainties. Fig. from [81] and [82].

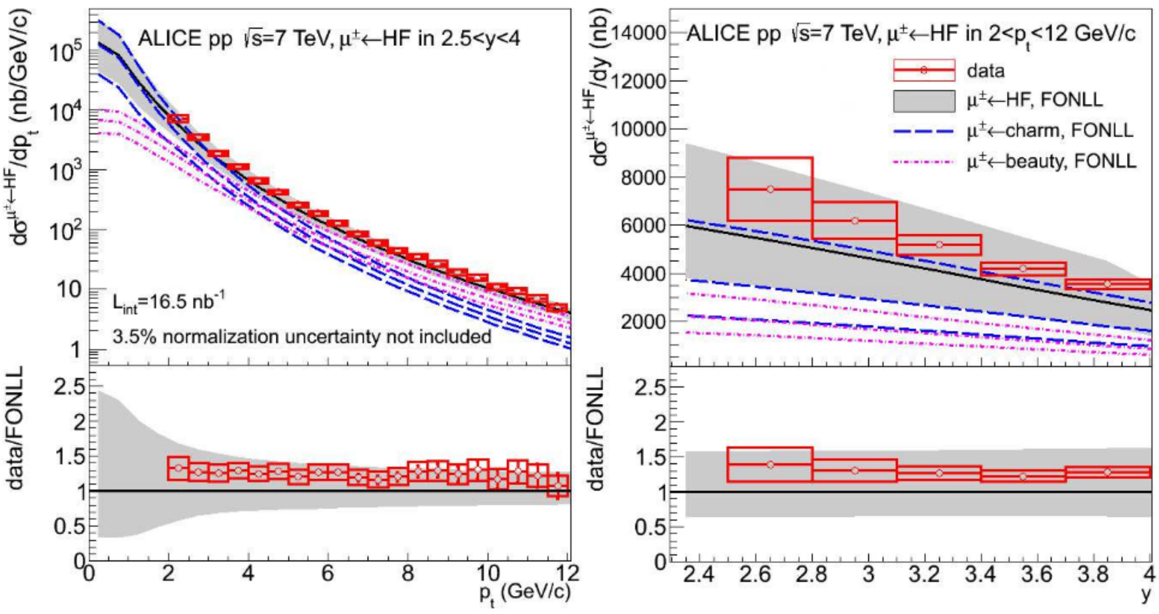

Figure 3.19: Production cross section of muons from heavy-flavour hadron decays measured by ALICE in pp at $\sqrt{s_{NN}} = 7$ TeV as a function of p_{T} (left) and rapidity (right). The results are compared to FONLL predictions. Fig. from [83].

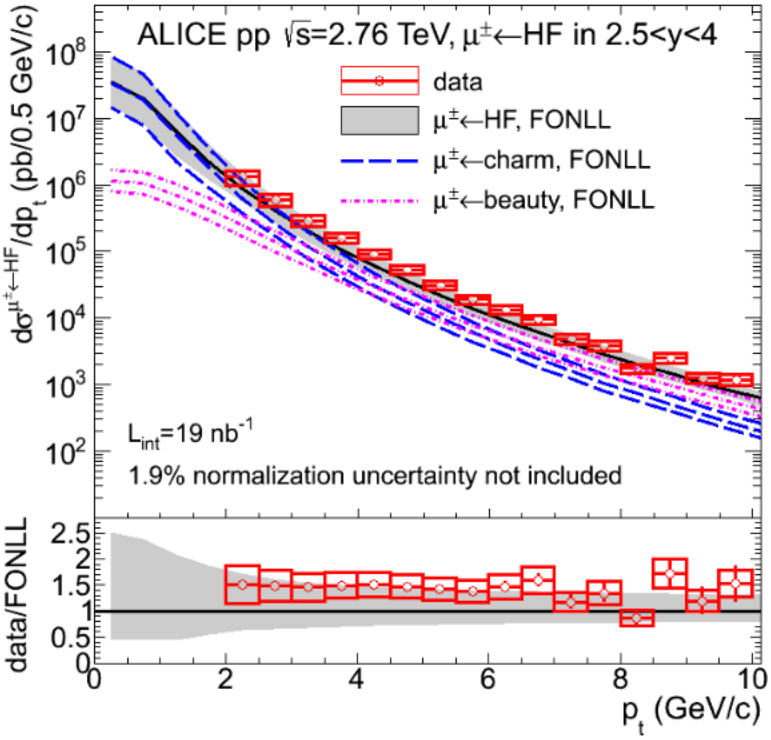

Figure 3.20: Production cross section of muons from heavy-flavour hadron decays measured by ALICE in pp at $\sqrt{s_{NN}} = 2.76$ TeV as a function of p_{T}. The results are compared to FONLL predictions. Fig. from [84].

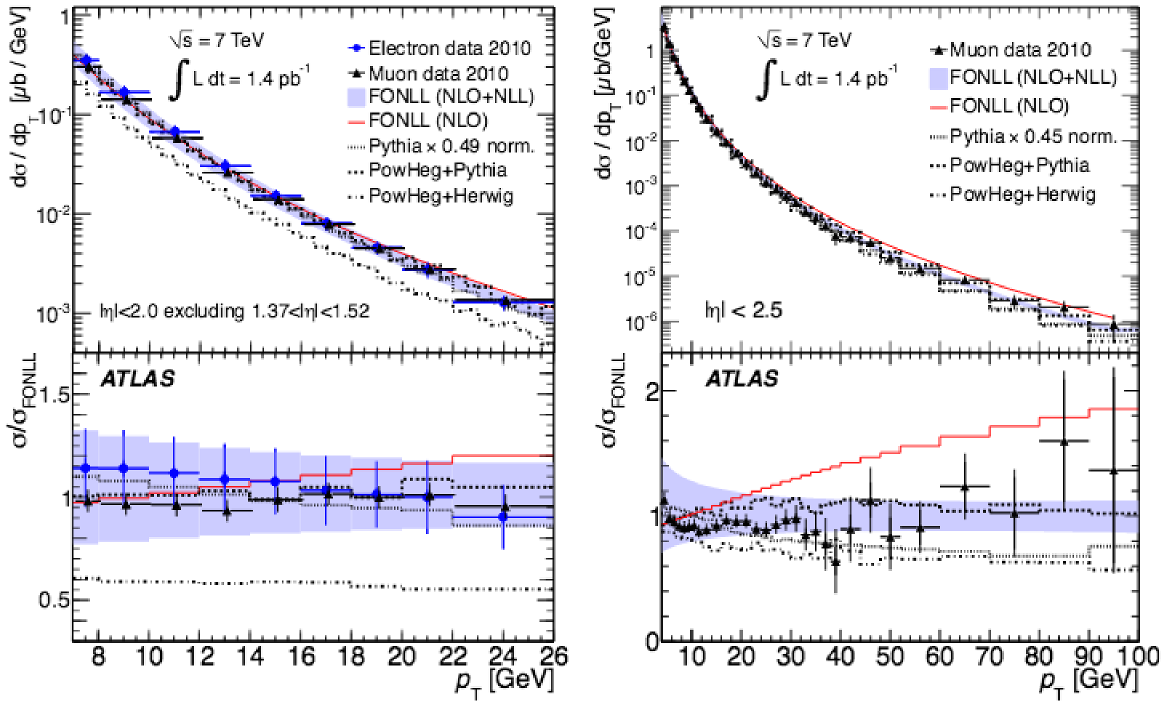

Figure 3.21: Production cross section of muons from heavy-flavour hadron decays measured by ATLAS in pp at $\sqrt{s_{NN}} = 7$ TeV as a function of p_{T} for two pseudo-rapidity intervals. The results are compare with different orders of FONLL calculations. Fig. from [85].

The comparisons of the experimental data with the perturbative QCD calculations and the consistency of the results is an evidence that the heavy-quarks are produced in the initial hard partonic scattering processes and they can be treated theoretically by the perturbative QCD. Thus, the pp measurements of heavy-quarks provided a testing ground for the pQCD calculations. In particular, the FONLL pQCD calculations of heavy-flavour production are in agreement with the experimental data from Tevatron, RHIC and LHC, in hadronic collisions.

Since they are well described theoretically, the heavy-flavour production in pp collisions serve as a solid baseline for heavy-flavour studies in the presence of a nucleus, as p-A or A-A collisions.

In the next section (3.2) we present the effects expected in p-A collisions, followed by a section (3.3) presenting theoretical models to describe the interactions of heavy-flavour with the medium formed in A-A collisions.

3.2 Cold Nuclear Matter effects

The Cold Nuclear Matter (CNM) effects are related to the nuclear medium. When studying collisions, these effects will be present when a heavy-ion participates in the reaction, like p-A or A-A collisions. Thus are effects originated by the presence of the nucleus in the collision. Since the ALICE main goal is to understand the properties of the QGP, which is the medium formed in A-A collisions, it is crucial a detailed understanding of the CNM effects that are also present in these collisions. The CNM are assessed via p-A measurements (p-Pb in case of ALICE and d-Au in case of RHIC), where one expects that the CNM effects are present but not the effects due to the QGP. The effects that are expected to be present in the CNM are the modification of the parton distribution function, the momentum broadening and energy loss. In this chapter we introduce these effects, which will be important in the interpretation of the data in the following chapters.

3.2.1 Modifications of the nuclear Parton Distribution Functions

The determination of the parton distribution functions (PDFs)[8] of protons in a wide range of momentum fractions and energies is of crucial importance to understand several measurements at the LHC. It describes the structure inside the protons, characterizing the number density of each kind of quark at different momentum fraction [86]. The PDFs are determined using Deep Inelastic Scattering (DIS) which is a process were a sufficiently energetic lepton scatters in a hadron exchanging a boson (virtual photon or Z^0 in case of charged leptons and $W^\pm$ in case of neutrinos) [86].

Since the scattering is inelastic, the scattering center absorbs part of the lepton kinetic energy and emits hadrons. The observed shower of hadrons together with measurements of the scattering angle of the incident lepton, provides information about the internal hadron

---

[8] Not to mislead with probability density function

structure. Fig. 3.22 shows two drawings of the DIS: on the left, a lepton with momentum k scattering in a nucleon with momentum p, exchanging a virtual neutral boson, having as final products the lepton with momentum k' and any final state with momentum $xp+q$ (x is a fraction of the nucleon momentum) and on the right, a neutrino scattering in a nucleon, with exchange of a $W^{\pm}$ where k, k' and p are the initial momentum of the neutrino, the final momentum of the neutrino and the initial momentum of the nucleon, respectively.

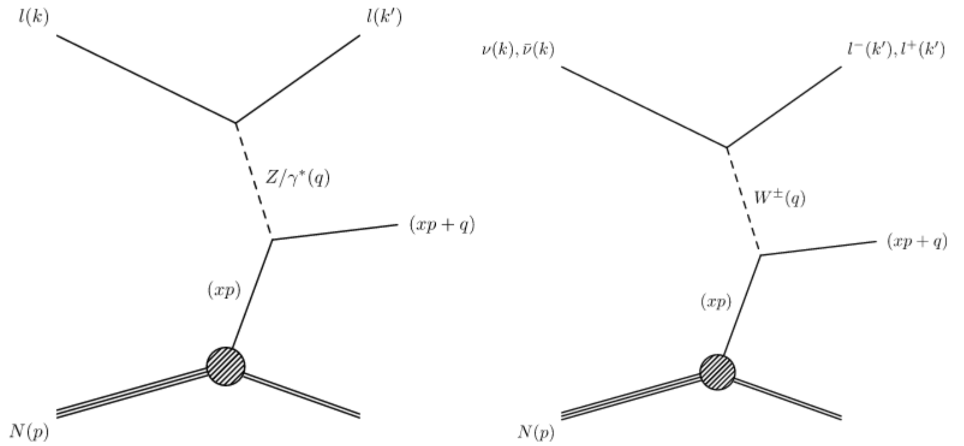

Figure 3.22: Drawing of deep inelastic scattering: (left) A scattering between one lepton and a nucleon via exchange of a virtual photon or Z^0 and (right) a scattering between a neutrino and a proton via exchange of a $W^{\pm}$. Fig. from [86].

The momentum fraction of the hadron carried by each parton is called Bjorken-x, which is defined as in Eq. 3.5 [86].

$$x = \frac{Q^2}{2p.q} \tag{3.5}$$

where Q^2 = - $q^2 \equiv -(k-k')^2$ is the squared modulus of the 4-momentum transfered by the lepton in the inelastic scattering and quantifies the virtuality of the exchanged boson.

The level of inelasticity is measured by the quantity w, given by Eq. 3.6 [86]. This quantity is the fractional energy loss by the lepton in the rest frame of the nucleon.

$$w = \frac{p.q}{p.k} = \frac{1}{2}(1 - cos\Theta) \tag{3.6}$$

where Θ is the lepton scattering angle, measured related to the lepton incidence direction in the center-of-mass frame.

The quantities x, w and Q^2 are related to the total energy $\sqrt{s}$ of the lepton-nucleon collision in the center-of-mass frame by the Eq. 3.7 [86].

$$Q^2 = sxw \tag{3.7}$$

In a hadron-hadron collision at $\sqrt{s}$ energy in the center-of-mass, the production of a particle with mass M and rapidity y is related to its momentum fraction by $x_{1,2} = \frac{M}{\sqrt{s}} e^{\pm y}$ [41]. In the LHC energy range, momentum fraction down to $x \approx 10^{-5}$ can be explored.

The PDFs parametrise the structure of the target as it is seen by the exchanged boson (see Fig. 3.22), and the PDFs are determined by global fits of DIS events data. Some examples of different PDF are: MRST [87], CTEQ [88] and MSTW [89, 90]. A comparison of this PDFs for up and charm quarks in low order of calculation are shown in Fig. 3.23, showing that even using different parametrisations the results are very similar. This PDFs are constantly being updated when new data is obtained.

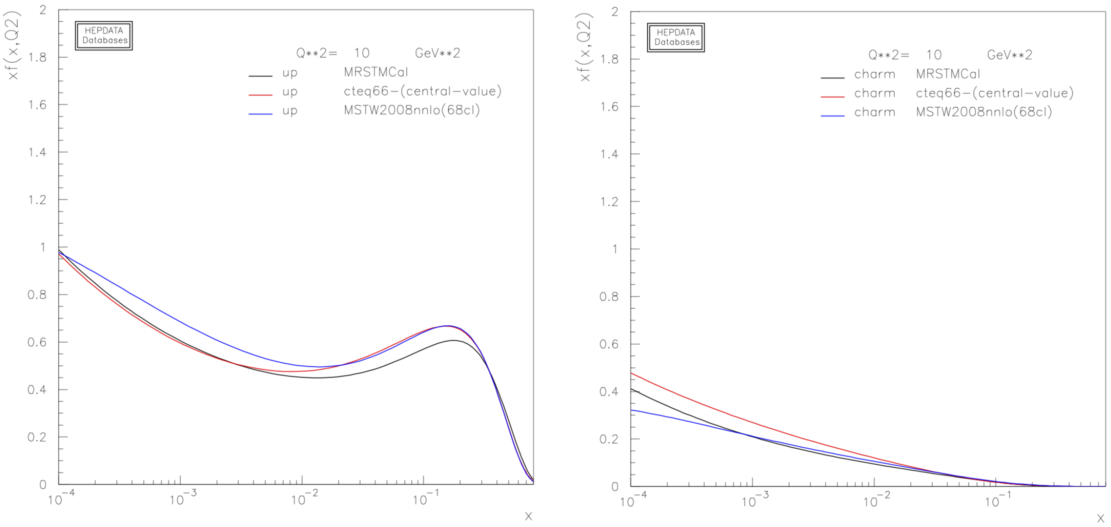

Figure 3.23: PDF for up (left) and charm (right) for different parametrizations: MRST [87], CTEQ [88] and MSTW [89, 90]. Fig. from [91].

Fig. 3.24 shows the PDF using the CTEQ parametrisation for each kind of quark inside the nucleon. As can be seen, the valence quarks (up and down) have PDF with peak in high values of x, showing that they carry more momentum fraction than the sea quarks (up, down, strange, charm and bottom). The gluons PDF is high for low x, meaning that for these values of x the gluons carry most of the proton momentum. Despite the continuous growth of the gluon density in the hadron towards small-x shown in the Fig. 3.24, several theoretical models predicts a *saturation* of gluons at this region [41, 92, 93].

The evolution of the PDF in Q^2 can be calculated using DGLAP[9] [94–97] equations, which relates the PDF with the coupling constant α_s (see discussion on α_s in Sec. 2.1). Thus, if the PDF have been measured in a given scale, the DGLAP equations allow the PDF calculation perturbatively at any scale [86].

Fig. 3.25 shows the parton distribution inside a proton for two different virtualities: $Q^2 = 1.9\ \text{GeV}^2$ (left) and $Q^2 = 10\ \text{GeV}^2$ (right). For low virtuality (low Q^2), the proton momentum

---

[9] Dokshitzer, Gribov, Lipatov, Altarelli and Parisi equation.

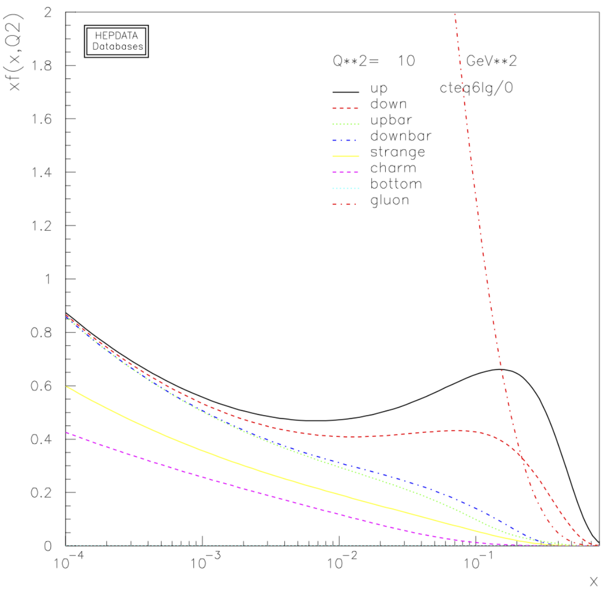

Figure 3.24: PDF for the CTEQ parametrisation for all quarks. Fig. from [91].

is concentrated in the three valence quarks, while for high virtuality, the contribution of gluons and sea quarks increases [98].

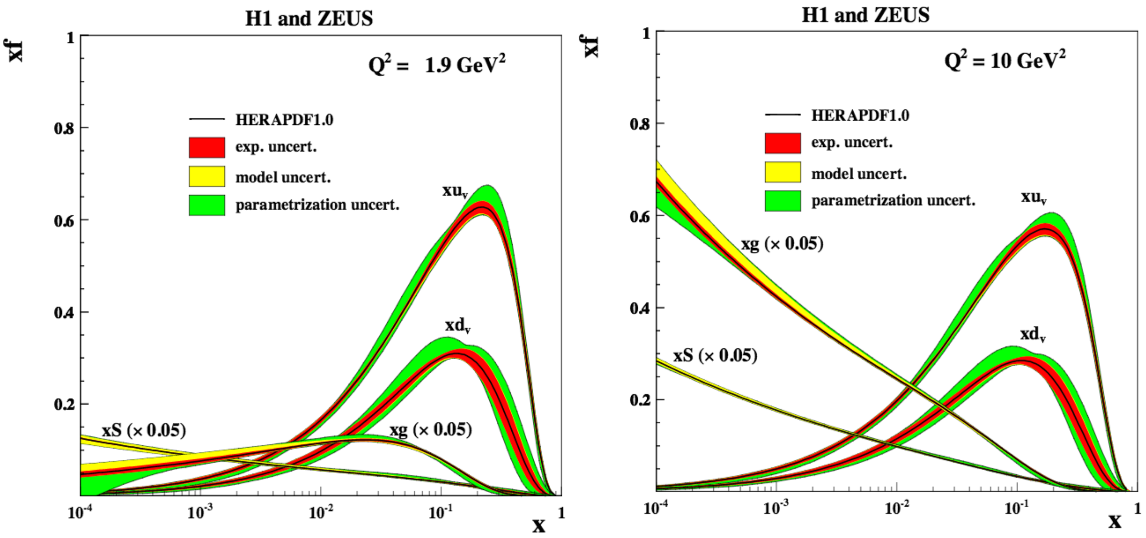

Figure 3.25: Parton distribution inside a proton for two different virtualities: $Q^2 = 1.9$ GeV^2 (left) and $Q^2 = 10$ GeV^2 (right). Fig. from [98].

The PDFs can also be evolved in rapidity of the partons using the BFKL[10] evolution equation and the BK[11] and JIMWLK[12] equations for the non linear regime of the evolution [99].

Fig. 3.26 shows a schematic view of the evolution of parton densities in rapidity y or in virtuality of the photon Q^2. For the evolution in rapidity, we can see that the system goes

---

[10] Balitsky, Fadin, Kuraev and Lipatov equation.

[11] Balitsky and Kovchegov equation.

[12] Jalilian-Marian, Iancu, McLerran, Weigert, Leonidov and Kovner equation.

from dilute to a dense regime and undergoes transition to saturation region, characterised by saturation scale $Q_s^2(y)$. For the evolution in Q^2, the distances at which the states are probed and the effective size of the partons decrease with the increase of Q^2.

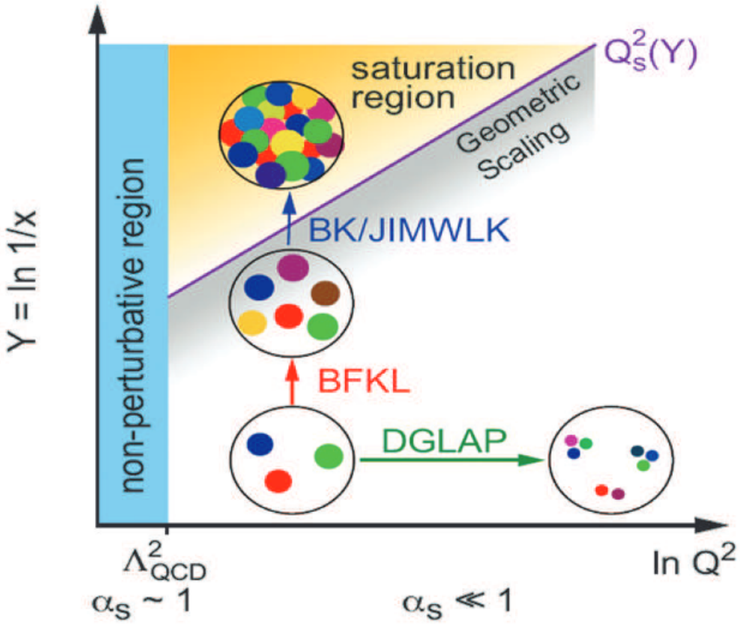

Figure 3.26: Evolution of parton densities in rapidity y (using BFKL, BK and JIMWLK equations) or in virtuality of the photon Q^2 (using DGLAP equation). Fig. from [99].

Nuclear DIS measurements are only sensitive to the sum of valence and sea quark distributions. Then, to separate nuclear effects in the valence and sea quark sectors and to measure the gluon distribution directly, the following processes are used:

- Drell-Yan lepton pair production: this is a process when a quark from one hadron $\mathrm{h_A}$ and an antiquark from another hadron $\mathrm{h_B}$ annihilate and create a pair of leptons ($\mathrm{l}\ \bar{\mathrm{l}}$) through the exchange of a virtual photon (γ^*) or a Z boson. A drawing of the Drell-Yan process is shown in Fig. 3.27.

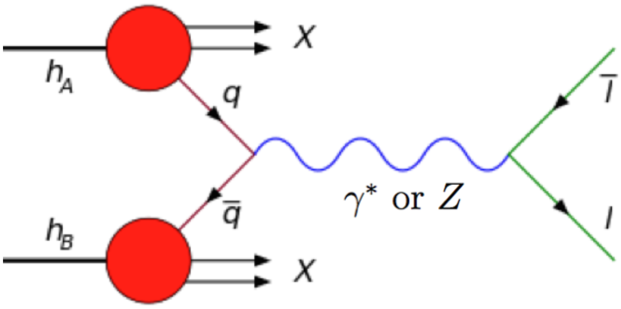

Figure 3.27: Drawing of the Drell-Yan process.

This experiment can explore possible modifications of nuclear sea quark distributions.

- Lepton-induced production of heavy quarks: this is a DIS process where the exchanged virtual photon between a lepton and the nucleon (or nucleus) couples with a gluon from the target, creating a heavy-quark pair. A drawing of this process is shown in Fig. 3.28. Since the distribution of charm and beauty inside nucleons is expected very small, the heavy-quark pair production is proportional to the gluon distribution of the target. A comparison of the heavy-quarks cross sections for nucleons and nuclei, for instance, can then be directly translated into a difference of the corresponding gluon distributions.

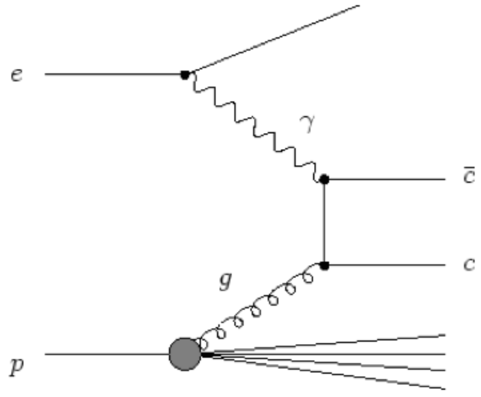

Figure 3.28: Drawing of lepton-induced production of heavy quarks.

While the proton PDF is still under investigation and being constantly updated, it is also important to understand the behaviour of the PDF of the protons when they are bounded inside a nucleus, which is a completely different situation, since nuclear effects can be present. Examples of nuclear effects observed in nuclear parton distribution function (nPDF) that can observed when comparing the PDF obtained by DIS of lepton in deuteron to the nPDF obtained by DIS of lepton in nucleus are the following [41, 100, 101]: shadowing, anti-shadowing, EMC-effect and Fermi motion (as can be seen in Fig. 3.29). To measure this effects, the structure functions[13] F_1 and F_2 for nucleon and nucleus are measured and compared [102]:

$$R^A_{F_i}(x,Q^2) = \frac{F_i^A(x,Q^2)}{AF_i^{nucleon}}(x,Q^2) \tag{3.8}$$

where $i = 1, 2$.

The nuclear effects shown in Fig. 3.29 are described below. Since the shadowing is the most relevant effect at the LHC energy, more details for this effects are given.

Shadowing

This is an effect where the parton density in the nuclei (bounded nucleons) suffers a decrement when compared to free-nucleons (unbounded) at low x regions.

The term *shadowing* comes from the fact that the total hadron-nucleus cross section σ_{hA}

---

[13] Structure functions are a measure of the partonic structure of hadrons.

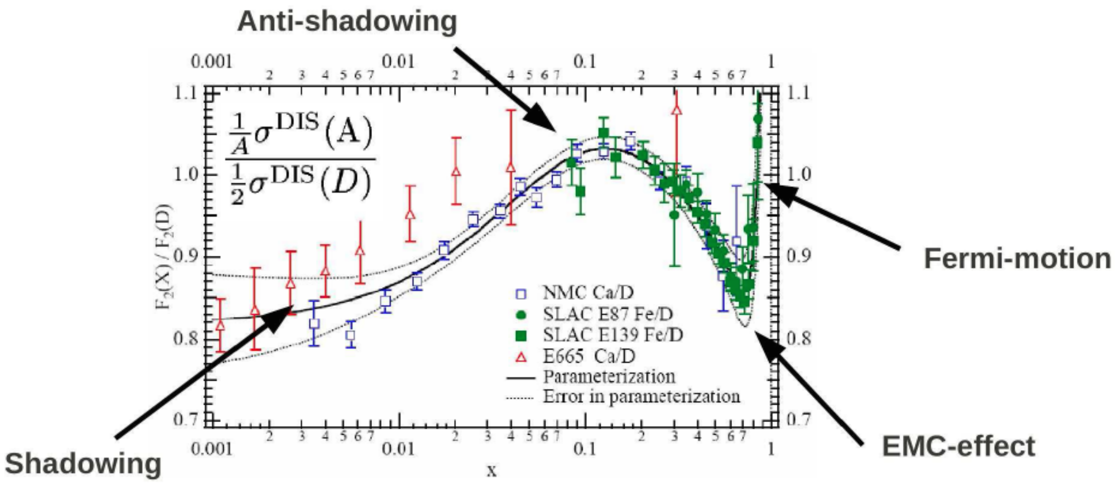

Figure 3.29: Nuclear effects observed in DIS measurements when the structure function F_2 in $l + A$ is divided by the F_2 in $l + d$ scatterings. Four different effects are shown: shadowing, anti-shadowing, EMC-effect and Fermi motion. Fig. from [100].

is known to be smaller than A times the total hadron-nucleon cross section σ_{hN}:

$$\sigma_{\mathrm{hA}} < \mathrm{A}\sigma_{\mathrm{hN}} \tag{3.9}$$

The shadow is explained by the fact that the nucleons on the surface of the nucleus overshadows the inner nucleons [101].

When the gluon density at low x suffers a depletion, the effect is called *gluon saturation*. The observed depletion can be explained by models based on multiple scatterings [41]: the hadronic component of the virtual photon wave function at high collision energies, will interact several times with different nucleons in the nucleus, experiencing multiple scatterings. Besides, multiple scatterings in the rest frame of the nucleus corresponds to recombinations in the Breit frame[14].

Bellow we describe these two scenarios:

- Generalized Vector Meson Dominance (GVMD): this is a model based on the Vector Meson Dominance (VMD) [103], used to describe photon-induced reactions. In the VDM, the photon fluctuates from its point like bare photon state into a superposition of vector mesons, like ρ, ω and ϕ. The inclusion of higher mass ressonances defines the GVMD. Then, the photon-nucleus cross section will be shadowed, since some of the interactions can exhibit characteristics of hadron-nucleus interactions [104, 105]. This

---

[14] Since the virtual photon is space-like ($q^2 < 0$), we can boost the photon along its direction of propagation, which points to the nucleon, such that the photon energy vanishes. This frame is called the Breit frame or infinite momentum frame since in this case, the nucleon moves with very large momentum towards the virtual photon.

effect can also be applied to virtual photons [106], and the shadowing was observed in several experiments [107–109]. Then, the nuclear multiple scattering of hadronic components of the virtual photon is an explanation of shadowing at low x.

- Partonic approach: in this model, if the Breit frame is considered, the low x partons, which have low momentum, are spread over a large longitudinal distance (due to the uncertainty principle $\Delta x \Delta p \geq \hbar/2$). Then, low momentum partons from different nucleons start to occupy the same region of space, interacting and merging into one [110]. For example, two gluons with momentum fraction x_1 and x_2 merge into a unique gluon with momentum fraction $x_1 + x_2$, reducing the number of gluons.

Antishadowing

It is an effect that occurs at medium x, where the parton density in nuclei is larger than in nucleons. Following the example of the partonic approach to the shadowing effect, when two gluons merge, due to the momentum conservation, the resulting gluon has a higher momentum fraction $(x_1 + x_2)$, enhancing the number of gluons in the medium x region.

EMC

This effect was first observed by European Muon Collaboration (EMC) and published in 1983 [111]. In this case the ratio (see Eq. 3.8) is smaller than unity with a minimum at $x \simeq 0.7$. There are several explanations for this depletion: nuclear binding, pion exchange, a change in the nucleon radius, etc [41].

Here, the sea-quark distribution is negligible and the ratio reflects a mitigation of the valence-quark distributions in this region for the nuclei case [112];

Fermi motion

In this case the ratio increases with increasing x which is explained by the Fermi motion[15][113] of the bounded nucleon inside the nuclei, which modifies the structure of nucleons inside the nucleus, since the structure function in nuclear target is a convolution of the bare nucleon structure with the momentum distribution function of the nucleons in the nucleus [109]. The Fermi motion can also be explained by the kinematic effect due to the fact that the free-nucleon PDF vanishes when $x \to 1$ [112].

One of the fundamental issues in high energy QCD is the dynamics of hard interactions at small x. In these interactions, the prime effect is an increase of the gluon densities at small x. Since the cross section for hard processes increases approximately linearly with A [114], not only the increase of energy from RHIC to the LHC but also the A increase will allow to

---

[15] Fermi motion is the quantum motion of bounded nucleons inside a nucleus.

assess new effects, by reason that lower x can be measured in the LHC. Then, measurements of the nuclear effects in the PDFs by the LHC reaches an unprecedented range of x and Q, allowing the investigation of the shadowing effect in a range never studied before. Thus, the LHC p-A data and its comparison with theoretical models offer the possibility to further constrain our knowledge on the behaviour of nuclear cross sections and structure functions. Fig. 3.30 shows the $x - Q^2$ plane and the respective regions that can be reached by the different experiments.

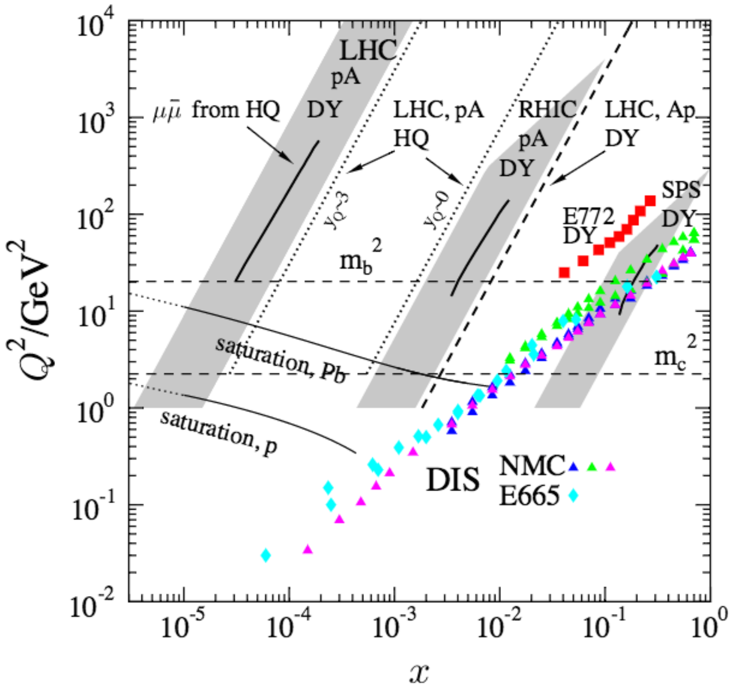

Figure 3.30: Values of x and Q^2 that can be reached in different experiments. Fig. from [114].

On the other hand, the knowledge of nPDFs is an important topic to be studied in order to have a proper reference for heavy-ion collision studies. The p-A collisions is a clean environment to test the nuclear PDFs. If the shadowing affects the production of a given particle, a suppression in p-A collisions relative to pp collisions would be observed. Then, a suppression due to the shadowing in A-A collisions would also be observed, but in this case can be an interplay of shadowing and medium effects. The EMC effect can also be present, leading also to a suppression of the produced particles. Additionally, the anti-shadowing effect can lead to an enhancement of the particles production when comparing p-A and pp collisions. This enhancement can be present in AA collisions, even if a suppression is observed. In this case, there is a competition of the suppression and the enhancement of the particles production.

Then, the p-A measurements help to understand the origin of the effects observed in A-A collisions. This is done comparing the R_{pPb} with theoretical models including nuclear modifications of the PDFs. From the comparisons it is possible to validate theoretical assumptions for the nuclear PDFs. Having in hand a good understanding of the R_{pPb}, the effects from CNM present in A-A collisions can be separated from the effects due to the formation of the QGP.

There is also other effects that can affect the particles production in p-A and A-A collisions, which are discussed below.

3.2.2 Momentum broadening or Cronin enhancement

The Cronin enhancement was first observed in 1970 [115] and it consists of an enhancement of hadron production in p-A relative to pp collisions, when scaled by number of binary collisions.

The main source for this effect was believed to be the partonic multiple re-scatterings in the initial state [116]. However, recent studies showed that only the initial partonic scattering and independent fragmentation cannot reproduce the experimental data, since in this case the model predicts that some enhancement effect would happen for all kinds of particles. However, the observed Cronin effect is dependent of the particle type. For example, in the first observation of this effect, it was larger for protons and anti-protons than for pions. This particle dependence was also observed in d-Au collisions at RHIC [116]

Some recent works are using recombination [117] and coherent multiple scattering [118] to explain the Cronin effect. At RHIC, the model including recombination can describe the protons, pions and kaons production in d-Au collisions, what means that the Cronin effect can also be interpreted as a combination of initial and final state effect simultaneously [116].

While this effect are still under investigation and its origin is still not fully understood, this is an effect that can be present in the measurements of the nuclear modification factor in p-A and A-A collisions. This is a momentum broadening that enhances the yield of particles at low momentum, leading to a small decrease in high momentum, in order to conserve the momentum.

One of the models that can also lead to a Cronin enhancement is discussed in the next section.

3.2.3 Energy loss in p-A collisions

Another effect that can be present in CNM is the initial-state energy loss. Before the hard parton scattering process, the incoming partons lose radiatively a fraction of their energy as a result of multiple interactions in the target nucleus.

The propagation of high-energetic partons throughout the cold matter can lead to energy losses by gluon radiation. Studies of the gluon radiation induced by the medium can be treated as coherent or incoherent, depending on the formation time of the radiation.

For instance, if the formation time (t_{form}) is much larger than the mean free path (λ), $t_{form} >> \lambda$, the radiation is called *coherent* with the many scattering centers acting as a single one. In this case, the radiation is suppressed and this effect, already known in QED, is called Landau-Pomeranchuk-Migdal (LPM) [119, 120]. This effect describes the suppression of medium induced bremsstrahlung due to interference effects between adjacent scatterings. If the wavelengths are large (which means longitudinal momentum transfer small) when compared to the mean free path in the medium (the average distance between subsequent scatterings in the medium), interference effects lead to a suppression of the radiation.

In case that $t_{form} < \lambda$, the scattering is called *incoherent* and in this case the parton modification is governed by the transverse momentum broadening, leading to a Cronin-like enhancement.

In the next section we present a model that includes energy loss, Cronin enhancement and nuclear shadowing as cold nuclear matter effects present in p-A collisions.

3.2.4 A model for the CNM effects

Using the idea of coherent and incoherent scatterings described in Sec. 3.2.3, the model proposed in [33] shows how these effects can be implemented.

The coherent and incoherent process leads to different CNM effects. These effects are implemented applying modifications to the kinematics of the hard parton scattering.

Energy loss

To describe the initial-state energy loss of a given parton a, the modification implemented in its distribution function $\phi_a(x_a)$ is presented in Eq. 3.10, where x_a is the momentum fraction carried by the parton a.

$$\phi_a(x_a) = \phi_a(\frac{x_a}{1-\Delta_a/E_a}) \tag{3.10}$$

where Δ_a is the energy loss of the parton a and E_a is the energy before the hard collision. Then, if fast quarks or gluons lose Δ_a of their energy prior to the hard scattering, to satisfy the same final-state kinematics they must initially carry a larger fraction of the colliding hadron momentum and, correspondingly, a larger value of x [44].

Nuclear shadowing

To take into account that the scattering can become coherent, the power corrections are implemented in the Bjorken-x variable as shown in Eq. 3.11 and 3.12 . This effective modification is necessary when the inverse longitudinal momentum transferred from the nucleus is larger than the Lorentz contracted longitudinal size ($\frac{1}{p_L} > L$)[16]. Considering the hard scattering $a + b \to c + d$, in a p-A collision, the modification will be[17]:

$$\check{x_a} = x_a \left[1 + \frac{\epsilon_d^2 (A^{1/3} - 1)}{-\hat{t} + m_d^2} \right] \tag{3.11}$$

---

[16] Which is the condition for the coherent scattering

[17] Here we are considering the particle production in the forward rapidity.

$$\check{x_b} = x_b \left[1 + \frac{\epsilon_c^2 (A^{1/3} - 1)}{-\hat{u} + m_c^2} \right] \tag{3.12}$$

where ϵ_d^2 is a parameter controlling the strength of the power corrections, m_d (m_c) is the mass of the parton d (c), A is the atomic mass number of the nucleus and $\hat{t}$, $\hat{u}$ are the Mandelstam variables at the partonic level [44]. This modification of the momentum carried by the partons leads to a shadowing, since the x of the partons are increased and less partons have small x.

Cronin effect

In the case of incoherent scatterings, the momentum broadening (that results in a Cronin enhancement) can be implemented relaxing the assumption that the incident partons a and b are collinear and allowing them to carry a transverse momentum, according to a gaussian distribution.

The modification in the transverse momentum distribution in p-A collisions follows the relation given by Eq. 3.13.

$$< k_{Ta}^2 >_{pA} = < k_T^2 >_{NN} + < \frac{2\mu^2 L}{\lambda_a} > \tag{3.13}$$

where $< k_T^2 >_{NN}$ accounts for the momentum distribution in collisions of two nucleons N and the last term in the right side is a modification in the transverse momentum due to the initial state scatterings, L is the Lorentz-contracted longitudinal size of the nucleus, μ is the transverse momentum transfer in a parton nucleon scattering and λ_a is the parton mean free path in the nuclear medium.

As can be noticed, all these cold nuclear matter effects grows with the system size L, which is proportional, in p-A collisions, to the nuclear size $R \approx 1.2A^{1/3}$ [121]. Then, we would expect these CNM effects more pronounced in the LHC p-Pb data than in the RHIC d-Au data. This is an assumption that we are going to test with our results of heavy-flavour decay electrons in p-Pb, which is the measurement performed in this thesis. As will be shown in the next section, an enhancement of electrons from heavy-flavour hadron decays were observed in d-Au collisions ($R_{\mathrm{d-Au}}$ >1). If this is a Cronin enhancement, in the LHC energy we would expect a more pronounced effect due to the larger system created.

3.2.5 Experimental results in d-Au collisions

In this section we present the PHENIX results of the nuclear modification factor of electrons from open-heavy flavour hadrons decays in d-Au collisions at $\sqrt{s}$= 200 GeV. In such a collision system, cold nuclear matter effects can be investigated. Fig. 3.31 shows the PHENIX results for the nuclear modification factor R_{dAu} of electrons from heavy-flavour hadron decays in two centrality bins[18] [122].

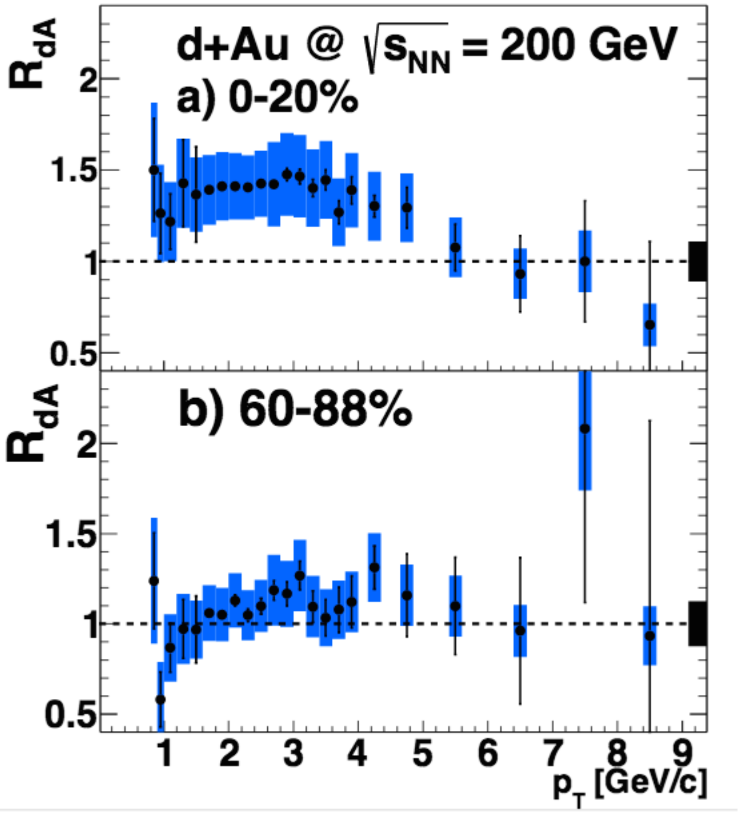

Figure 3.31: Nuclear modification factor R_{dAu} of electrons from heavy-flavour hadron decays for central and peripheral d-Au collisions measured by PHENIX. Fig. from [122].

From Fig. 3.31, it can be noticed that R_{dAu} for peripheral collisions is consistent with unity within the uncertainties while for central collisions an enhancement of the yield of electrons from heavy-flavour hadron decays is observed. This effect can be explained by the Cronin enhancement, which is a CNM effects. Then, when studying the nuclear modification factor in Au-Au collisions, this enhancement has to be taken into account to interpret the results correctly.

Additionally, as discussed in Sec. 3.2.4, the model that describes the Cronin enhancement shows that it is proportional to the size of the medium created, which implies that this effect would be bigger in the LHC data, since the medium created in d-Au collisions is smaller than the system created in p-A collisions. This is an hypothesis that our measurements of heavy-flavour decay electrons in p-Pb can endorse.

3.3 Hot matter: Heavy quarks interactions with the QGP

Several theoretical approaches have been proposed to describe the propagation of the heavy quarks in the QGP. There are several ingredients in each energy loss model that has to be

---

[18] In p-A collisions the centrality dependence of the results are actually measured in multiplicity bins.

taken into account to understand the properties of the QGP. Different energy loss models can be divided in three different categories, concerning its approaches: pQCD, resonance scatterings, and strong coupling interactions (AdS/CFT);

Each of this categories have five major parts, that differs from each other:

- Parton generation: Different PDFs can be used for the generation of the partons.
- Initial effects: Some models include momentum broadening and/or shadowing. Shadowing is included in the PDF used for the parton generation in A-A collisions.
- Description of the partonic transport: The propagation of the quarks can be described by different equations, such as Langevin, Boltzmann, etc. And models using the same equation can differ in the way the transport coefficients are obtained.
- Description of the formed medium: For example, ideal or viscous hydrodynamics, with different initialisation time and different equation of state.
- Mechanisms of hadronization: Can include fragmentation and/or recombination.

In this chapter we choose some of the energy loss models for the heavy quarks propagation in the QGP, and we summarise the main idea and assumptions of each model. The models selected have different assumptions to the interactions of the heavy-quarks with the QGP and the idea is to compared these theoretical calculations with experimental data, in order to model the interactions of the particles with the medium, trying to extract properties of the physics of the QGP. Then, in this chapter we have chosen models that have comparisons with experimental data.

The heavy quark interactions based on pQCD cross section are the following:

- POWLANG [123, 124];
- Langevin Modified [125];
- BAMPS [126–128];
- MC@sHQ [129];
- WHDG [130].

The models based on resonant scattering, using a thermodynamic T-matrix approach are:

- TAMU [131, 132] ;
- UrQMD [133–135].

And there are also several models based on AdS/CFT, where the strong coupling interactions are considered, being more realistic than weakly interactions considered in pQCD.

In the following sections we give a brief summary of the main ingredients in each of these models.

3.3.1 Model based on Langevin equation: POWLANG

POWLANG [123] is a model based on POWHEG (POsitiv Weight Hard Event Generator) + Langevin equation. The POWHEG package [136] is used to produce the initial heavy-quarks pairs. It is a hard event generator for heavy-quark production in hadronic collisions, employing pQCD in next-to-leading-order (NLO). The energy loss of heavy quarks is based on the Langevin equation:

$$\frac{d\mathbf{p}}{dt} = -\eta_D \mathbf{p} + \xi(t) \tag{3.14}$$

where η_D is the drag force, $\mathbf{p}$ is the momentum and $\xi(t)$ represents the thermal random force experienced by a heavy quark, while it diffuses inside a thermal medium, due to multiple scatterings. Since the relativistic Langevin equation relies on the picture of many uncorrelated random collisions, this model only consider the collisional energy loss.

The transport coefficients, which are necessary to solve the Langevin equation, accounts for the interactions of heavy quarks with the medium. In this model [123] the calculations relies on separate treatment of soft (exchange of long wavelength gluons) and hard (high-momentum exchange) collisions. The soft collisions are described by the Hard Thermal Loop (HTL) [137] while the hard collisions is calculated in kinetic theory using leading order pQCD. The same authors published in [124] calculations where the transport coefficients were obtained using the non-perturbative lattice QCD, in order to make comparison with weakly-coupled scenario (pQCD). Lattice QCD results seems to indicate values of the momentum diffusion coefficient significantly larger than pQCD calculations. Also, it has no information on their momentum dependence.

In this model, the background is described by an expanding deconfined medium within two different scenarios: ideal and viscous hydrodynamics. The ratio of shear viscosity to entropy density is taken to be $\eta/s = 0.08$ in the viscous case and $\eta/s = 0$ in the ideal case. Different values of the starting time of the hydrodynamical evolution (initial proper time, τ_0) have been used in order to explore different scenarios. Lower values, as $\tau_0 = 0.1$ fm, provide longer propagation leading to an exposition of heavy quarks to higher temperatures, giving rise to a more pronounced quenching. The maximum value used for the calculations was $\tau_0 = 1$ fm.

In order to study the propagation of the heavy-quarks in the medium, the first step is to sample them in the space and define their momentum distribution.

The position of the heavy quarks in the transverse plane is calculated based on Glauber model[19], employing the nuclear overlap function $T(x+b/2,y)T(x-b/2,y)$, where

$$T(x,y) = \int \rho(x,y,z)\mathrm{d}z \tag{3.15}$$

b is the impact parameter and ρ is a Fermi parametrization of the nuclear density.

In the longitudinal direction, the model uses $z = \tau_0 \sinh \eta_s$, with

$$\eta_s \equiv \frac{1}{2} ln \frac{E + p_z}{E - p_z} \tag{3.16}$$

where E is the energy of the particle and p_z its longitudinal momentum.

The momentum distribution of the heavy quarks are determined by the event generator (POWHEG) employing the CTEQ6M PDF for the pp collisions and the EPS09 [138] for AA collisions.

In addition to the production cross section, this model also implements the momentum broadening, which is one of the cold nuclear matter effects discussed in Sec. 3.2.2. The procedure consists in to add to the heavy quarks a transverse momentum contribution randomly generated using a Gaussian distribution. For the pp case, the variance of the gaussian is $\langle k_T^2 \rangle_{NN} = 1$ GeV$^2/c^2$. If the transverse momentum broadening is not considered in the POWHEG production in pp collision, the cross section of electrons from beauty and charm quarks has a big discrepancy (50%) when compared to PHENIX data [123]. Including the momentum broadening the discrepancy is 12%, which is within the theoretical and experimental uncertainties. Comparisons of POWHEG + PYTHIA calculations (including the momentum broadening), FONLL and D^0 data measured at ALICE in pp at 7 TeV were performed in [124] and both predictions are compatible with data within the uncertainty band.

The hadronization of the quarks occurs around the phase transition of the energy density and only the fragmentation is implemented in this model, using the Peterson fragmentation function [139].

After the hadronization, hadrons are made to decay to electrons, to allow for a comparison between the model and experimental data. The decays are performed using the PYTHIA event generator.

---

[19] Glauber model is an approach to calculate geometrical quantities in the initial time of heavy-ion collisions, like impact parameter and number of participants. The nucleons positions inside each nuclei is determined stochastically, taking into account a Fermi distribution as a probability density function. The nuclei collide assuming that all the nucleons travel in straight line (eikonal approximation) and they are tagged as *participants or spectators.*

3.3.2 Model based on Langevin equation including a radiative term: Langevin modified (Duke)

This model [125, 140] uses a modified Langevin equation, where an additional term is introduced in Eq. 3.14 to describe the recoil force exerted on the heavy quarks while experiencing the medium-induced gluon radiation:

$$\frac{d\mathbf{p}}{dt} = -\eta_D \mathbf{p} + \xi(t) + \mathbf{f}_g \tag{3.17}$$

In Eq. 3.17, the first two terms are the same as in Eq. 3.14 and the last term on the right side is the additional term to describe the recoil force. This additional term is proportional to the time variation of the momentum of the radiated gluon:

$$\mathbf{f}_g = -\frac{d\mathbf{p}_g}{dt} \tag{3.18}$$

The gluon distribution function incorporates the heavy quark mass, leading to a mass dependence of the radiative energy loss.

To take into account the balance between gluon emission and absorption process, it is imposed a cut-off in the radiated gluon energy: $\omega_0 = \pi T$. Below this cut-off, the gluon radiation do not occur and heavy quarks motion is governed by quasi-elastic scatterings.

With this approach, it can be seen in Fig. 3.32 [125] that for high initial energies of the quark, the dominant process of energy loss is the radiative and with the decrease of the quark energy, the collisional energy loss is dominant. The crossing point is higher for bottom than for charm, since bottom has a larger mass which leads to a greater suppression of gluon radiation.

The medium considered in this model (quoted as *Duke* in some plots) is an expanding medium simulated with a (2+1)-dimensional viscous hydrodynamical model [141–143]. This simulation generates the space-time evolution of the local temperature and flow velocity profiles of the QGP. The hydrodynamical evolution of the medium is initialized with Monte Carlo Glauber Model or Kharzeev-Levin-Nardi (KLN) parametrization [144, 145]. A smooth initial condition is used for the bulk matter.

The starting time of the QGP evolution has been used as $\tau_0 = 0.6$ fm. The quarks are assumed to stream freely from their production vertices in hard collisions up to $\tau_0 = 0.6$ fm, which is the initial time that the hydrodynamical evolution commences. The energy loss in the pre-equilibrium stage is expected to be negligible given its short period of time compared to the evolution of the QGP.

The shear viscosity to entropy has been tuned as $\eta/s = 0.08$ for the case where the Glauber Model is used for initial conditions and $\eta/s = 0.20$ when KLN is used, which were tuned to RHIC and LHC data of spectra of soft hadrons.

The MC Glauber model is used to initialize the position of the produced heavy quarks. For their initial momentum distribution calculations, it is used NLO pQCD. The process

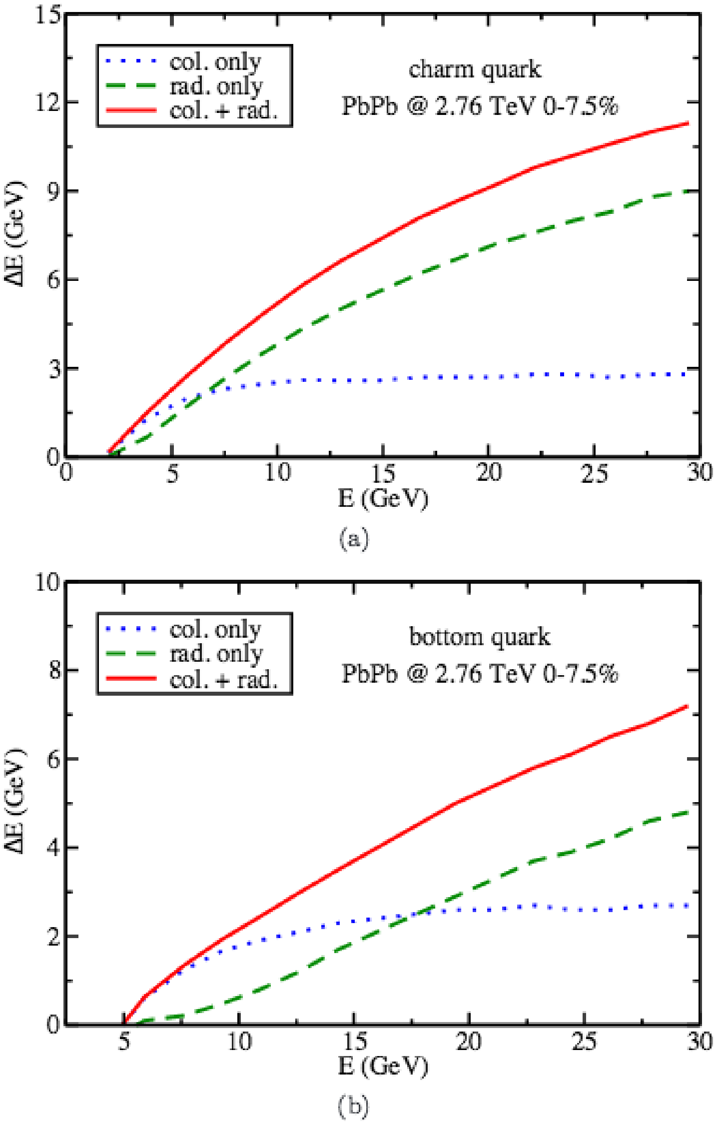

Figure 3.32: Comparison between radiative and collisional energy loss for charm (a) and bottom (b). Fig. from [125].

considered are pair production and flavour excitation.

In order to calculate the heavy flavour cross section in nuclear collisions, it is used the CTEQ for the parton distribution function and the EPS09 parametrisation is used to include the nuclear shadowing/anti-shadowing effect in heavy-ion collision.

The hadronization of the heavy quarks and of the bulk matter of the QGP occurs around $T_c = 165$ MeV. For the bulk matter, the hadronization is based on the Cooper-Frye formula [146] in order to obtain soft hadrons from the medium, given by:

$$E\frac{dN}{d^3p} = \int_{\sigma} f(x,p)p^{\mu}d\sigma_{\mu} \tag{3.19}$$

where $f(x,p)$ is the thermal distribution of soft hadrons and σ is the hyper surface of the freeze-out.

For heavy quarks hadronization, it is used a hybrid model that includes fragmentation and coalescence, based on the Wigner function, which denotes the probability for the two or three quarks to combine [125]. Heavy-light quark coalescence is important in low momenta, while fragmentation dominates in the high momenta regimes. To calculate the spectra from fragmentation process, it is used PYTHIA simulations. For the coalescence process, it is used the instantaneous coalescence model. The momentum dependence of the relative probability between both mechanisms is determined using the Wigner function in the instantaneous coalescence model. The Wigner function denotes the probability for the two or three quarks to combine. For the calculation of the coalescence, the thermal mass for light quarks are used (u and d at 300 MeV and s at 475 MeV). In the case of heavy quarks, they are not thermal and the masses used are 1.27 GeV for c and 4.19 GeV for b quarks. Thermal gluons contribution is also taken into account in this coalescence model: first they are split into light quark pairs and then, they are combined with heavy quark to create a hadron.

Fig. 3.33 [125], shows the probabilities of coalescence for charm and beauty as a function of the heavy quark momentum. It can be noticed that the probability of coalescence generally decreases with momentum. Also, for higher temperatures (higher fluid velocity) the coalescence probability is higher.

After hadronization, this model also includes hadronic scatterings inside a hadron gas. This feature is implemented using a framework called Ultra-relativistic Quantum Molecular Dynamics (UrQMD) [147], which is a Monte Carlo package to simulate pp, p-Pb and Pb-Pb collisions. This hadronic interactions further suppress the heavy meson production and enhances its elliptic flow.

Although this model has several ingredients to describe the interaction of the heavy quarks with the QGP, some authors [148] argue that including a radiative term in the Langevin equation is not possible, since the radiative energy loss involves quantum effects (interferences) and the Langevin simulation is purely classical.

3.3.3 Model based on Boltzmann equation: BAMPS

BAMPS [126] stands for Boltzmann Approach to MultiParton Scatterings. The Boltzmann equation describes the statistical behaviour of a thermodynamic system outside the thermodynamical equilibrium.

$$\frac{\partial f_i}{\partial t} + \frac{\overrightarrow{p}}{E}\frac{\partial f_i}{\partial r} = C_i^{2\rightarrow 2} + C_i^{2\rightarrow 3} + ... + C_i^{3\rightarrow 2} \tag{3.20}$$

where C_i are the collision terms (cross section) for the possible interactions: $C_i^{2\rightarrow 2}$ is the collisional term, $C_i^{2\rightarrow 3}$ is a term where two partons collide and the final state includes also a radiated gluon and $C_i^{3\rightarrow 2}$ is a term where a gluon is absorbed. Thus, in this model, the interaction probabilities are calculated from pQCD cross sections for elastic and inelastic processes.

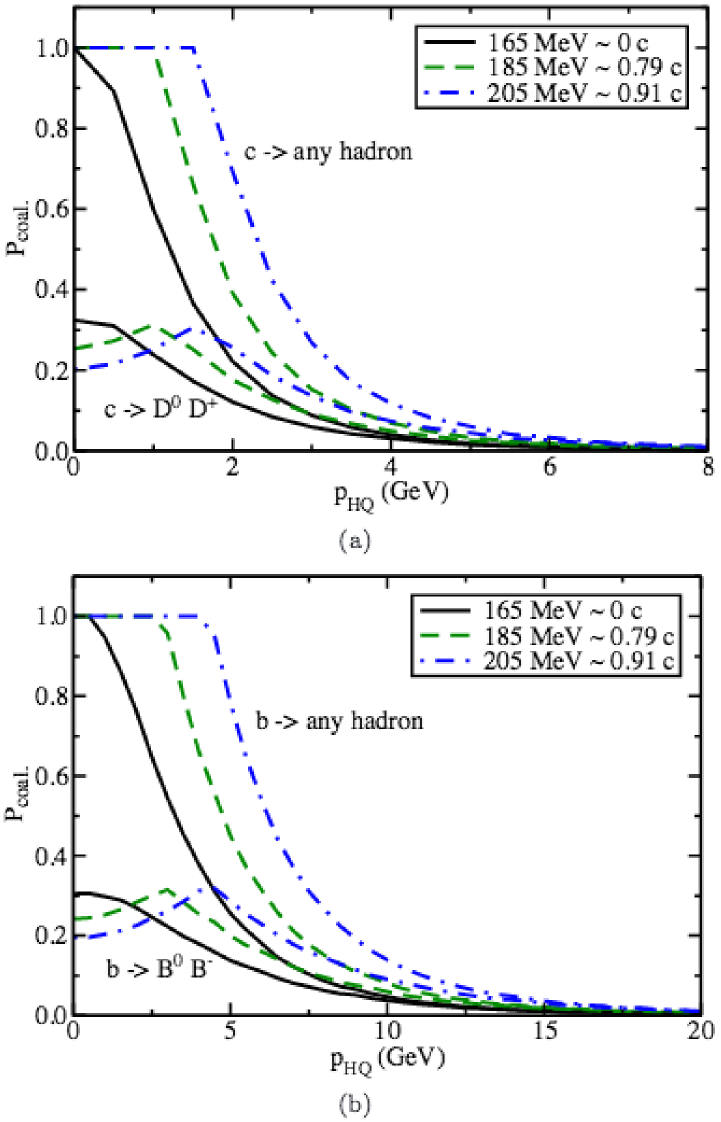

(a)

(b)

Figure 3.33: Coalescence probabilities as a function of momentum at different flow velocities: (a) for charm and (b) for bottom. Fig. from [125].

The model was first implemented considering only elastic energy loss. In [127], only the interactions between heavy quarks and gluons were considered (number of flavours n_f = 0 + 2). The cross section obtained after the evolution in the medium had to be scaled by a factor K = 4 in order to agree with RHIC data (that happens only in high-p_T). This factor is justified in [127] as a phenomenological factor to account for radiative contributions. In [128] the interaction of heavy quarks with gluons and light quarks were considered (n_f = 3 + 2) and the phenomenological factor that makes the model to agree with data is K = 3.5. The decrease in the factor K can be explained by the different behaviour of a purely gluonic plasma and a quark gluon plasma. The number of scatterings in the latter is higher, leading to a slight increase of the suppression and elliptic flow.

All cross sections are calculated in LO pQCD. In the t-channel, the cross section for small Mandelstam t (long range interactions) diverges due to the gluon propagator. This interactions are screened by the medium in thermal field theory. The gluon propagator is screened with a screening mass μ, which is proportional to the Debye Mass m_D:

$$\mu^2 = \kappa m_D^2 \tag{3.21}$$

The prefactor κ is determined calculating the energy loss of a heavy quark in a static medium in HTL and in LO pQCD and comparing the results. The value found is $\kappa = \frac{1}{2e} \approx 0.2$.

The Debye mass is calculated from non-equilibrium distribution functions f of gluons and light quarks:

$$m_D^2 = \pi \alpha_s \nu_g \int (N_c f_g + n_f f_q) \frac{1}{p} \frac{\mathrm{d}^3 p}{(2\pi)^3} \tag{3.22}$$

where $\nu_g = 16$ is the gluon degeneracy, $N_c = 3$ is the number of colours and n_f is the number of flavours.

In equilibrium and in Boltzmann statistics, the Debye mass reduces to

$$m_{D,eq}^2 = \frac{8\alpha_s}{\pi}(N_c + n_f)T^2 \tag{3.23}$$

In this model, the running of coupling α_s is considered for all heavy flavour process:

$$\alpha_s = \frac{4\pi}{\beta_0} \begin{cases} L_-^{-1} & Q^2 < 0 \\ \frac{1}{2} - \pi^{-1} arctan(L_+/\pi) & Q^2 > 0 \end{cases} \tag{3.24}$$

where $L_\pm = ln(\pm Q^2/\Lambda^2)$ and $\beta_0 = 11 - \frac{2}{3}n_f$.

The radiative interactions were implemented in the model in [126] also using the LO pQCD. The implementation of radiative bremsstrahlung processes of heavy quarks are done using Gunion-Bertsch approximation [149]. This approximation gives a simple expression for the gluon radiation amplitude in terms of the transverse momentum of the radiated gluon and the transverse exchanged momentum. It is also derived in the high-energy limit, considering the radiated gluon and the momentum transfer of the process as soft [149]. The matrix elements are calculated using the Feymann diagrams for $q + Q \to q + Q + g$.

The background considered in this model is a static thermal medium with a temperature of T = 400 MeV.

The initial heavy flavour distribution is produced using MC@NLO [72, 73] in next to leading order, while the light parton distribution is obtained from PYTHIA. The Glauber model is used to determine the spatial distribution of all particles.

It is interesting to note that the result for the radiative energy loss includes the dead cone effect. The dead cone is an effect where the gluon radiation is suppressed at angles given by the following equation:

$$\theta < m_q/E_q \tag{3.25}$$

where m_q and E_q is the mass and energy of a given quark q [150]. The dead cone effect in the BAMPS results can be seen in Fig. 3.34 [126] where D is the suppression factor (radiation spectrum of a gluon emitted off a heavy quark divided by the spectrum for the massless case), θ is the angle between the emitted gluon and the heavy quark and $\sqrt{s}$ is the energy of the heavy quark. The dead cone is the valley around $\theta \approx 0$. As can be noticed, the suppression is narrow for small $M/\sqrt{s}$ but very wide for large $M/\sqrt{s}$. For the same value of $M/\sqrt{s}$, the suppression factor is stronger in forward direction (with respect to the propagating heavy quark) and in the backward region the suppression factor saturates to unity.

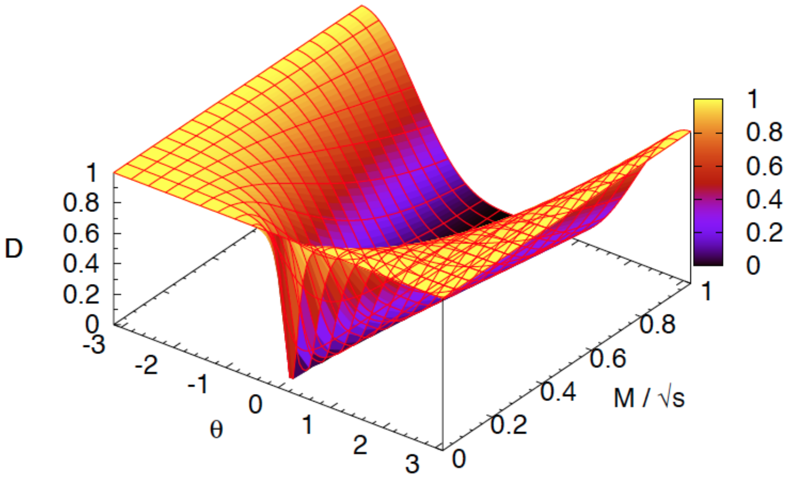

Figure 3.34: The suppression factor D (radiation spectrum of a gluon emitted off a heavy quark divided by the spectrum for the massless case) as a function of θ and $M/\sqrt{s}$. Fig. from [126].

Another effect which is included in this model and affects the results for the radiative energy loss is the LPM effect (see Sec. 3.2.3). The LPM effect leads to a suppression of the gluon radiation, due to the interference effect between adjacent scatterings.

The LPM effect produces a second dead cone at small emission angles that overshadows the dead cone due to the heavy quark mass. This overshadow is more pronounced for charm than for bottom, since the dead cone for bottom is wider due to its higher mass.

The implementation of the LPM effect is done in this model allowing only process that satisfies the following relation:

$$\lambda = X_{LPM}\tau \tag{3.26}$$

where λ is the mean free path of the considered particle, τ is the formation time of the emitted gluon and X_{LPM} is a free parameter, expected to be between 0 and 1. To apply this constraint in the model, the matrix element of the radiative process is multiplied by a step function:

$$\Theta(\lambda - X_{LPM}\tau) \tag{3.27}$$

After the propagation through the medium, the heavy quarks are fragmented to D and B hadrons using the Peterson fragmentation [139]. For the fragmentation of light quarks, it is used the AKK fragmentation function [151]. This model does not consider coalescence as a hadronization mechanism.

This model gives a possible explanation for the comparable suppression (in the ALICE data) found for D mesons and charged hadrons while non-prompt J/ψ ($B \rightarrow J/\psi$) has a smaller suppression: The explanation lies in the fact that LPM cut-off produces a second cone that overshadows the dead cone, especially for charm (D meson). For the beauty (J/ψ) the dead cone is not completely overshadowed and the heavy quark mass still plays a hole.

The results including only the collisional energy loss with the phenomenological factor $K = 3.5$ could explain the nuclear modification factor and the elliptic flow of heavy flavour decay electrons better than after including the radiative energy loss [126].

3.3.4 MC@sHQ + EPOS: SUBATECH

This model proposed in [129, 152] is also based on Boltzmann equation as BAMPS, but it has some differences in the determination of the screening mass and description of the background. It also considers the collisional and radiative energy loss, where the transition matrix are calculated from pQCD and the inclusion of the radiative energy loss also considers the LPM effect. The running of the coupling is considered as in BAMPS.

The gluon propagator in the t-channel is screened by an effective scalar propagator[20], given by Eq. 3.28 derived from HTL calculations.

$$\frac{1}{t} \rightarrow \frac{1}{t - \kappa m_D^2(T)} \tag{3.28}$$

where $\kappa m_D^2(T)$ is the screening mass and the Debye mass (m_D) is given by Eq. 3.29

$$m_D^2 = \frac{N_c}{3}(1 + n_f/6)4\pi\alpha_s(-m_D^2(T))T^2 \tag{3.29}$$

where N_c are the number of colours and n_f are the number of flavours. Note that, differently from the BAMPS model, which calculates the screening mass dynamically from the distribution of gluons and light quarks, in the MC@sHQ model, the equilibrium Debye mass is used with quantum statistics for temperatures from the medium.

---

[20] Due to the fact that the gluon is in a medium, it has a thermal mass.

The initial parton distribution is based on FONLL calculations and the quark-antiquark pairs are initialised randomly over the spacial points of the nucleon-nucleon collisions.

In this model, the background medium is described by the EPOS model [153, 154]. The initial conditions are obtained from multiple scattering of the nucleons. The dynamics are described by relativistic strings and the string breaking leads to hadron formation. In A-A collisions, when the string segments are slow or far from the surfaces, they are considered as locally thermalised and evolves as a fluid. The dynamical simulation in 3+1 dimensions of the fluid is evolved using a equation of state from lattice QCD. The ideal and viscous medium are tested with variations of the string radii.

The heavy quarks are evolved via free streaming until the evolution of the medium that starts at τ_0= 0.35 fm.

When the energy density of the medium falls to 0.64 GeV, the hadronization starts to happen, based on fragmentation and coalescence. After the hadronization, the heavy quarks do not interact with the hadronic environment. Fig. 3.35 shows the probability of hadronization by coalescence for charm and beauty and for different mass of light quarks (m_q). All heavy quarks which do not coalesce is assumed to form mesons by fragmentation.

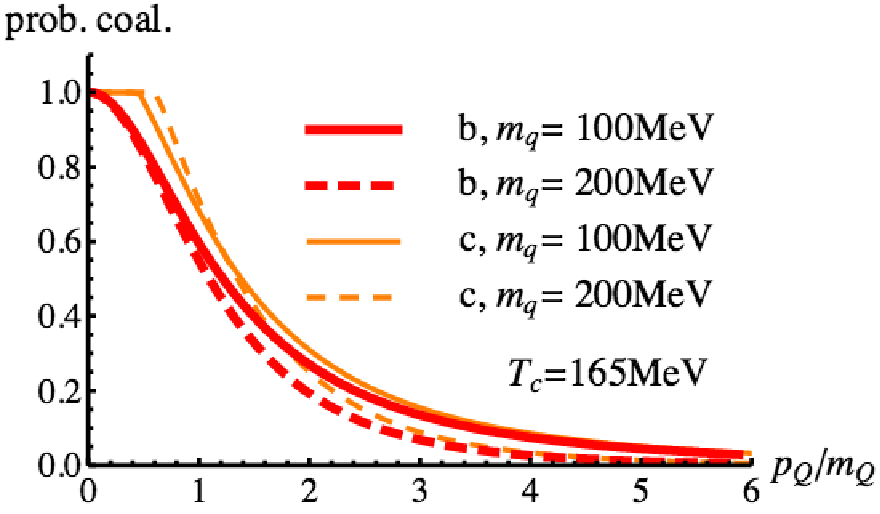

Figure 3.35: Probability of hadronization by coalescence for charm and beauty for different values of mass for light quarks (m_q). Fig. from [155].

3.3.5 Jet tomography: WHDG

This model [130] uses perturbative QCD, including elastic and inelastic parton energy losses and also includes path length fluctuations. The path length is the distance that the parton with high momentum travels through the medium and this path is different for each parton, since they are created in different locations of the overlap of the A-A collision [148].

The authors argue in their paper [130] that radiative and elastic energy losses for heavy quarks are comparable and neither of them can be neglected. In Fig. 3.36 this finding is shown for heavy and light quarks, where the medium considered is an expanding QGP with path length L = 5 fm and with initial density fixed by dN_g/dy. Additionally, the coupling was fixed as $\alpha_s = 0.3$.

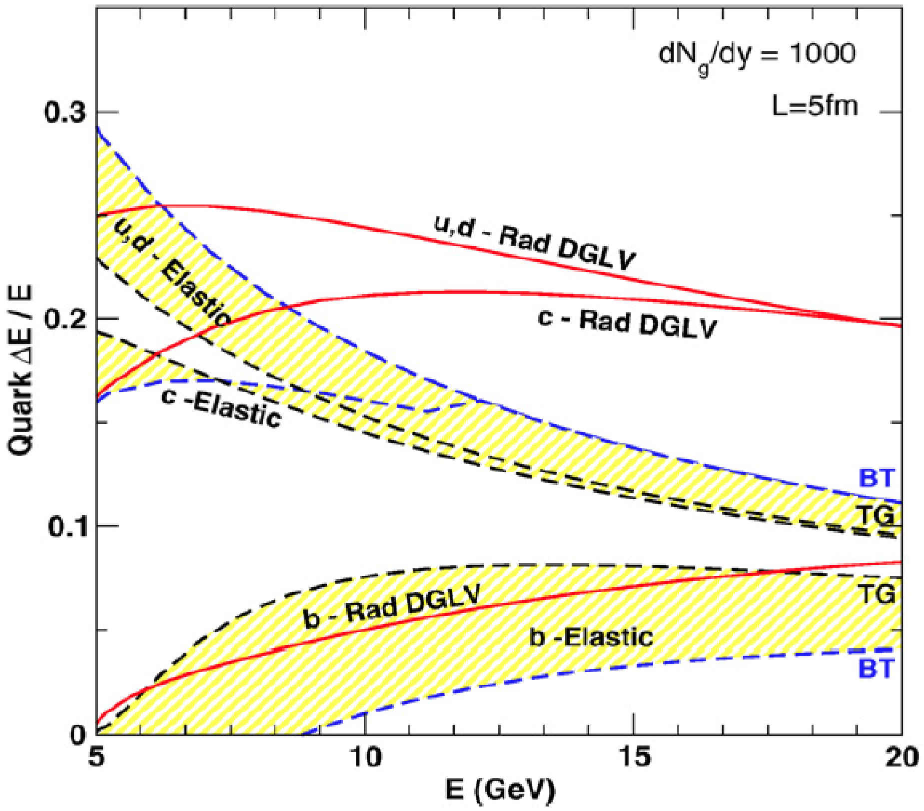

Figure 3.36: Average energy loss for u, d, c, b quarks as a function of E. The red line are the radiative energy loss (first order) and the yellow bands are the elastic energy loss. Fig. from [130].

The initial parton spectrum is calculated in LO and NLO, where the PDF used is the CTEQ5M. No intrinsic momentum broadening is considered neither shadowing of the nuclear PDF, which means that this energy loss model do not consider any cold nuclear matter effect. The nuclear density profile is created using the Woods-Saxon [156] and the Glauber profiles.

The spectra of partons, hadrons and leptons are calculated from the generic pQCD convolution:

$$\frac{Ed^3\sigma(e)}{dp^3} = \frac{E_i d^3\sigma(Q)}{dp_i^3} \otimes P(E_i \to E_f) \otimes D(Q \to H_Q) \otimes f(H_Q \to e), \tag{3.30}$$

where Q denotes quarks and gluons and the initial quark spectrum is computed in NLO while the gluons spectrum is computed in LO. $P(E_i \to E_f)$ is the energy loss probability, including elastic and inelastic losses and their fluctuations, $D(Q \to H_Q)$ is the fragmentation function of a quark Q to a hadron H_Q, and $f(H_Q \to e)$ is the decay function of the hadron Q to a single electron e. The hadronization mechanism considered is only the fragmentation and in this model it is assumed that the jet fragmentation function into hadrons in Au-Au collisions is the same as in e^+e^- collisions.

The energy loss probability includes the elastic energy loss (P_{el}), the radiative energy loss P_{rad} and also the geometric path length fluctuations L:

$$P(E_i \to E_i - \Delta_{rad} - \Delta_{el}) = \int \frac{d\phi}{2\pi} \int \frac{d^2\vec{x_\perp}}{N_{bin}(b)} T_{AA}(\vec{x_\perp}, \vec{b}) \otimes P_{rad}(\Delta_{rad}; L(\vec{x_\perp}, \phi)) \otimes P_{el}(\Delta_{el}; L(\vec{x_\perp}, \phi)) \tag{3.31}$$

where $\vec{x_\perp}$ is the initial production point, ϕ is the azimuthal direction relative to the impact parameter plane and L is given by:

$$L(\vec{x_\perp}, \phi) = \int d\tau \rho_p(\vec{x_\perp} + \tau \hat{n}(\phi)) \tag{3.32}$$

ρ_p is the transverse density of the nucleons computed using the Glauber model.

3.3.6 Heavy quark interactions based on resonant scatterings: TAMU

The model presented in [131, 132] (TAMU) implements the notion of strongly coupled QGP for the diffusion and hadronization of heavy quarks in high-energy heavy-ion collisions. The diffusion process is simulated using relativistic Fokker-Planck dynamics [157] for elastic scattering in a medium described by hydrodynamics.

In this model, the two-body interactions are performed using potentials, $V(t)$ where t is related to the momentum transfer. The transport coefficients are calculated using non-perturbative T-matrix interactions which build up resonant correlations close to the transition temperature. The resonant correlations are also used for the hadronization of heavy quarks into heavy flavour mesons via recombination with light quarks from the medium. The probability of the recombination is derived from the resonant heavy-quark scattering rate, which implies in recombination specially in low transverse momentum and fragmentation in high transverse momentum. The hadronization occurs in the phase transition using the Resonance Recombination Model (RRM) [158].

The initial HQ spectra are calculated with PYTHIA and the EPS09 parton distribution function is used to include shadowing [132].

The medium considered in this model is an expanding medium which is described by ideal 2+1-dimensional hydrodynamics. The code AZHYDRO [159] is used at RHIC energies.

The thermal relaxation rate[21], which is related to kinetic equilibration, are faster in resonant scattering calculations than in LO pQCD, as it is shown in Fig. 3.37 for charm. The resonant scattering accelerates the kinetic equilibration by up to a factor of ≈ 3-5 relative to LO pQCD. Similar acceleration is also found for beauty, but the absolute magnitude of

---

[21] The relaxation rate, also called friction coefficient, is proportional to the HQ-parton scattering amplitude

the thermal relaxation rate is smaller due to the larger mass of beauty compared to charm quarks.

Modifications of the HQ potential V by the medium is computed employing the l-QCD[22].

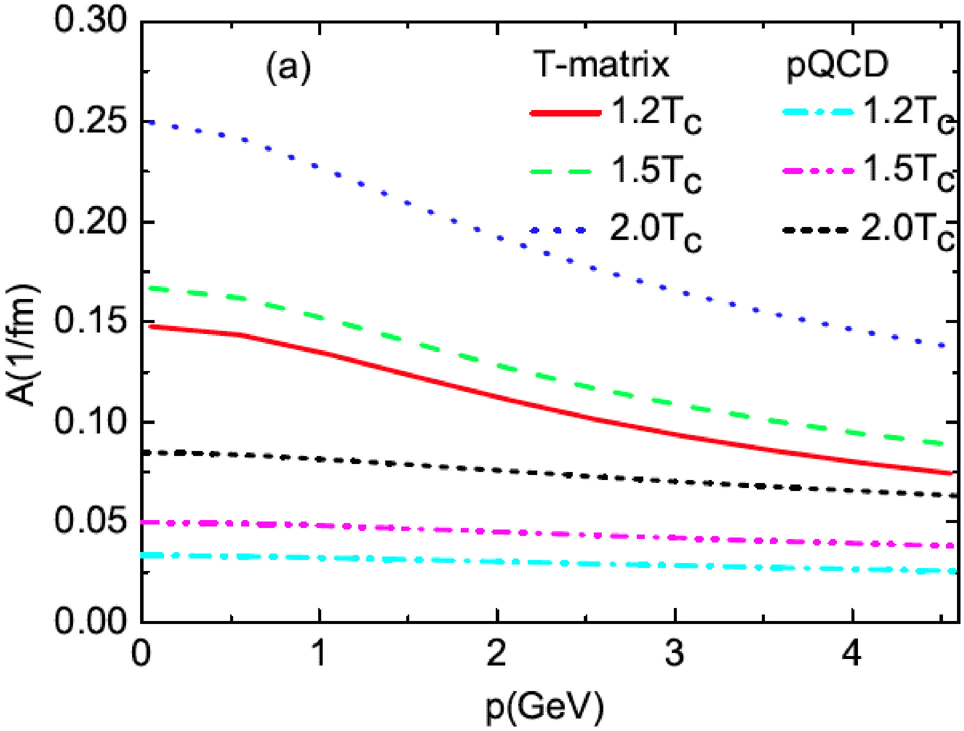

Figure 3.37: Relaxation rate for charm quarks as a function of momentum using heavy-light quark T-matrices plus pQCD gluon scattering with $\alpha_s = 0.4$ (upper three curves) and pQCD scattering off quarks and gluons with $\alpha_s = 0.4$ (lower three curves) Fig. from [131].

For the hadronization of light quarks it is used the Cooper-Frye [146] freeze-out procedure.

The diffusion of heavy-flavour mesons in the hadronic phase is also considered. The interactions in this phase is based on D-meson scattering amplitudes of light hadron.

This model does not take into account a possible local reheating if the expanding QGP phase swallows again an already hadronized heavy quark due to the increasing matter flow.

3.3.7 Heavy quark interactions considering a realistic background: UrQMD

This model, proposed in [133–135] uses the non-perturbative T-matrix idea as used in TAMU model, but applies a different description for the background medium. The UrQMD [147, 160, 161], (same used in Duke model 3.3.2 for the hadronic interactions) is a hybrid model, including hydrodynamics and Boltzmann equation.

The authors of this model [133–135] argue that using the UrQMD they can take into account that the medium is not homogeneous but it is locally fluctuating and it consists of a fast expanding medium, which are effects usually not considered in other models.

---

[22] Since the HQ potential V modification in medium is still an open question, l-QCD is employed to determine the limiting cases: HQ free and internal energy.

In the description of the background, this energy loss model uses the UrQMD to describe the initial and final stages of the medium. The intermediate stage of the medium is described by a (3+1) dimensional ideal fluid.

The partons spectrum are obtained by PYTHIA and the initial position of each nucleon inside the nucleus are sampled according to the Glauber Model.

The transport of the particle are done using the Langevin equation.

In this model, it is not used the running of the coupling constant, i.e. it is taken as $\alpha_s = 0.4$.

The hadronization of light quarks is done using the Cooper Frye equation [146], while the hadronization of heavy-quarks can occur via coalescence or fragmentation, using the Peterson fragmentation function [139].

3.3.8 Strong coupling interactions (AdS/CFT)

The QGP produced at RHIC and LHC behaves as a strongly-coupled fluid [162]. This happens because the QCD coupling constant cannot be considered small at temperatures at which the plasma is produced in these experiments (which is not so far above the deconfinement temperature). This makes the use of perturbation theory problematic, or even impossible in the study of the QGP. Lattice QCD can be used to study this new phase of matter, but this approach has some limitations concerning the computation of transport coefficients and other observables. Fortunately, this strongly-coupled behaviour of the QGP can be studied using the so-called AdS/CFT correspondence (Anti-de-Sitter/Conformal Field Theory) [163].

The AdS/CFT correspondence or gauge/gravity duality is a conjecture equivalence between Conformal Field Theories em d dimensions and gravity theories in $d + 1$ dimensions. In the most known example of this duality a certain conformal field theory in $4-$dimensional Minkwoski space-time known as $N = 4$ Super Yang-Mills (SYM) theory is dual to a string theory living in AdS_5 x S^5. (Anti-de-Siiter space in five dimensions times a $5-$sphere) [163].

The advantage of using this duality is that when the field theory is strongly coupled, the dual gravity theory is weakly coupled and can be studied using perturbation theory. This special property allows one to study non-perturbative physics of the field theory performing calculations in a weakly coupled gravity theory [163].

The most simple models based on the AdS/CFT correspondence use the $N = 4$ SYM theory at finite temperature as a models for the QGP produced in heavy-ion collisions. This simple approach has several limitations because the $N = 4$ SYM and QCD are very different theories. Despite the fact that the $N = 4$ SYM theory has a lot of more symmetries than QCD (supersymmetry, conformal symmetry, etc), the duality is strictly valid in the limit where the number of colour N_c and the coupling $\lambda = N_c^2 g$ are both infinity. However, one can use this duality to study qualitative aspects of strongly-coupled gauge theories [163]. Besides that, it is possible to extend this correspondence in order to consider more realist theories [164].

One of the models using the AdS/CFT is proposed in [165], where the medium is considered as strongly-coupled plasma coupled to a high-p_T probe. The energy loss of heavy-flavour is calculated using the following equation:

$$\frac{dp_T}{dt} = \frac{\pi \lambda^{1/2} T^2}{2 M_Q} p_T \tag{3.33}$$

where $\lambda = g^2 N_c \approx 12$, T is the temperature of the medium, M_Q is the mass of the heavy quark and p_T its momentum.

The authors of [165] argue that the comparison between AdS/CFT calculations and data are difficult because there is no unique mapping from predictions of pQCD to those of $N = 4$ SYM and AdS_5 x S^5.

3.3.9 Summary of the energy loss models in QGP

In Tab. 3.3.9 we summarize the main assumptions adopted in each energy loss model presented in this section.

Model	Parton generation	Initial effects	Partonic transport	medium	hadronization mechanism
POWLANG	POWHEG	momentum broadening	Langevin (collisional)	expanding medium (ideal/viscous)	fragmentation
Langevin Modified	CTEQ EPS09	shadowing	Langevin + radiative term (collisional and radiative) hadronic interactions	(2+1)d-expanding medium (viscous)	fragmentation coalescence.
BAMPS	PYTHIA	not used	Boltzmann + LPM effect (collisional and radiative)	static thermal medium	fragmentation
MC@sHQ	FONLL	shadowing	Boltzmann + LPM effect (collisional and radiative)	(3+1)d-EPOS model	fragmentation coalescence
WHDG	CTEQM05	not used	generic pQCD convolution (collisional and radiative)	expanding medium	fragmentation
TAMU	FONLL EPS09	shadowing	Langevin resonant scatterings hadronic interactions	(2+1)d-expanding medium	fragmentation coalescence
UrQMD	PYTHIA	not used	Langevin (collisional)	UrQMD + (3+1)d-ideal expanding medium	fragmentation coalescence
AdS/CFT	FONLL	not used	AdSCFT drag	strongly coupled plasma	fragmentation

Table 3.1: Summary of the main ingredients used in the different energy loss models in the QGP presented in this section.

3.3.10 Experimental results in A-A collisions

PHENIX and STAR have recorded data in pp, Au-Au and d-A collisions at $\sqrt{s_{NN}}$ = 200 GeV. Measurements of Cu-Cu collisions at $\sqrt{s_{NN}}$ = 200 GeV and U-U collisions at $\sqrt{s_{NN}}$ = 193 GeV were also recorded in order to study the system size dependencies of the open heavy-flavour production[23].

In the Fig. 3.38 the heavy-flavour decay electrons R_{dAu} and R_{AuAu} are compared to the ones obtained for π^0. For $p_T > 5$ GeV/c, the cold nuclear matter effects are small for both species and their R_{AuAu} are consistent within the uncertainties. On the other hand, for low p_T, the cold nuclear matter effects are large for electrons from heavy-flavour hadron decays and small for π_0, and additionally the R_{AuAu} for electrons are above the R_{AuAu} for π_0. This result could suggest that the cold nuclear matter effects is reflected in the final state spectra considering a mass-dependent Cronin enhancement [122].

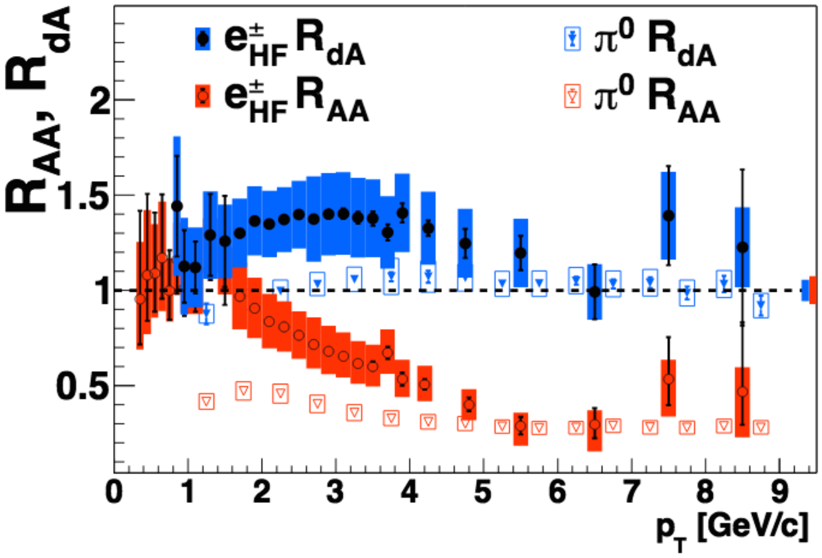

Figure 3.38: Nuclear modification factor R_{dAu} of electrons from heavy-flavour hadron decays in minimum bias d-Au collisions measured by PHENIX. Fig. from [122].

Fig. 3.39 shows the corresponding STAR results for the R_{dAu} and R_{AuAu} at $\sqrt{s}$ = 200 GeV. In this case the results have large uncertainties and the R_{dAu} is consistent with one, while the R_{AuAu} shows a suppression for the most central collisions (0-5%).

Some theoretical models for the energy loss of electrons from heavy-flavour hadron decays are compared to the STAR results. Curve I is a result proposed in [167], which is similar to the WHDG model (see Sec. 3.3.5) but without considering collisional energy loss and path length fluctuations. Curve II shows the calculation of a model called BDMPS, which includes only radiative energy loss, via multiple soft collisions, presented in [168, 169]. Both calculations predict less suppression than observed in data and this can be an indication

---

[23] Other collision systems and other energies were also used at RHIC, but the main results for open heavy-flavour observables were obtained in the described systems.

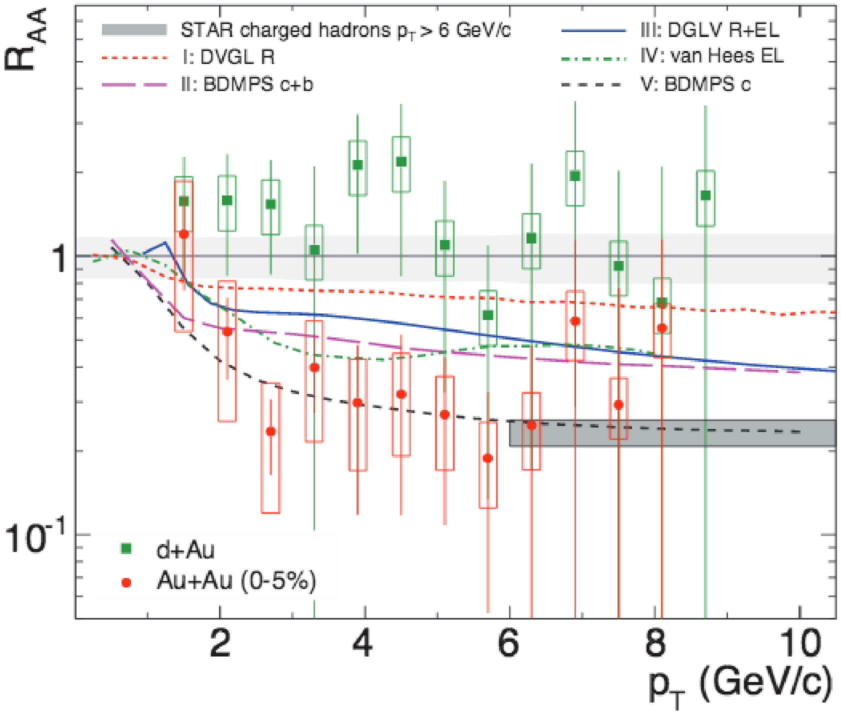

Figure 3.39: Electrons from heavy-flavour hadrons decay nuclear modification factor measured by STAR in Au-Au collisions at $\sqrt{s}$= 200 GeV. Fig. from [166].

that the collisional energy loss can play a significant role in the interactions of heavy flavour with the medium. Curve III is the model presented in Sec. 3.3.5. Even including the elastic energy loss and the path length fluctuations, the predicted suppression is still smaller than the observed in the experimental data. Curve IV is the theoretical model presented in Sec. 3.3.6, where elastic scatterings mediated by resonance excitations and gluon exchanges are used. This model also predicts less suppression than seen in the data. Curve V is the model BDMPS (which includes only radiative energy loss) calculated only for charm quarks (only D-meson decays to electrons), where the authors argue that the bottom energy loss contribution should be suppressed by the dead cone effect.

PHENIX results showed that the suppression of electrons from heavy-flavour hadron decays is similar to the suppression of π^0, for $p_{\mathrm{T}} > 5$ GeV/c (Fig. 3.38). Moreover, in the low p_{T}, the observed suppression of electrons from heavy-flavour hadron decays is smaller than the observed suppression of π^0. Then, to understand the R_{AA} results, the data is compared to the R_{dA} results of electrons from heavy-flavour hadron decays and π^0. The latter has a R_{dA} compatible with one while the former presents an enhancement in the low p_{T}. The enhancement can be interpreted as CNM effects, like the Cronin enhancement. This effect is also present in R_{AA} results, what can be an explanation for the smaller suppression of the electrons from heavy-flavour hadron decays when compared to π^0 results. We also see in Fig. 3.31 that this enhancement is higher in the most central collisions. The STAR measurements of electrons from heavy-flavour hadron decays (Fig. 3.39) also show similar suppression in

Au-Au collisions and a compatible enhancement in R_{dAu}, within the statistical uncertainties.

PHENIX also measured the heavy-flavour decay electrons in different A-A collisions systems (Fig. 3.40) and it shows a stronger suppression for heavier nucleus, where Au-Au is compared to Cu-Cu collisions.

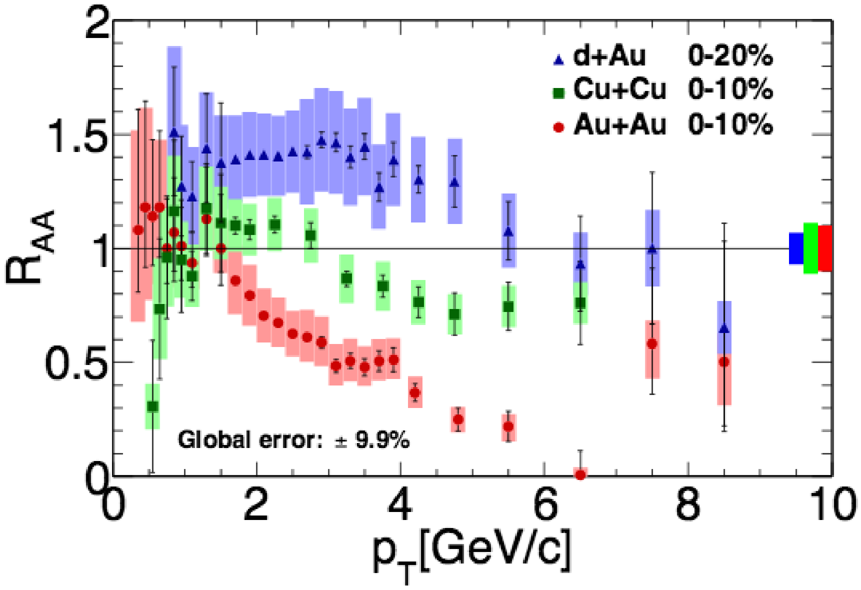

Figure 3.40: Heavy-flavour decay electrons nuclear modification factor in Cu-Cu, Au-Au and d-Au measured by PHENIX at $\sqrt{s_{\mathrm{NN}}}$= 200 GeV in central collisions. Fig. from [170].

Also, the nuclear modification factor of electrons from heavy-flavour hadron decays measurements in Cu-Cu collisions (Fig. 3.41) in different centralities bins, shows that, for the most central collision, a suppression is observed while for peripheral collisions, an enhancement is detected. This can be an indication of CNM effects present in the Cu-Cu collisions. An understanding of these results requires d-Cu collisions measurements, which are not available yet.

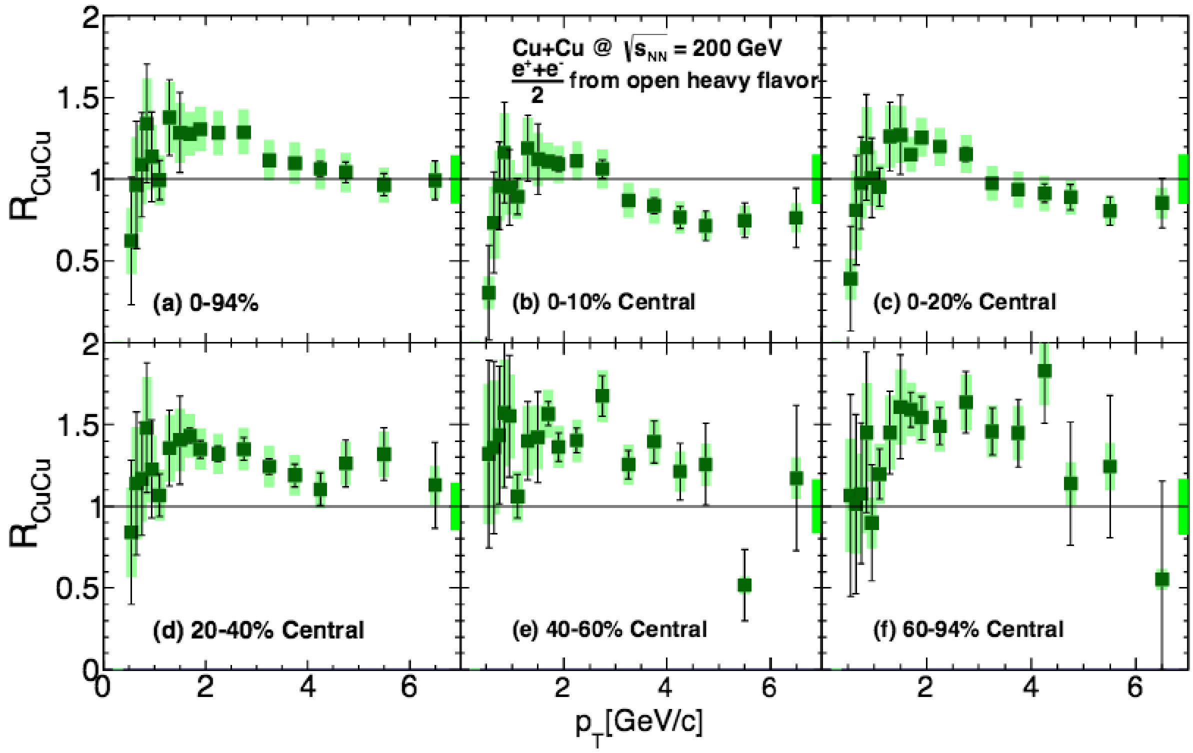

Figure 3.41: Heavy-flavour decay electrons nuclear modification factor in Cu-Cu measured by PHENIX at $\sqrt{s}$= 200 GeV at different centralities. Fig. from [170].

3.4 Final considerations of this chapter

In the first section of this chapter (Sec. 3.1), we have presented experimental results presented for pp collisions for the LHC, RHIC and fixed-target experiments where they were compared to FONLL, GM-VFMS and/or k_{T}-factorization theoretical predictions and they were compatible within the systematic uncertainties. Then, for all the measured energies, the heavy-flavour production can be described by the pQCD. Heavy-quarks are produced through initial-hard parton scatterings, thus, they can be treated by the pQCD and the perturbative treatment can be used even at very low momenta. Then, the heavy-flavour observables are a unique probe for the pQCD calculations and the agreement between the calculations and data provides a solid experimental and theoretical reference for the understanding of the heavy-ion collisions.

In the second section of this chapter (Sec. 3.2) we have presented the effects that are expected in the cold nuclear matter. A good understanding of the CNM effects is a key ingredient to understand heavy-ion collisions and the properties of the QGP. The CNM effects are accessed via p-A collisions, in which it is not expected an extended QGP formation. The nuclear modification of the PDF is one of the effects that have already been observed experimentally and it is largely used in models that try to explain results from p-A and A-A collisions. The Cronin enhancement was discovered experimentally, and there are different models with different assumptions that lead to different explanations for the observed enhancement. In fact, the energy loss considering incoherent scattering is an effect that leads to momentum broadening, being also one possible explanation for the Cronin enhancement. On the other hand, energy loss including coherent scattering can also affect particle production in p-A collision, since the medium-induced gluon radiation in this case can suffer a suppression. Then, all these effect have to be well understood in order to give a baseline for the understanding of the interactions of heavy-favour decay particles with the QGP. We have also presented the electrons from heavy-flavour hadrons decays measured by PHENIX in d-Au collisions and the result shows a Cronin enhancement in the most central collisions.

The third section of this chapter (Sec. 3.3) was dedicated to present the main ideas of some energy loss models in the QGP. To understand the properties of the QGP, theoretical calculations, with given assumptions, are compared to the experimental data. The assumptions are used as evidences to validate or invalidate descriptions. Thus, as the energy loss is a result of many interactions of a particle in the medium, modelling these phenomena can provide us a tool to assess the physics of the QGP. Several energy loss models have been proposed in the last decade, and in this chapter we discussed those that have been compared to the LHC data. The results of the comparisons and the implications to the understanding of the QGP properties will be shown in Chap. 7.

We have seen that each model uses a different partonic generation and some of the models do not include any initial effects from CNM. For instance, the shadowing can affect the particle production in low transverse momentum, and the models that do not take this effect into account will present a different shape in low-p_{T} region when compared to models that include the nuclear parton distribution function.

Several models assumes Langevin or Boltzmann equations to propagate the particles through the QGP. In [171], the author shows that Langevin equation can be obtained from Boltzmann equation when considering small momentum transfer. However, even studying heavy-quarks, which have large mass, the condition of soft collisions (small momentum transfer) may not always be fulfilled, and differences can be found when comparing solutions of Langevin and Boltzmann equations for the charm quarks, as can be seen in Fig. 3.42 (left). For bottom, the Langevin and Boltzmann lead to a very similar results, as can be seen in Fig. 3.42 (right).

Another difference among the models is how they calculate the transport coefficients. The use of pQCD assumptions implies in considering that the heavy-quarks are weakly coupled with the medium, while AdS/CFT and resonant scatterings assume a strongly-coupled medium. Some years ago, it was expected that heavy-quarks would interact perturbatively with the QGP due to its large masses, however the first experimental data showed similar suppression for light and heavy-flavours and also suggested that heavy quarks flows with the medium. This scenario encourage the idea of treating the heavy quarks as strongly-coupled with the QGP.

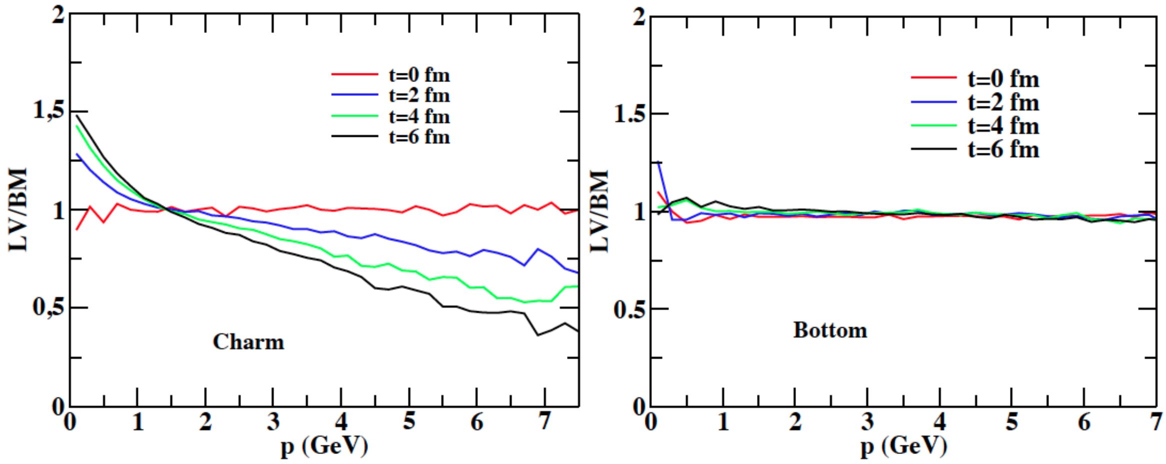

Figure 3.42: Ratio of Langevin (LV) and Boltzmann (BM) spectra results after the transport of charm (left) and beauty (right) in the medium for various values of time. Deviations between the two approaches are present in the case of charm, while for beauty the Langevin equation is always a good approximation. Fig. from [171].

The medium considered in each model also differs. Most of the models uses a homogeneous expanding medium without local fluctuations or reheating of the plasma in case one formed hadron is absorbed by the medium.

Another difference is the way the hadronization is assumed to occur. It is known that recombination plays a crucial role in the low transverse momentum hadron spectra. And the models that only use the fragmentation also plan to include this mechanism in their models.

And, at last, most of the models include radiative and collisional energy losses in their calculations but we still can find models only including collisional energy loss, since they believe that the dead cone effect would suppress the radiative energy loss.

In Sec. 3.3.10 we have shown some previous experimental results obtained at RHIC. The nuclear modification factor of electrons from heavy-flavour hadron decays is smaller than one, showing that the heavy-flavour particles interacts with the medium, loosing their energy. In high p_{T}, the amount of suppression is similar to the one for light particles. However, if there is an enhancement in d-Au collisions, the same enhancement due to CNM effects will increase the R_{AuAu} results. And this can be a possible explanation for the similar suppression observed for light and heavy particles.

Concerning the results of R_{CuCu}, it is necessary data of d-Cu collisions to investigate the possible reason of the enhancement observed, which are probably related to CNM effects.

The LHC data can help to elucidate these previous results and also serve as a constraint to the theoretical models. In this thesis, we have measured electrons from heavy-flavour hadron decays in p-Pb collisions at $\sqrt{s_{NN}} = 5.02$ TeV. Our measurement is used to quantify CNM effects and to understand its properties, which is done by comparing experimental results with theoretical models. Additionally, this measurement serve as a baseline for the measurements in Pb-Pb collisions, where the effects from cold matter is together with effects due to the QGP. Thus, if the effects from CNM are understood in p-Pb collisions, similar effects are expected in Pb-Pb due to the CNM and the effects from the QGP can be quantified. Given that both effects are separated, the interactions of the particles with the QGP can be extracted from the comparison of the experimental data and theoretical models.

Finally, in this thesis, we present our measurement of electrons from heavy-flavour hadron decays in p-Pb and its comparison with theoretical models for the CNM effects. Then, we use our result to further understand the results in Pb-Pb collisions and the possible explanations for the interactions of the particles with the QGP.

Chapter 4

Experimental Setup

In this chapter we present the ALICE detector and its sub detectors used to obtain data for the analysis of electrons from heavy-flavour hadron decay studied in this thesis. We also present how the vertex reconstruction of each collisions is performed by the offline computation and the algorithm used for track reconstruction. We also briefly describe how the clusters of energy in the electromagnetic calorimeter can be found and how the trigger system works.

4.1 An overview on the ALICE Detector

The data used in this thesis was taken by the ALICE detector at LHC. The ALICE is a detector dedicated to the studies of the physics of strongly interacting matter and the QGP in heavy-ions collisions [172]. It is composed by several subdetectors, with different purposes and performance.

It consists of two separated parts, one in the central rapidity region part and other in the forward direction. The latter consists of a muon spectrometer, while the former measures electrons, hadrons and photons, and is located inside a large magnetic solenoid (the magnet responsible for the production of a magnetic field in all detectors). Starting from the inner part, the ALICE central barrel have the following sequence of sub detectors: the Inner Tracking System (ITS), the Time Projection Chamber (TPC), the Time-Of-Flight (TOF), the High-Multiplicity Particle Identification Detector (HMPID), the Transition Radiation Detector (TRD) and two calorimeters, the Electromagnetic Calorimeter (EMCal)[1] and the Photon Spectrometer (PHOS). The PHOS, EMCal and HMPID do not cover the full azimuth while all the others detectors in central barrel have acceptance of 2π.

In the forward region, the muon arm consists of absorbs, a dipole magnet and ten tracking chambers. There are also some smaller detectors located at small angles, like Zero Degree Calorimeter (ZDC), Photon Multiplicity Detector (PMD), Forward Multiplicity Detector (FMD), T0 and V0 which are used for global event characterization and as trigger.

---

[1] For the LHC run-2, the Di-jet Calorimeter (DCAL) was installed and it is being used for data taking. It is a complementary part of the EMCal, built with the same technology, allowing measurements back-to-back, since they form a two-arm electromagnetic calorimeter.

Fig. 4.1 shows an schematic view of ALICE. The central barrel has a cylindrical geometry, where the z direction is along the beam line. The spatial coordinates of the particles are described by the azimuthal angle ϕ and the pseudorapidity η, which is defined as a function of the polar angle θ, as shown in the equation 4.1.

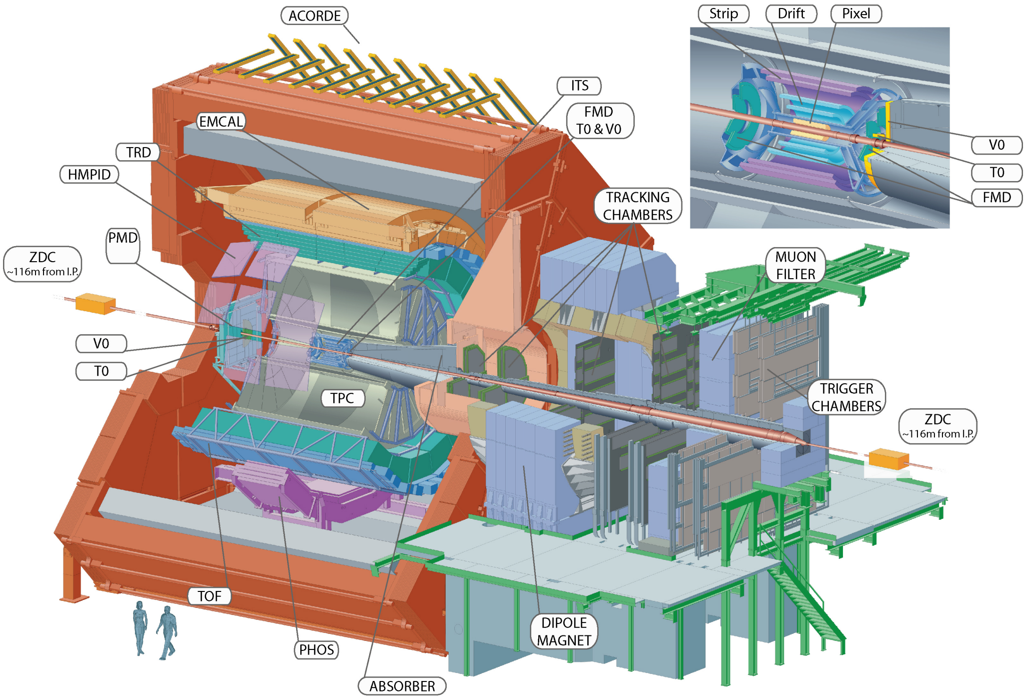

Figure 4.1: Schematic of the ALICE detector. Fig. from [172].

$$\eta = -ln(tan\frac{\theta}{2}) \tag{4.1}$$

More information about the ALICE detector can be found in [172]. The main detectors of ALICE used in this analysis are:

- ITS: Used for track reconstruction.
- TPC: Used for track reconstruction and for particle identification.
- TOF: Particle identification and track reconstruction.
- EMCal: Used for particle identification and trigger.
- V0: Used as trigger.

These detectors are described bellow:

4.1.1 Eletromagnetic Calorimeter - EMCal

The EMCal is an electromagnetic calorimeter that measures energy of electrons and photons [173]. When these particles traverse the material, they produce an electromagnetic shower.

The signal produced by the particle is proportional to the energy deposited and this information can be used to identify the particles. The matching of EMCal data with the tracks measured by the TPC enables the calculation of the ratio between the energy deposited in a given EMCal cluster divided by the momentum measured in the TPC (E/p). Since electrons deposit all their energy in the EMCal, and have a small mass, this ratio is expected to be equal to one. On the other hand, hadrons deposit only a small part of their energy on the EMCal, leading to a small E/p ratio. Hence, the EMCal and TPC together provide a good separation of electrons and hadrons.

The EMCal covers 107 degrees in the azimuthal direction and $-0.7 < \eta < 0.7$ acceptance in pseudo-rapidity. The geometry of the EMCal was designed regarding the integration with other ALICE detectors that were designed previously. It is located inside the magnet, between the TPC and the solenoid coils.

The EMCal is composed of alternating layers of Pb and scintillator (polystirene). It has 76 Pb layers of 1.44-mm thick each, and 77 scintillator layers of 1.76-mm thick each. The readout of the scintillator is done via wavelength shifting fibres (WLS), running through the Pb-scintillator tiles perpendicular to the front surface (Shashlik technology).

The calorimeter is segmented into 12288 towers, each of which is approximately projective in η and ϕ to the interaction vertex [16]. Each tower is 6×6 cm^2 resulting in an acceptance of $\Delta\eta \times \delta\Phi \approx 0.014 \times 0.014$ in $\eta = 0$. The advantages of the EMCal are twofold: it may serve as trigger for events with high p_{T}, and the relative energy resolution is better than the relative momentum resolution for higher energies.

The towers in the EMCal are divided into modules, and a module is composed by 4 towers (2 x 2 towers). A TRU (Trigger Region Unit) is composed by 4 x 24 modules (8 x 48 towers), forming a total of 16 x 2 TRU. A combination of 3 x 1 TRU is called Super-Module (SM). The Fig. 4.2 shows the EMCal design and its 10 SM and Fig. 4.3 shows its modules and towers.

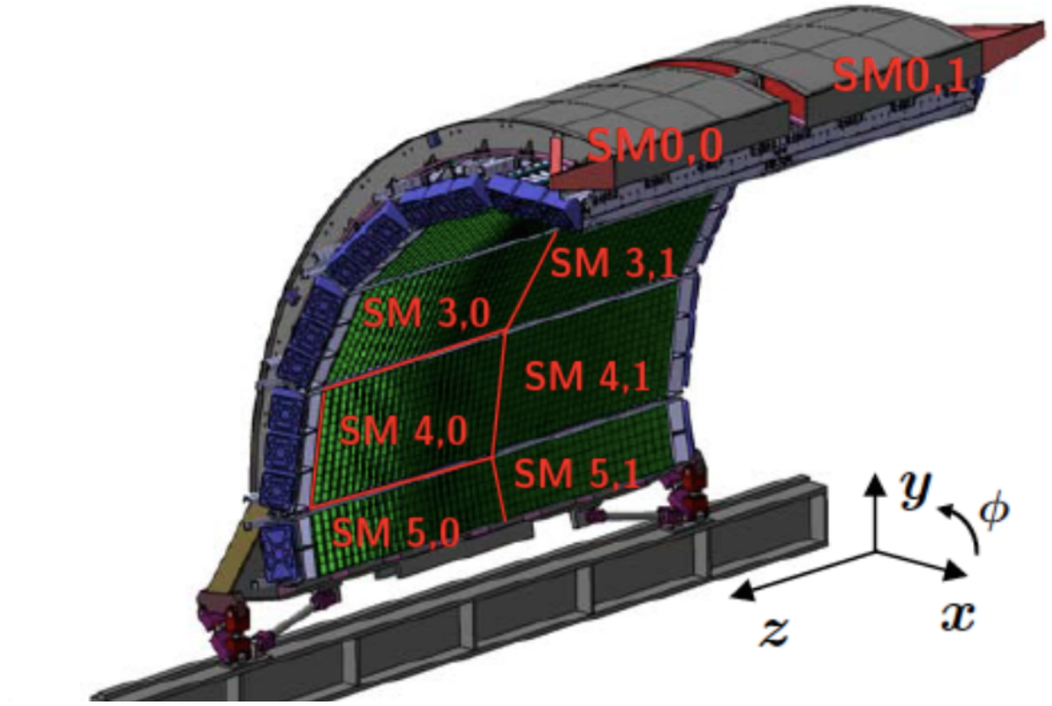

Figure 4.2: The EMCal detector and its 10 super modules. Fig. from [172–174].

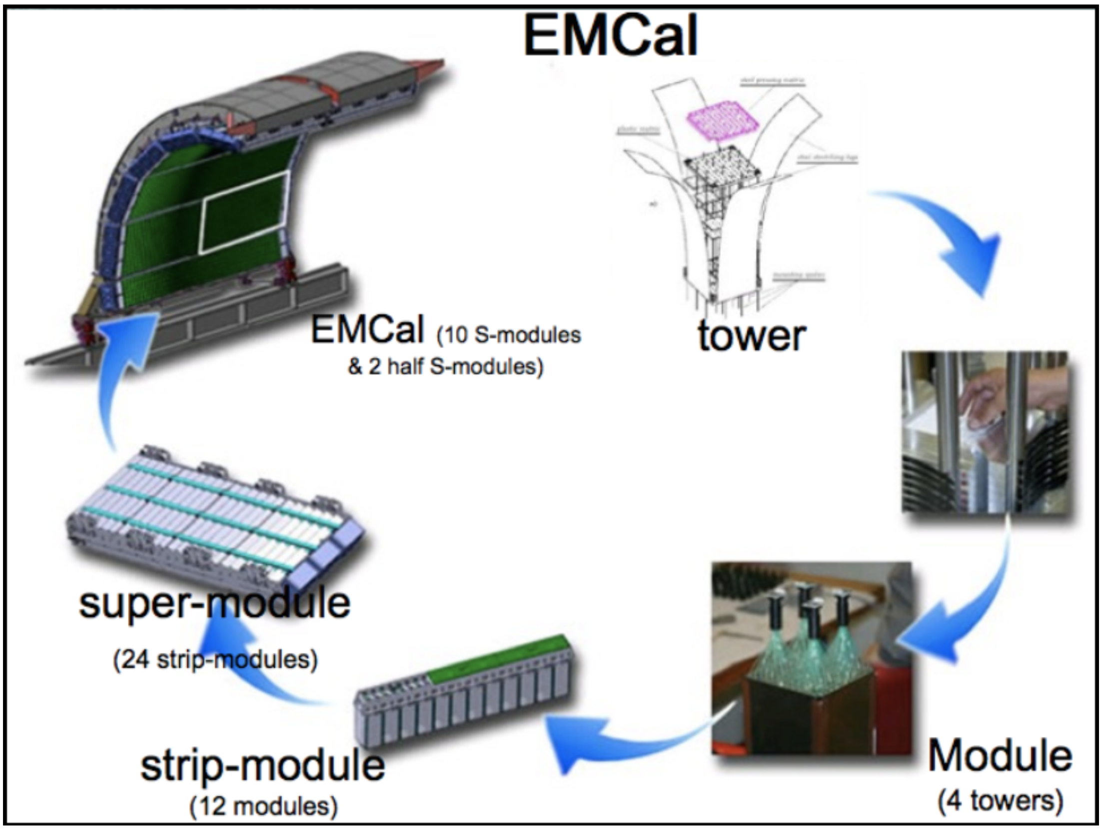

Figure 4.3: The EMCal detector and its modules and towers [173, 175].

4.1.2 Time Projection Chamber - TPC

The TPC is a gaseous detector. It is the main tracking detector of ALICE. It consists of a big cylinder with 85-cm internal radius and 250-cm external radius. Its length in the beam direction is 500 cm. The TPC is filled with Ne/CO_2 (90%/10%)[2] [172]. When the charged particles traverse the TPC, they ionize the gas along their trajectories. Due to the electric field applied between the end-plates and the central plate of the TPC, the primary electrons (from the ionization) are transported to the end-plates, and the signal is multiplied by multi-wire proportional chambers [15]. The space points along a particle trajectory, formed by the ionisations, also called clusters, are then recorded for each particle traversing the TPC. The cluster data is used to calculate the specific energy loss dE/dx of the particle in the TPC gas, which is proportional to the number of ionisations. The TPC is also used to measure the momentum of the particles based on the curvature of their trajectories. The simultaneous measurement of the momentum and dE/dx allows for the identification of the particle species for a given track. The acceptance of the TPC is 360 degrees in the azimuthal direction and $-0.9 < \eta < 0.9$ rapidity range. A schematic view of TPC is shown in Fig. 4.4.

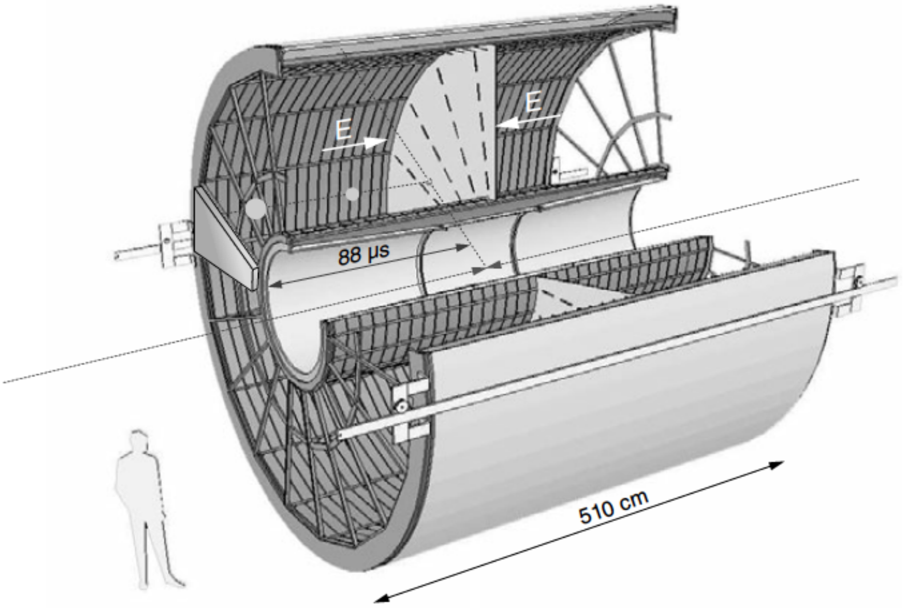

Figure 4.4: TPC schematic. Fig. from [176].

4.1.3 Inner Track System - ITS

The ITS is a silicon detector used to identify trajectories and to determine the primary and secondary vertices. It consists of 6 layers located at r = 4, 7, 15, 24, 39 and 44 cm. The acceptance of the ITS is 360 degrees in the azimuthal direction and $-0.9 < \eta < 0.9$ rapidity range (for determination of vertices located up to 10.6 cm away from the ideal interaction point) [15]. The layers of the ITS consists of three different technologies [172]:

- SPD - Silicon Pixel Detector: The two first layers (located at r = 4 and 7 cm) are made of pixelized detector, due to the high particle density close to the interaction point

---

[2] This is the gas for the LHC run-1 data. For the LHC run-2 data, the gas was changed to Ar/CO_2 (90%/10%)

(around 80 particles/cm^2). This technology also allows for a precise impact parameter determination.

- SDD - Silicon Drift Detector: The two layers in the middle (located at r = 15 and 24 cm) are made of drift detectors.
- SSD - Silicon Strip Detector: The two last layers (located at r = 39 and 44 cm) are made of micro-strip technology. In this region the density of particles is smaller than 1 particle/cm^2.

The ITS contributes to the track identification in ALICE, improving the resolution of the momentum and angle measurements obtained using the TPC. It can also be used for particle identification through the measurement of specific energy loss in the non-relativistic region.

The Fig. 4.5 shows the schematic view of ITS.

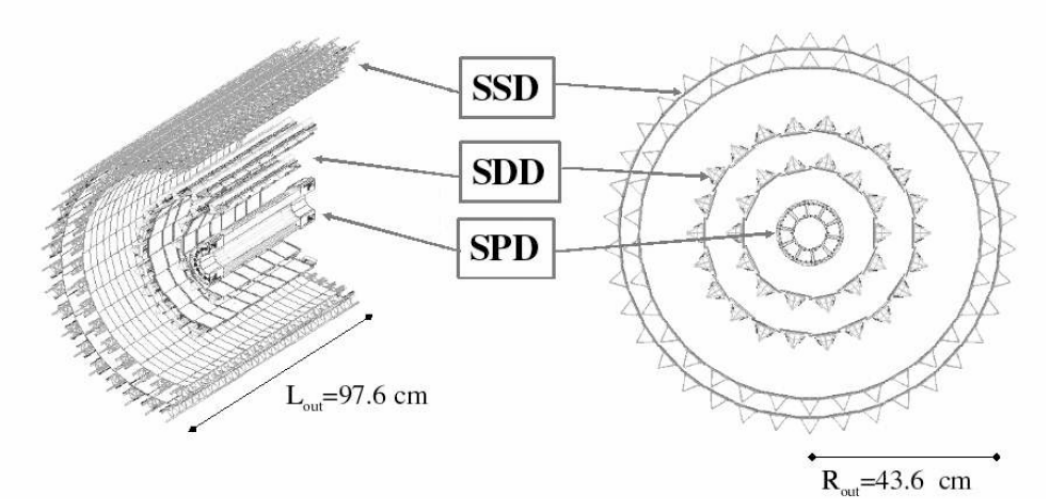

Figure 4.5: ITS schematic. Fig. from [176].

4.1.4 V0

The V0 is a scintillator detector used as trigger for minimum bias events. It is also used to measure the centrality of the collisions. The V0 is composed of two sections: V0A and V0C, located in each side of the interaction point. The V0A is located 340 cm away from the vertex and the V0C is located 90 cm away from the vertex. Each section is segmented in 32 parts, distributed in four rings, as it is shown in Fig. 4.6 [172].

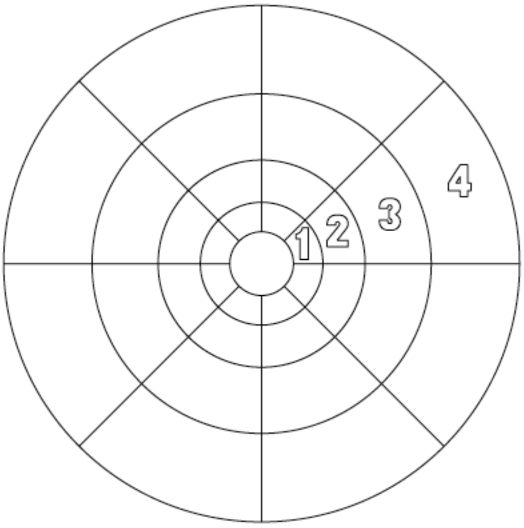

Figure 4.6: V0 schematic. Fig. from [176].

4.1.5 Time-Of-Flight - TOF

TOF is a detector used to identify particles in the momentum range between 0.2 and 2.5 GeV/c. The particle identification is based on measurements of the time-of-flight of the particles. It consists of a large area array in the pseudo-rapidity region of $-0.9 < \eta < 0.9$. The azimuthal coverage is 360 degrees. The detector consists of a Multi-gap Resistive-Plate Chamber (MRPC), filled with gas and measures the time-of-flight of the particles. An schematic of the TOF is shown in Fig. 4.7.

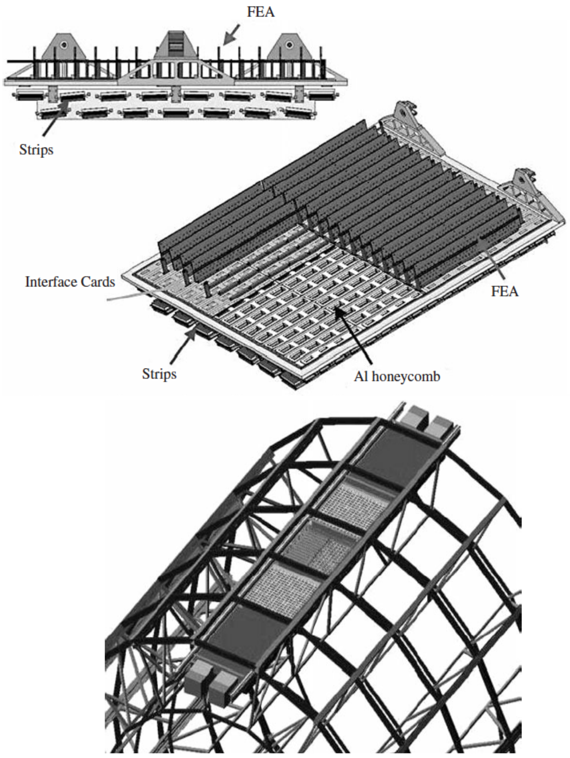

Figure 4.7: Supermodule of the TOF sector, consisting of 5 modules. Fig. from [176].

Using the combination of data obtained with ALICE subdetectors described above, it is possible to have a good event selection, track determination and particle identification. In this project, the combination is done by event selection using the V0 detector and tracks determination by TPC and ITS. And the electron identification is performed by the TPC and EMCal.

4.2 Data reconstruction in ALICE

The data reconstruction in ALICE is done by offline computing and is based in the AliRoot framework [172], which is part of the ROOT platform. ROOT [177] is a software written in C++, largely used for data analysis. Classes and libraries that form the AliRoot code are used to access the data and provide the reconstruction based on several detector signals.

The AliRoot is also used for simulations, calibrations and alignment of the detectors based on the reconstruction of the data. The AliRoot is being updated continuously, since the users can provide what we call *Analysis Task* to perform specific studies. The stored output of the reconstruction will have vertex and tracks information, clusters on the calorimeters, particle identification, trigger decisions, etc, and all this information can be accessed using the *Analysis Task*.

There is also a system called *Alien* which gives access to the computing GRID , where the users can submit their tasks to perform the analysis.

In this section we present how the vertex and tracks are reconstructed by the offline computing. The trigger decisions and the algorithm to find clusters on the EMCal are also presented.

4.2.1 Vertex reconstruction

The primary vertex reconstruction is based on the information obtained from the SPD detector, which corresponds to the two innermost layers of the ITS. When a energetic charged particle crosses the ITS, it produces an electrical signal in each of these two layers of the SPD, forming a pair of signals that can be located in space, since the SPD is a position sensitive detector. Pairs of points in these two layers that have close azimuthal angle in the transverse plane are used in a linear fit to extrapolate in the beam line axis and determine the z position of the event that generate this particle (vertex).

For the coordinates in the transverse plane ($x-y$), the positions of the vertex is determined using the intersections of the straight lines that connect pairs of points. Only the pairs with estimated z positions, as described above, are selected. The distribution of this intersections has a minimum width close to the true vertex coordinates. The effect of the magnetic field in the determination of vertex in the transverse plane can be neglected, due to the short distances to the interaction point. This estimate of the x and y position is then used to recalculate the measurement of the z coordinate.

The vertex position determined as described above is used as a constraint to the first track determination, as will be described in Sec. 4.2.2. Then, the position of the primary vertex is recalculated using the reconstructed final tracks. In pp events, the resolution of the vertex determination is improved by almost a factor of 3 after the tracking step.

Fig. 4.8 shows the expected resolution (σ_z) on the primary-vertex position determined using the reconstructed tracks as a function of the charged-particle density ($dN_{ch}/d\eta$) in pp collisions.

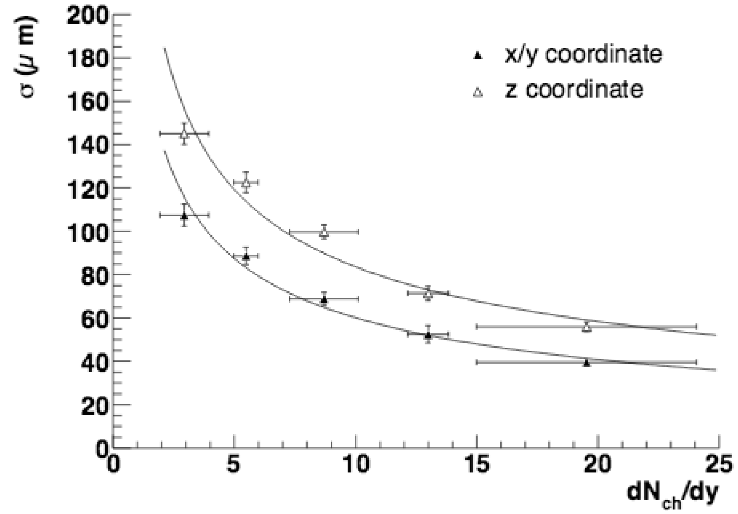

Figure 4.8: Resolution on the primary vertex position determined using reconstructed tracks, as a function of charged-particle density in pp collisions. Fig. from [172].

The dependence of the resolution on the track multiplicity can be fitted using the function [172]:

$$\sigma_z = \frac{A}{\sqrt{dN_{ch}/d\eta}} + B \tag{4.2}$$

where A and B are free parameters.

4.2.2 Track reconstruction

The main tracking detector in ALICE is the TPC, but several other detectors can also be used as tracking detectors. When a charged particle goes through the TPC, it induces ionization along its trajectory. The signal from each ionization can be used to measure the trajectory of the particle in space, leading to the track reconstruction. Reconstruction algorithms are used to assign ionizations to tracks.

The method employed for the reconstruction of tracks is the Kalman filter, proposed by P. Billoir in 1983 [178]. The first step for tracks determination is the finding of the track seed. This seeding is done twice: the first time using the nearest outer two TPC clusters and the vertex, and the second time using the nearest outer three TPC clusters and no vertex as a constrain. In the latter case, it is assumed that the track was originated somewhere else like coming from decays or secondary interactions.

Using the TPC, the track seeds are combined to the nearest cluster that passes some cuts from the algorithm. The procedure is repeated many times choosing a different set of pad rows, each time closer to the center of the TPC. This procedure is based on Kalman Filter and it is done following the given steps:

- The vector of the track parameters and its covariance matrix are propagated to the next pad row;
- A noise term is added to the inverted covariance matrix. This noise term represents the information loss due to stochastic process, like energy loss fluctuation and multiple scattering;
- If in the new pad row exists a space point compatible with the track prolongation, then this space point is added to the track determination, thus the track parameters and covariance matrix are updated.

The same procedure is repeated without the vertex as a constraint.

The highest-momentum tracks are determined first, since these tracks are more precise. Then, the remaining space points are assigned to lower-momentum tracks. The tracks are updated with the ITS points using the Kalman procedure. For the TPC tracks that have the vertex as a constraint, the propagation to the ITS is done by imposing and not-imposing the primary vertex position as a constraint, and both sets of tracks are stored for further analysis. Different prolongation in the ITS are used, and they can be selected using the χ^2 of the track fit.

The next step in the track determination is to use the ITS tracks and their propagation from the inner layer to the TPC, also using the Kalman procedure. These tracks are then propagated to the space points in TRD, to the hits in the TOF, to the space points in the EMCal, and to other outer detector in ALICE. After this propagation, the Kalman procedure is used one last time to refit all tracks from outside inwards, in order to determine the track parameters and its position in relation to the primary vertex.

Fig. 4.9 shows the comparison of the efficiency of finding tracks using different combinations of the tracking detectors [172]. The inclusion of the TRD leads to a drop in the efficiency due to the interactions in the materials and decays. On the other hand, the inclusion of the TRD improves the resolution of the transverse momentum, as shown in Fig. 4.10. Then, the TRD is optionally used in the track reconstruction.

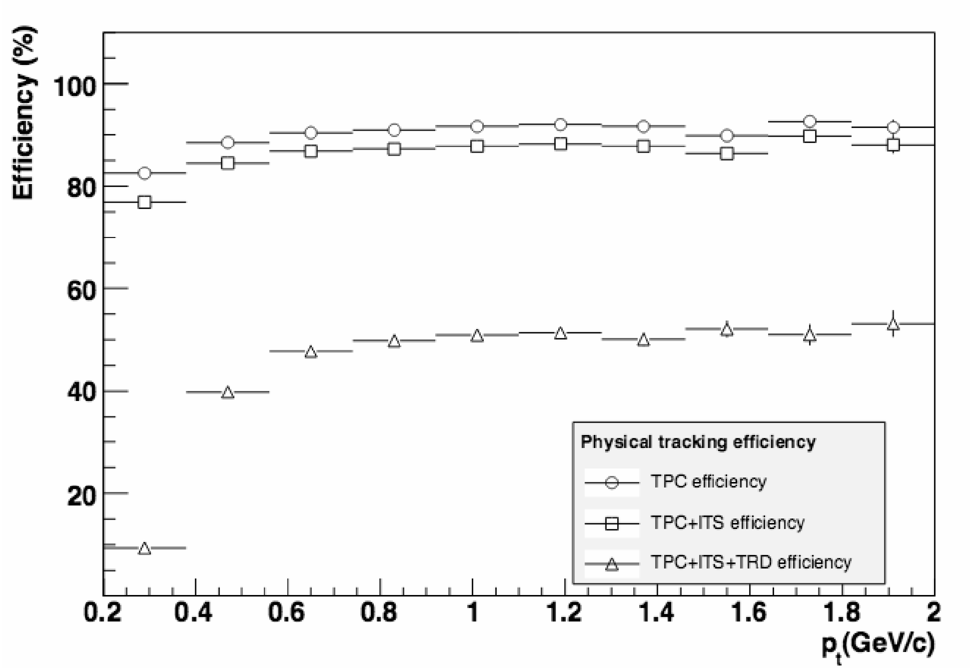

Figure 4.9: Efficiency of finding tracks for different combination of the tracking detectors for central Pb-Pb collisions. Fig. from [172].

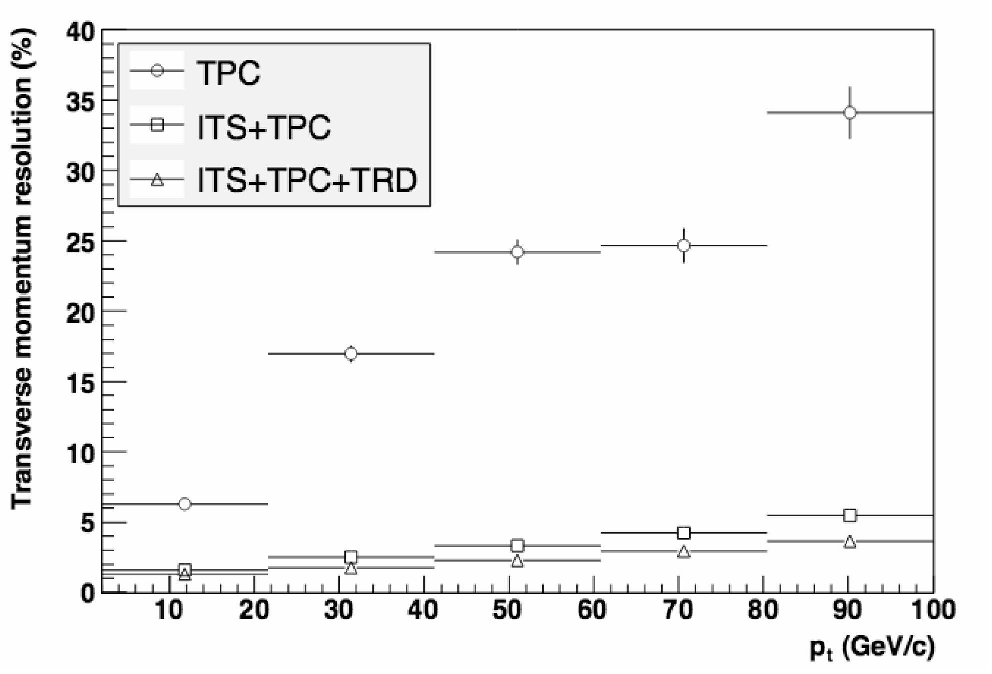

Figure 4.10: Resolution on the transverse-momentum determination for different combination of the tracking detectors for central Pb-Pb collisions. Fig. from [172]

4.2.3 Cluster finding in the EMCal

A group of cells in the EMCal which are related somehow between each other is called a cluster. Cluster algorithms, or clusterizers, are used to group the cells together and calculate their total energy. In the EMCal, there are four different clusterizers algorithms: Clusterizer V1, Clusterizer V2, Clusterizer V1 with unfolding and Clusterizer NxN. This section will present the main features of each clusterizer.

Clusterizer V1

This algorithm consists of checking all the cells (following the absolute index of the cells of the EMCal) in order to find the first cell with energy above a threshold of 100 MeV. This cell will be the seed of a cluster, even if the next cell has a higher energy. The other cells that are part of this same cluster are determined looking for neighbours of the seed. If the energy of the neighbour cell is higher than 10 MeV and the cell has a common side with the seed cell (which means row index difference or column index difference equal 1), the cell is associated to the cluster. Note that if for a given cell, the row index and column index difference are equal to one at the same time, this cell is not considered as a neighbour of the seed. In this algorithm, each cell can have four neighbour at maximum.

After associating the cells to a cluster, neighbours are searched again. The procedure are repeated until there is no more cells to be associated with the first cluster. The whole process is repeated to form the next cluster, given that a seed is found.

This algorithm has some disadvantages, such as, one cluster can contain all digits in a super-module, and it is possible to exist cells that are not associated to any cluster.

The advantage of this algorithm is that it can be formed by digits in two super-modules at same SM-ϕ.

Clusterizer V2

The clusterizer V2, instead of following the order of rows and columns to find the first seed, as in V1, it starts with a pool of cells. The most energetic cell over the threshold of 100 MeV is taken as seed of the first cluster to be formed.

The next step is to find the neighbours and associate them to the cluster. In this case, a time cut is applied to accept the cell as neighbour. Also, the cell energy should be smaller than the central cell, to be considered a neighbour. In the case where the central cell is the seed, this condition is automatically satisfied by the construction of the algorithm, but when searching for neighbours of neighbours, the condition is not always satisfied.

When a given cluster is formed, the process initiates again: from all remaining cells, the most energetic cell is searched and marked as a seed and the neighbours are searched again as described above.

Clusterizer V1 with unfolding

The V1 algorithm can generate clusters with more than one maximum. To divide the multi-maxima clusters into single-maximum clusters, an unfolding method is applied. The unfolding is applied by finding the maxima of a given cluster, fitting the maxima based on shower shape of photons and reclusterizing around the maxima, using the weights based on the fit function to share the cells energy among the clusters. If the energy of a cell is found to be smaller than the threshold (10MeV) for a given cluster, this cell is not considered for such a cluster and its energy is fully considered to be shared with other clusters.

Clusterizer NxN

In this clusterizer, a pool of cells is considered and the cell with highest energy above 10 MeV is taken as a seed for a pre-cluster.

A cell is considered a neighbour of the seed if they have common side or common corner. This means that row index difference and/or column index difference must be smaller or equal one, leading to eight neighbour at maximum, for a given seed, and maximum size allowed for a cluster is 3X3 cells.

As in V2, a time cut is applied to accept the neighbours and its energy should be smaller than the seed (also valid for the neighbours of neighbours). However, in this case the neighbours are not required to have energy above 10 MeV, but the pre-cluster is considered a cluster only if it has total energy above 100 MeV. If a cluster is formed, the procedure is repeated for a new seed.

Comparison between the clusterizers

In Fig. 4.11 we show a comparison of different clusterizer algorithms. It shows a histogram representing the energy of the cells. Considering the energy threshold (E_{th}), the histograms show the different clusters that can be formed using each algorithm. Fig. 4.11a shows the energy in different cells before clusterization (green cells). Fig. 4.11b shows a cluster formed using the V1 clusterizer, which are the cells in blue. The cells not associated with any cluster are shown in green. The result of the V1 clusterizer is one big cluster. Fig. 4.11c shows the result of the clusterizer V2, where two clusters were found, one marked as blue and the other marked as orange. Again, the green cells were not associated to any cluster by this algorithm. Fig. 4.11d shows the two clusters formed by the clusterizer NxN, one cluster shown in blue and the other in orange. Fig. 4.11e shows the result of V1 algorithm with unfolding. Two clusters were found by this algorithm and there is one cell which is associated to two clusters (blue and orange) and its energy is shared between them. It can be noticed that different clusterizer can lead to different clusters.

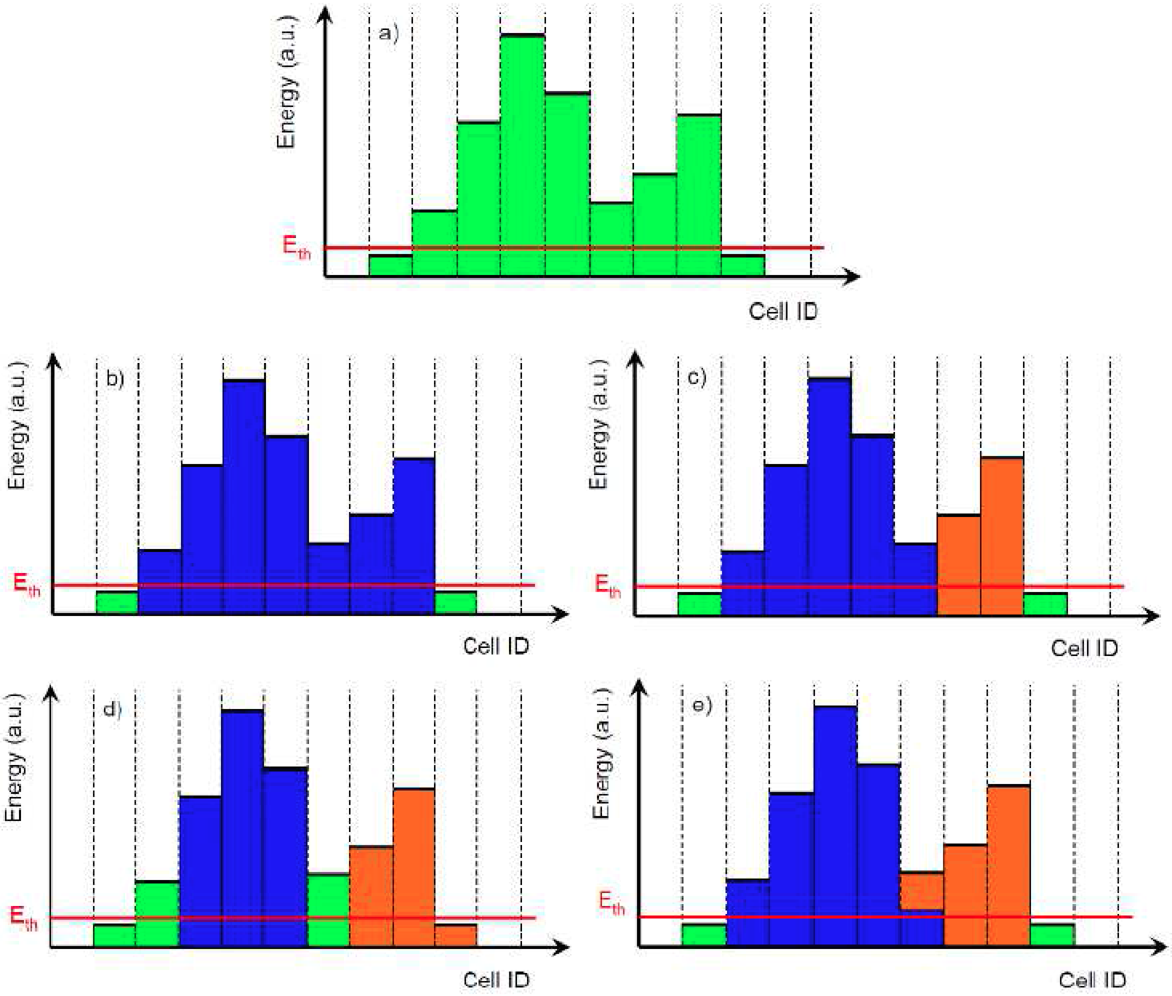

Figure 4.11: Comparison of different algorithms for clusterization of the EMCal cells. The green cells are the cells not associated to any cluster, while the blue and orange cells are the ones associated to clusters. (a) The energy in different cells before clusterization. (b) A cluster formed using the V1 clusterizer. The result of the V1 clusterizer is one big cluster. (c) The result of the clusterizer V2, where two clusters were found. (d) The two clusters formed by the clusterizer NxN. (e) The result of V1 algorithm with unfolding. Two clusters were found by this algorithm and there is one cell which is associated to two clusters (blue and orange) and its energy is shared between them. Fig. from [174].

4.2.4 Trigger systems

A trigger is a system that uses a criterion to rapidly decide which events should be measured by the detectors and used for further analysis.

The trigger that ensures that a collision has happened is called the minimum bias (MB) trigger. It requires one hit in the V0 detector or in the SPD detector in coincidence with a bunching crossing, that can be measured by a beam monitor. When the MB trigger is satisfied, all detectors measure the collision.

In the case of the EMCal trigger, the amount of the energy deposited in the detector is used as a criterion to select events containing high p_{T} particles.

The EMCal has three different levels of trigger:

- L0: In this level of trigger, the energy is summed over sliding window of 4 x 4 towers (2 x 2 modules) (see Sec. 4.1.1) and compared to a threshold above the noise. The energy is summed only inside a TRU border limit.

- L1: It is known as gamma trigger. The energy is summed over sliding window of 4 x 4 towers (2 x 2 modules) and compared to a multiplicity dependent threshold (from V0 detector). There is no TRU border limit as in the L0 case to sum the energy.

- L2: It is known as jet trigger. The energy is summed over a sliding window of n x n subregions and compared to a multiplicity corrected threshold (a subregion is defined as 8 x 8 towers).

Fig. 4.12 shows two TRU and examples of the trigger L0 level and L1 level. The L0 level is shown in blue and the energy is summed only inside each TRU. The L1 level is shown in green and the energy is summed taking into account 2 modules from one TRU and 2 modules from the subsequent TRU.

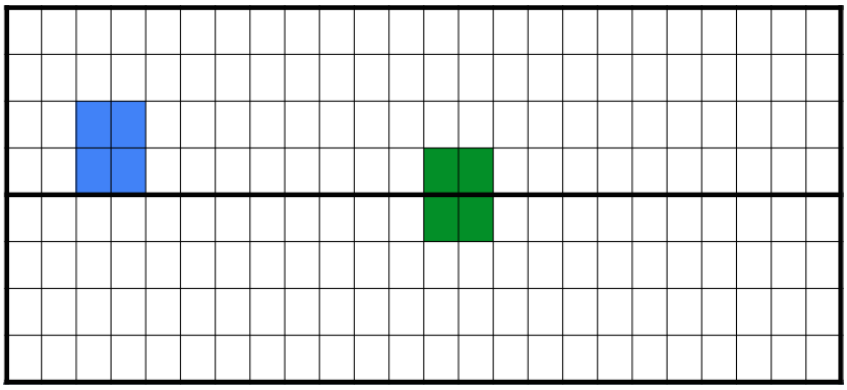

Figure 4.12: Two EMCal TRU and examples of the L0 and L1 levels of trigger. L0 is shown in blue and only sum the energy inside a given TRU. L1 is shown in green and sum energy of two subsequents TRU.

In this analysis, we use the L1 level trigger of the EMCal. Two thresholds were used for p-Pb data, one in 7 GeV and the other in 11 GeV.

4.3 Final considerations of this chapter

In this chapter, we have presented the main features of the detectors used in the analysis. The electron analysis is performed using data of detectors located at the central barrel part of the ALICE, and the main detectors used for track reconstruction are the ITS and TPC, and the particle identification is done using the TPC and the EMCal signals.

We have also presented the algorithm for the vertex and track reconstruction, which is based on the Kalman filter in offline computation.

The EMCal clusterizers and the trigger systems were also presented.

We developed a task to access the data generated by the ALICE offline computation to perform the heavy-flavour hadron decay analysis. The task is now available as part of the AliRoot framework, and can be used by the collaboration in further analysis, like in multiple centralities analysis and in the LHC run-2 data.

Chapter 5

Results using the MB trigger

The results obtained in this thesis on the nuclear modification factor using electrons from heavy-flavour hadron decays in p-Pb collisions are divided into two chapters. This is the first of these two and is dedicated to the description of the analysis using the trigger of minimum bias (MB). As explained in Sec. 4.2.4, the MB trigger is a trigger that inform all the detectors that a collision has happened, and the detectors can start to measure such a collision.

We present how we select the data and events to be included in the analysis, as well as the strategies for electron and background identification and corrections applied to the data. The selection method of electrons from heavy-flavour hadron decays (HFE), and results for the invariant yield and for the nuclear modification factor are presented. The HFE spectrum and the nuclear modification factor in MB collisions were measured in this thesis in the transverse momentum ranging from 2 GeV/c up to 12 GeV/c.

5.1 Summary of the analysis steps

To measure the electrons from heavy-flavour hadron decays, we have used signals from the TPC and EMCal detectors for the electron identification (eID). The analysis steps to measure the HFE invariant yield, and for the calculation of the HFE nuclear modification factor are the following:

- Choice of data set: the data used in the analysis were almost all LHC runs obtained in 2013 for p-Pb collisions. The runs not included are the ones that had not passed in the data quality criteria or were not good for the electron identification using TPC and EMCal. For example, runs where the TPC or EMCal had technical problems in the data taking were excluded.

- Event selection: events are removed from the analysis when they do not pass some quality cuts, like the position of the vertex, that have to be within ± 10 cm range of distance to the nominal center along the beam line.

- Track selection: some cuts on the tracks were applied to reduce as much as possible the number of particles from secondary weak decays or fake tracks reconstructed in the TPC.

- Electron identification: the electron identification is based on a combination of the TPC and EMCal signals. The combination of the signals of both detectors can lead to a good electron identification in the range of intermediate to high transverse momentum.
- Removal of hadron contamination: the hadron contamination is subtracted using a data-driven method, based on the signals distributions obtained from TPC and EMCal.
- Background identification: electrons from other sources than heavy-flavour hadrons decay are identified using an invariant mass method, and subtracted from the electron spectrum. For those sources of electrons that are not reconstructed by the invariant mass method, the cocktail is used (see Sec. 5.7).
- Efficiency corrections: it was used results from Monte Carlo (MC) simulations to correct the spectrum and the background for the efficiencies of the cuts. The corrections are the following: background correction (applied only in the background spectrum), and HFE spectrum correction (applied on the spectrum obtained after the subtraction of the background). The latter is composed by track reconstruction correction, electron identification correction (EMCal eID and TPC eID) and acceptance correction.
- Invariant yield and the nuclear modification factor: the invariant yield is calculated using the electron spectrum after background reconstruction and efficiencies corrections. The nuclear modification factor is calculated using a pp collision at same energy as reference.

All the details of each step of the analysis are presented in the next sections.

5.2 Choice of data set

The data used in this analysis were collected in January and February 2013, when the LHC had dedicated runs for p-Pb collisions.

In order to select runs for the analysis, we have tested the stability, run by run, of our method to select of electron candidates. A list of the used runs is presented in App. D. Tracks after the TPC and EMCal eID were used to obtain the total number of electrons per event, in each run. The electron selection is based on the TPC signal expected for electrons and on the energy (E) deposited in the EMCal, divided by the momentum (p) measured by the TPC, since E/p for electrons is expected to be one (more details about the electrons identification will be given in Sec. 5.5).

The number of electrons per event, for each run, is shown in Fig. 5.1. For all runs used in the analysis, the number of electrons per event oscillates around a constant value, showing that the electron selection is stable for all used runs.

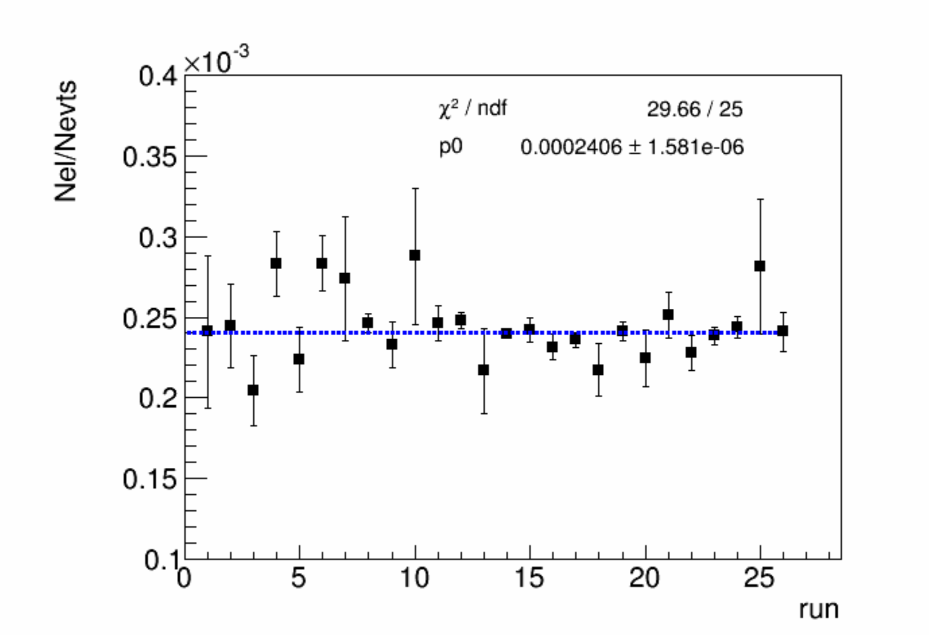

Figure 5.1: Number of electron candidates per event, in each run used in the analysis. The selection was done using the TPC eID and EMCal eID. Uncertainties bars are calculated as the square root of the total number of electrons divided by the number of events.

In total, 124 million events were available for the analysis. We select for this analysis only minimum bias triggers resulting in 121 million events. After all the quality selection, about 100 million events were selected to be used in this analysis.

5.3 Event selection

Quality assurance cuts were applied in order to select for good events. As explained in Sec. 4.2.1, vertex of the collision can be determined by the reconstructed hits in the SPD, but it can be also estimated by the reconstructed tracks, which is not necessarily the same vertex position obtained by the SPD detector (the default one). The selected events have to provide both: SPD vertex, and a primary vertex from tracks. This means that a first estimation of the primary vertex is determined after the reconstruction of the tracks by the two layers of the silicon pixel detector. Another estimation for the primary vertex comes from the global track reconstructed, which also includes the TPC detector for the track determination. Both vertex estimations have to be consistent: Their difference in beam direction has to be smaller than 0.5 cm, and the resolution of the z-position of the SPD vertex has to be smaller than 0.25 cm. Both cuts affect only a small amount of events. The position of the primary vertex in beam direction has to be less than 10 cm away from the nominal center of the ALICE apparatus, in order to minimise edges effects at the limit of the central barrel acceptance. Approximately 90% of the events satisfies this condition.

5.4 Track selection

After the event selection, some cuts are required to ensure the quality of the selected tracks. This is necessary to reduce the number of fake tracks and particles from secondary weak decays. The tracks are reconstructed using the TPC, ITS and TOF detectors of ALICE. The pseudorapidity range used in the analysis was restricted to $|\eta| < 0.6$ in order to avoid the boundaries of the EMCal acceptance that is 0.7.

Electron candidate tracks are required to satisfy several track selection cuts, summarized in Tab. 5.1.

Table 5.1: Track selection cuts for electron identification

Track property	Cut applied
Minimum number of TPC clusters	100
Minimum number of TPC clusters for PID	80
Minimum number of ITS clusters	3
Minimum ratio of TPC clusters	0.6
η range	[-0.6,0.6]
Reject kink candidates	yes
ITS pixel	kAny
DCA	(r=1, z=2) cm

The cuts selection presented in Tab. 5.1 are described below:

A track reconstructed in the TPC can be characterised by the number of clusters used for the track reconstruction (the maximum available is 159 clusters). As discussed in Sec. 4.2.2, clusters are the space points, formed by ionization along the particle trajectory. In this analysis we required 100 clusters. For the particle identification (PID) the energy loss on TPC is used. For this calculation, the clusters which are close to the TPC borders are not used and the number of clusters required is 80.

Minimum ratio of TPC clusters is a relation between clusters found and findable[1]. This cut is used in order to avoid threshold effects.

The ITS detector can provide at maximum 6 clusters for the track determination. In this analysis we require a minimum of 3 clusters, to avoid fake tracks.

kAny means that the particle can hit the first or the second layer of the ITS detector (SPD), and this cut helps to remove electrons from gamma conversion.

The η range cut is applied in order to assure that all tracks are within the EMCal acceptance.

Tracks which do not have a continuous particle trajectories, but show deviations due to decays in flight or the emission of Bremsstrahlung, are reconstructed as so-called kinks. The kink-daughters, which are the second part of the trajectory, were discarded from the analysis.

---

[1] A cluster is defined as findable if there is another cluster within some pad rows.

A cut on the distance of closest approach (DCA) to the primary vertex in the transverse plane (xy) as well as in the beam direction (z) was applied to reject background tracks and non-primary tracks.

5.5 Electron identification

In order to identify electrons, it is used the information from TPC and EMCal detectors. The TPC is a gaseous detector that can measure the energy loss (dE/dx) of the charged particles that traverse it. The mean energy loss per path length <dE/dx> is calculated, each specie of particle, using the Bethe-Bloch equation, as follows:

$$< dE/dx >= \frac{C_1}{\beta^2}\left(ln(C_2\beta^2\gamma^2) - \beta^2 + C_3\right) \tag{5.1}$$

where C_1, C_2 and C_3 are constants related to the detector properties, and β is the velocity of the particle normalized by the speed of light. The γ is given as:

$$\gamma = \frac{1}{\sqrt{(1-\beta^2)}} \tag{5.2}$$

Fig. 5.2 shows a comparison of the <dE/dx> for electrons, pions, kaons and protons, reconstructed in the ALICE-TPC, for two different interval of momentum.

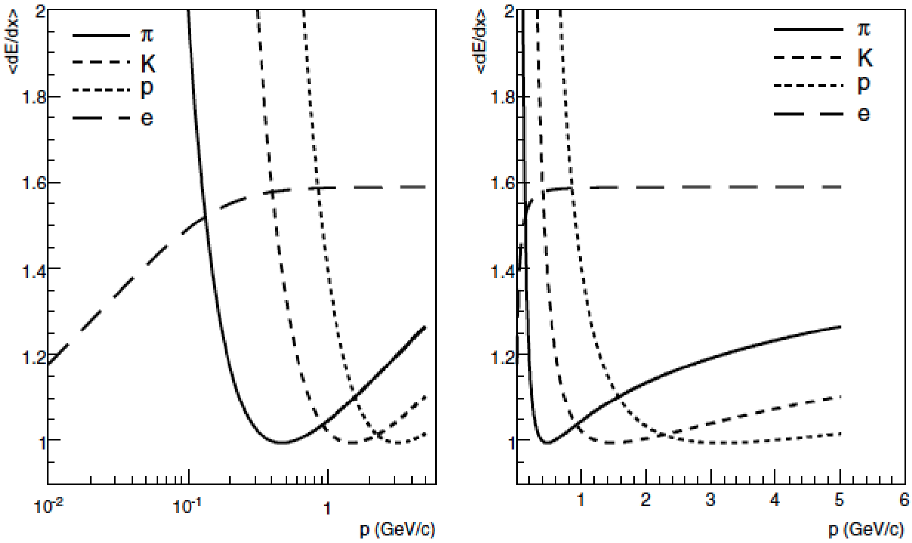

Figure 5.2: Energy loss dE/dx as a function of momentum for pions, kaons, protons and electrons according to the parametrization of the Bethe–Bloch equation adapted to the ALICE TPC. Figure from [179].

The calculated values of the Beth-Block equation are compared with the ones measured experimentally. Therefore, the TPC signal can be shown in terms of expected values: the measured value in the detector minus the expected value for a given charged particle, normalised by the dE/dx measurement resolution that is called TPC Nσ.

Fig. 5.3 shows the dE/dx in the TPC as function of momentum, where the signal expected for electrons and different hadrons species are shown as black curves. We can see that the hadron bands intercepts the electron band in several values of transverse momentum. We can also see that the π band gets closer to the electron band when increasing the momentum. Then, the selection only using the TPC signal around the electron band still demands the removal of the hadronic background. In this analysis, we use the combination of the TPC and EMCal to improve the electron selection.

The charged particle tracks reconstructed in the TPC and ITS are propagated to EMCal detector. If the distance between the track projection on the EMCal surface and the reconstructed shower is smaller than 0.05 in η, and 0.05 radians in ϕ, the track is accepted. This matching is necessary in order to identify on the same time, the momentum of a given particle (measured by the TPC) and its energy (measured by the EMCal).

Actually, the sample of identified electrons is actually a sample of electrons and positrons, since they have similar behaviour in their interaction with the detectors. In order to have only a sample of electrons, the final spectrum will be divided by two, since we expected the same amount of electrons and positrons[2].

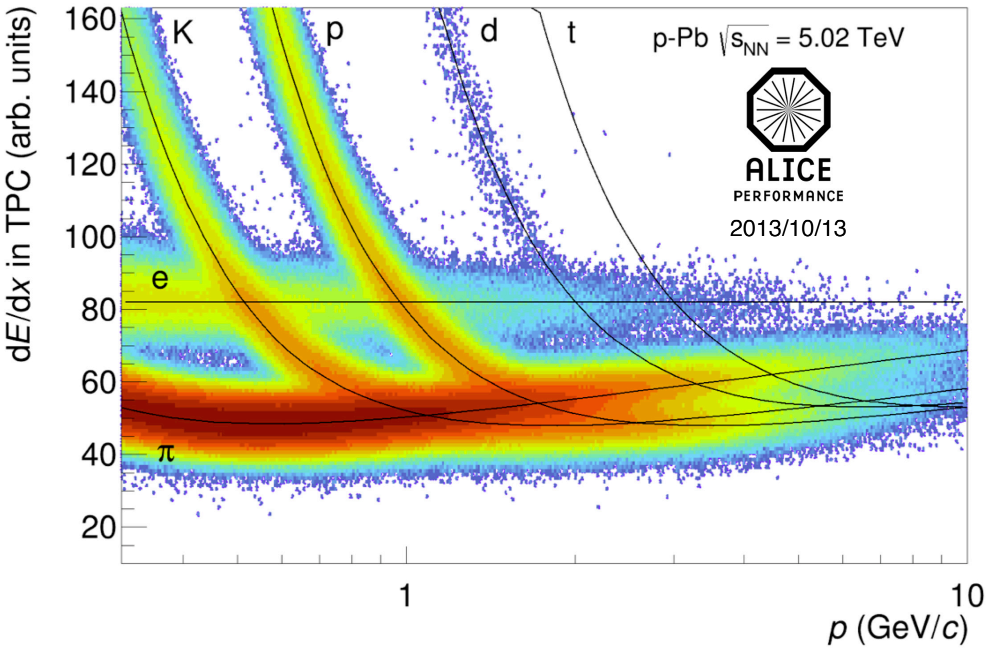

Figure 5.3: dE/dx in the TPC as function of momentum in p-Pb collision at $\sqrt{s_{NN}}$=5.02 TeV. The expected signal for electrons and different hadron species are shown as black curves.

Thus, tracks with TPC Nσ between -1 and 3 are selected as electrons and since this selection will still have some hadrons, we use the EMCal to improve the electron selection.

---

[2] Indeed, it is possible to measure the charge in each track by using the curvature of their trajectory, and the number of positive and negative charged particles after the electrons selection measured in this analysis was the same.

For these candidates, the ratio of the energy deposited in the EMCal and the track momentum measured on TPC (E/p) is calculated.

The E/p distribution for $2 < p_T^e < 4$ GeV/c is shown in Fig. 5.4. Electrons deposit their total energy in the EMCal and due to their small mass, the ratio E/p should be equal to one. Then, the peak seen in Fig. 5.4 around one are the electrons candidates. The left tail is due to hadron contamination, which is subtracted as will be explained in Sec. 5.6.

We can see on Fig. 6.19 the correlation between TPC Nσ and E/p distribution. The peak around E/p equal one are the possible electrons candidates. Tracks with E/p between 0.8 and 1.2 are selected as electrons.

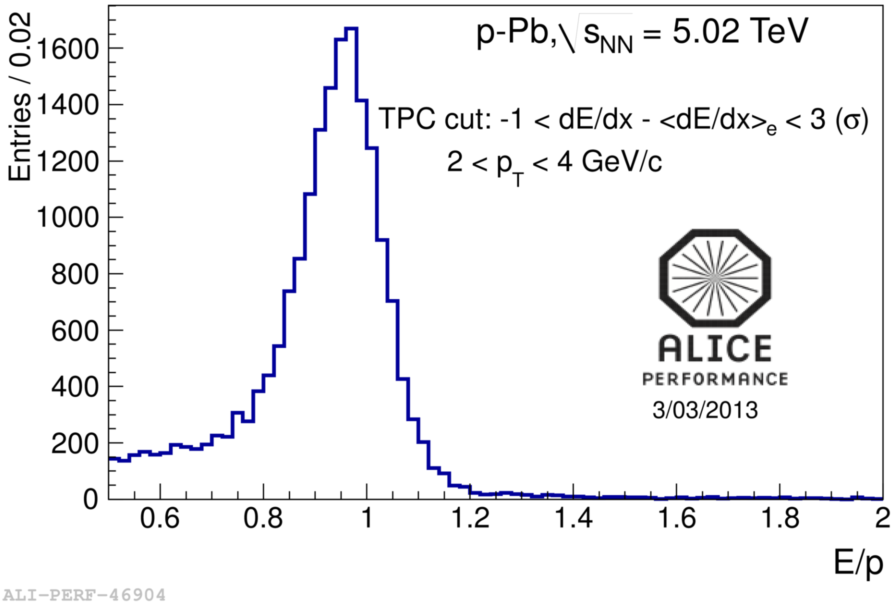

Figure 5.4: E/p distribution for the $2 < p_T^e < 4$ GeV/c bin.

The cuts used for electron identification are summarized in Tab. 5.2.

Table 5.2: PID cuts.

detector	Cut applied
TPC	-1 $<$ TPC N$\sigma < 3$
EMCal	$0.8 < E/p < 1.2$

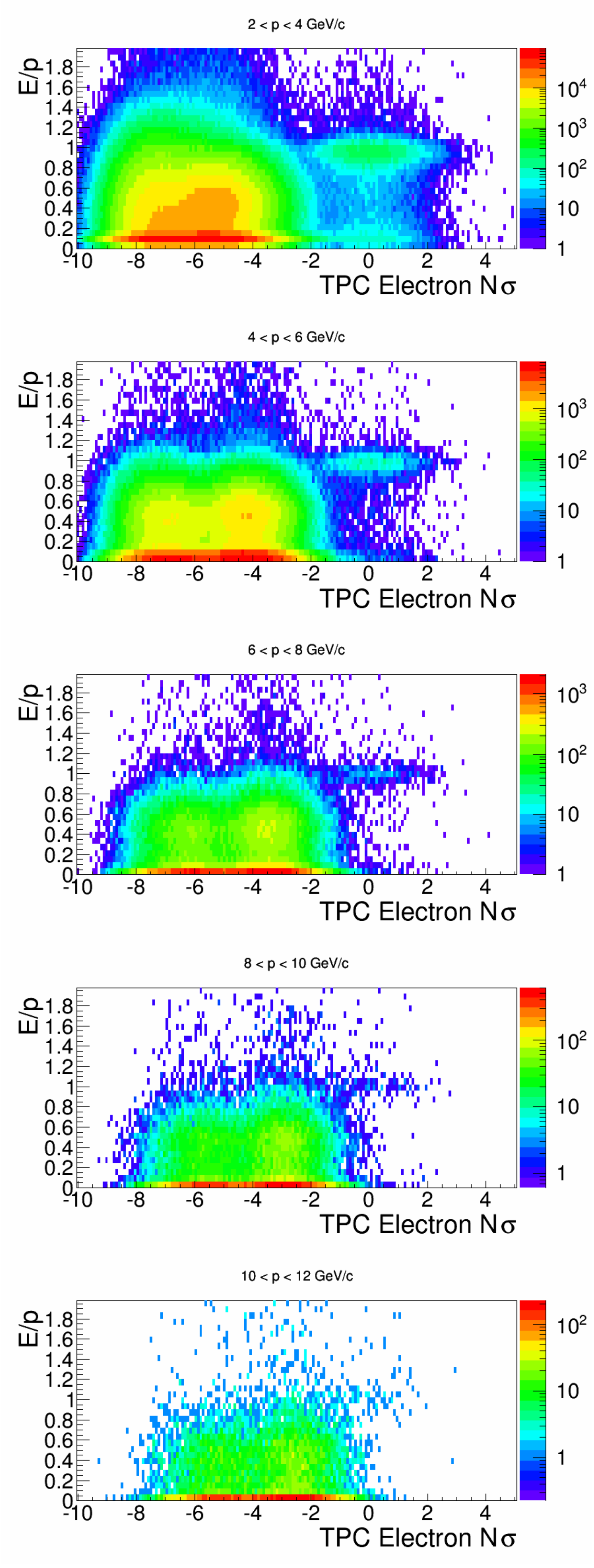

Figure 5.5: Number of sigma in TPC as a function of E/p

5.6 Removal of hadron contamination

After the selection of electrons using the TPC and EMCal information, the electron-counting still has some hadrons, what is called *hadron contamination*. This contamination has to be parametrised and subtracted from the inclusive sample.

Fig. 5.6 show the TPC Nσ distributions for electrons in different bins of p_{T}. The Fig. 5.6 (left) shows the TPC Nσ distribution without any selection and the 5.6 (right) shows the TPC Nσ distribution after applying a cut in the E/p values expected for electrons, which is $0.8 < E/p < 1.2$. The plots show the fits on the distributions for all particles, which were modelled as the sum of two gaussians and a Landau distribution multiplied by an exponential. The Landau distribution is presented in App. A. The latter is used to perform a fit on the pions distribution while the gaussians are used to fit the protons + kaons and the electrons distributions. Since the signal is the one expected for electrons, the gaussian centered at zero is the distribution of the electrons candidates. The quality of the total fit ($\chi^2_{red} = \chi^2/n$, where n is the number of degree of freedom of the fit) as well the mean $(N\sigma)^{elec}$ and sigma $\sigma^{elec}_{dE/dx}$ of the electrons distribution are shown for each bin of momentum, for the case where the EMCal was also used. Fig. 5.7 shows the TPC Nσ distributions for electrons in higher bins of p_{T}.

The superposition of the pions and the electrons distributions is higher for the case where the E/p were not used. Then, in this case we say that the hadron contamination is higher. Also, we can clearly see that the gaussian of the electrons is better defined in the case where the E/p cut is used, showing that the combination of TPC and EMCal results in a more pure electron selection.

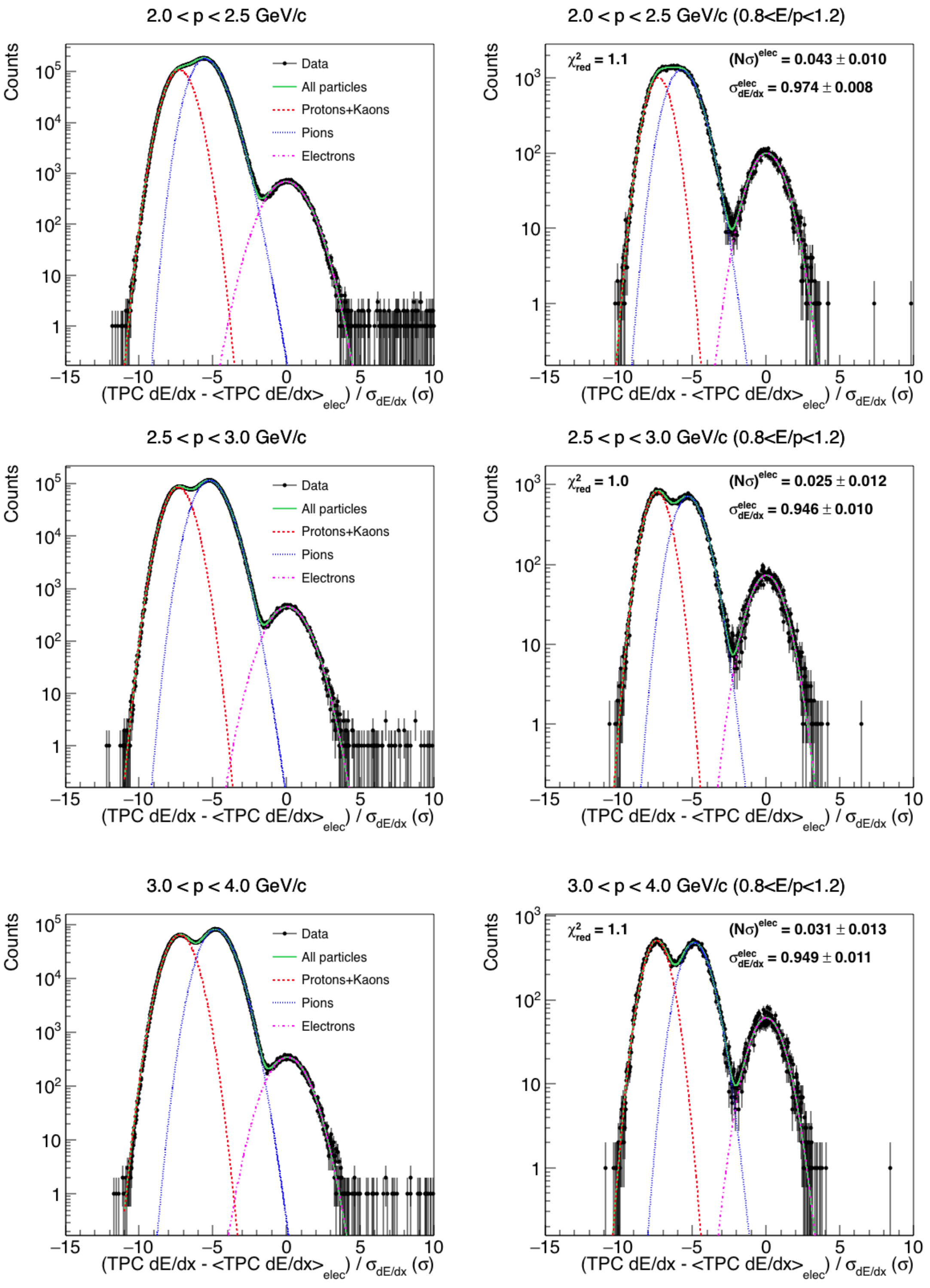

Figure 5.6: TPC dE/dx expressed in number of sigmas (TPC Nσ) from the electron line for various momentum slices (before (left) and after (right) EMCal PID; $0.8 < E/p < 1.2$.). The electron contribution is fitted with a Gaussian and the pion contribution with a Landau multiplied with an exponential tail. The other hadron species are resembled by a Gaussian fit. All pions that have TPC N $\sigma > -1$ contribute to the hadron contamination.

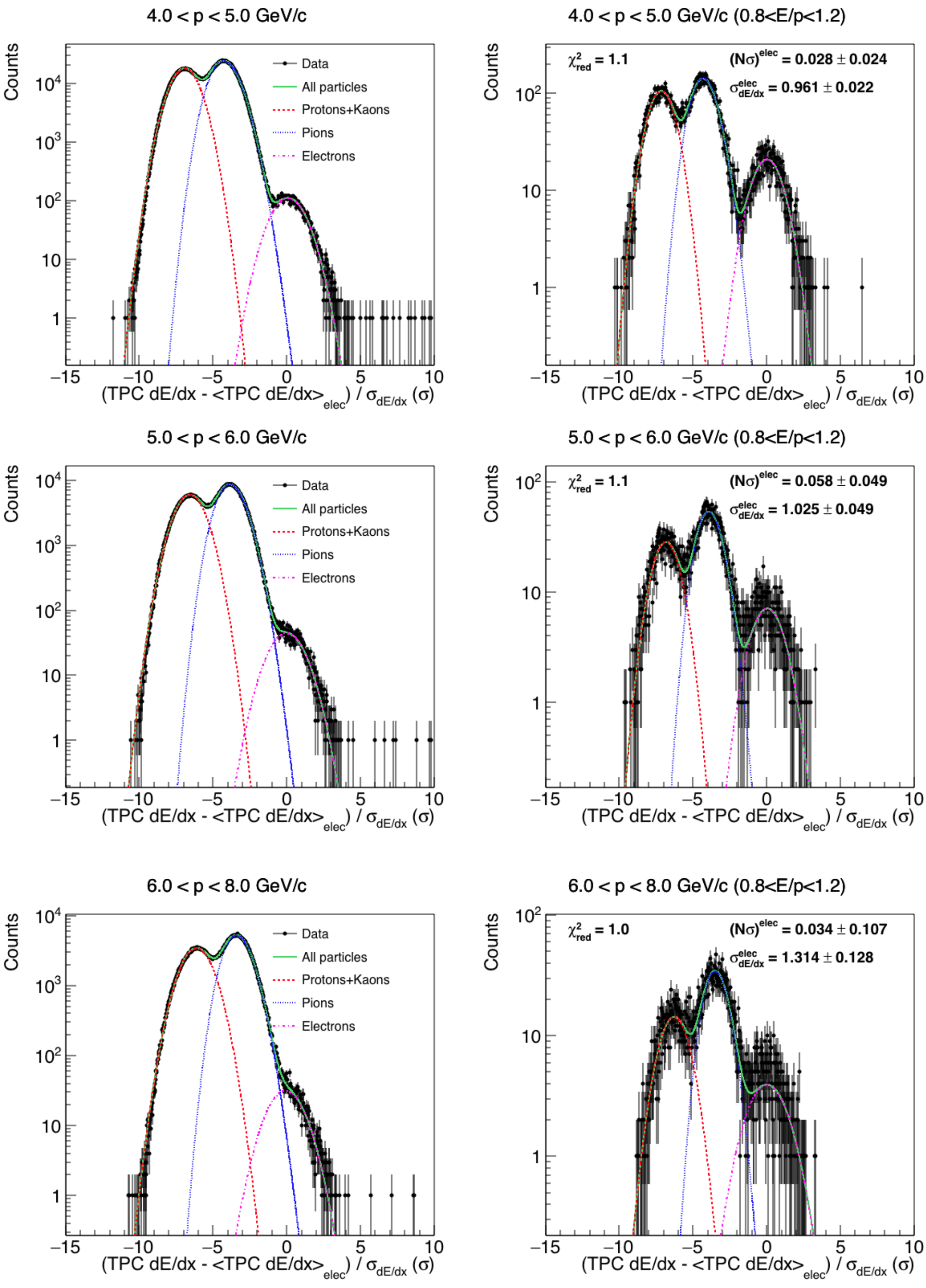

Figure 5.7: More bins: TPC dE/dx expressed in number of sigmas (TPC Nσ) from the electron line for various momentum slices (before (left) and after (right) EMCal PID; $0.8 < E/p < 1.2$.). The electron contribution is fitted with a Gaussian and the pion contribution with a Landau multiplied with an exponential tail. The other hadron species are resembled by a Gaussian fit. All pions that have TPC N $\sigma > -1$ contribute to the hadron contamination.

Even using the combination of TPC and EMCal, there is still a remaining hadron contamination that has to be subtracted. In this analysis, the procedure of hadron subtraction is done using information of the TPC and EMCal detector. The first step is the selection of a pure hadron sample, using the TPC Nσ for hadrons and/or taking the particles outside the electron band. In this analysis, we have used TPC N$\sigma_{electrons}<$ -3.5 and TPC N$\sigma_{hadrons}$ between -3 and 3. The electron candidates are selected by requiring -1 $<\sigma_{electons}<$ 3.

The method to subtract the hadron contamination is based on the E/p distributions of hadrons and electrons, previously selected by the TPC signal. The E/p distributions found for electrons and hadrons are shown in Fig. 5.8. The hadrons E/p distribution was scaled to match the electron E/p distribution in the region 0.4 $<$ E/p $<$ 0.5. In Fig. 5.8 we can see, in the E/p values for the hadrons, for higher transverse momentum, the hadron contamination is bigger. This happens because the TPC signal pion band start to get closer and closer to the electron band.

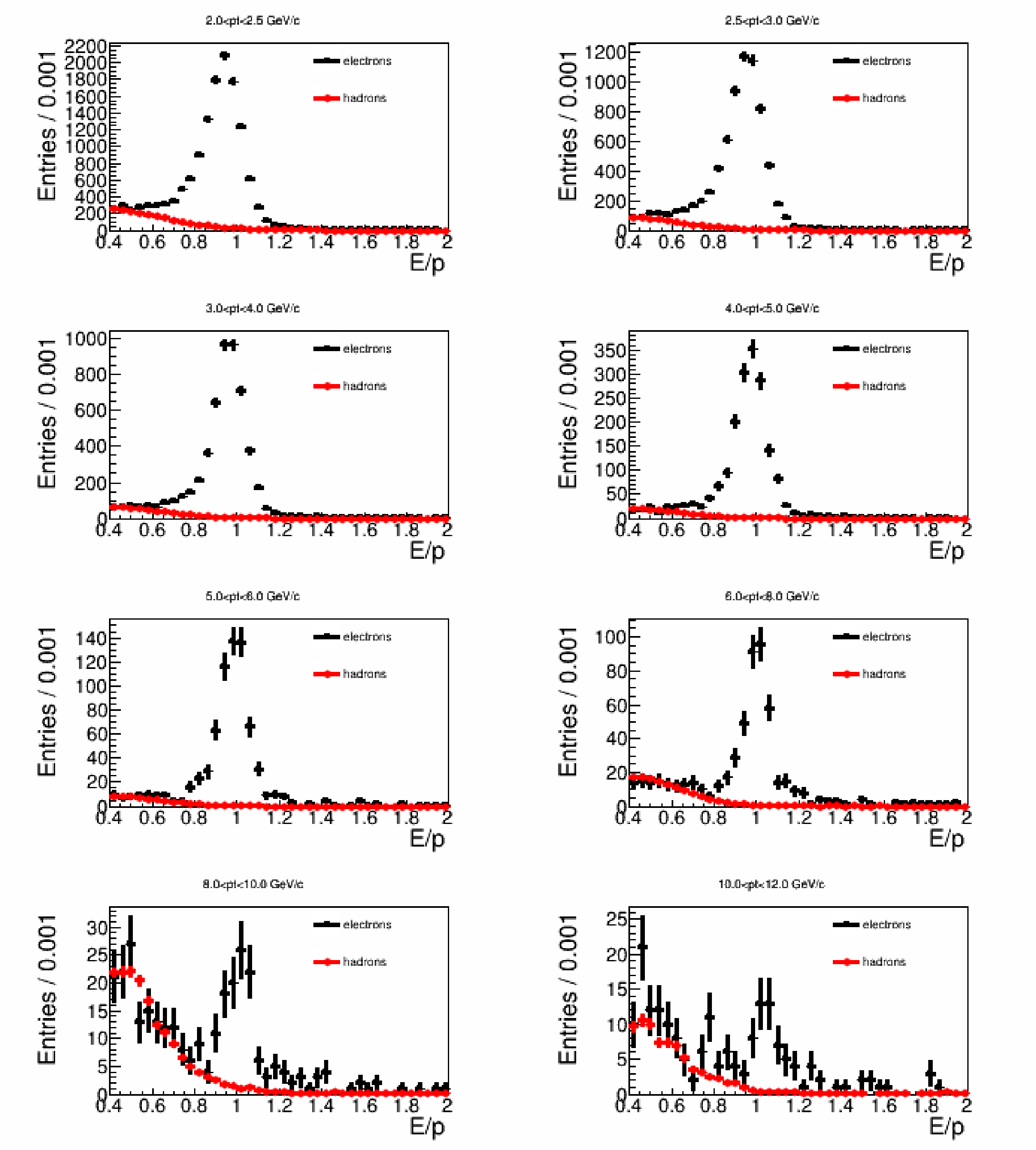

Figure 5.8: E/p distributions for electron candidates and hadrons.

The integral between 0.8 and 1.2 of the scaled hadron E/p distribution is considered as the hadron contamination, which have to be subtracted from the electron sample. Fig. 5.9 shows the hadron contamination in bins of p_{T}. The contamination is bigger for higher values of p_{T}.

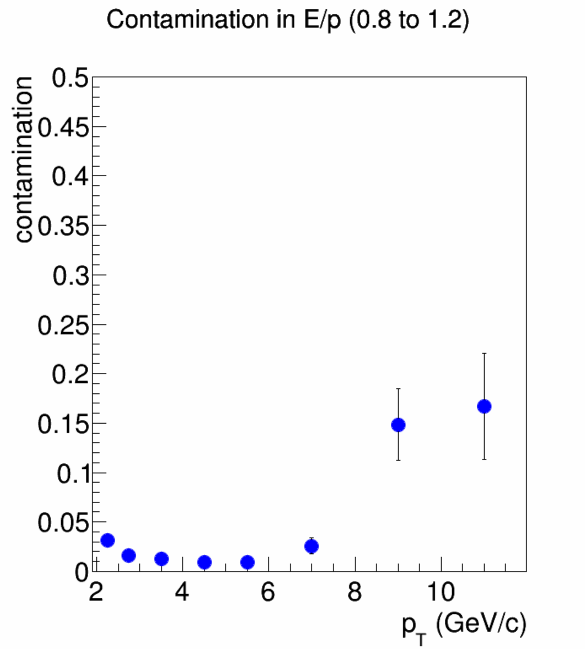

Figure 5.9: Hadron contamination as a function of p_T for $-1 <$TPC N$\sigma < 3$ and $0.8 < E/p < 1.2$.

After subtracting the hadron contamination, the integral of E/p is done to obtain the first spectrum of electrons, called in this analysis *inclusive electrons*, since it has electrons from heavy-flavour hadron decays and electrons from other sources. In the next section we discuss how this background electrons are identified and subtracted from the inclusive electrons, in order to obtain the spectrum of heavy-flavour decay electrons.

5.7 Background identification

The inclusive electrons are all the electrons found based on particle identification using the TPC and EMCal. This includes electrons from heavy-flavour hadron decays, from gamma conversions, from η and π^0 Dalitz decays, from J/ψ di-electron decays, from kaons and also electrons from W decays. Since we want to measure the electrons from heavy-flavour hadron decays, it is necessary to identify the number of electrons from these other sources (also called non-HFE) and consider them as background in this analysis.

To determine the contribution from gamma conversions and from η and π^0 Dalitz decays, we use an invariant mass method. The expected invariant mass for e^- and e^+ pairs from these sources is very small and its contribution can be obtained from the p_T distribution of the pairs that have an invariant mass with lower values.

In this procedure we take each electron or positron identified in the analysis (called main electron) and we combine it with every positron or electron (called partner electron) that we can find applying electron identification cuts. The invariant mass of the pair is calculated and this information is used to resolve if such a main electron is from background or not.

Electrons partner were selected with the cuts listed in the Tab. 5.3. The cuts used for the partner electron identification are less restrictive than the ones used for the main electron, in order to increase the statistics and the efficiency of finding background electrons.

Table 5.3: Track selection cuts for the associated electron.

Track property	Cut applied
Minimum number of TPC clusters	80
Maximum χ^2 per TPC cluster	4.0
Minimum p_T	0
Reject kink candidates	yes
TPC and ITS refit	yes
Pseudorapidity	$-0.9 < \eta < 0.9$
TPC cut for eID	$-3.5 <$ TPC N$\sigma < 3.5$

In the table 5.3, the cut "maximum χ^2 per TPC cluster" is a cut regarding the fit done in the track reconstruction. Minimum p_{T} is the minimum transverse momentum that the track has to have to be accepted. "TPC and ITS refit" is a refit of the tracks in inward direction in order to get the track parameters at the vertex, as explained in Sec. 4.2.2. The TPC cut for eID is the cut used in the TPC signal in order to select electrons. The other cuts were described in the Sec. 5.4.

The combination of particles (electrons and positrons) with opposite sign is called *unlike sign* (ULS). This combination contains the true background but can also contain a combinatorial background, which are an aleatory combination of particles pairs that has a small invariant mass. To estimate the combinatorial contribution, we use the pairs formed by particles with same sign (electrons with electrons or positrons with positrons), and they are called *like sign* (LS).

Fig. 6.31 shows the invariant mass distribution for ULS and LS pairs. We can see that the ULS has an enhancement close to zero and an increasing tail when the invariant mass values rises. This shape in high values of invariant mass is well described by the LS distribution, showing that the ULS indeed has a combinatorial contribution that has to be subtracted.

Selecting the particles that have a partner with an invariant mass distribution $m < 0.15$ GeV/c^2, it is possible to determine the p_{T} distribution of electrons with ULS and LS combinations.

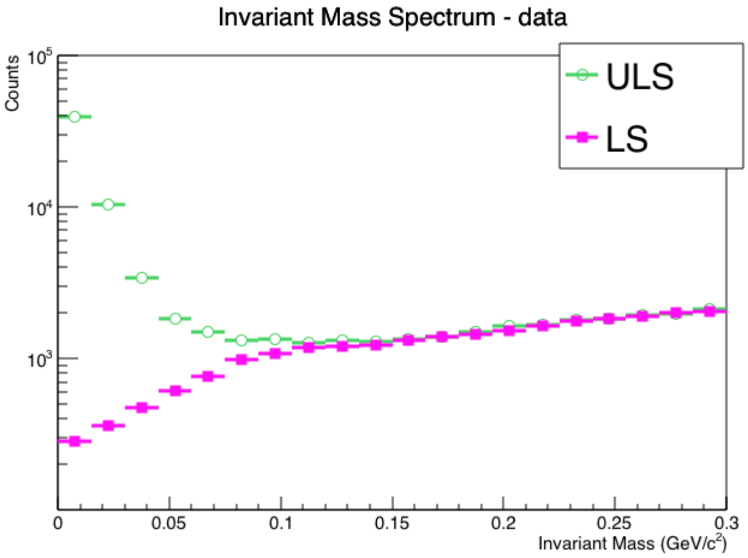

Figure 5.10: Invariant mass spectrum.

The yield as a function of p_{T} for inclusive electron, for the ULS background and for the LS combinatorial background are shown in Fig. 5.11.

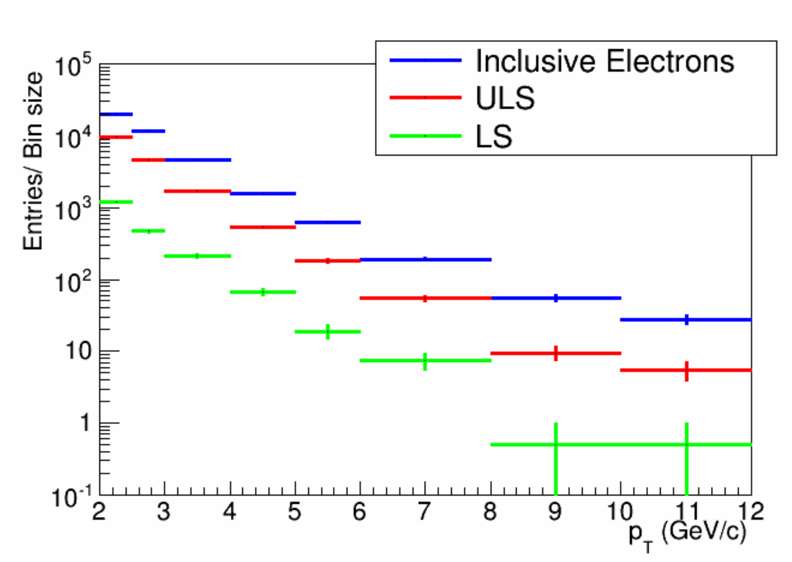

Figure 5.11: Inclusive electrons and non-HFE spectrum background.

The background can be obtained by removing LS paired electrons from the ULS sample. Then, the contribution of the background ($\mathcal{B}$) is calculated as shown in the Eq. 5.3.

$$\mathcal{B} = ULS - LS \tag{5.3}$$

This background is divided by $\epsilon_{\mathcal{B}}$, which is the efficiency of finding pairs using the invariant mass method calculated using Monte Carlo simulations, as will be discussed in the next section.

The remaining contribution to the background was from J/ψ, K_{e3} and W. For the p_{T} range of our measurement, W contributions were found to be negligible. The contribution of J/ψ and K_{e3} is shown in Fig. 5.12, in comparison with the HFE spectrum. The invariant yield of J/ψ and K_{e3} ($K \rightarrow e\pi\nu$) decays to electrons where obtained from the cocktail [79, 180, 181]. The cocktail is a method to calculate the yield of electrons from hadronic decays. The relevant primary mesons that can decay to electrons are π^0, η, η', ρ, ω, ϕ, J/ψ, and ψ'. The method uses a parametrisation (that can be a Hagedorn function, a Tsallis function, etc.) to the experimental pions spectrum as input. The contribution from other particles that are not pions are estimated using the m_T scaling. The Tsallis function is given by Eq. 5.4 and was used to obtain the p-Pb cocktail [182].

$$E\frac{d^3\sigma}{dp^3} = \frac{c(n-1)(n-2)}{nT(nT+m(n-2))}(1+(m_T-m)/(nT))^{-n} \tag{5.4}$$

where c, T and n are obtained by fitting the experimental data of π^0, m is the mass of the meson and m_T its transverse mass, given by:

$$m_T = \sqrt{m^2+p_T^2} \tag{5.5}$$

Then, given that the parameters of Eq. 5.4 are determined for π^0, the same parameters are used to get the function for the other particles, rewriting the function with the corresponding m and m_T and multiplying the function by the expected ratio between the given particles and the π^0 at high p_{T}.

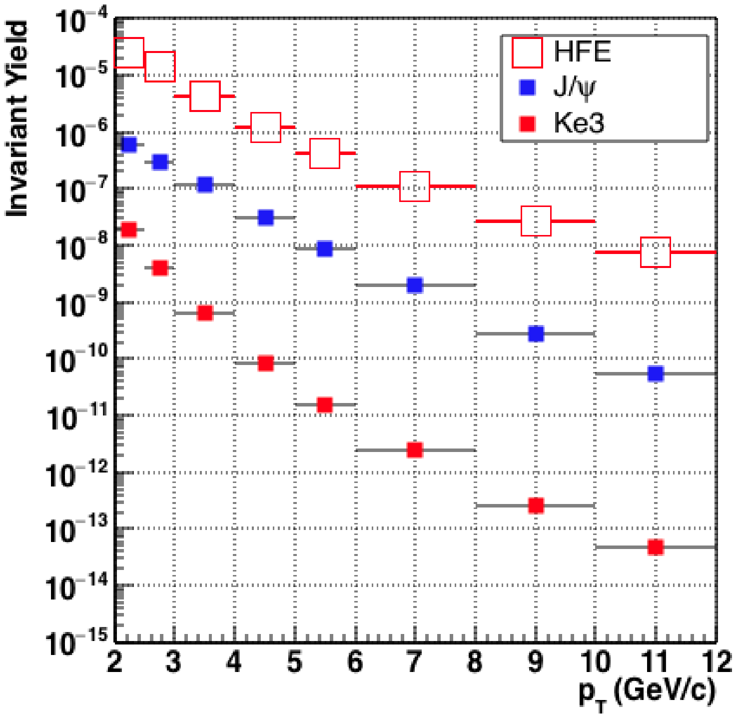

Figure 5.12: Invariant yield of electrons from J/ψ and kaons compared to the HFE invariant yield.

Fig. 5.13 shows the ratio of the J/ψ spectrum with the HFE spectrum. This contribution was subtracted from our electron sample.

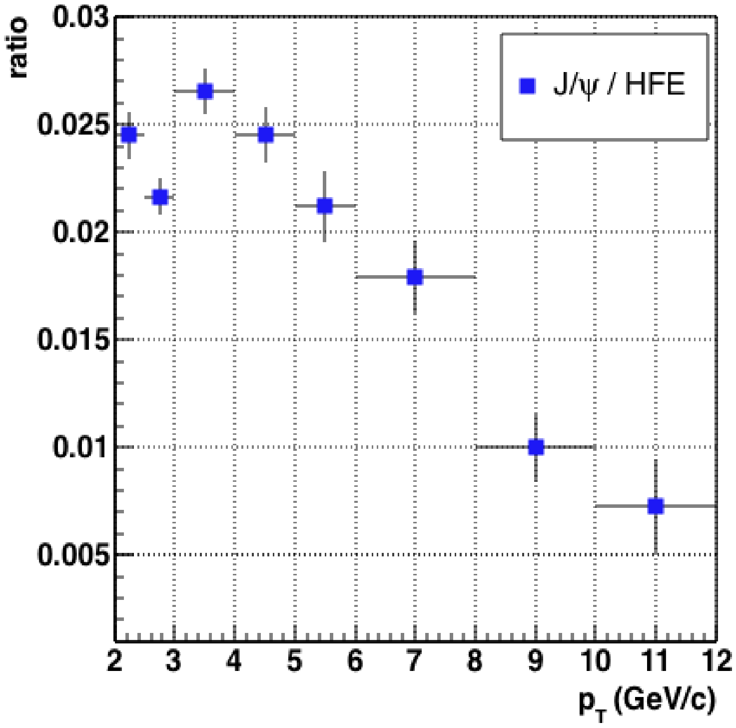

Figure 5.13: Relative contribution of electrons from J/ψ to the HFE spectrum.

Once we have the electrons yield and the background yield, efficiency corrections are necessary to obtain the final HFE spectrum. In the next section we discuss the determination of the efficiencies.

5.8 Efficiency correction

To determine the efficiency for each step of the analysis and also for the background reconstruction, we use MC simulations done with AliRoot framework. Here we describe how the efficiencies are calculated.

5.8.1 Monte Carlo samples

The AliRoot framework is used to simulate the events, the detector response and the reconstruction of the particles through the detectors. The Monte Carlo simulation has the full information of the created particles, but in order to evaluate the reconstruction software and the detector performance, simulated events are stored as raw data.

Fig. 5.14 shows schematically the AliRoot data processing. Initially, the MC stores the full information of the created particles. Then the particles are transported through the detectors, and the response of the detectors are simulated, creating the hits in each detector. The hits are converted into digits, according to the electronics response function of each detector. Then, the digits are stored in the same format as the real data, called raw data.

At this stage, the MC raw data can be reconstructed exactly like the real raw data, and this information is used to determine the efficiencies involved in the steps of a given analysis.

The efficiency is determined as a ratio of particles after given cuts and the initial produced particles. For example, for the TPC eID efficiency, we measure the spectra of true electrons (since it is a MC production, this information is available) as a function of transverse momentum before and after the TPC cut -1 $< TPCN\sigma <$ 3. The ratio between these two spectra is the efficiency.

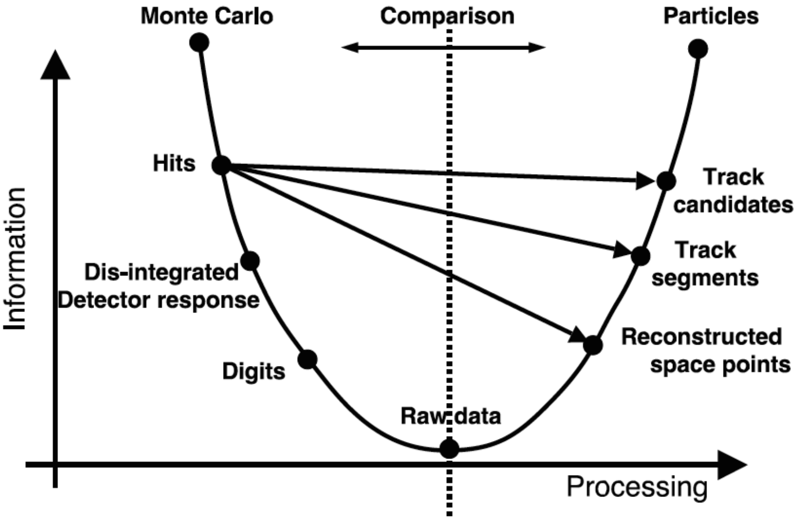

Figure 5.14: AliRoot data processing for MC simulations. Fig. from [172].

The same run-by-run check presented for data is repeated for the used MC samples and shown in Fig. 5.15. In this case we see a bigger variation than seen in data, especially for the runs with low statistics (bigger statistical errors), but still, there is a constant that can be fitted to the data with an acceptable χ^2 value.

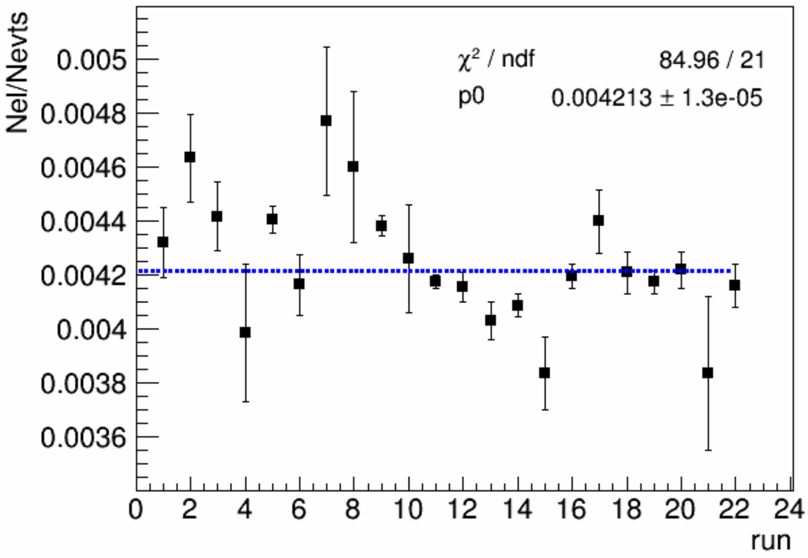

Figure 5.15: Number of electron candidates per event, in the simulation sample used in the analysis.

5.8.2 Electron identification in MC

In the simulated sample, it is possible to know the number of electrons before and after the selection used. In order to have a reliable efficiency correction, it is important to have a simulation with a good description of the data. Then, comparisons between data and MC are crucial to ensure the reliability of the MC simulations.

Fig.s 5.16 and 5.17 show the comparison between E/p distributions for data and MC. Data and MC has a good agreement as can be seen in Fig. 5.18. The difference in the mean value is around 2%. In order to obtain the mean and width the E/p distributions were fitted with a Crystal Ball function. This function is usually used to described process of losses in high energy physics, and its expression and parameters are presented in App. B. In the case of the E/p distribution, it is used to take into account that some electrons with low momentum can loose part of its energy before hitting the EMCal.

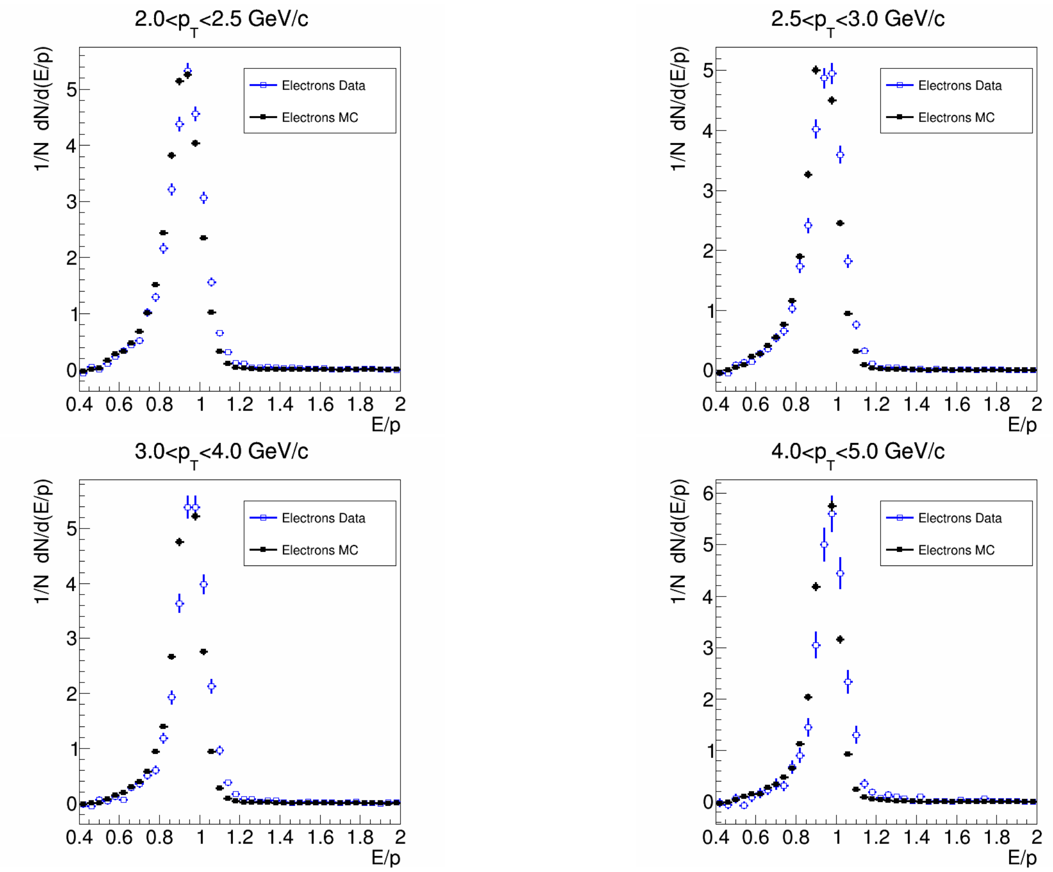

Figure 5.16: E/p distribution for data and MC in low p_T.

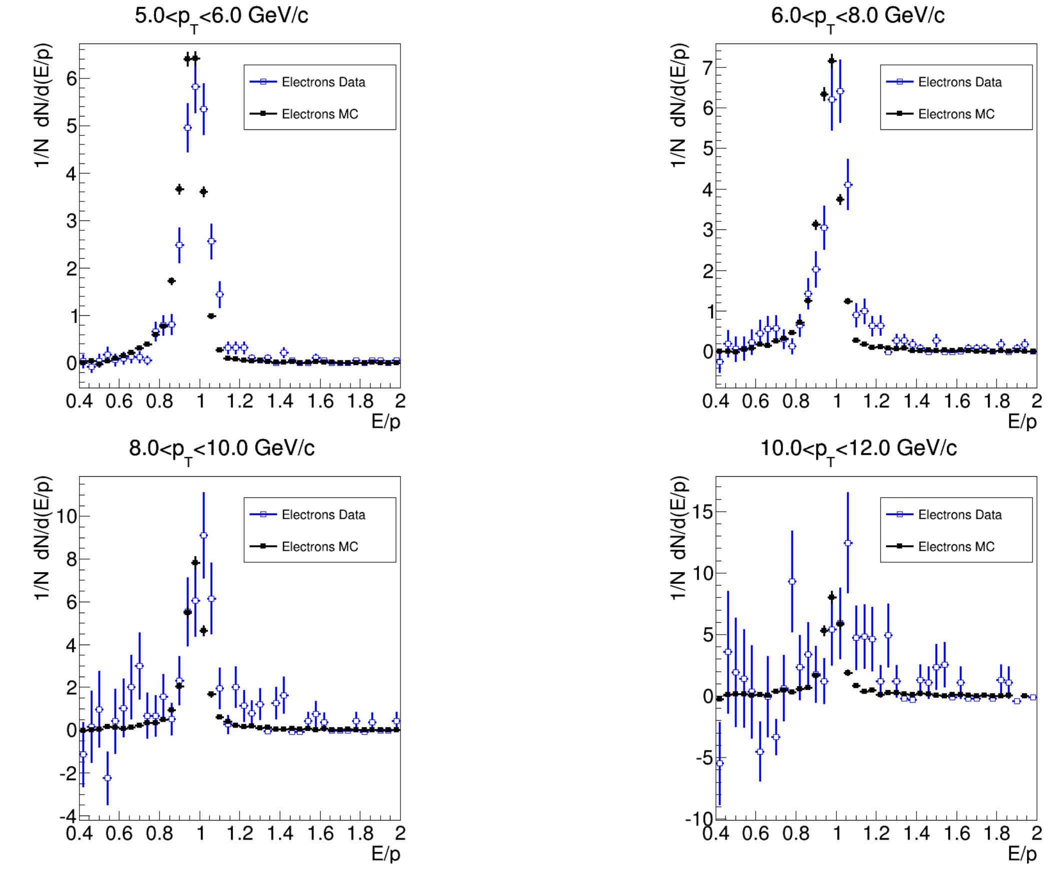

Figure 5.17: E/p distribution for data and MC in high p_T.

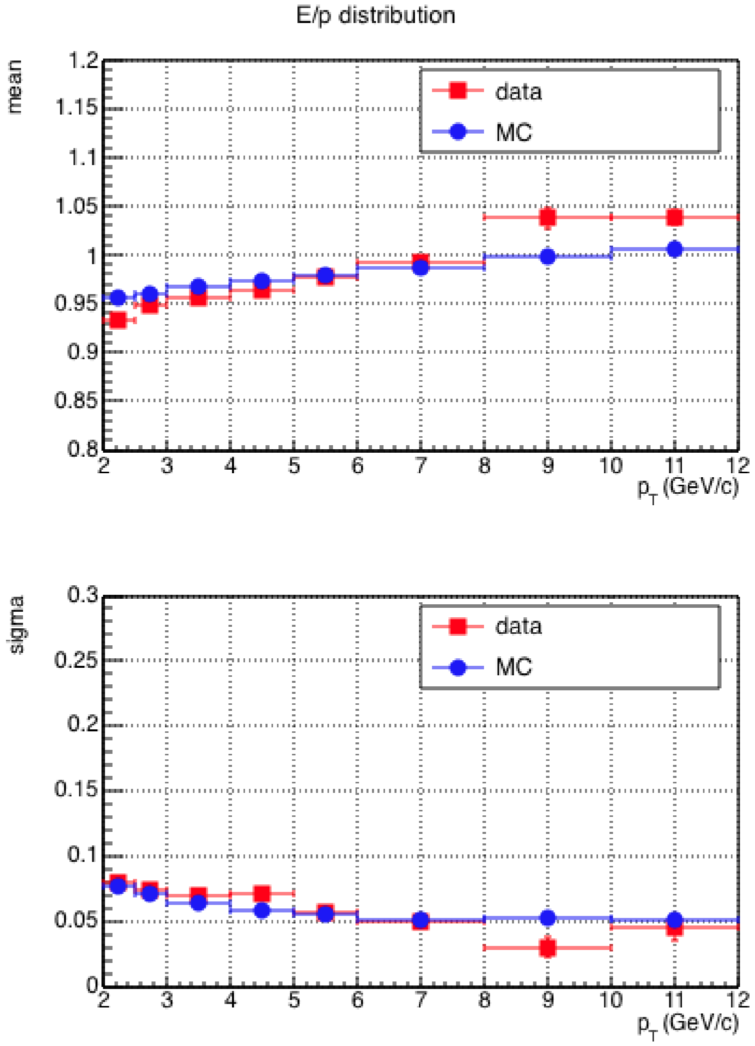

Figure 5.18: E/p mean and sigma for data and MC

5.8.3 Background identification efficiency

The reconstruction efficiency of non-HFE using invariant mass is calculated using the MC sample LHC13d3. The efficiency is defined as the ratio between the number of non-HFE electrons found using the same procedure as in the data analysis and the original number of non-HFE generated in the MC sample.

Fig. 5.19 shows the efficiency of the invariant mass method using two different combinations of detectors to select the main electron: EMCal + TPC and TPC-only. The main electrons sample in our analysis is selected using the TPC and EMCal information, but since in the MC production the statistics to calculate the efficiency is low in high p_{T}, we have checked how the efficiency determination is improved when we only require the particle identification in the TPC. Since for the latter case we have the efficiency values compatible with the ones obtained using EMCal + TPC, but with smaller statistic uncertainties, we have used this values for the analysis.

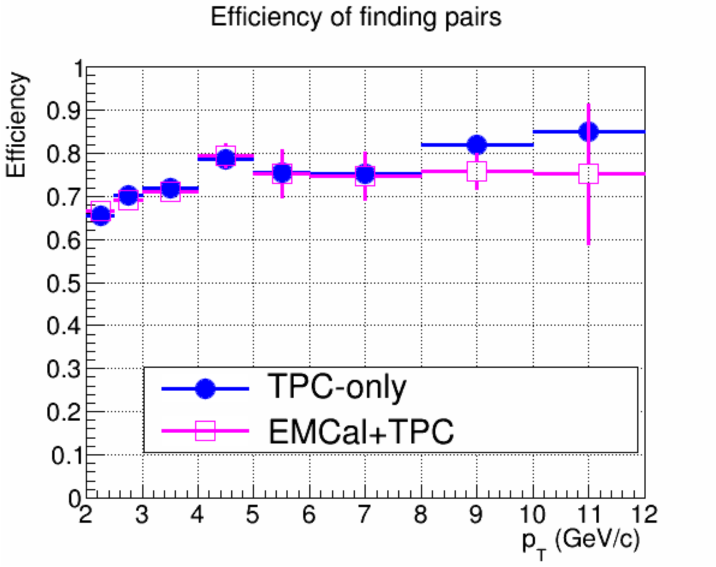

Figure 5.19: Invariant mass method efficiency.

Fig. 5.20 shows the ratio of the inclusive electrons and background (non-HFE) when we correct the non-HFE using the efficiency estimated using TPC only. We can observe that for the $p_{\mathrm{T}} < 3$ GeV/c, the signal to background ratio is smaller than 2, but it increases for higher p_{T} values.

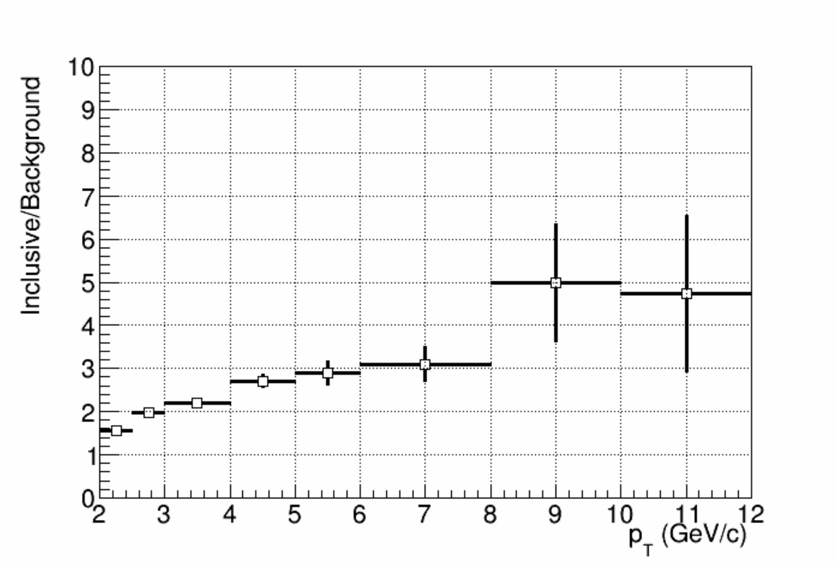

Figure 5.20: Ratio of inclusive electrons to background

When we use a MC sample, in some cases the simulated spectra do not have the same shape as in the data. This usually happens when the MC has enhancement[3] of some particle type, which is an usual technique done to increase the statistics for efficiencies determination in simulations.

In our analysis, the most part of the background comes from π_0, which decays in two gammas, and then, each of the gammas is converted into electron-positron pairs. Thus, it

---

[3] Usually the enhancement of the particles are done requiring a minimum of a given particle per event.

is important to check if the π_0 shape in MC corresponds to the π_0 shape in real data. The contribution of electrons from η is smaller, but has also to be corrected.

In this analysis, the event generator used (HIJING), does not reproduce the measured π or η spectra. Then, a correction has to be applied in the efficiency determination, based on the ratio between the shapes in MC and real data.

In order to correct for this effect, we use the experimental charged pion spectra (π^+ and π^-), since the π_0 spectrum is not available[4]. For the case of η, there is no experimental data available, then, the spectrum is obtained using a m_T-scaling (see Sec. 5.7) of the π_0 spectrum.

Fig. 5.21 shows a comparison between these two spectra with the spectra in MC simulations. We can see that the shape is different in both cases, showing that corrections are necessary.

Fig. 5.22 shows the ratio between data and MC for π^0 or η. The ratios are used as weight factor for the number of electrons in each p_T bin.

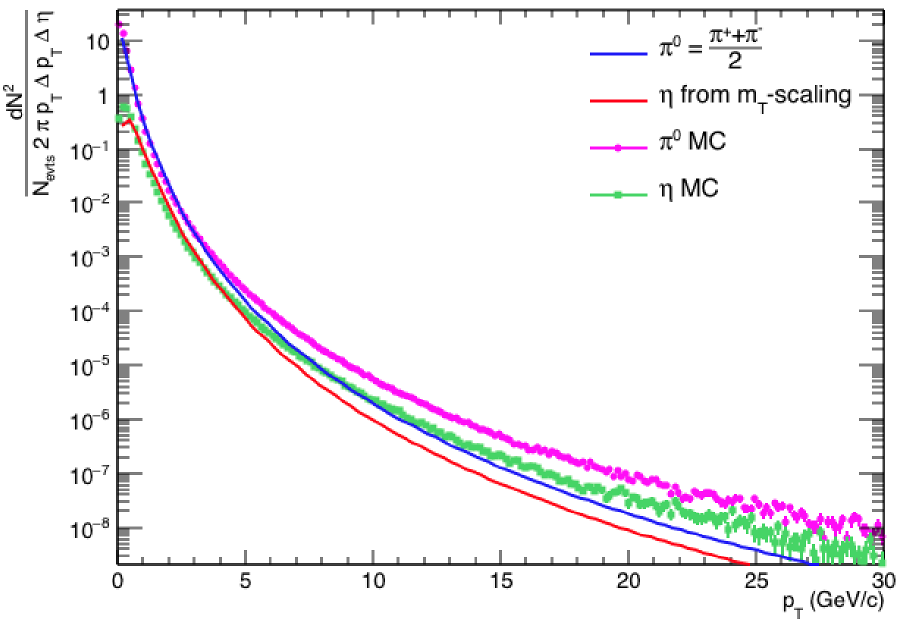

Figure 5.21: Comparison of π^0 and η spectra in data and in MC simulations.

Fig. 5.23 shows the efficiency without the usage of the weights compared to the case where the weights are used. The effect of the weights are more relevant in the low p_T. The weighted efficiency is the one used to correct the background spectrum.

---

[4] The π_0 spectrum can be estimated using the charged pions spectrum: $\pi_0 = \frac{\pi^+ + \pi^-}{2}$.

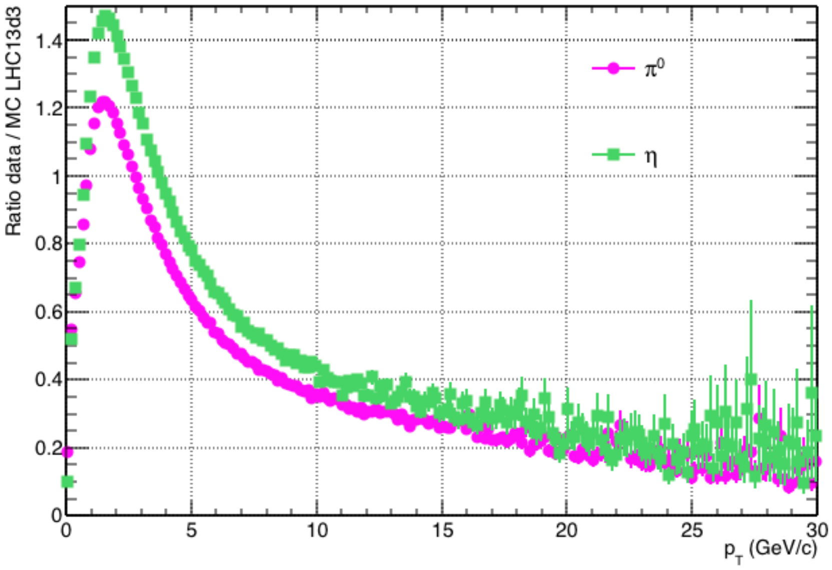

Figure 5.22: Weighting factors for electrons from π^0 and η decays.

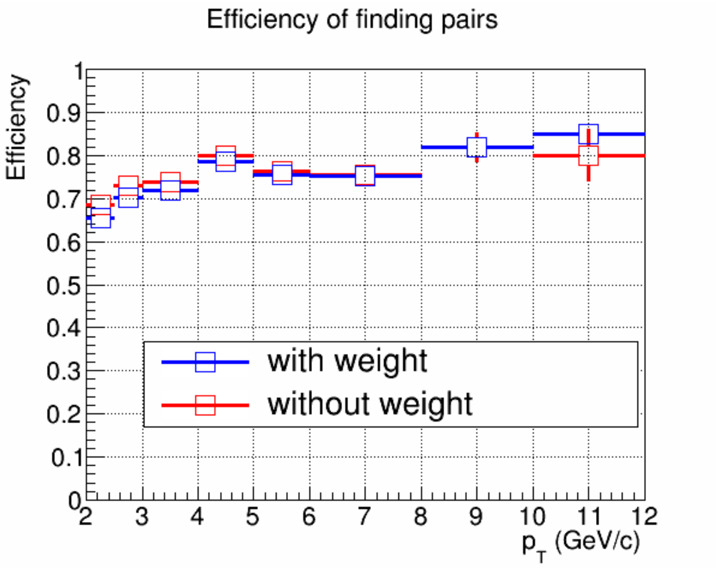

Figure 5.23: Comparison of efficiency of finding pairs with and without weight.

A important check was performed regarding the non-HFE measurement that corresponds to a comparison between the result obtained in this analysis using the invariant mass approach and the cocktail method [79]. Fig. 5.24 shows the comparison between non-HFE using the invariant mass method and using the cocktail. Both methods are in good agreement within statistical and systematic uncertainties. In the analysis, we use the invariant mass method instead of the cocktail, since the cocktail have a larger systematic uncertainty.

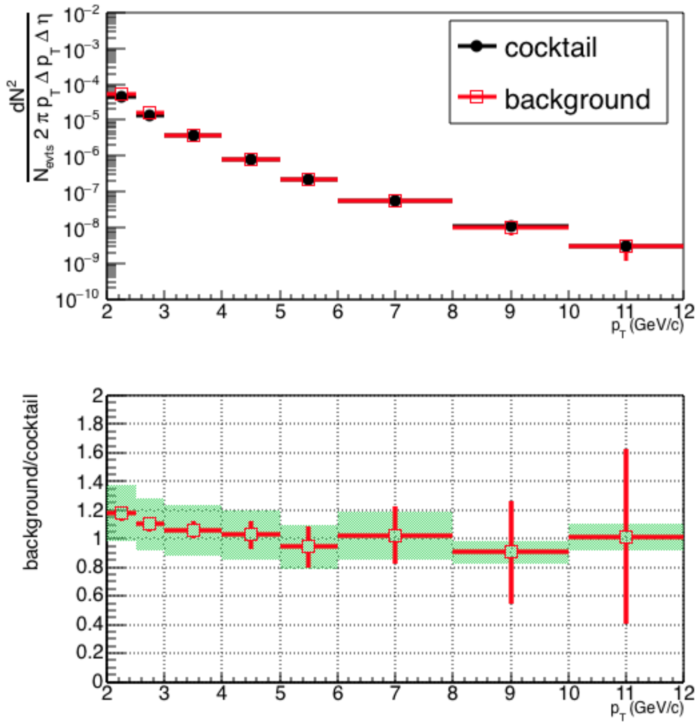

Figure 5.24: Comparison of non-HFE spectrum using invariant mass method and using the cocktail.

5.8.4 Electron reconstruction and identification efficiencies

Finally, it is necessary to correct the spectrum for the efficiency of track reconstruction (cuts applied as shown in table 5.1), for the efficiency of PID from TPC and EMCal (cuts applied as shown in table 5.2) and for the detector acceptance.

As explained in Sec. 5.8.1, the efficiencies are determine as the ratio of the electron spectrum obtained after given selection cut and the initial electron spectrum before the selection cut. Since they are determined using MC samples, it is possible to obtain spectra of true electrons. In order to allow a better efficiency determination, the MC sample used for the corrections was enhanced with charm and beauty. Then, to determine the efficiency, we have used the MC information to check if electrons that comes from B and D particles (heavy-flavour hadron decay electrons).

The efficiency correction are applied in the electron spectrum, after subtracting the background (the non-HFE).

In Fig. 5.25 it is shown the EMCal PID efficiency, which is around 60% for $p_{\mathrm{T}} \approx 2\mathrm{GeV}/c$ and increases to around 80% in high p_{T}. The EMCal PID efficiency is the ratio of the electron spectrum that passes the selection $0.8 < E/p < 1.2$ and the electrons before this selection.

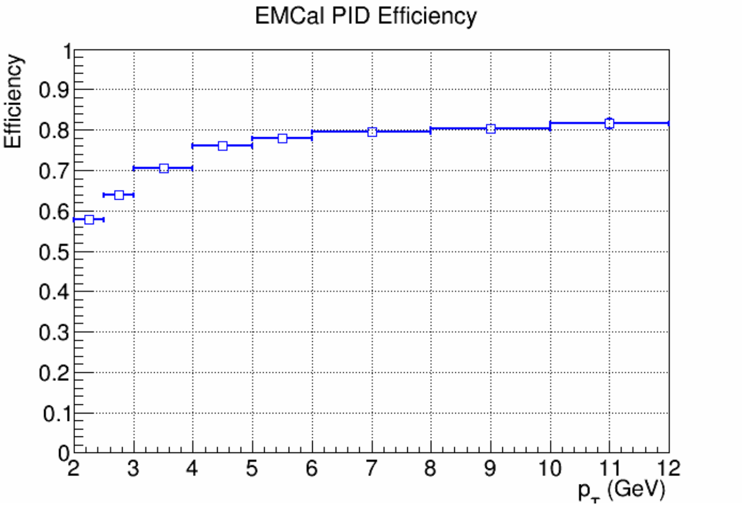

Figure 5.25: EMCal PID efficiency.

In Fig. 5.26 it is shown the track-match efficiency, which corresponds to the tracks from TPC matched with clusters from EMCal, with the EMCal acceptance included. This efficiency is the ratio of the electron spectrum that passes the selection $\delta\eta < 0.05$ and $\delta\phi < 0.05$ and the electrons before this selection. $\delta\eta$ and $\delta\phi$ are the distance between the track projection on the EMCal surface and the reconstructed shower in η and ϕ, respectively. The efficiency is around 25% in the range of transverse momentum used in this analysis.

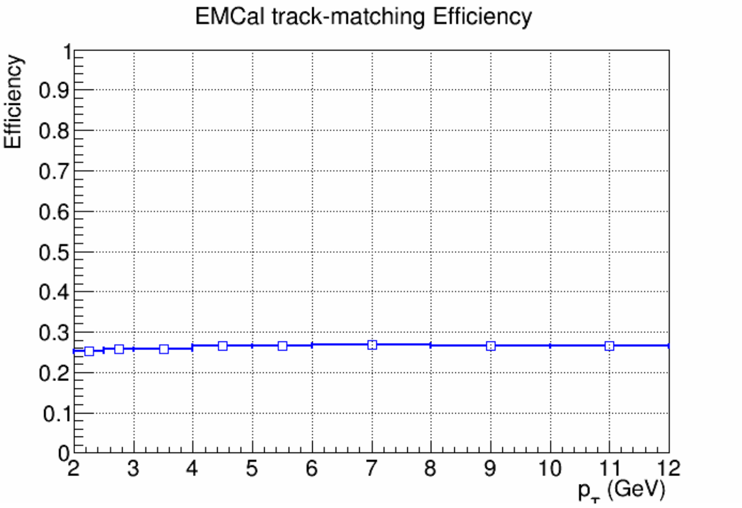

Figure 5.26: Track-matching efficiency and EMCal acceptance.

In Fig. 5.27 it is shown the tracking reconstruction efficiency which is around 70% in low p_{T} and increases to 80% in the last p_{T} bin. The efficiency was calculated as the ratio between the electron spectrum obtained after the AliRoot track reconstruction and the spectrum of generated electrons in the MC.

Fig. 5.28 shows the TPC PID efficiency, which is constant in 84%. This value is expected for the electron selection that we use for the TPC signal ($-1 <$ TPC N$\sigma < 3$), since the integral of a gaussian centered at zero with sigma equal one, from -1 to 3, divide by the integral from -3 to 3 is 0.84 .

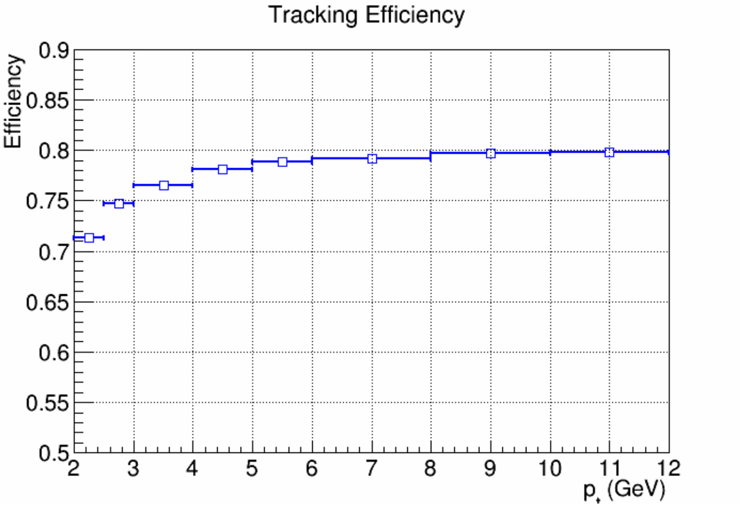

Figure 5.27: Tracking reconstruction efficiency.

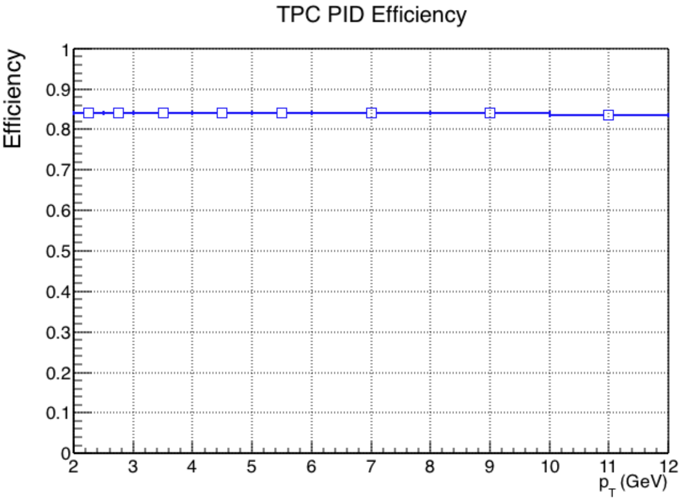

Figure 5.28: TPC PID efficiency.

These efficiencies are combined, resulting in the total efficiency of electron reconstruction, which is shown in Fig. 5.29 as a function of p_T.

Due to the response of the detector, the particle momentum reconstructed can lead to a different momentum value than the true one. This effect can be seen when we compare the momentum reconstructed and the true momentum of the particles in MC simulations.

Fig. 5.30 shows the correlation between the reconstructed and the true momentum in MC. This is an effect that has to be corrected in the final spectrum. The basic idea is that the measured p_T^{rec} is related to the true p_T^{true} by the correlation matrix C (also called *smearing matrix*):

$$p_T^{rec} = C p_T^{true} \tag{5.6}$$

Then, to obtain the true transverse momentum, p_T^{true}, it is necessary to invert the corre-

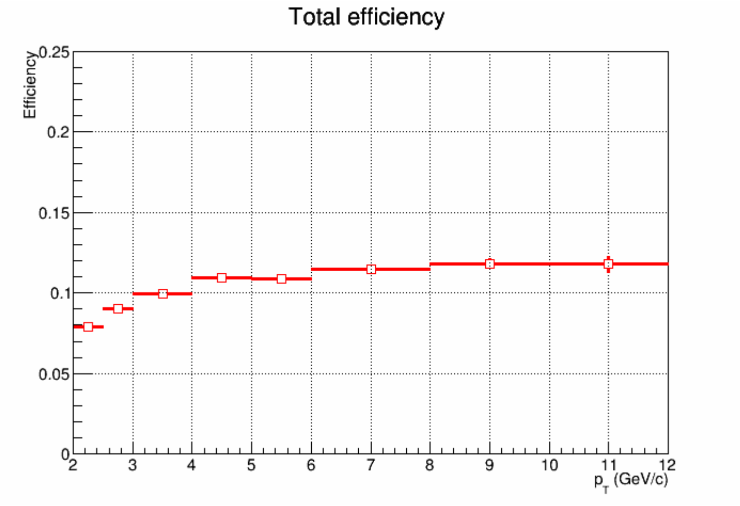

Figure 5.29: Total efficiency of finding electrons methodology.

lation matrix C:

$$p_T^{true} = C^{-1} p_T^{rec} \tag{5.7}$$

Since the C^{-1} is not always calculable, the Eq. 5.7 is resolved iteratively, as proposed in [183]. The Aliroot has a class to unfolding the spectrum (called AliCFUnfolding), using the method proposed in [183].

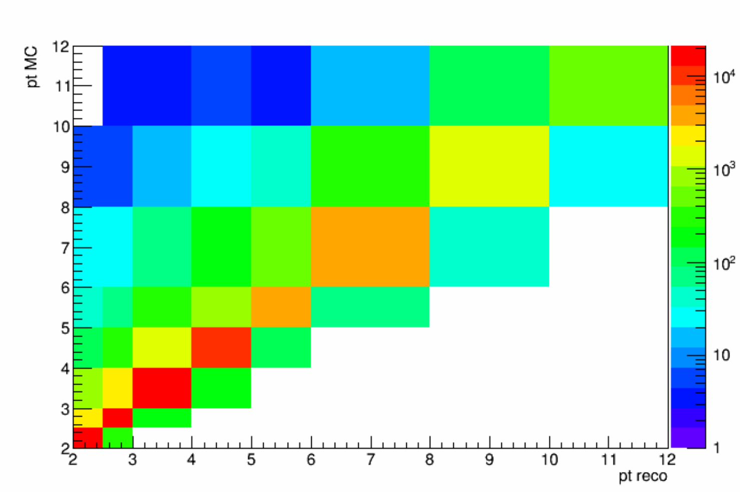

Figure 5.30: Correlation matrix of the p_T reconstructed by the detector (in MC) and the one from true MC.

Another method to compute the correcting factor of this effect is to calculate the efficiency using the p_T reconstructed in the numerator and p_T from true MC in the denominator. This is method used in this analysis, and the comparison with the one from the AliRoot is used to validate our method.

Fig. 5.31 show the spectra obtained using each method cited above and the ratio between them, what shows that the methods are compatible.

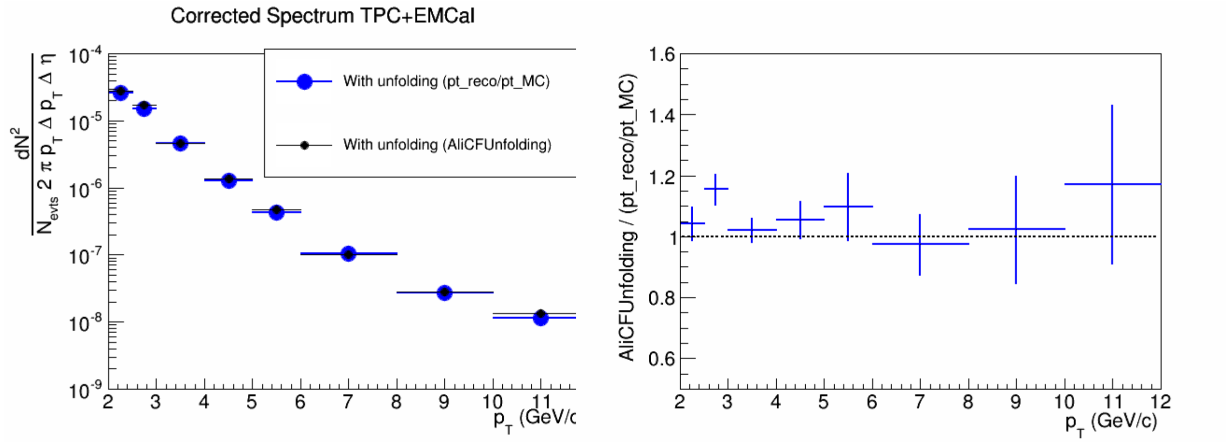

Figure 5.31: Right: comparison of the electron spectrum obtained using two different unfolding method (AliCFUnfolding and p_T^{rec}/p_T^{MC}). Left: ratio between both spectrum.

5.9 Invariant yield and nuclear modification factor

The spectrum of electrons from heavy-flavour hadron decays ($\mathcal{N}_{HFE}$) is obtained after subtracting the background contribution ($\mathcal{B}$), corrected for the background efficiency ($\epsilon_{\mathcal{B}}$), from the inclusive electron spectrum ($\mathcal{I}$). The result of the subtraction is corrected for the total efficiency (ϵ_T). Eq. 5.8 shows the expression for the $\mathcal{N}_{HFE}$.

$$\mathcal{N}_{HFE} = \frac{\mathcal{I} - \mathcal{B}/\epsilon_{\mathcal{B}}}{\epsilon_T} \tag{5.8}$$

The invariant differential yields of heavy flavour decay electrons ($d^2N_{HFE}^{inv}/dp_{\mathrm{T}}d\eta$) is given by Eq. 5.9.

$$\frac{dN_{HFE}^{inv}}{dp_{\mathrm{T}}} = \frac{1}{2}\frac{1}{2\pi p_{\mathrm{T}}}\frac{d^2\mathcal{N}_{HFE}}{\Delta p_{\mathrm{T}}\Delta\eta}\frac{1}{N_{evts}} \tag{5.9}$$

Fig. 5.32 shows the corrected spectrum, that was obtained by the expression 5.9. The systematic uncertainty is represented by the box and the procedure to determine them is described in section 5.10.

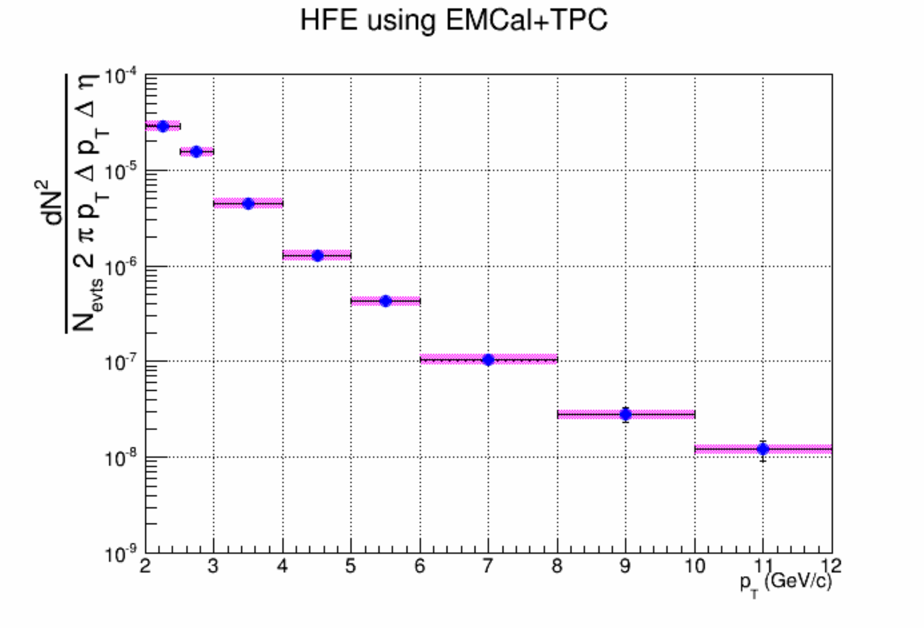

Figure 5.32: Invariant differential yields of electrons from heavy-flavour hadron decays in pPb collision.

To calculate the nuclear modification factor of electrons from heavy-flavour hadron decays, it is necessary a pp reference. The ALICE Collaboration has measured the cross section of electrons from heavy-flavour hadron decays at $\sqrt{s} = 7$ TeV [79] and at $\sqrt{s} = 2.76$ TeV [80]. An interpolation of this data were provided by the ALICE Collaboration [184] and this data were used as reference for the determination of the nuclear modification factor.

Eq. 5.10 shows the expression to calculate the nuclear modification factor ($R_{\rm pPb}$) in p-Pb collisions.

$$R_{\rm pPb} = \frac{1}{< T_{\rm pPb} >} \frac{{\rm d}N^{\rm pPb}/{\rm d}p_{\rm T}}{{\rm d}\sigma^{\rm pp}/{\rm d}p_{\rm T}} \tag{5.10}$$

where ${\rm d}N^{\rm pPb}/{\rm d}p_{\rm T}$ is the invariant yield of electrons from heavy-flavour hadrons decays, measured in p-Pb collisions, $\sigma^{\rm pp}/{\rm d}p_{\rm T}$ is the cross section of heavy-flavour hadron decays measured in pp collisions and $< T_{\rm pPb} >$ is the average nuclear overlap function, obtained with the Glauber Model, as explained in Sec. 2.4.2. The value used was $< T_{\rm pPb} > = 0.0983 \pm 0.0035$.

The measurement of HFE $R_{\rm pPb}$ was also performed by GSI group [182, 184], but in a complementary interval of lower transverse momentum. While our analysis is in the interval of $2 < p_{\rm T} <12$ GeV/c, the GSI analysis was performed in the interval of $0.5 < p_{\rm T} < 6$ GeV/c. Additionally, the measurements of the GSI group were based on the TPC and TOF signals. Fig. 5.33 shows R_{pPb} comparison of the results and they are consistent in the intersection range, within the statistical uncertainties.

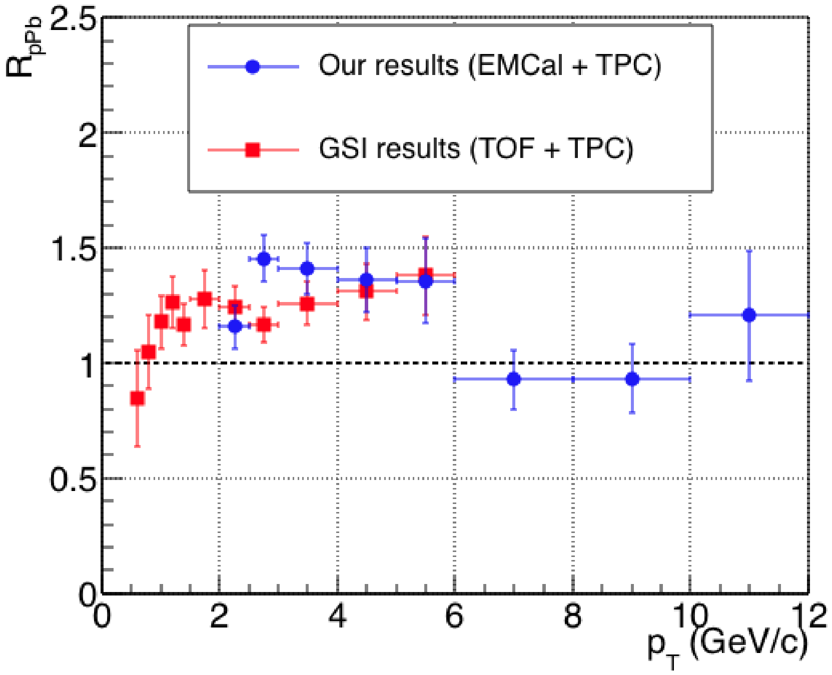

Figure 5.33: Comparison of HFE R_{pPb} obtained in this analysis, using the TPC and EMCal detectors, with the corresponding results obtained by the GSI group, using the TPC and TOF detectors. The results are consistent within statistical uncertainties.

The combined results were published in the interval of $0.5 < p_{\mathrm{T}} < 12$ GeV/c. The detectors with the best performance in each interval of p_{T} were used.

The HFE cross section and the HFE nuclear modification factor of the combined result was published in the *Physics Letter B* [4]. Fig. 5.34 shows the combined HFE spectrum in p-Pb and also the HFE spectrum in pp, used for the calculations of the nuclear modification factor. The HFE pp spectrum is an interpolation of measured results at $\sqrt{s} = 2.76$ TeV and $\sqrt{s} = 7$ TeV.

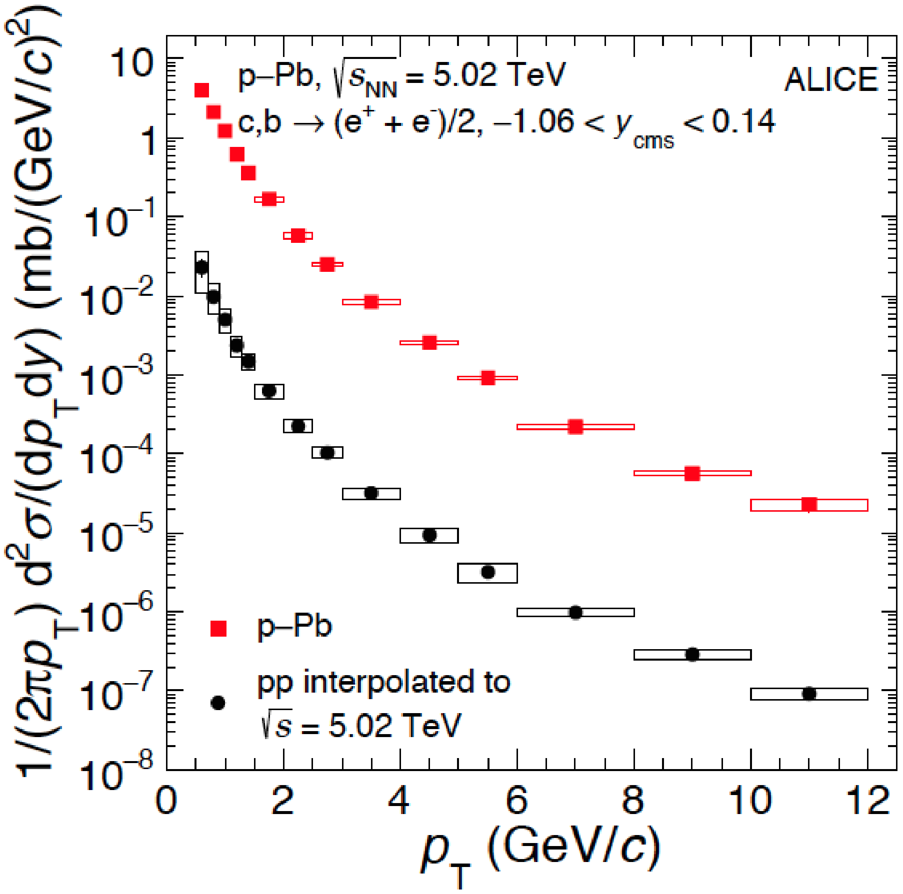

Figure 5.34: Invariant yield of electrons from heavy-flavour hadron decays measured in p-Pb and in pp. The p-Pb results is a combination of the results obtained in this analysis, using the TPC and EMCal detectors, with the results obtained by the GSI group, using the TPC and TOF detectors. The pp results is an interpolation of HFE measurements at $\sqrt{s} = 2.76$ TeV [80] and $\sqrt{s} = 7$ TeV [79].

Fig. 5.35 shows the combined HFE nuclear modification factor. The box represents the systematic uncertainties, which were determined using the procedure discussed in 5.10. The theoretical models compared to the data are discussed in Chap. 7, where we also discuss the physics message that this result, combined with other results, can reveal.

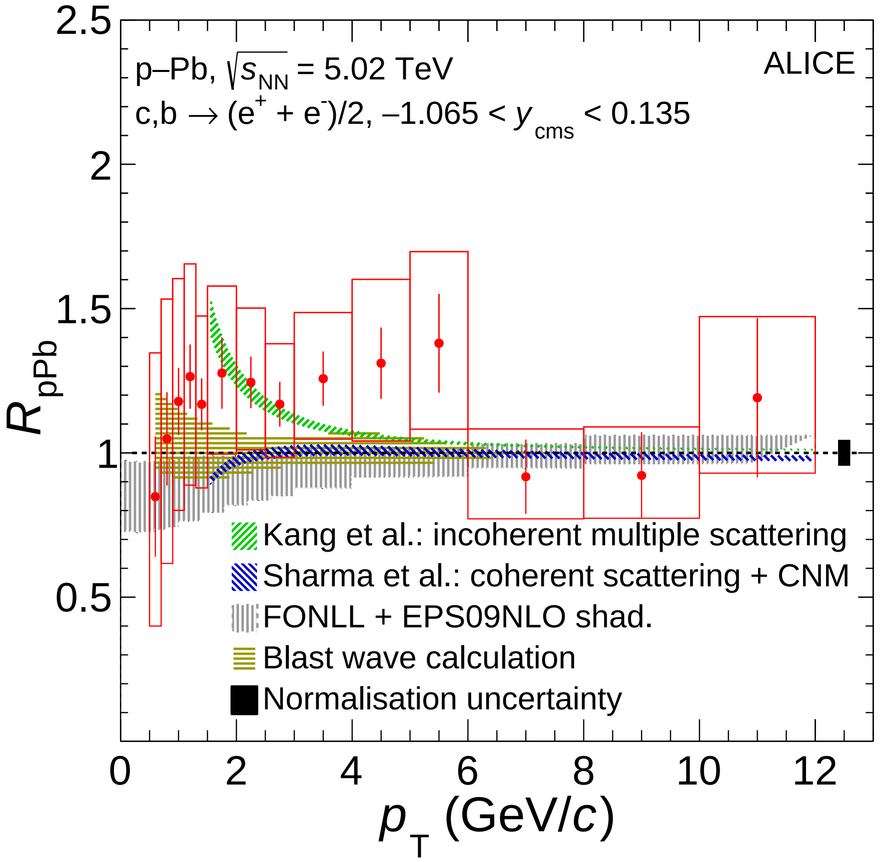

Figure 5.35: Nuclear modification factor of electrons from heavy-flavour hadron decays measured in p-Pb, as a combination of results from this analysis, using the TPC and EMCal detectors, and the results obtained by the GSI group, using the TPC and TOF detectors.

5.10 Evaluation of systematic uncertainties

The systematic uncertainties of the HFE spectrum were obtained performing variations of the several selection cuts used in the analysis. The spectrum obtained with each variation is compared with the one obtained using the default cut selection. To decide if a given variation has a systematic effect, we use a method proposed by R. Barlow [185]. The method consists of calculating the difference ($\Delta(p_{\mathrm{T}})$) between the spectra as given by Eq. 5.11, and calculating the uncertainty of the difference ($\sigma_{\Delta}(p_{\mathrm{T}})$), given by Eq. 5.12. According to Barlow, the uncertainty can be calculated by this expression if one sample is a subsample of the other.

$$\Delta(p_{\mathrm{T}}) = \left(\frac{1}{2\pi p_{\mathrm{T}}}\frac{d^2N}{dp_{\mathrm{T}}dy}\right)_{reference}(p_{\mathrm{T}}) - \left(\frac{1}{2\pi p_{\mathrm{T}}}\frac{d^2N}{dp_{\mathrm{T}}dy}\right)_{variation}(p_{\mathrm{T}}) \tag{5.11}$$

$$\sigma_{\Delta}(p_{\mathrm{T}}) = \sqrt{|\sigma^2_{\left(\frac{1}{2\pi p_{\mathrm{T}}}\frac{d^2N}{dp_{\mathrm{T}}dy}\right)_{reference}}(p_{\mathrm{T}}) - \sigma^2_{\left(\frac{1}{2\pi p_{\mathrm{T}}}\frac{d^2N}{dp_{\mathrm{T}}dy}\right)_{variation}}(p_{\mathrm{T}})|} \tag{5.12}$$

Then, the procedure consists in calculating the ratio $\frac{\Delta(p_{\mathrm{T}})}{\sigma_{\Delta}(p_{\mathrm{T}})}$, which is the difference in number of sigmas between the two spectra. If this variation is smaller than 1, both spectra are compatible and there is no systematic effect (differences are within statistical fluctuations). On the other hand, if the variation is bigger than 1, a systematic effect can be present.

In case where $\frac{\Delta(p_{\mathrm{T}})}{\sigma_{\Delta}(p_{\mathrm{T}})} > 1$, we use the ratio between both spectra to quantify the relative uncertainty.

Fig. 5.36 shows one example of the difference plot and Fig. 5.37 shows the ratio plot used to extract the numerical value of the systematic uncertainty. These are example of a variation considered as statistical fluctuation.

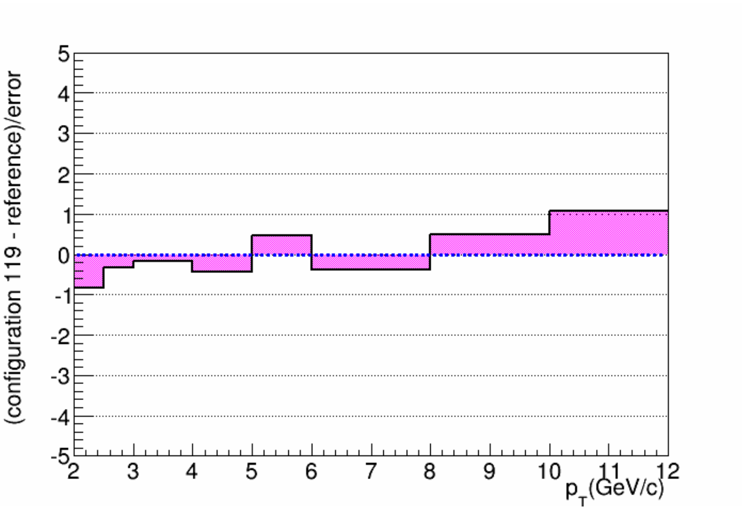

Figure 5.36: Example of the procedure to determine the systematic uncertainties: The difference shows it is statistical fluctuation.

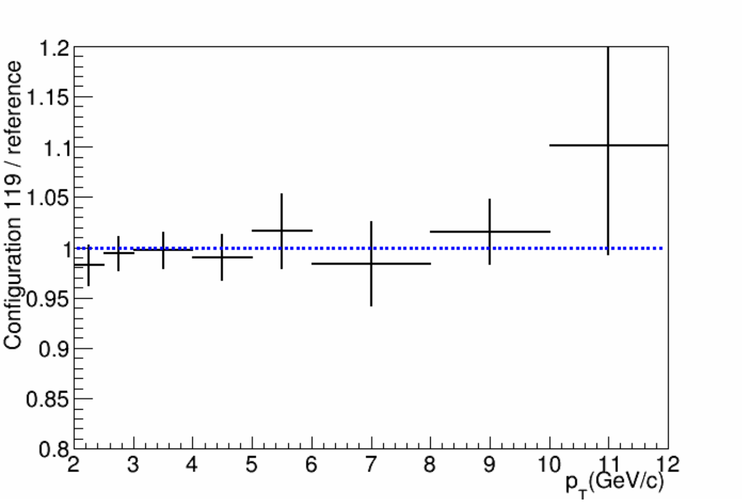

Figure 5.37: Example of the procedure to determine the systematic uncertainties.

Figs. 5.38 and 5.39 show respectively the difference and ratio plots for a case where we consider a systematic effect.

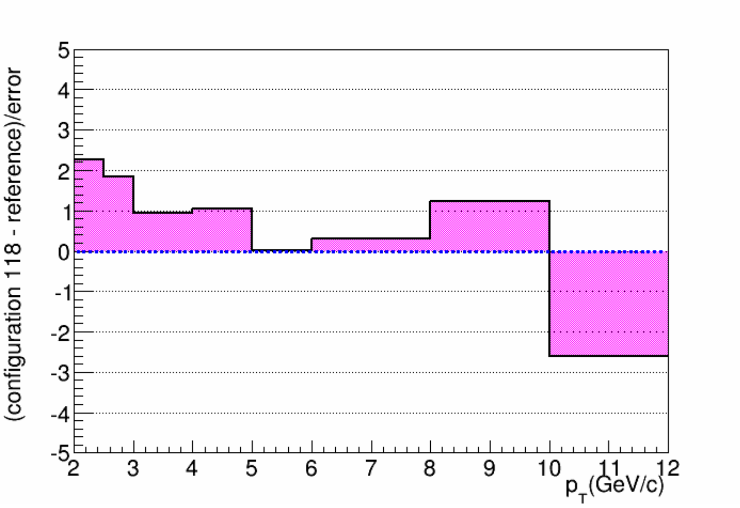

Figure 5.38: Example of the procedure to determine the systematic uncertainties: The difference shows it is not statistical fluctuation.

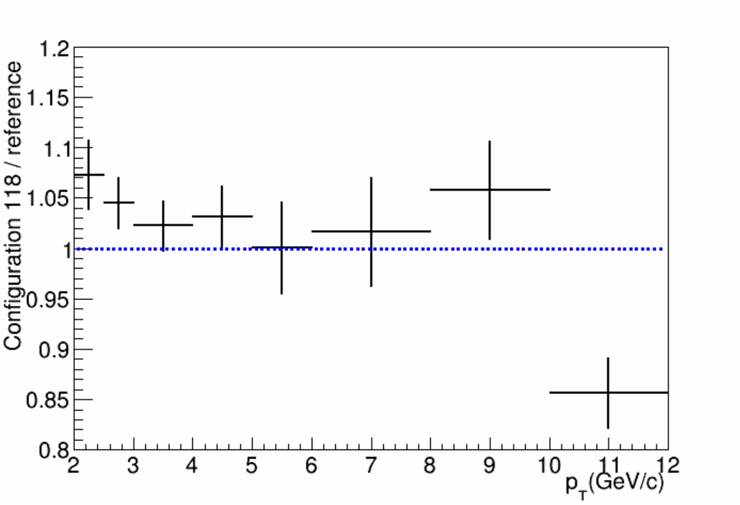

Figure 5.39: Example of the procedure to determine the systematic uncertainties: The ratio is used to extract the numerical value of the systematic uncertainty.

The summary of the configuration with a systematic effect is shown in Tab. 5.10. The list of the variations in each cut is shown in App. F.

Parameter	**1 σ of confidence**
ClustersTPC	no effect
ClustersTPCPID	no effect
CutITSpixel	2%
ClustersITS	2%
SetMaxImpactParam	no effect
NonHFEmassCut	no effect
Opening angle	no effect
p_{T} associated	no effect
NClustersTPC associated	no effect
NClustersITS associated	2%
η window	no effect
($\delta\eta$, $\delta\phi$)	no effect
E/p	(4%, 2%, 2%, 1%, 1%, 3%, 5%, 15%)*
TPC nσ	2%
TPC-ITS matching	3%
EMCal-TPC matching	3%
Total	(7%, 6%, 5%, 5%, 5%, 6%, 7%, 16%)*

Table 5.4: Configurations with systematic effect. For the cases marked with (*), the uncertainties are p_{T} dependent and the values of each bin are presented.

5.11 Final considerations of this chapter

In this chapter, we presented the analysis performed using the MB data for the p-Pb collisions at $\sqrt{s_{\mathrm{NN}}} = 5.02$ TeV. We have measured electrons from heavy-flavour hadron decays in the transverse momentum range of $2 < p_{\mathrm{T}} < 12$ GeV/c, using the TPC and EMCal detectors. The background electrons were subtracted using an invariant mass method for the contributions from gamma conversions, π^0 and η Dalitz decays. The contribution from J/ψ was obtained from the cocktail. Other background electrons sources showed to be negligible. The efficiencies were determined using MC simulations.

The results were combined with the results of the GSI group, which measured the HFE spectrum in the transverse momentum range of $0.5 < p_{\mathrm{T}} < 6$ GeV/c, using the TPC and TOF detectors. The nuclear modification factor was calculated using a pp spectrum, which is an interpolation of $\sqrt{s} = 2.76$ TeV and 7 TeV results, provided by the GSI group. The combined result was published in *Physics Letter B* [4].

In Chap. 7 we discuss the comparison of this result with theoretical models and the conclusions that we can extract from the comparisons.

Chapter 6

Results using the EMCal trigger

The Chap. 5 was dedicated to describe the analysis performed in data using the MB trigger, and the present chapter is dedicated to the analysis of data obtained using the EMCal trigger. The EMCal trigger enhances the recorded sample in high p_{T}, enabling the extension of the range of measurements that we have performed in MB collisions. The trigger system used in this analysis was the L1 (explained in Sec. 4.2.4), also called gamma trigger (EGA). The p-Pb collisions were recorded using two thresholds of L1: one at 7 GeV (EGA2) and other at 11 GeV (EGA1). Both thresholds were analysed in this thesis extending the MB results up to 20 GeV/c transverse momentum.

6.1 Summary of the analysis steps

The strategy of the analysis of the triggered data by EMCal signal is quite similar to the analysis performed in MB data, described in Sec. 5.1. The electron identification is based on the combination of TPC and EMCal signals, and performed after the selection of the data set, events and tracks. One of the differences for the electron identification in the EMCal triggered data is the use of the *shower shape* information in the EMCal, which provides information to remove hadron contamination. As in the MB analysis, the electrons from background are reconstructed via the invariant mass method (for electrons from π^0, η and γ) and via cocktail (for electrons from J/ψ). Since this analysis is performed in high transverse momentum, the contribution of electrons from W decays is not negligible, as it is in the MB analysis, and it was estimated via simulations using the POWHEG package. Another difference in this analysis is the efficiency correction due to the EMCal trigger, since the trigger enhances the measurements.

A detailed explanation of the analysis is given in the next sections.

6.2 Choice of data set

Fig. 6.1 shows the comparison of the cluster energy distribution for both thresholds (7 and 11 GeV), and also the MB distribution (data analysed in Chap. 5). We can clearly see the enhancement of counts around 7 and 11 GeV, where the trigger thresholds are set.

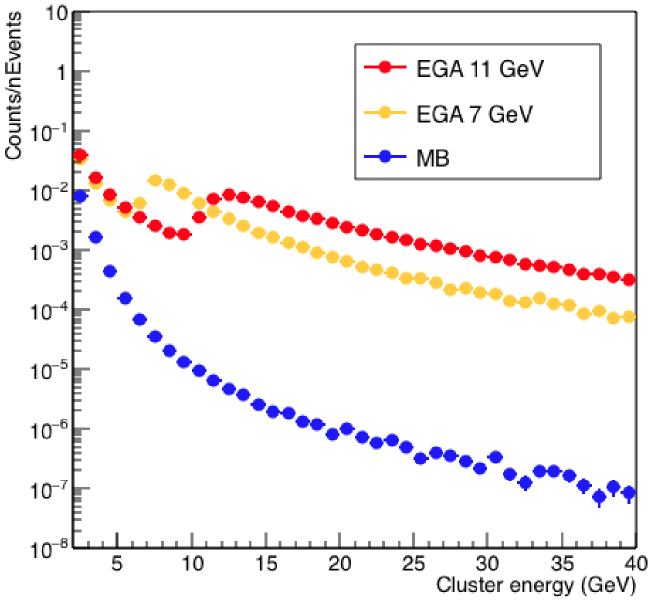

Figure 6.1: Cluster energy distribution on EMCal for the EGA trigger at 7 GeV (EGA2) and 11 GeV (EGA1) and for the MB trigger (in LHC13b and LHC13c periods).

The runs were selected regarding the EMCal and TPC performance. Only runs containing the EMCal gamma trigger were selected, and the η-ϕ map of the EMCal cells was also used to assure the full EMCal acceptance was being used for each run. One example of the EMCal η-ϕ map is shown in Fig. 6.2. In this figure we also show the track-cluster residuals for tracks on TPC that were matched to clusters on EMCal. The residuals are the difference between the $\Delta\eta$ ($\Delta\phi$) measured for the track and the $\Delta\eta$ ($\Delta\phi$) of the corresponding matched cluster. The total residuals is called ΔR and is given by Eq. 6.1.

$$\Delta R = \sqrt{\Delta\eta^2 + \Delta\phi^2} \tag{6.1}$$

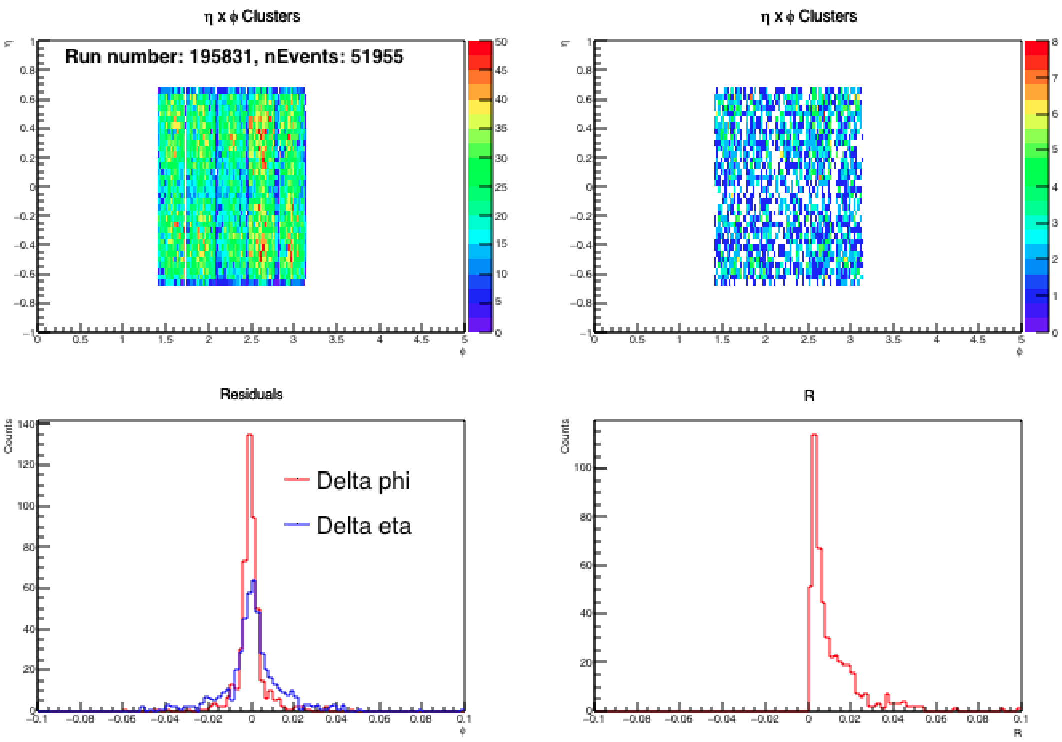

Figure 6.2: Left top: η-ϕ map of the EMCal for all tracks selected. Right top: η-ϕ map of the EMCal for all electrons. Left bottom: Track-matching residuals in η and ϕ distributions. Right bottom: Total track-matching residuals ΔR.

For each run, we checked the TPC performance based on the number of electrons per events, similarly to the MB analysis. The number of electrons are presented in Figs. 6.3 and 6.4 , for three different intervals of TPC Nσ. Different intervals of TPC Nσ were used in order to optimize the purity of the electron sample:

- $2 < p < 5$: The TPC Nσ values were used from -1 to 3 since in this p_T range the electron gaussian is well separated from hadrons.
- $5 < p < 10$: The TPC Nσ values were used from 0 to 3. In this p_T range the hadrons distribution starts to merge with electrons distribution.
- $10 < p < 20$: The TPC Nσ values were used from 1 to 3. In this p_T range the hadron contamination is very high.

This optimisation was not performed in the MB data since the hadron contamination in a MB sample is smaller than in a sample were a trigger is used.

Fig. 6.3 and Fig. 6.4 show the number of electrons per events run by run, for the 11 GeV and 7 GeV thresholds, respectively. We can see that the number of electron is fluctuating around the same value for all runs.

The runs used in the analysis are presented in App. E.

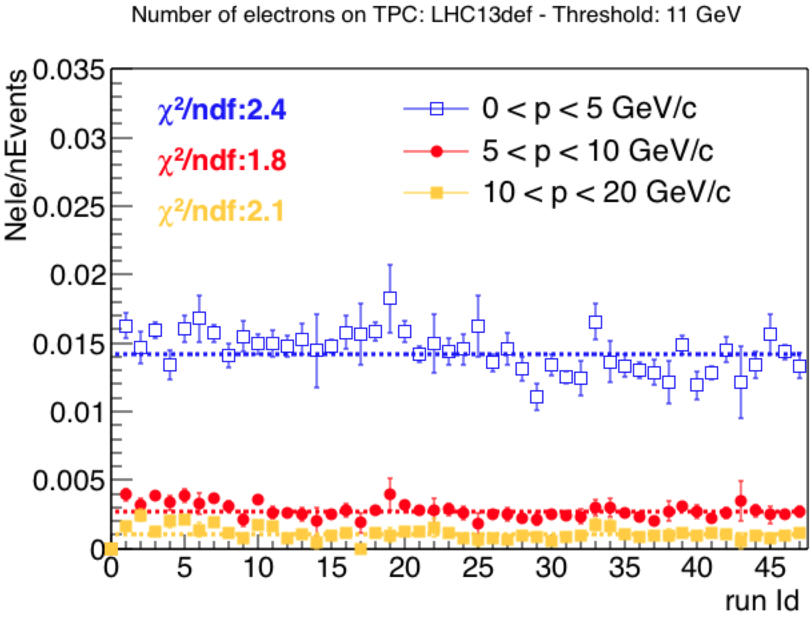

Figure 6.3: The number of electrons per events with TPC electron identification for the EGA1 trigger.

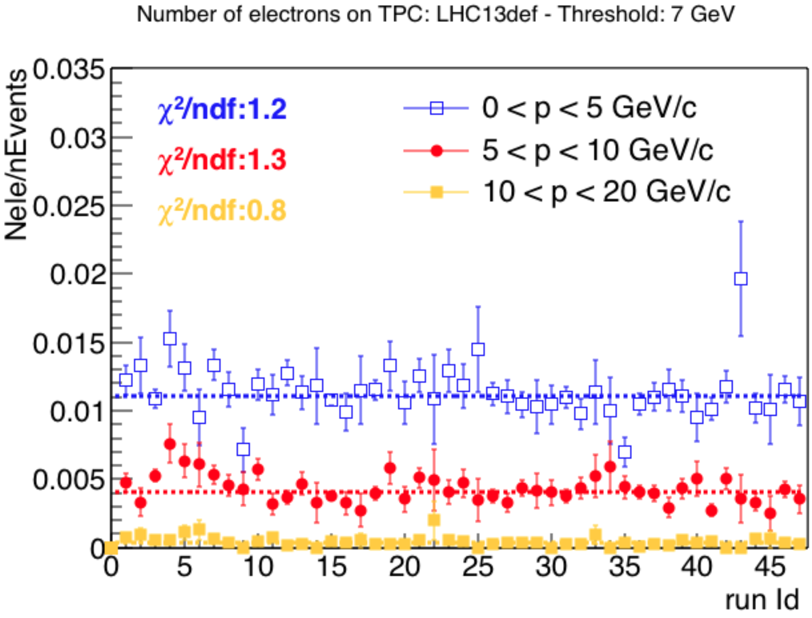

Figure 6.4: The number of electrons per events with TPC electron identification for the EGA2 trigger.

We also checked the number of electrons on EMCal, after applying the cut $0.8 < E/p < 1.2$, and the results are shown in Fig. 6.5 for the 11 GeV threshold and in Fig. 6.6 for the 7 GeV threshold. We can see that the number of electrons is fluctuating around a constant value in each threshold. Then, for all the runs used in the analysis, the same value of electrons are found.

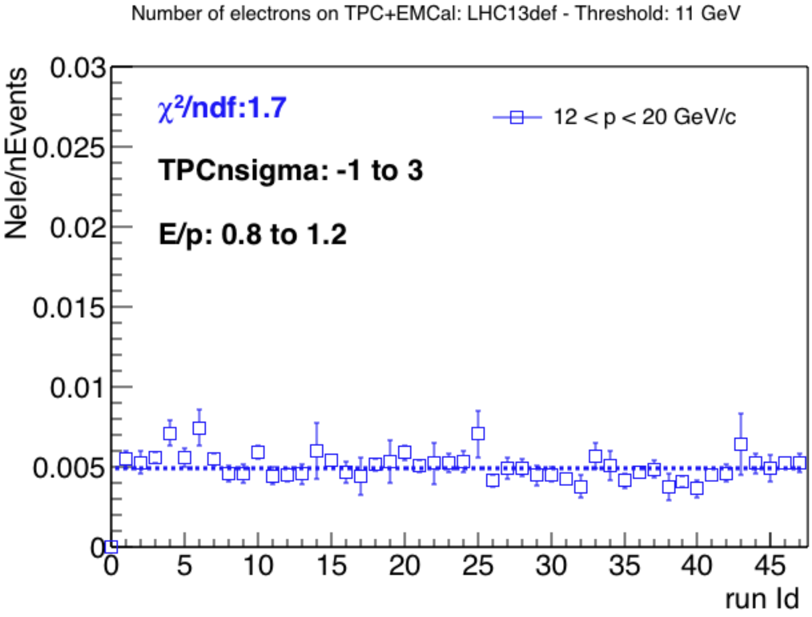

Figure 6.5: The number of electrons per events with TPC+EMCal for the 11 GeV threshold.

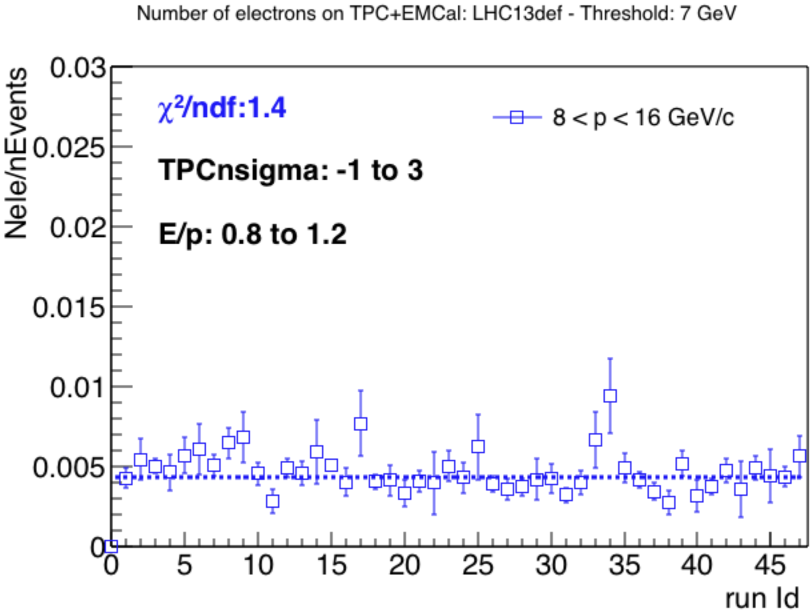

Figure 6.6: The number of electrons per events with TPC+EMCal for the 7 GeV threshold.

6.3 Event selection

The event selection included the requirements of the MB analysis: consistent vertex obtained from SPD and from the tracks were required and the vertex position have to be within 10 cm away from the nominal center of the ALICE apparatus. In addition to that, only events with the L1 trigger fired were selected. The number of events selected are 435323 for the EGA2 and 1079251 for the EGA1.

6.4 Track selection

The track selection is the same used in the MB analysis, presented in Tab. 5.1. In summary, we required 100 clusters in the TPC, for the particle identification, the number of clusters required was 80. In the ITS detector we required a minimum of 3 clusters and a hit on the first or the second layer of the ITS detector, since this cut helps to remove electrons from gamma conversion. An η cut was applied in order to assure that all tracks are within the EMCal acceptance. The kink-daughters were rejected from the analysis. A cut on the distance of closest approach (DCA) to the primary vertex in the transverse plane (xy) as well as in the beam direction (z) was applied to reject background tracks and non-primary tracks. More details about each of these cuts can be found in Sec. 5.4.

6.5 Clusters properties

In this section we show the clusters properties for MB and EGA. One of the corrections that we need to apply in the data, due to the usage of the EGA trigger is performed using a ratio of the clusters energy distribution in EGA divided by MB (called rejection factor, discussed in Sec. 6.10). Thus, it is important to investigate if the clusters obtained using the EGA trigger have a bias, due to the selection of different physics (like more jets) or even issues due to the additional amount of data measured by the EMCal.

Then, our goal is to check if a given cluster on EGA trigger is similar to a cluster with approximately the same energy in MB trigger. For both cases, we select clusters in energy intervals, where we plan to analyse the data and get the HFE spectrum. For the comparison between MB and EGA1, the selected energy range is from 12 up to 20 GeV and for the comparison of MB and EGA2, the selected energy range is from 8 up to 16 GeV. This allow us to investigate an artificial trigger in MB events, in the same range as the measurements with the EGA trigger. For the selected clusters, we have compared the distributions of the number of cells per cluster, the η-ϕ map, the distributions of number of clusters per event, and track-matching residuals distribution.

Figs. 6.7 and 6.8 show the number of cells distribution for the MB trigger and EGA trigger for the 7 and 11 GeV, respectively. The distributions are similar for both triggers.

Fig. 6.9 shows the number of clusters distribution for events selected in the energy range described above, in both trigger. The distributions are similar for the MB and EGA trigger cases.

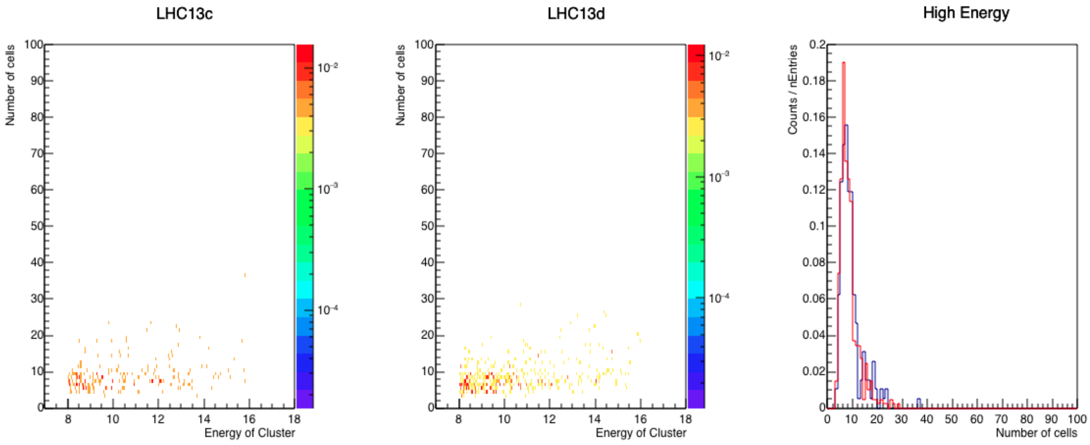

Figure 6.7: Number of cells distribution as a function of energy for MB (left) and EGA2 (midlle) events. The plot on the right shows the projection in the energy range considered (8 to 16 GeV), for the MB (in blue) and for EGA2 (in red).

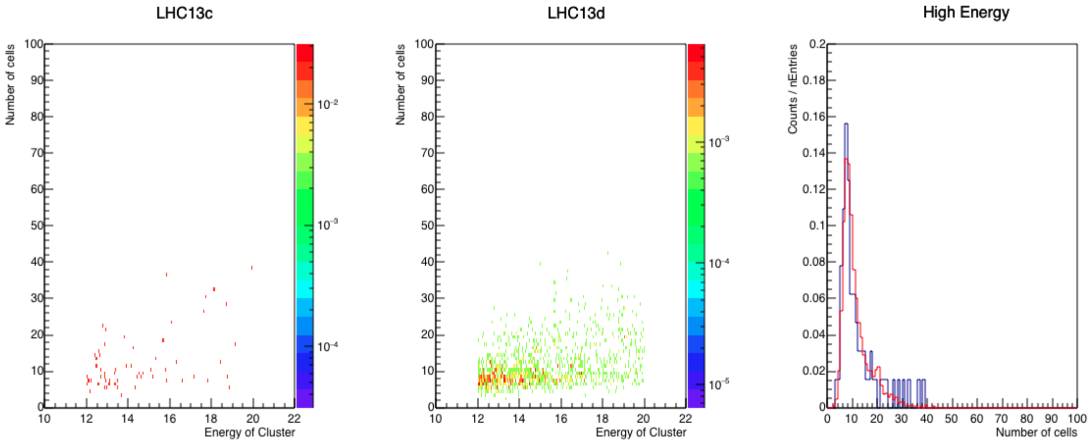

Figure 6.8: Number of cells distribution as a function of energy for MB (left) and EGA1 (midlle). The plot on the right shows the projection in the energy range considered (12 to 20 GeV), for the MB (in blue) and for EGA1 (in red).

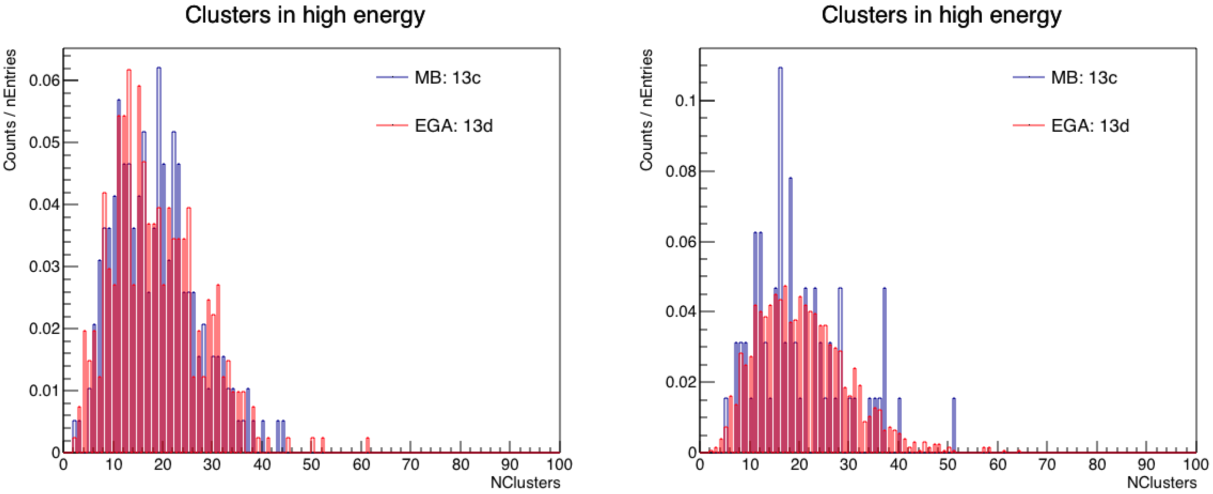

Figure 6.9: Comparison of number of clusters in the EMCal in events with MB and GA trigger. Left: EGA2. Right: EGA1.

Figs. 6.10, 6.11 and 6.12 show the comparison of the distance between the track projection and the cluster position (track-matching) for events in both triggers. Again, for the comparison between MB and EGA1, the selected energy range was from 12 up to 20 GeV and for the comparison of MB and EGA2, the selected energy range was from 8 up to 16 GeV. The distributions are similar for $\Delta\eta$, $\Delta\phi$ and ΔR for the MB and EGA triggers.

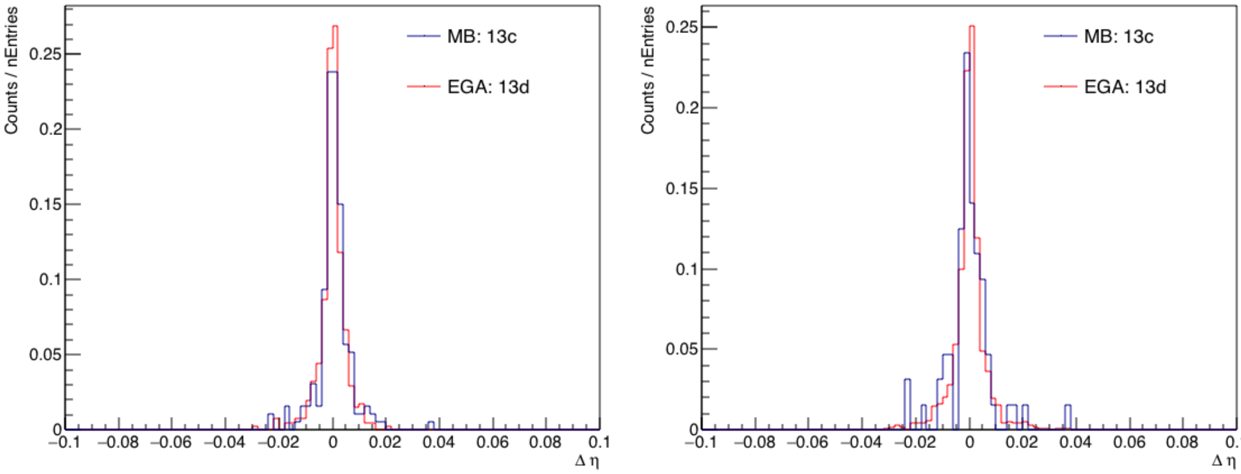

Figure 6.10: Track-matching $\Delta\eta$ distribution for EGA2 (left) and EGA1 (right).

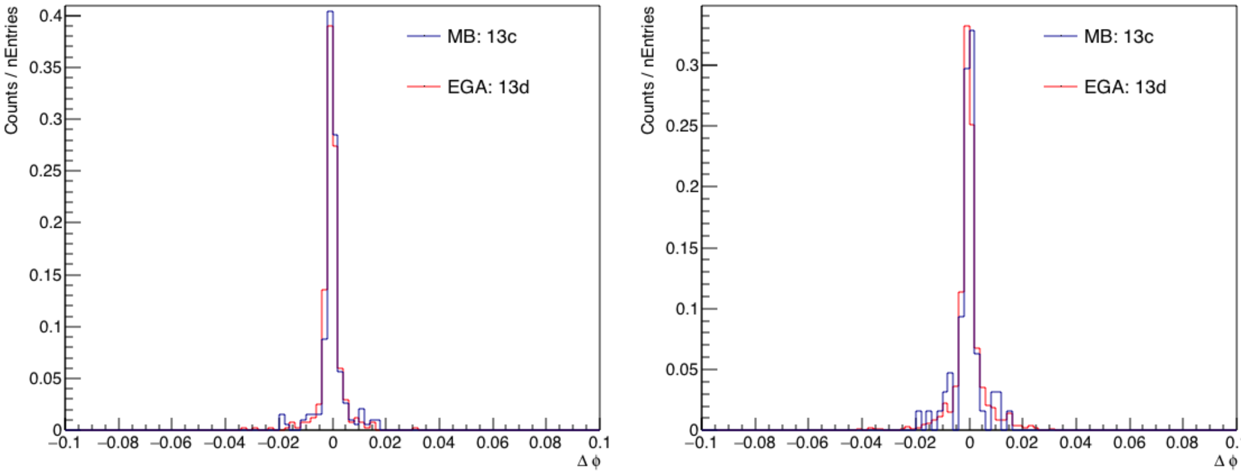

Figure 6.11: Track-matching $\Delta\phi$ distribution for EGA2 (left) and EGA1 (right).

Given a cluster on the same range for both triggers (MB and EGA), the distributions of the cluster properties are consistent. This means that there is no bias on the cluster information if it belongs to the trigger data.

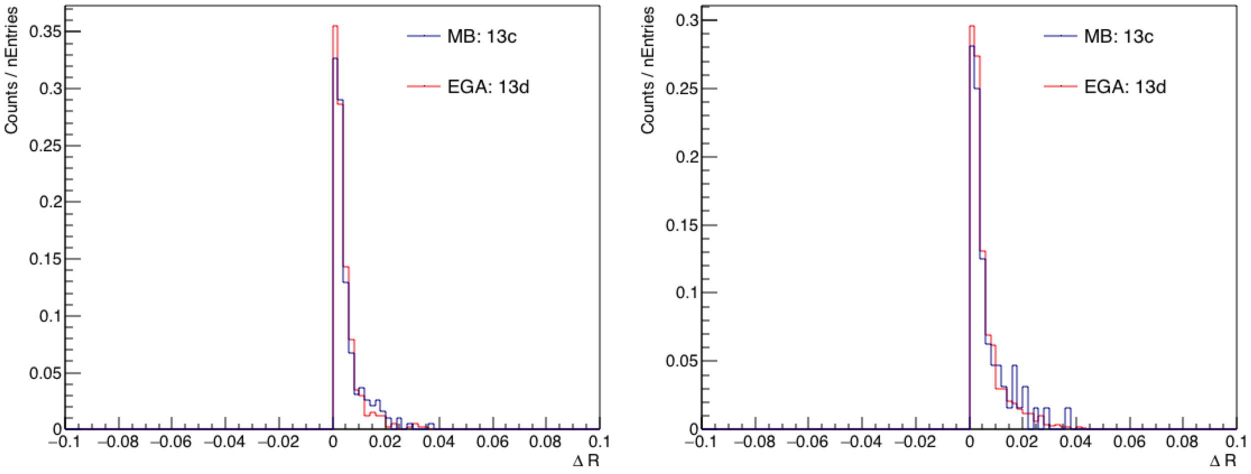

Figure 6.12: Track-matching ΔR distribution for EGA2 (left) and EGA1 (right).

In the runs used in the EMCal triggered data (EGA) analysis, there is also available events with the MB trigger. However, the events with MB data have a low statistics. Since to perform the corrections due to the EGA trigger (rejection factor), it is necessary to use a sample of MB trigger, we have used different LHC run periods for the MB data. Then, it was important to assure that the MB events in both periods were similar, in order to not introduce any bias in our result.

The η-ϕ maps in MB for the two different periods are shown in Fig. 6.13. The ratio of the map is shown in the bottom plot and is around one, showing that the distribution is similar for both trigger systems.

Fig. 6.14 shows the projections of η and ϕ in MB for the two different periods, and the distributions are the same.

These studies between same trigger (MB) in different periods showed that the events are similar and will not introduce any bias in the results.

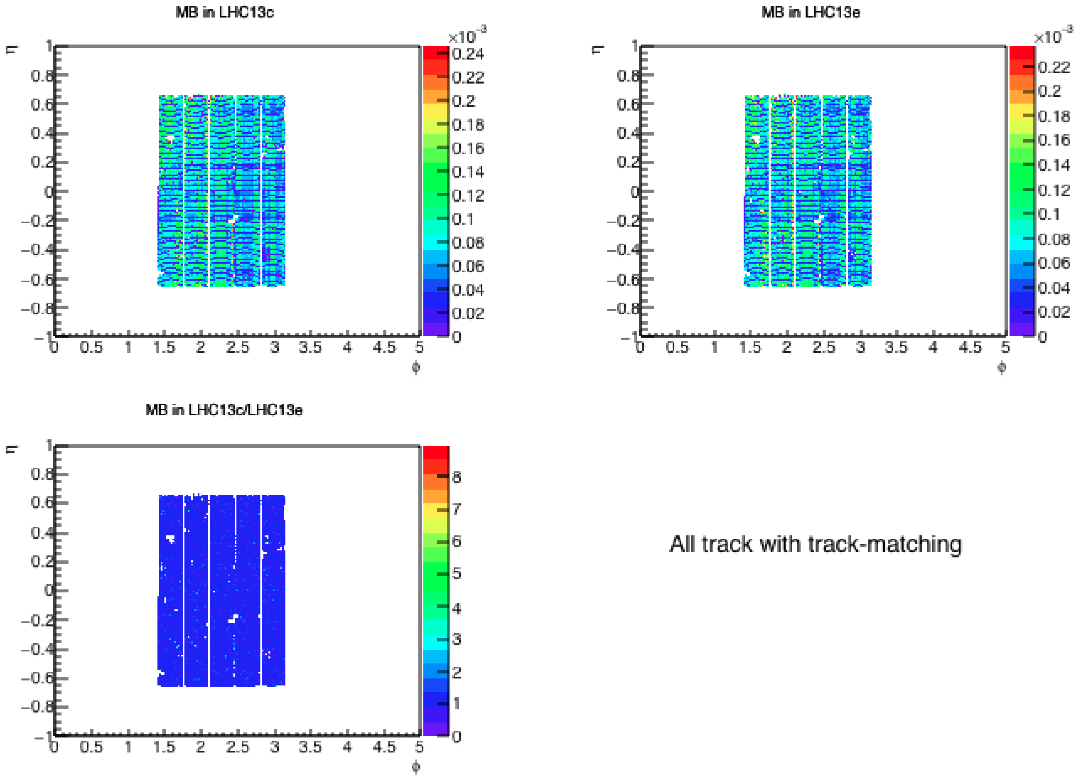

Figure 6.13: Comparison of η-ϕ map in MB sample for the two different periods of the LHC.

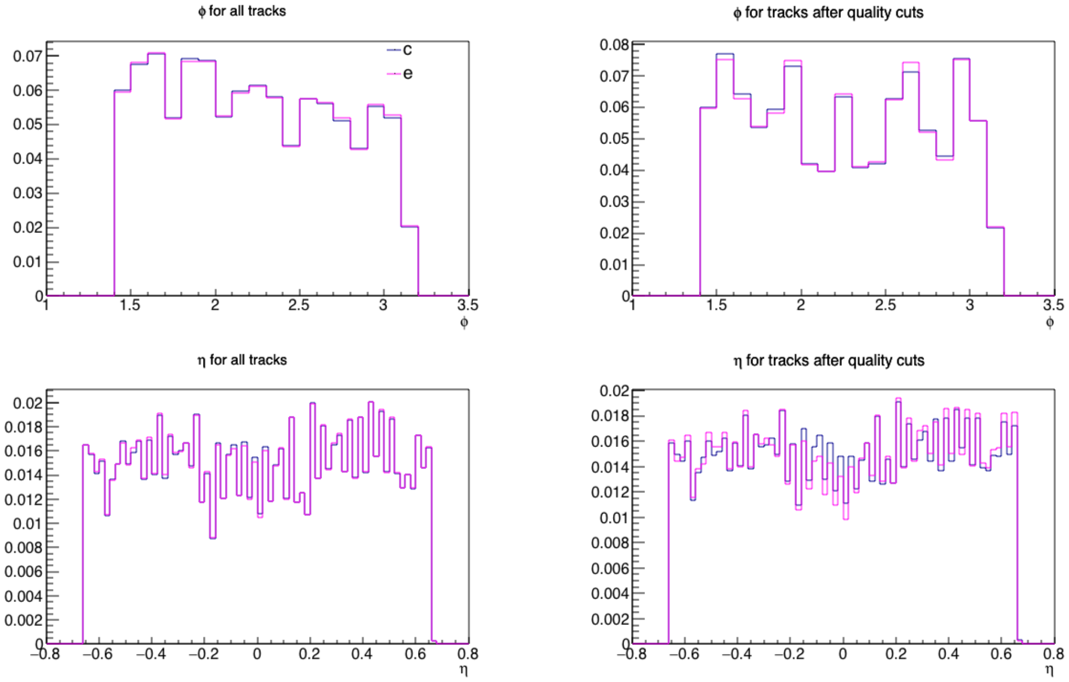

Figure 6.14: Projections of η and ϕ in MB for the periods LHC13c and LHC13e.

6.6 Electron identification

As in the MB analysis, the electron identification is based on the TPC and EMCal detectors.

The TPC tracks are accepted only if the distance between the track projection on the EMCal surface and the reconstructed shower satisfies the conditions: $\Delta\eta < 0.05$ and $\Delta\phi < 0.05$, as in the MB analysis. One difference in this analysis is the usage of the shower shape on the EMCal, in order to improve the purity of the selected electrons, as will be explained bellow.

Fig. 6.15 shows the distribution of the TPC Nσ for electrons for the period LHC13d. The electrons are expected to be around zero, since we are looking the TPC Nσ for electrons. The procedure to find the electron distribution is the same as in the MB analysis: we parametrize the TPC Nσ using two gaussians and a Landau distribution multiplied by an exponential. Fig. 6.15 (top) shows the result of the fit and Fig. 6.15 (bottom) shows the ratio data/fit. The mean and standard deviation (sigma) from the fit of the gaussian in the electron region is shown in the top of the plot.

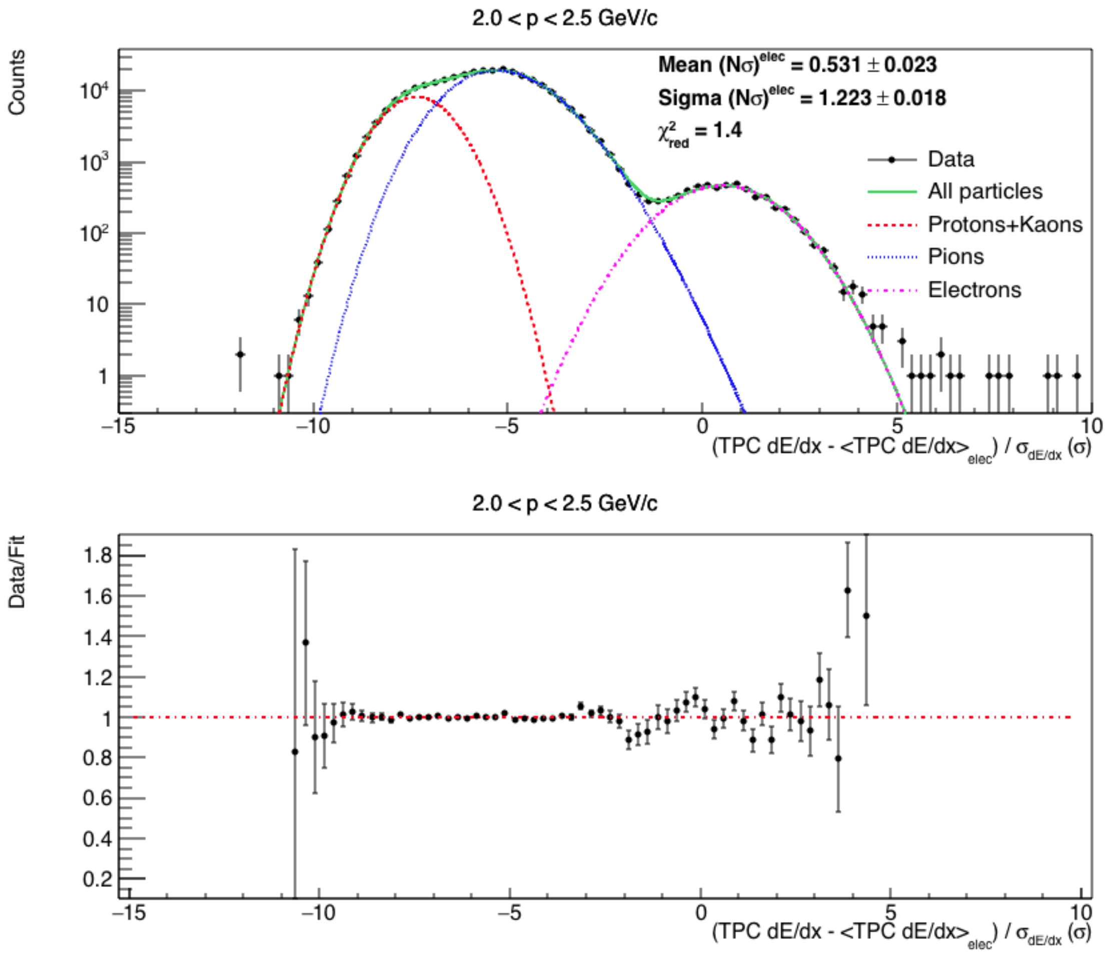

Figure 6.15: Electrons TPC Nσ distribution for the period LHC13d.

The Fig. 6.16 shows the mean and sigma of the gaussian fit for the electron, for each period and both EMCal trigger thresholds. We can clearly see that the period LHC13d has a mean shifted from zero and a sigma higher than 1. We use this shift to correct the distributions, to have mean = 0 and sigma = 1. The values used for the calibration were obtained from the 11 GeV threshold, which is the sample with more statistics.

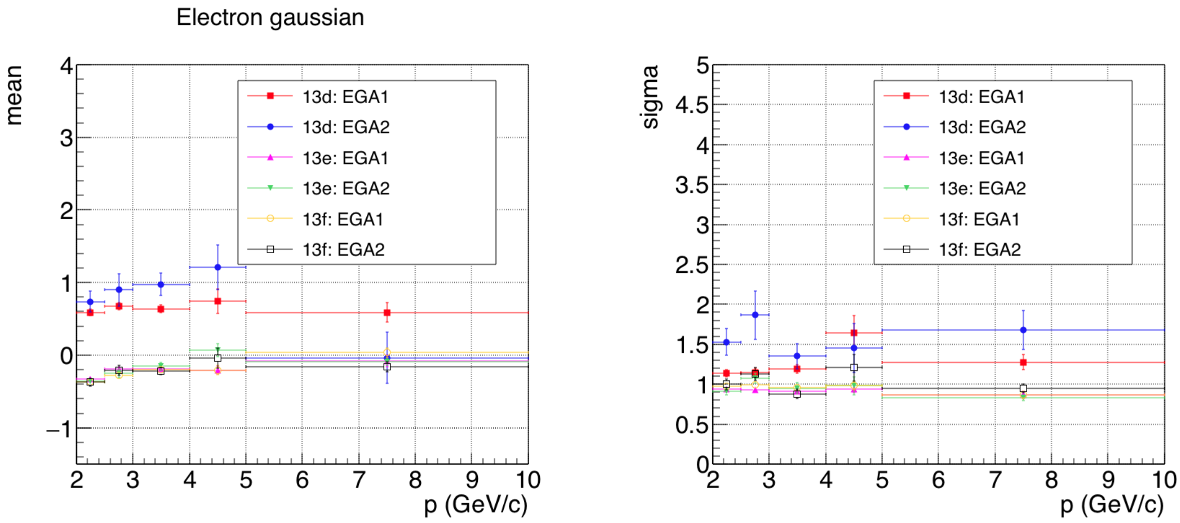

Figure 6.16: Fit results on the TPC Nσ electron distribution for the periods LHC13d, LHC13e and LHC13f and for both thresholds (EGA1 and EGA2): left plot shows the mean of the electrons gaussian and the right plot shows its sigma. The period LHC13d has a shift for mean and sigma that has to be corrected.

The Fig. 6.17 shows the TPC Nσ distribution after the calibration. We can see that the electron gaussian mean is closer to zero with sigma closer to one. The Fig. 6.18 shows the mean and sigma values as a function of p_{T} bins, only for the period LHC13d, before and after the calibration, for both thresholds. For the 11 GeV threshold, the calibration worked better than for the 7 GeV, since the values used for the calibration was obtained for the 11 GeV data. Since the TPC signal should not depend on the EMCal trigger, we used the sample with more statistics to determine the calibration.

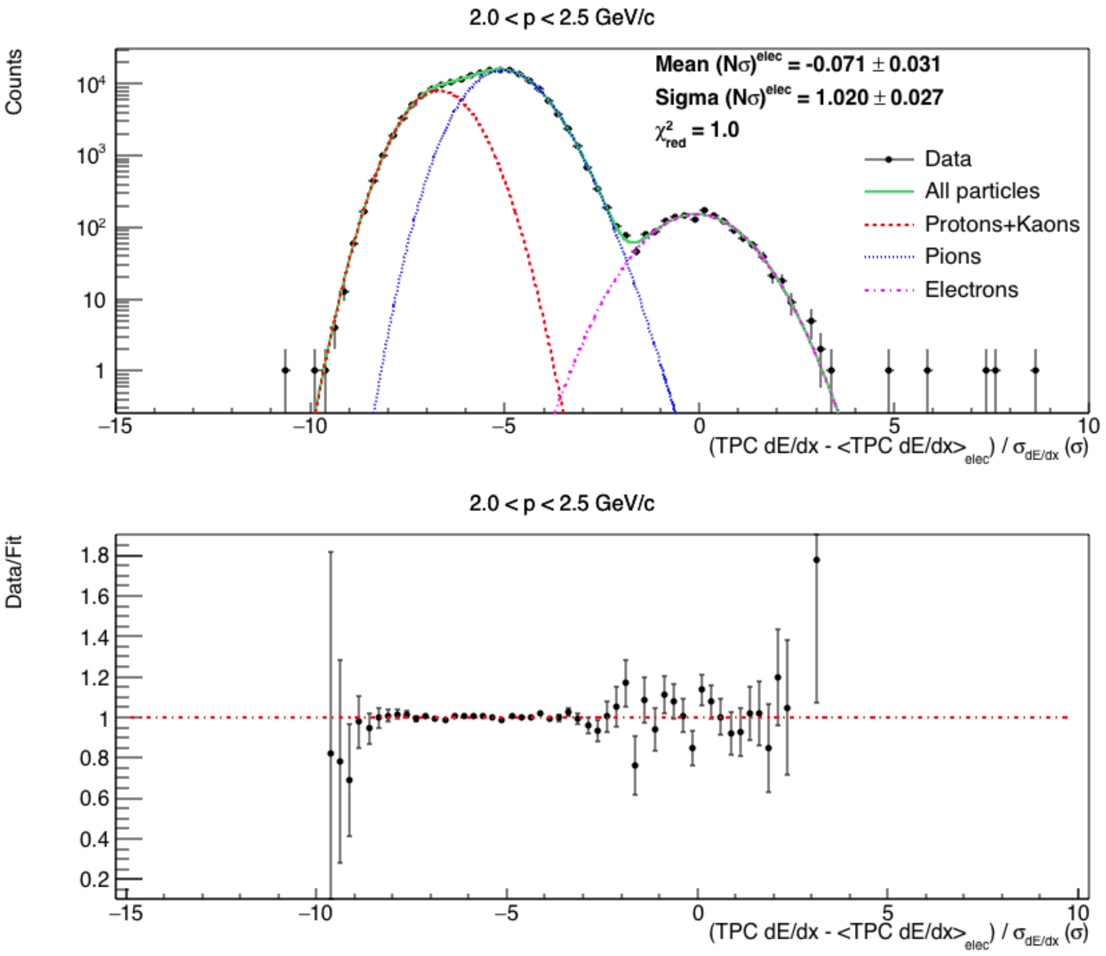

Figure 6.17: TPC Nσ distribution for the period LHC13d after calibration.

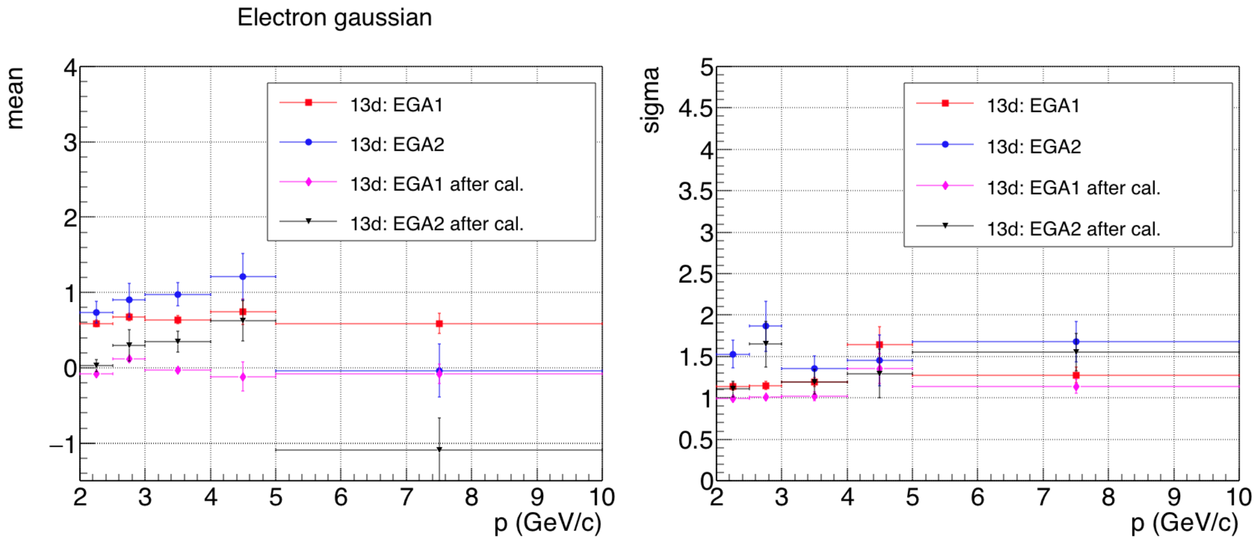

Figure 6.18: Fit results on the TPC Nσ electron distribution for the period LHC13d and for both thresholds (EGA1 and EGA2), before and after the calibration: left plot shows the mean of the electron gaussian and the right plot shows its sigma.

Fig. 6.19 shows the correlation between the TPC Nσ and E/p distribution for the 7 GeV (left) and 11 GeV (right) thresholds. Differently from the MB analysis, in this case the electrons around -1 < TPC Nσ < 3 and $0.8 < E/p < 1.2$ are not evident in the plot.

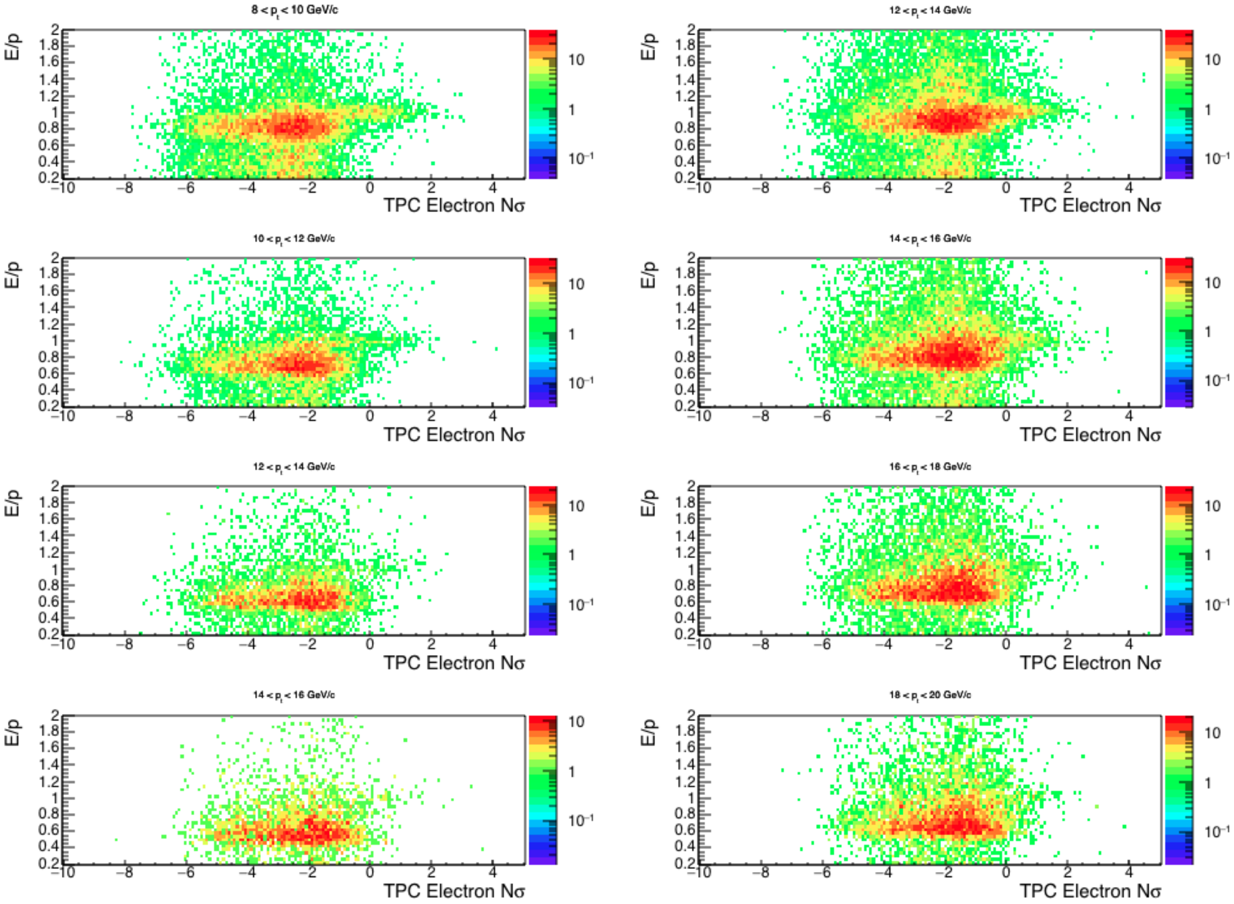

Figure 6.19: Correlation between TPC Nσ and E/p distribution for the EMCal Gamma trigger at 7 GeV (left) and 11 GeV (right) thresholds.

The cuts used for electron identification were the same as in the MB analysis and they are summarized in table 6.1, with the addition of the shower shape cut, that will be justified in the Sec. 6.7.

Table 6.1: PID cuts.

detector	Cut applied
TPC	$-1 < \sigma_{TPC-dE/dx} < 3$
EMCal	$0.8 < E/p < 1.2$
EMCal shower shape	M20 < 0.3

For high p_{T} values, the hadron band start to merge with the electron band in the TPC Nσ. The shower shape on the EMCal can be used to determine the hadron contamination in the selected sample, since the shower shape for hadron and electrons are different: the dispersion of the shower produced by electrons is smaller than the one produced by hadrons

[186].

Since the EMCal is segmented, it allows the determination of the incident of the position of the incident particle that will start the shower. The coordinates of the shower can be calculated from the coordinates of weighted mean of the cells containing the shower [186]. The various moments of a given shower in $\eta - \phi$ map is given by [187]:

$$\langle \phi \rangle = \frac{\sum_i w_i \phi_i}{\sum_i w_i} \tag{6.2}$$

$$\langle \eta \rangle = \frac{\sum_i w_i \eta_i}{\sum_i w_i} \tag{6.3}$$

$$\langle \phi\eta \rangle = \frac{\sum_i w_i \phi_i \eta_i}{\sum_i w_i} \tag{6.4}$$

$$\langle \phi^2 \rangle = \frac{\sum_i w_i \phi_i^2}{\sum_i w_i} \tag{6.5}$$

$$\langle \eta^2 \rangle = \frac{\sum_i w_i \eta_i^2}{\sum_i w_i} \tag{6.6}$$

where w_i is the weight of the cell i, which is proportional to the energy E_i of the cell and the total energy of the shower E_T, given by [186]:

$$w_i = max\,\{0, [w_0 + ln(E_i/E_T)]\} \tag{6.7}$$

The spread of the image is given by:

$$\sigma_{\phi^2} = \langle \phi^2 \rangle - \langle \phi \rangle^2 \tag{6.8}$$

$$\sigma_{\eta^2} = \langle \eta^2 \rangle - \langle \eta \rangle^2 \tag{6.9}$$

$$\sigma_{\phi\eta} = \langle \phi\eta \rangle - \langle \phi \rangle \langle \eta \rangle \tag{6.10}$$

With all this exposed, we can write the expressions of the squared length and the squared width of the shower. The Fig. 6.20 shows the shower shape example in the EMCal.

$$\lambda_0^2 = \frac{\sigma_\eta^2 + \sigma_\phi^2}{2} + \sqrt{\frac{(\sigma_{\eta^2} - \sigma_{\phi^2})^2}{4} + \sigma_{\eta\phi^2}} \equiv M02 \tag{6.11}$$

$$\lambda_1^2 = \frac{\sigma_\eta^2 + \sigma_\phi^2}{2} - \sqrt{\frac{(\sigma_{\eta^2} - \sigma_{\phi^2})^2}{4} + \sigma_{\eta\phi^2}} \equiv M20 \tag{6.12}$$

Since the shower produced by electrons is more collimated than the one produced by hadrons [186], the information of the shower shape in the calorimeter can be used to improve the separation of electrons and hadrons. In this analysis, we have used a data driven method to optimise this separation, as will be explained in the next section.

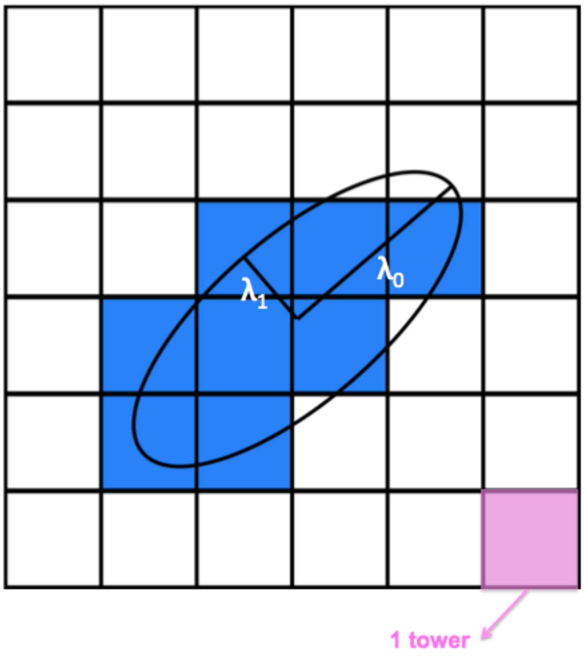

Figure 6.20: Shower shape distribution on the EMCal (adaptation from Gustavo Conesa figure).

6.7 Removal of hadron contamination

To remove the hadron contamination of the data, the M02 and M20 shower shape parameters, defined in Eq. 6.11 and Eq. 6.12 were used. We have selected a sample of electrons and a sample of hadrons, and we studied the parameters of the shower shape for each sample, in order to optimise the purity of our electrons sample.

The selection of electrons and hadrons were done using the E/p values. Electrons were selected using $0.8 < E/p < 1.2$ and hadrons were selected using the $E/p > 1.2$ and $E/p < 0.8$. Fig. 6.21 and Fig. 6.22 show the M20 and M02 distributions, respectively, for electrons and hadrons. It is possible to observe that for M20 $>$ 0.3, most of the particles are hadrons. Thus applying the cut M20 $<$ 0.3 enables the suppression of hadron contamination from the electrons sample. On the other hand, looking the M02 distribution, we see that most of the particles are electrons, for any value of M02. A cut on this shower shape axis would imply in loosing electrons signal.

Figs. 6.23 and 6.24 show the E/p distributions, for electrons and hadrons, in EG2 (E $>$ 7 GeV) for the case without and with shower shape cut, respectively. Electrons are selected using -1 $<$ TPC Nσ $<$ 3 and hadrons are the particles outside the electron band: TPC Nσ $<$ -3.5. The hadrons peak is higher in Fig. 6.23, where the shower shape cut was not used.

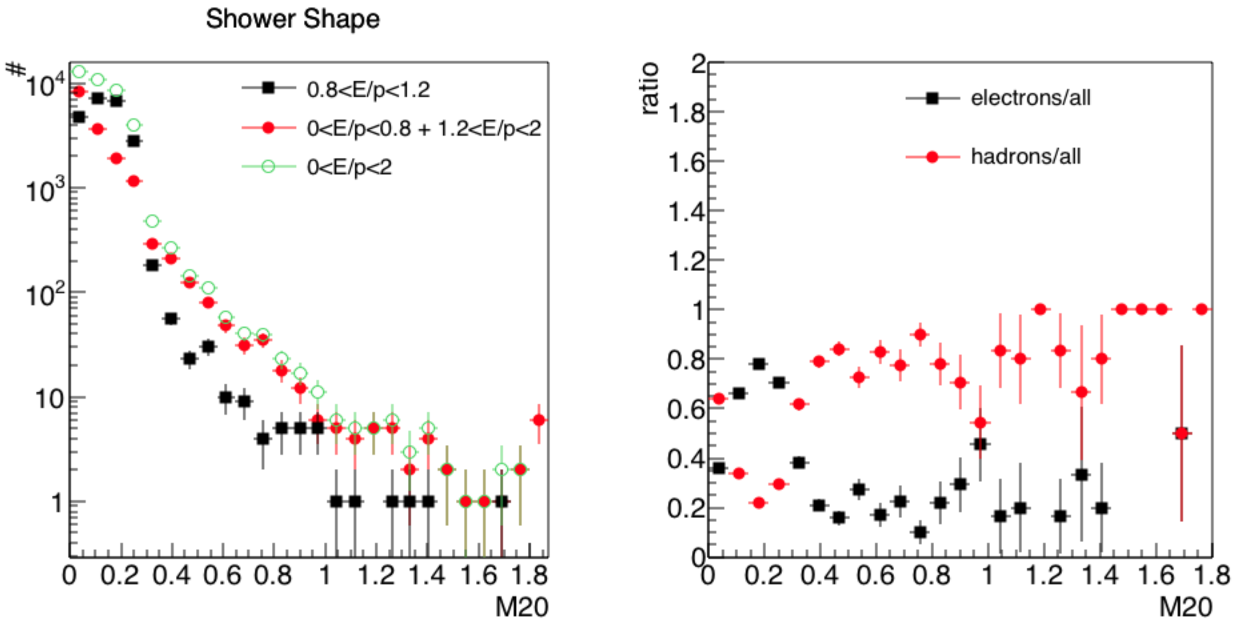

Figure 6.21: Left: shower shape distribution for the M20 for electrons and hadrons. Right: relative amount of electrons or hadrons compared to the total number of particles as a function of shower shape parameter value.

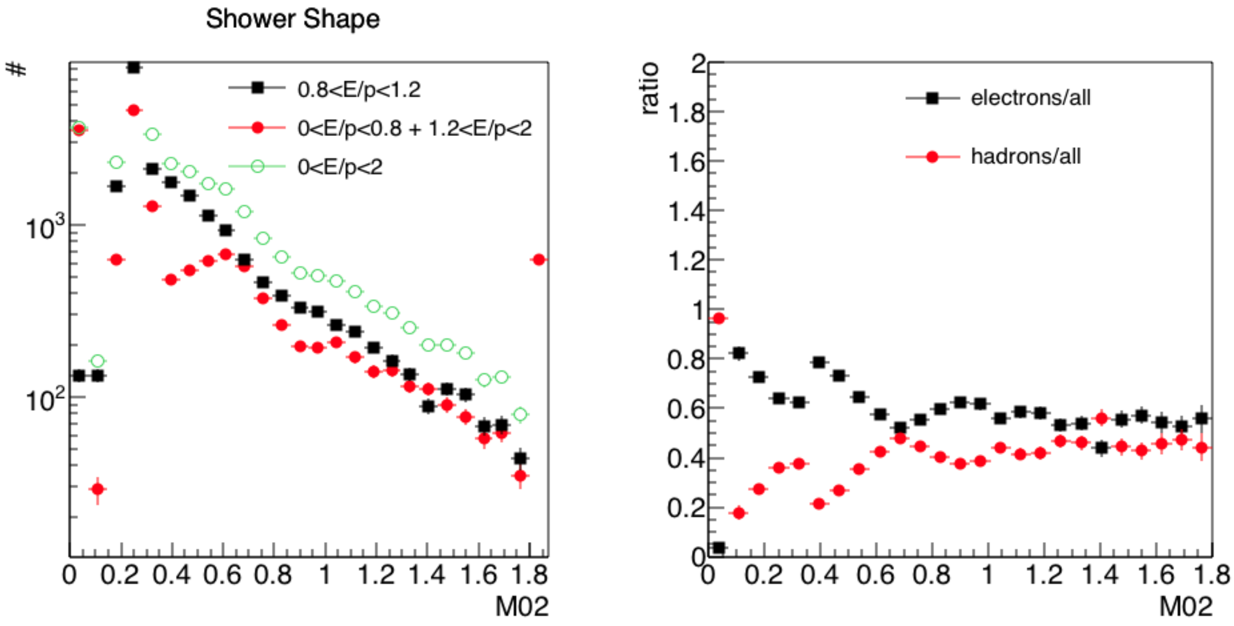

Figure 6.22: Left: shower shape distribution for the M02 for electrons and hadrons. Right: relative amount of electrons or hadrons compared to the total number of particles as a function of shower shape parameter value.

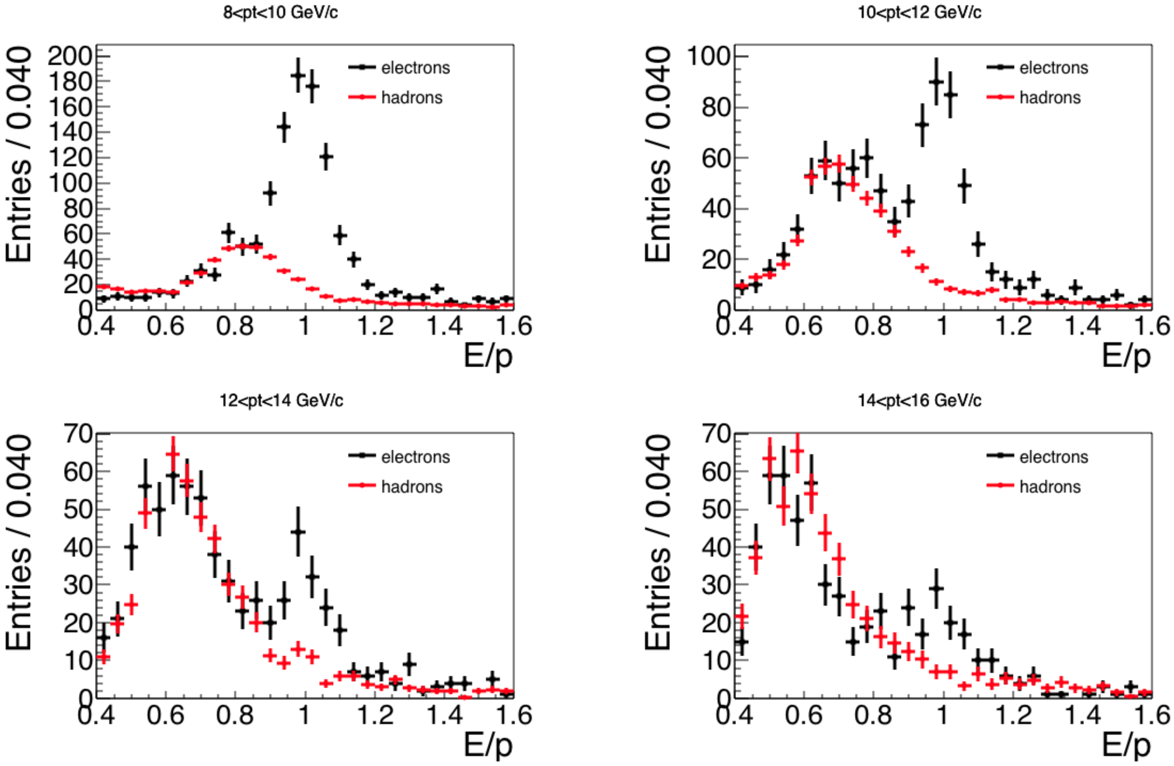

Figure 6.23: E/p distribution for 7 GeV threshold without a shower shape cut.

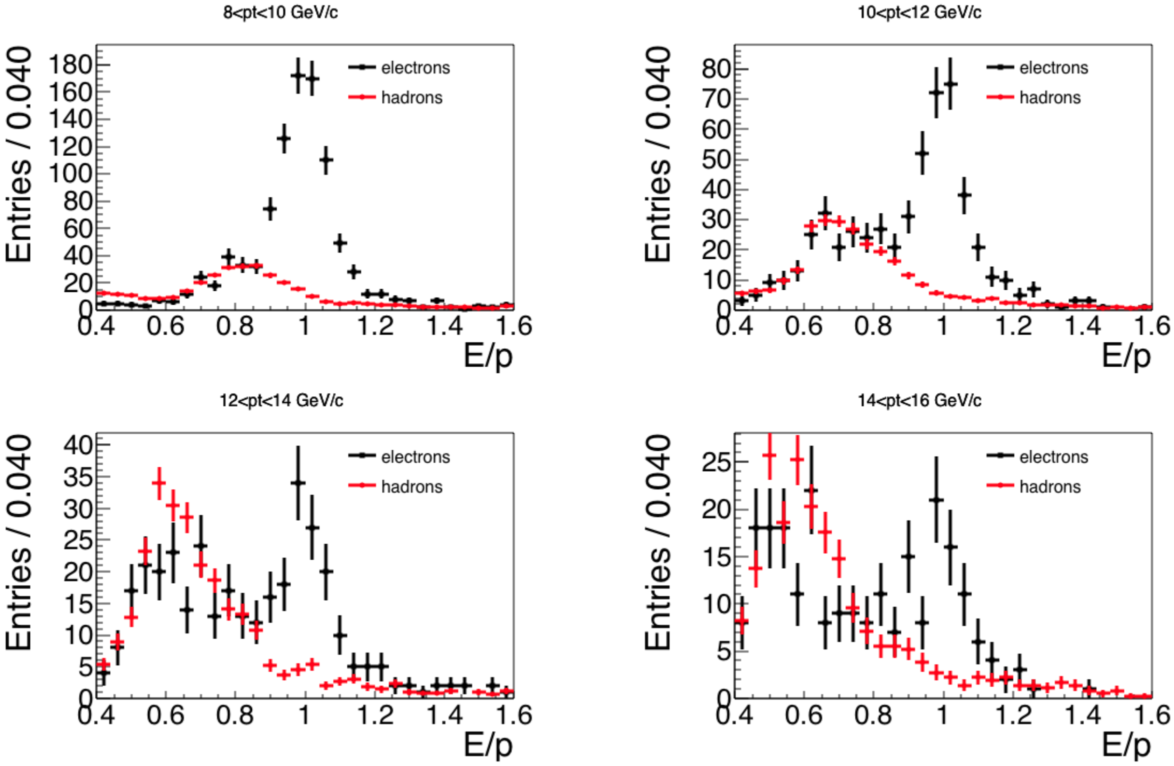

Figure 6.24: E/p distribution for 7 GeV threshold for the case where the shower shape cut (M20 < 0.3) was applied.

Figs. 6.25 and 6.26 show the E/p distributions in EG1 (E > 11 GeV) for electrons and hadrons for the case without and with shower shape cut. The case with a shower shape cut (Fig. 6.26) shows a smaller hadron contamination.

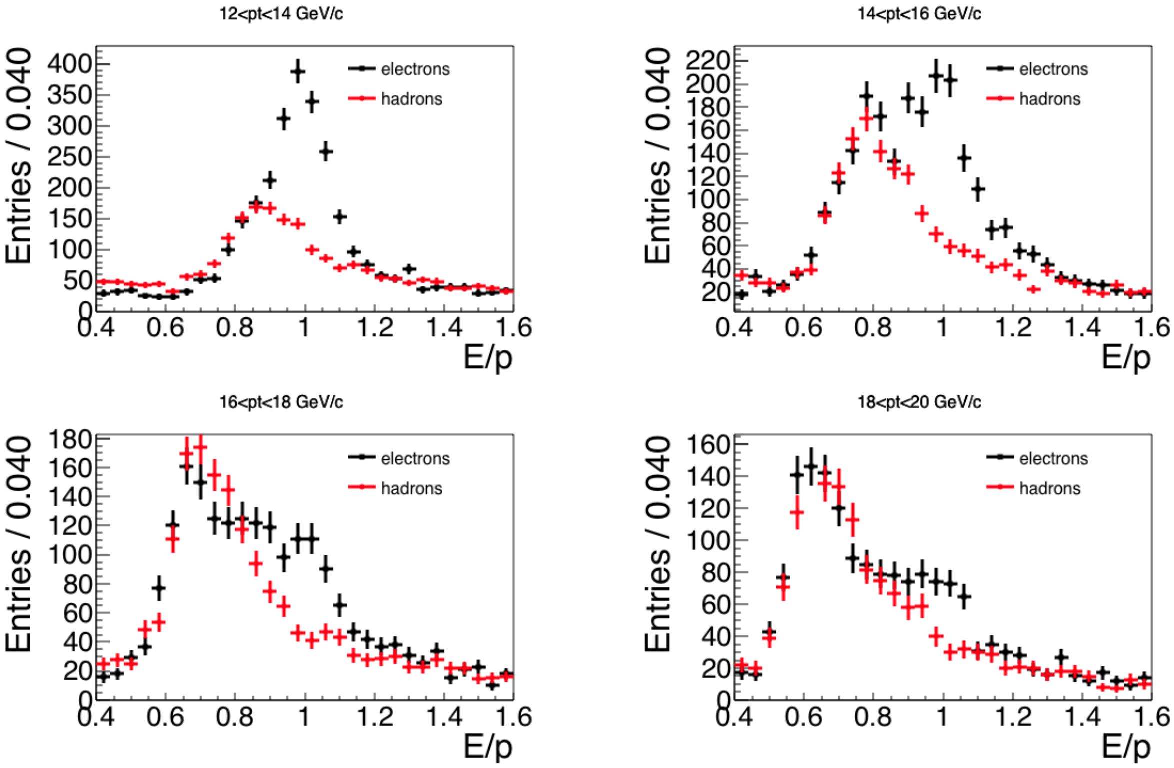

Figure 6.25: E/p distribution for 11 GeV threshold without a shower shape cut.

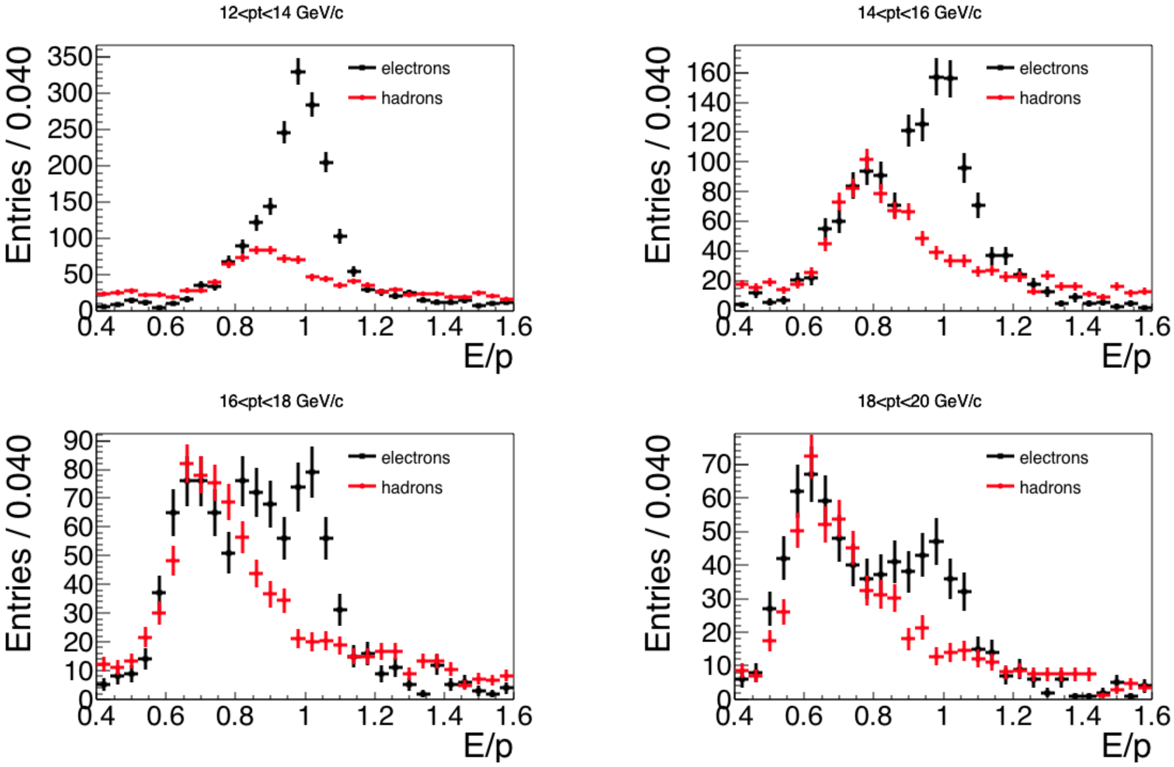

Figure 6.26: E/p distribution for 11 GeV threshold for the case where the shower shape cut (M20 $<$ 0.3) was applied.

In both trigger thresholds, after applying a shower shape cut, the hadrons peak close to the electrons peak in the E/p distribution is suppressed leading to a smaller hadron contamination in the electron sample. Besides the good efficiency of the shower shape cut (99.5% of efficiency, explained later), there are still a remaining hadron contamination that needs to be subtracted.

As in the MB analysis, we used a data driven method to subtract hadron contamination from the selected electrons. Using TPC Nσ for electrons, it is possible to select a pure sample of hadrons by requiring TPC Nσ (for electrons) smaller than -3.5. Looking to the E/p of this two types of particles, we can subtract hadrons from the E/p distribution of electron candidates.

Due to the threshold of the trigger, we have a high probability of measuring hadrons with the energy of the threshold. Thus, the E/p peak position for hadrons is p_{T} dependent, since the energy is the one of the threshold and the p_{T} is the one where we are counting the particles.

The E/p distribution for hadrons was scaled to match electrons E/p distribution in the region around the hadron peak. The expected hadron position, dependent on p_{T}, and the range of the scaling is presented in Tab. 6.2. The E/p peak position was determined calculating the E/p of a hadron with energy of the threshold and the momentum in the center of the p_{T}-bin. For example, for the threshold of 7 GeV and p_{T}-bin approximately 9 GeV/c, we have E/p = 7/9 = 0.78. Therefore, the scaling region used is 0.78 ± 0.05. After the scaling, the hadron contamination is subtracted.

Table 6.2: Range of scaling of the hadron peak

p_T (GeV/c) for 7 GeV	peak position	range of scaling
8-10	0.78	0.73-0.83
10-12	0.64	0.59-0.69
12-14	0.54	0.49-0.59
14-16	0.47	0.42-0.52
p_T (GeV/c) for 11 GeV	peak position	range of scaling
12-14	0.85	0.80-0.90
14-16	0.73	0.68-0.78
16-18	0.63	0.58-0.68
18-20	0.58	0.53-0.63

Fig. 6.27 shows the hadron contamination as a function of p_T after applying the shower shape cut.

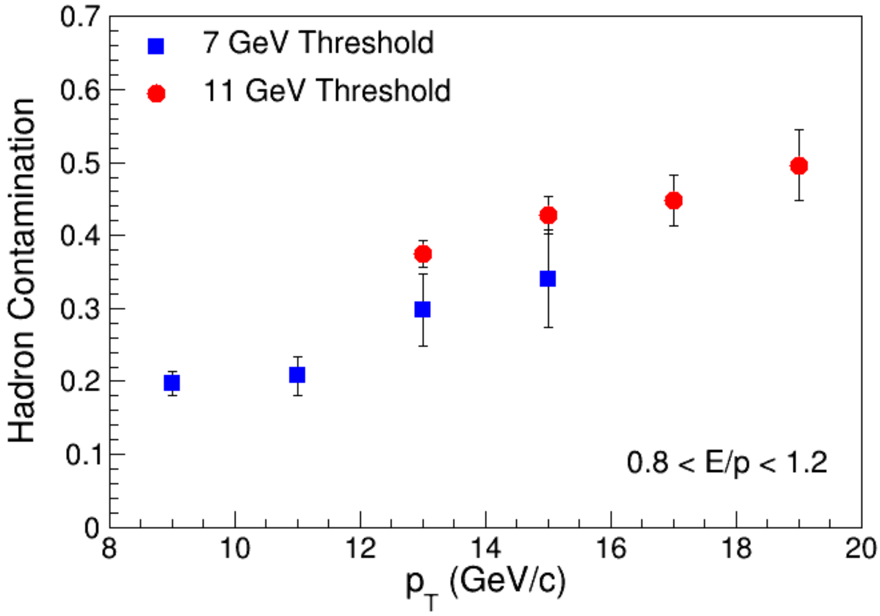

Figure 6.27: Hadron contamination as a function of p_T after applying the TPC Nσ cut and the shower shape cut. This hadron contamination was subtracted from the electrons sample.

Figs. 6.28 and 6.29 show the E/p distributions after the hadron contamination subtraction, for EGA2 and EGA1, respectively. The integral in the range $0.8 < E/p < 1.2$ in both distributions was used to calculate the efficiency of the shower shape cut by data-driven method. The efficiency is determined by the ratio of both integral (with shower shape cut, divided by the case without shower shape cut). The values are shown in Fig. 6.30 and compared with values obtained by MC simulations. Both methods are compatible and show a value of 100% for the efficiency of the shower shape cut.

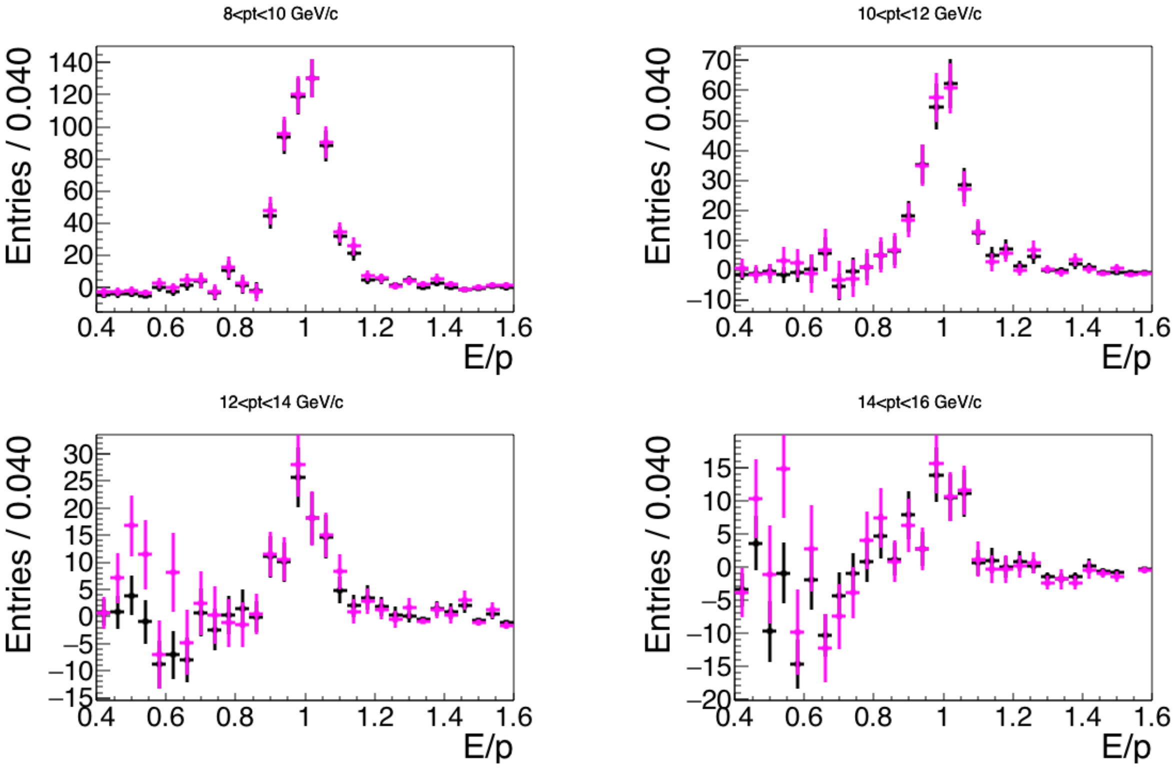

Figure 6.28: E/p distribution for 7 GeV threshold after subtraction of hadron contamination with shower shape cut (black points) and without shower shape cut (magenta points).

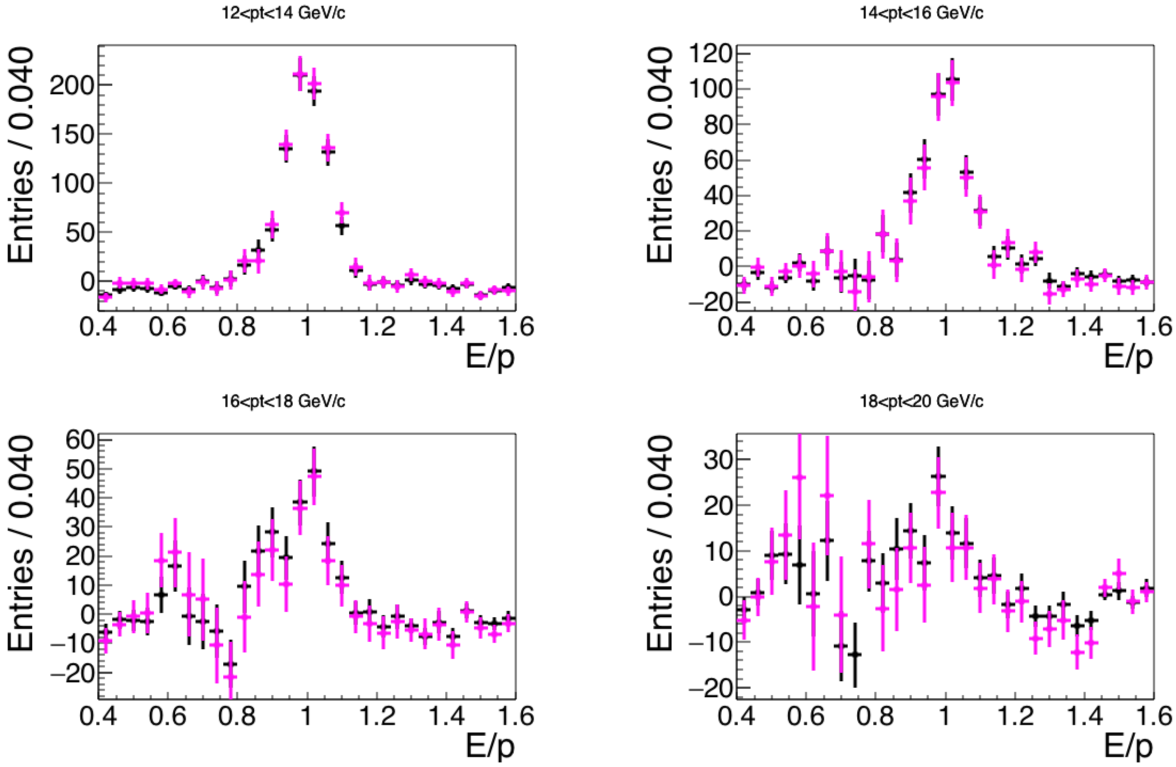

Figure 6.29: E/p distribution for 11 GeV threshold after subtraction of hadron contamination with shower shape cut (black points) and without shower shape cut (magenta points).

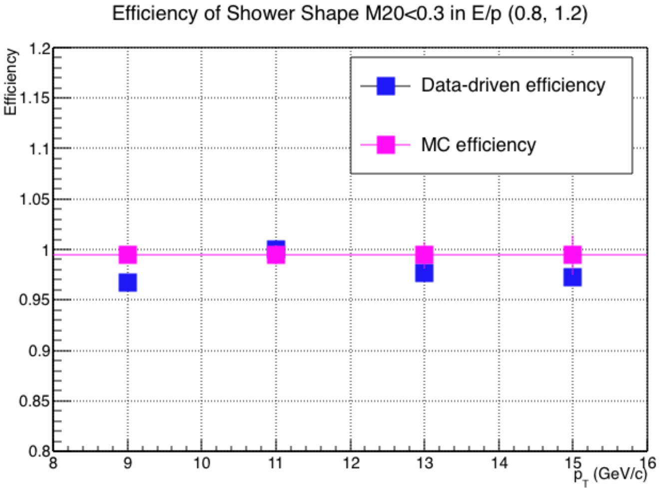

Figure 6.30: Shower shape efficiency calculated by data-drive and MC simulations. The data driven-method has a statistical uncertainty of 10%, not shown in the plot.

6.8 Background identification

The background electrons in the range of the transverse momentum of this analysis are from π^0 and η Dalitz decays, γ conversions, J/ψ, Ke_3 and W decays. As in the MB analysis, the contribution from π^0, η and γ are obtained using the invariant mass method, and the J/ψ and Ke_3 contributions are estimated using the cocktail method (described in Sec. 5.7). The difference in this triggered analysis to the MB one is that in this case the W contribution is not negligible and was determined using POWHEG [188] simulations.

For the invariant mass method, the cuts applied in the selection of the associated particle are the same as in the MB analysis, listed in Tab. 5.3.

Fig. 6.31 shows the invariant mass distribution for ULS and LS pairs for both thresholds. The ULS and LS p_T spectra are obtained for the tracks with $m < 0.15$ GeV/c^2.

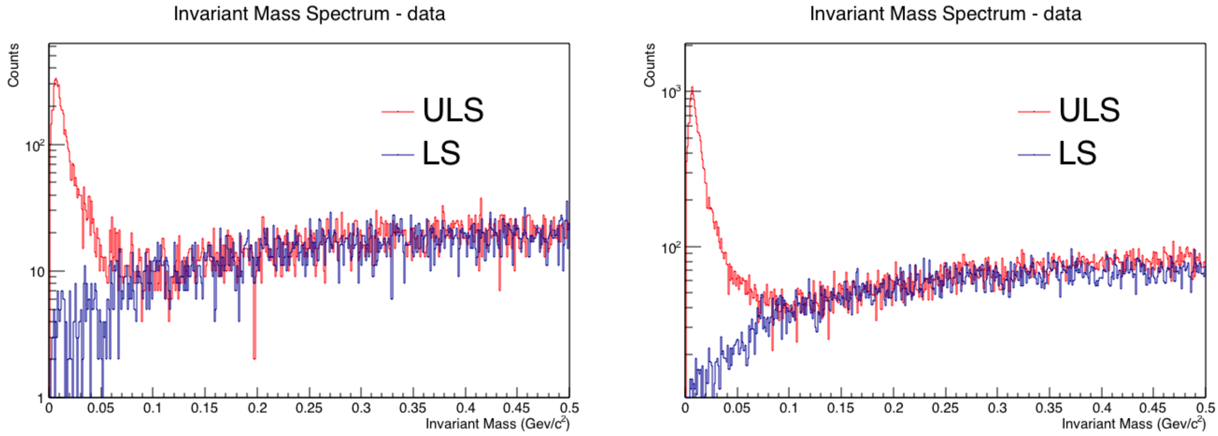

Figure 6.31: Invariant mass spectrum for the 7 GeV threshold (left) and 11 GeV threshold (right).

The yield as a function of p_T for inclusive electrons, ULS background and LS combinatorial background are shown in Fig. 6.32. The background is obtained by subtracting LS from ULS distributions.

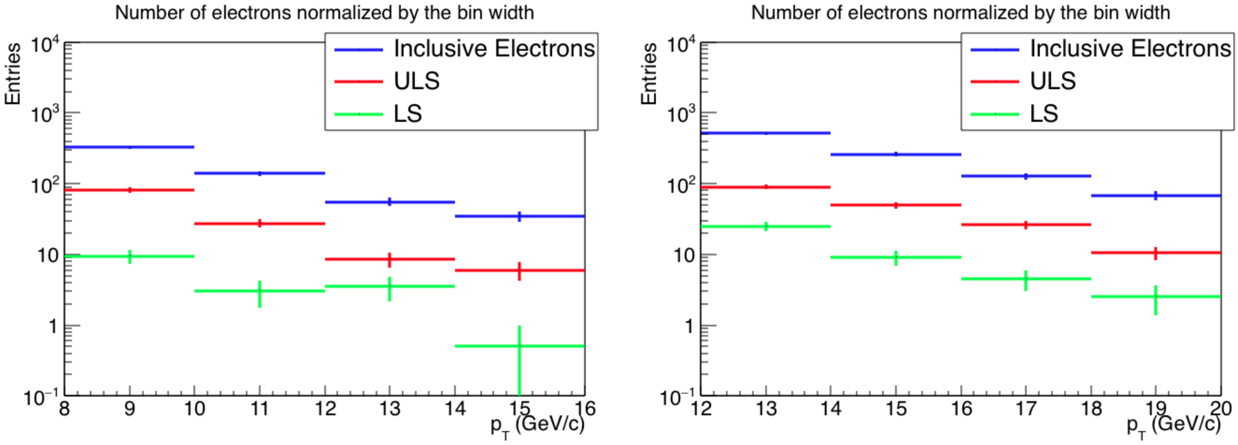

Figure 6.32: Inclusive electrons and the background contribution determined using an invariant mass method for the 7 GeV threshold (left) and 11 GeV threshold (right).

The spectrum of electrons coming from J/ψ and Ke_3 are shown in the Fig. 6.33 compared to the HFE spectrum. J/ψ and Ke_3 were obtained using the cocktail method [79]. The procedure to obtain the HFE invariant yield is similar to the one in MB analysis, with an additional correction, due to the trigger usage, as will be explained in the next sections.

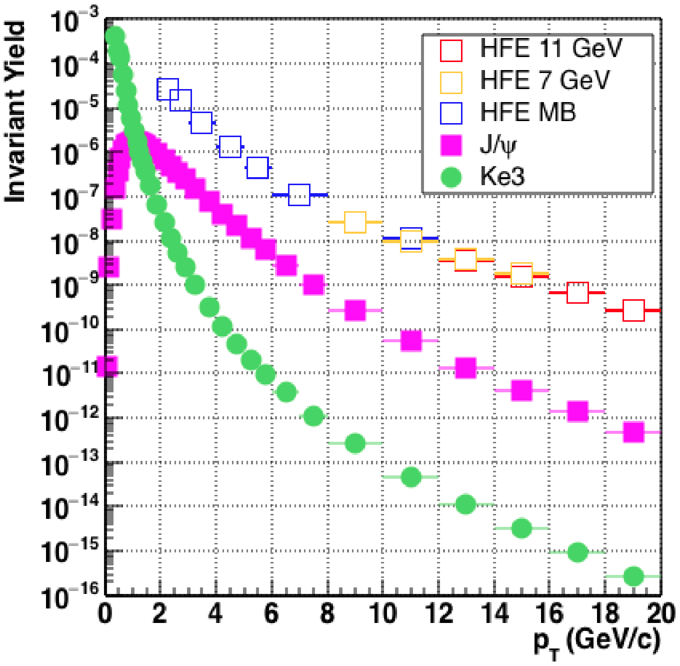

Figure 6.33: Other electrons sources that are not included in the invariant mass method.

Tab. 6.3 and 6.4 summarise the contribution of this sources for 7 GeV and 11 GeV EMCal thresholds respectively. Ke_3 contribution is negligible and J/ψ contribution is 1% for the first p_{T} bin and 0.2% for the last p_{T}. This contribution is subtracted from the HFE spectrum.

Table 6.3: J/ψ and Ke_3 contributions for the spectrum obtained for 7 GeV threshold

p_{T} range (GeV/c	J/ψ / HFE	ke_3 / HFE
$8 < p_{\mathrm{T}} < 10$	0.01	0.00001
$10 < p_{\mathrm{T}} < 12$	0.006	0.000005
$12 < p_{\mathrm{T}} < 14$	0.003	0.000003
$14 < p_{\mathrm{T}} < 16$	0.002	0.000002

Table 6.4: J/Ψ and Ke_3 distributions for the spectrum obtained for 11 GeV threshold

p_{T} range (GeV/c)	J/ψ / HFE	ke_3 / HFE
$12 < p_{\mathrm{T}} < 14$	0.004	0.000003
$14 < p_{\mathrm{T}} < 16$	0.003	0.000002
$16 < p_{\mathrm{T}} < 18$	0.002	0.000001
$18 < p_{\mathrm{T}} < 20$	0.002	0.000001

For the W decays contributions in p-Pb, a POWHEG simulation was done by a researcher from Laboratori Nazionali di Frascati (LNF) [189].

Fig. 6.34 shows the comparison of the simulated p_T distribution of electrons from heavy-flavour and electrons from W, in mid-rapidity and forward rapidity. The shape of the spectra are very different for electrons from heavy-flavour hadron decays and electrons from W, and the W contribution increases with p_T.

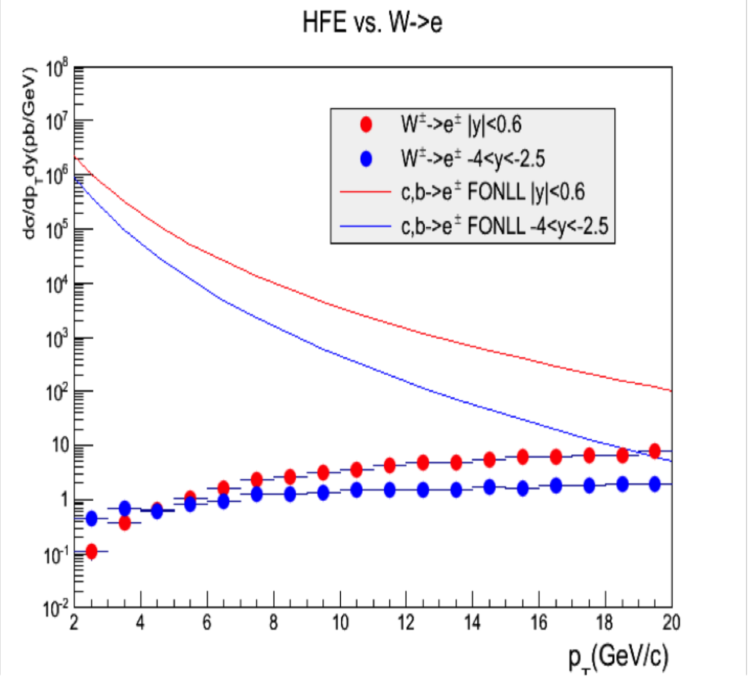

Figure 6.34: W→ e cross section p_T distribution compared to the electrons from heavy-flavour hadron decays distribution. Figure from [189].

The simulations were validated with a comparison to CMS data, and the results are shown in Fig. 6.35.

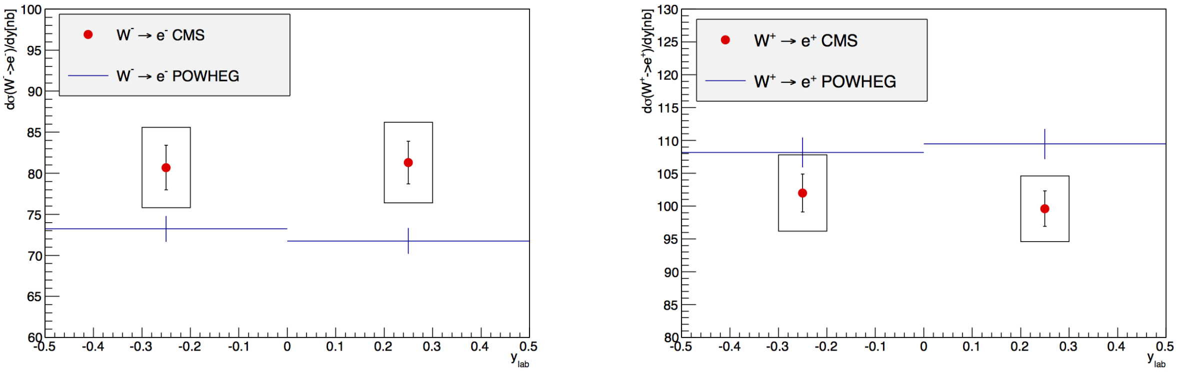

Figure 6.35: W→ e cross section from POWHEG simulations and from CMS results for $W^- \to e^-$ (left) and $W^+ \to e^+$ (right). Figure from [189].

Bellow is presented the summary of the differences between CMS results and the POWHEG simulations:

- $W^+ \to e^+$: 108.8 (POWHEG) / 100.62 (CMS) = 1.08

- $W^- \rightarrow e^-$: 81.0 (CMS) / 72.48 (POWHEG) = 1.1

The 10% difference between data and POWHEG is used as systematic uncertainty. The W contribution on the HFE level is around 3%, which results in a systematic effect of 0.3% at 18< p_{T} <20 GeV/c.

After validating the POWHEG simulation, the obtained electron spectrum as a function of p_{T} was subtracted from the HFE spectrum. The comparison of W contribution and HFE spectrum is shown in Fig. 6.36, as a function of p_{T}. Tabs. 6.5 and 6.6 summarise the contribution of W for 7 GeV and 11 GeV EMCal thresholds, respectively.

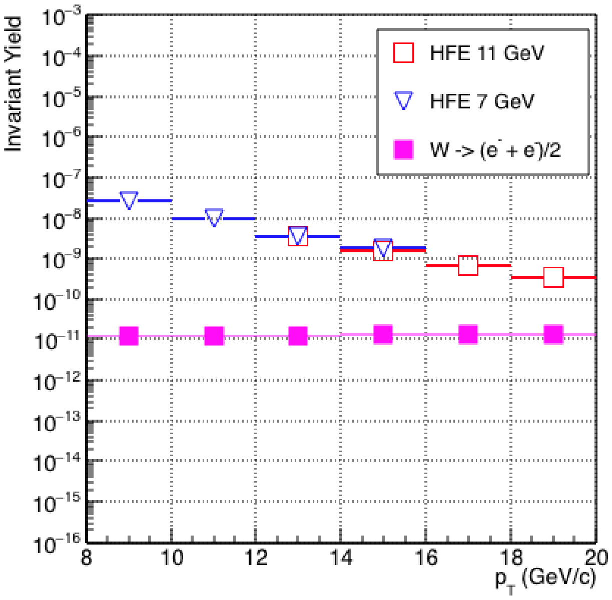

Figure 6.36: W decays to electrons.

Table 6.5: W contribution for the HFE spectrum at 7 GeV

p_{T} range (GeV/c)	W $->e^- + e^-$ / HFE
$8 < p_{\mathrm{T}} < 10$	0.000375
$10 < p_{\mathrm{T}} < 12$	0.000986
$12 < p_{\mathrm{T}} < 14$	0.002675
$14 < p_{\mathrm{T}} < 16$	0.005341

Table 6.6: W contribution for the HFE spectrum at 11 GeV

p_{T} range (GeV/c)	W $->e^- + e^-$ / HFE
$12 < p_{\mathrm{T}} < 14$	0.002709
$14 < p_{\mathrm{T}} < 16$	0.006390
$16 < p_{\mathrm{T}} < 18$	0.015266
$18 < p_{\mathrm{T}} < 20$	0.028286

6.9 Efficiency correction

The efficiency corrections were calculated using two different MC productions: the one used in the MB analysis (called MC1) and another one, produced anchored[1] in the runs where the EGA trigger was used (called MC2). The production of the MB analysis (MC1) was used to cross check some of the results obtained with the dedicated production for the triggered data (MC2). The main difference between this two MC production is that the MC1 has electrons enhancement, which helps with the determination of the electrons identification efficiency, while the MC2 has π^0 and η enhancement, which increases the statistics of background electrons leading to a more precise efficiency determination for the background corrections.

For the MC production, the same runs listed for data were used in the MC2, since this is a production anchored in the triggered data.

6.9.1 Electron identification in MC

The electron identification in MC have to follow the same strategy as in data, since the intention of the MC studies is to determine the efficiency of the electrons reconstruction and identification. Then, in this section we show comparison of data and MC, which is a validation of the MC samples.

The Fig. 6.37 shows mean and standard deviation of the TPC Nσ for electrons, in the MC productions MC1 (shown as “d3” in the plot) and MC2 (shown as “b3a”, “b3b” and “b3c”, which corresponds to three different data taking (13d, 13e and 13f), but all with the EGA trigger). The gaussian fit were performed as shown in data (e.g. Fig. 6.15). Considering that the MC productions are used to correct the data for the efficiencies, it is important to verify if the MC production reproduce the data. One of the investigations that need to be done is the mean and standard deviation of the TPC Nσ, where we expect consistent parameters of the fit for data and MC. If this condition is not satisfied, calibrations are necessary.

Since we are looking the TPC Nσ for electrons, we expect to see, in Fig. 6.37, the distribution centered at zero with standard deviation equal one. This condition is satisfied in low p_{T}, but we start to see a deviation for higher values of p_{T}. This happens because the hadron contamination is higher in high p_{T} and the electrons gaussian start to be more

---

[1] This means that this production used each run of data to simulate the detectors with the same conditions that they had in the data taking.

affected by the pions distribution. Then, the performed fit is not really reliable. To confirm this statement, we used an E/p cut before looking the TPC Nσ, since using an E/p cut the hadron contamination is smaller, and we fit the distributions again, for the production MC1 (MB production, called as "d3" in the plot), which is the production with enhancement of electrons and the statistics for the fits are higher. In the Fig. 6.37 we can see the "d3" results (where no E/p was used) and "d3 after E/p cut" (where the E/p cut was used) and the mean and standard deviation for the later case are closer to zero and one respectively.

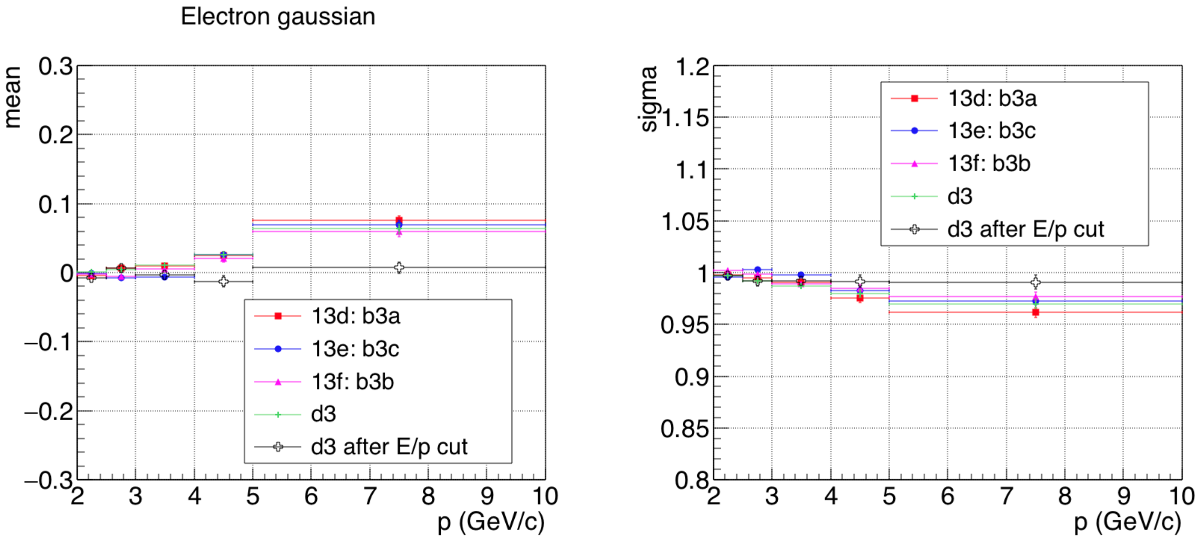

Figure 6.37: Electrons fit results on the TPC Nσ distribution for MC simulations: left plot shows the mean of the electron gaussian and the right plot shows its sigma.

Another important control check is the comparison of the E/p distribution between data and MC. For the reason that the MC productions are used to correct the electron spectrum for the EMCal efficiency, it is important to evaluate if the MC reproduce the data, having similar mean and standard deviations.

Fig. 6.38 and Fig. 6.39 show the E/p distribution in data and MC1 production, for the 7 and 11 GeV thresholds, respectively, after subtracting the hadron contamination.

Fig. 6.40 and Fig. 6.41 show the E/p distribution comparison between data and the MC production of MC2 for the 7 and 11 GeV threshold, respectively.

A Crystal Ball fit, which is a gaussian with power low tail, was performed in the E/p distributions, in data and MC, as it was done in MB analysis (see Sec. 5.8.2).

Figs. 6.42 and 6.43 show the comparison between data and MC fit results of the mean and standard deviation (sigma, σ), respectively for both MC productions, obtained using the Crystal Ball fit. The fit parameters are presented in the App. C. The comparisons were done after subtracting hadron contamination in data.

The sample MC2 shows a better agreement with data than the sample MC1. This can be seen comparing the mean and sigma in the Figs. 6.42 and 6.43, where MC2 are closer to

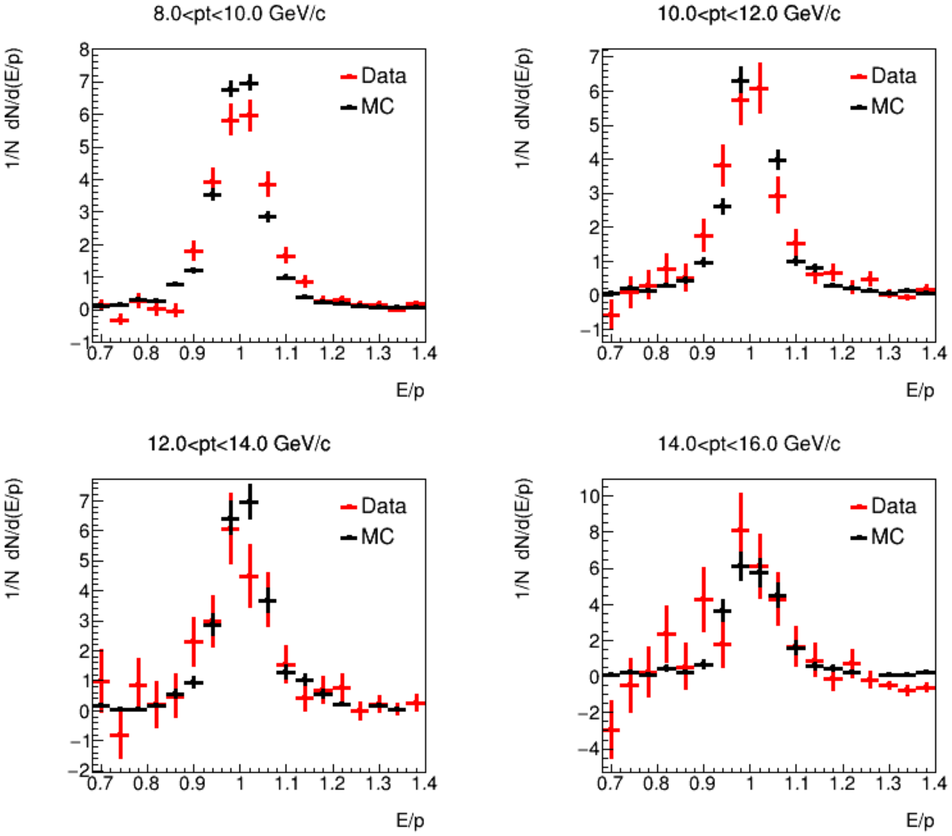

Figure 6.38: Comparison of E/p distribution for the 7 GeV threshold for MC1.

data than MC1.

The difference found for MC2 is reflected in systematic uncertainties in the final result, when we variate the E/p cuts.

The production used in the end is the MC2, which has a better agreement with the data. However, the comparison with MC1 were necessary in order to check if there is a bias due to the enhancement of π^0 and η in the MC2 production.

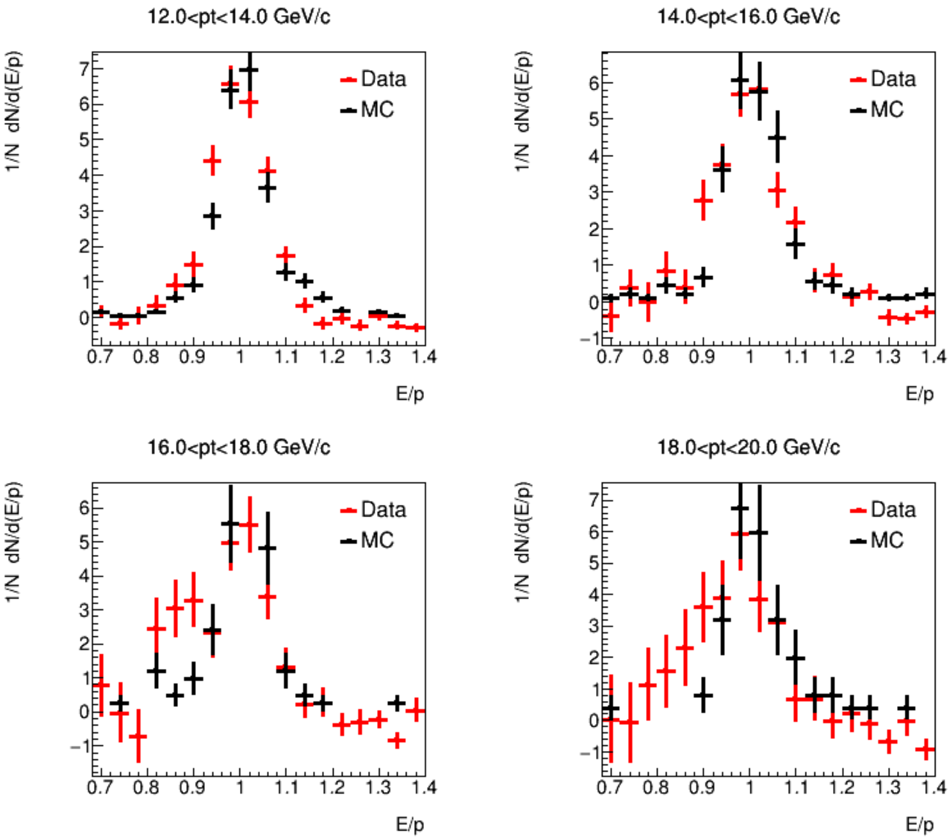

Figure 6.39: Comparison of E/p distribution for the 11 GeV threshold for MC1.

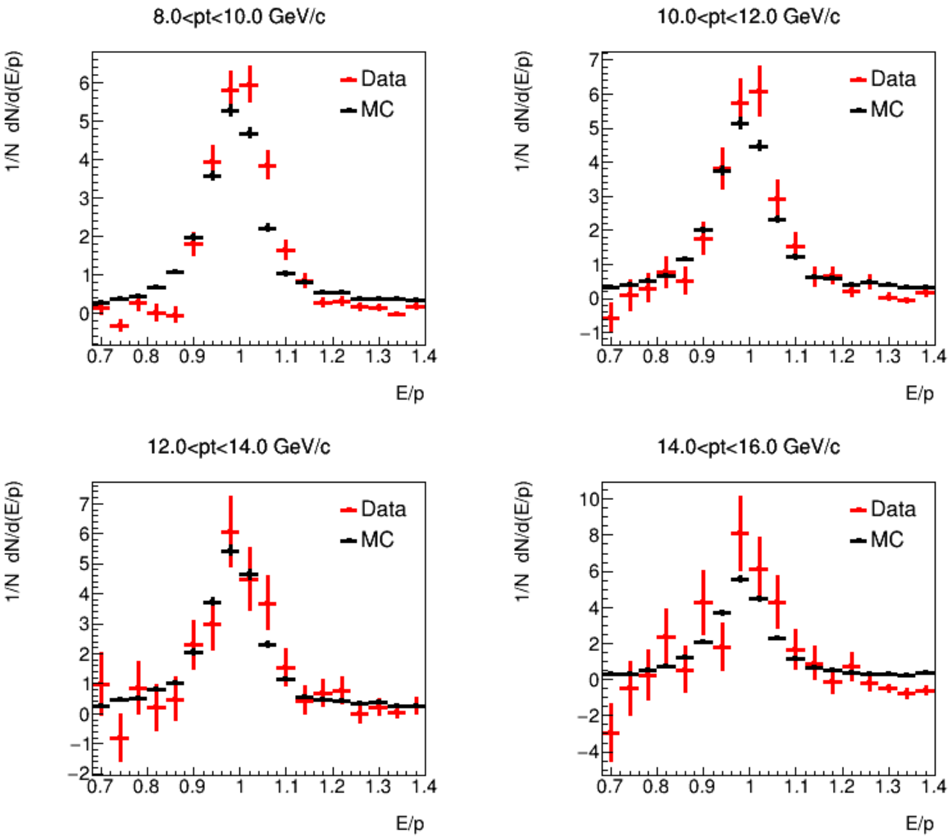

Figure 6.40: Comparison of E/p distribution for the 7 GeV threshold for MC2.

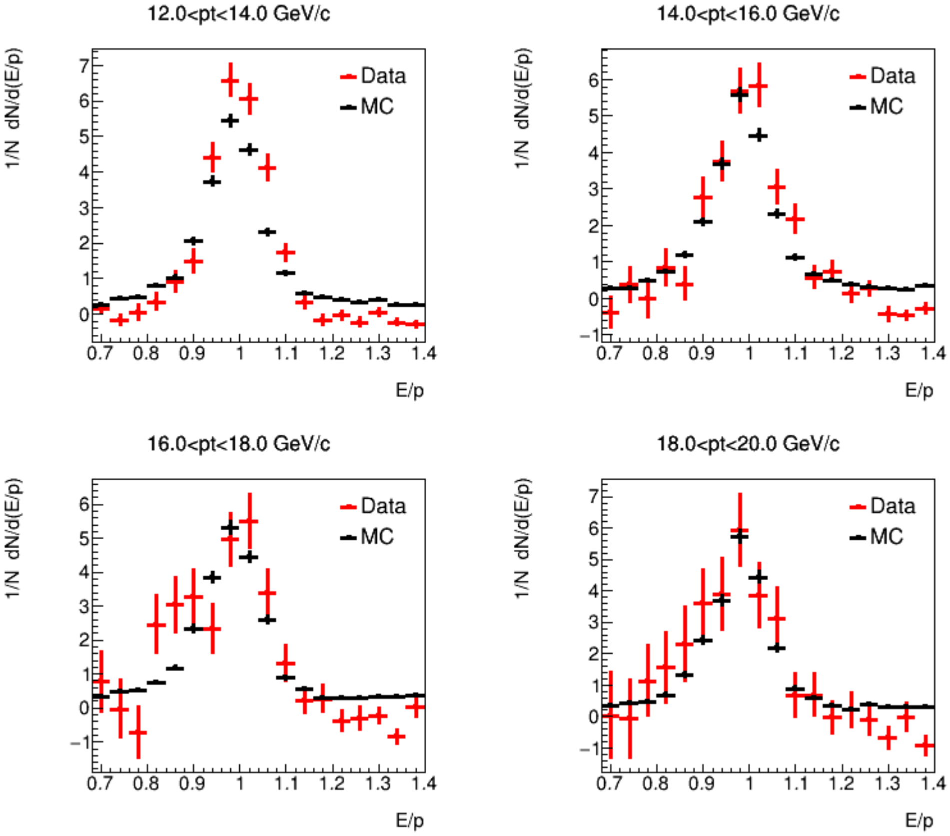

Figure 6.41: Comparison of E/p distribution for the 11 GeV threshold for MC2.

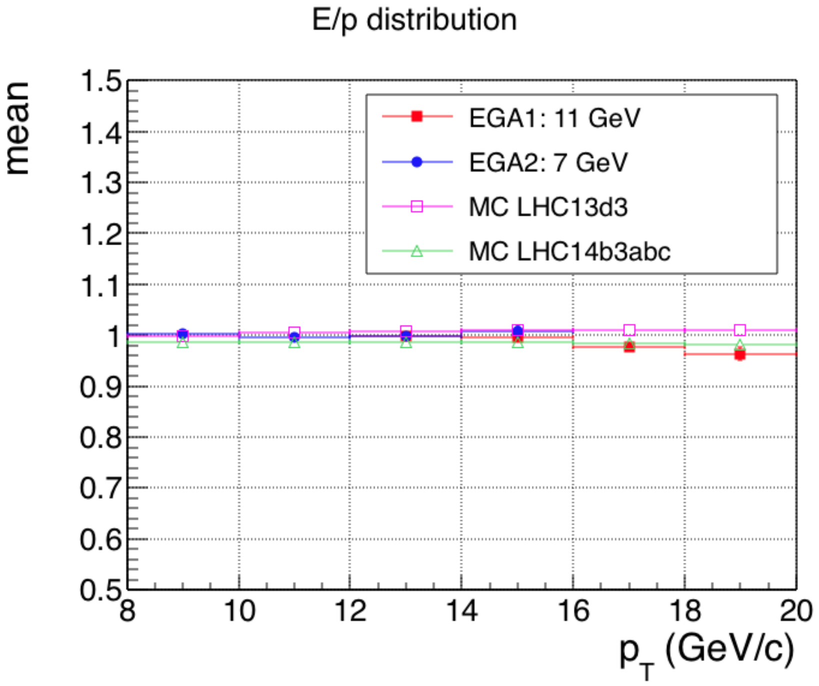

Figure 6.42: Mean of a crystal ball fit in the E/p for data and MC for the 7 GeV and 11 GeV thresholds and for MC1 (LHC13d3) and MC2 (LHC14b3abc).

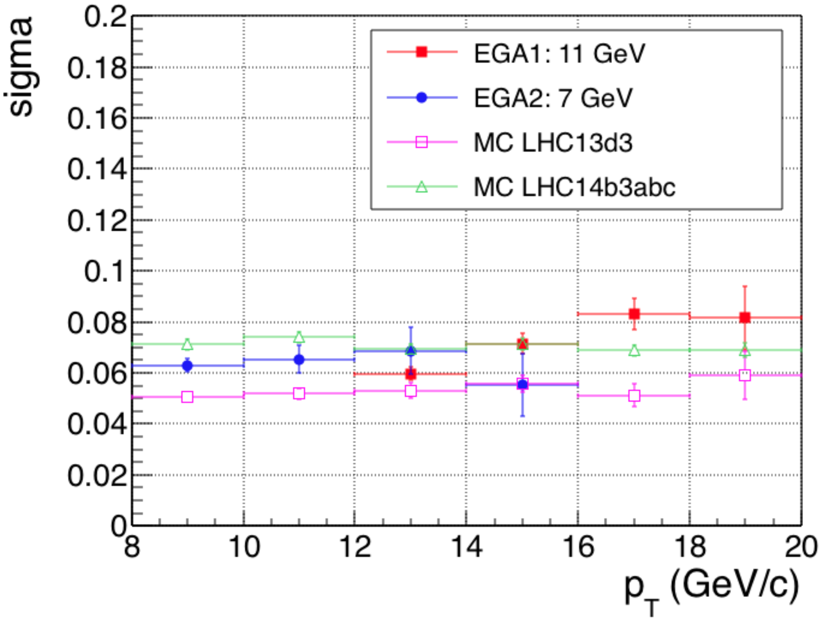

Figure 6.43: Sigma of a crystal ball fit in the E/p for data and MC for the 7 GeV and 11 GeV thresholds and for MC1 (LHC13d3) and MC2 (LHC14b3abc).

6.9.2 Background identification efficiency

The MC production used has η and π^0 enhancement in order to improve the determination of the efficiency of finding pairs of electrons and positrons generated by these particles. Due to the enhancement, the shape of η and π^0 spectra in MC is different from data. Then, to calculate the efficiency, corrections are necessary, as explained in Sec. 5.8.3.

Fig. 6.44 shows the results in data and MC for η and π^0, where $\pi^0 = (\pi^+ + \pi^-)/2$ and η was obtained from m_T-scaling of π^0. The data spectra are the same used in MB analysis.

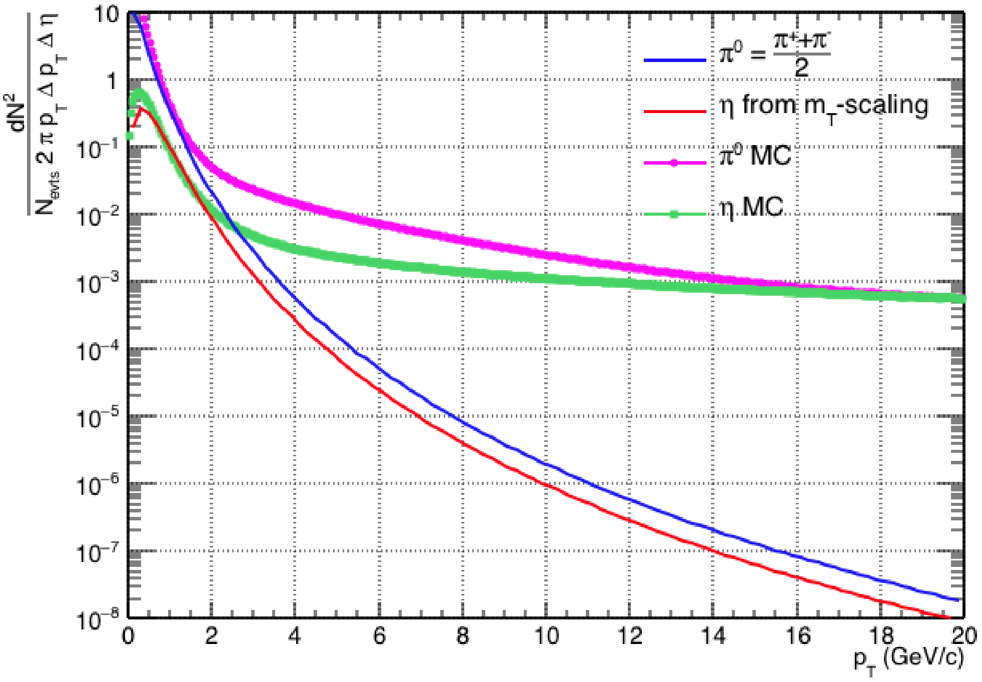

Figure 6.44: π^0 and η spectra in data ($\pi^0 = (\pi^+ + \pi^-)/2$ and η from m_T-scaling of π^0) and MC.

The weights are presented in Fig. 6.45 and it is a function of η or π^0 p_{T}. For all electrons coming from η or π^0, the weights were applied in their p_{T} values, according to the mother or grandmother p_{T}.

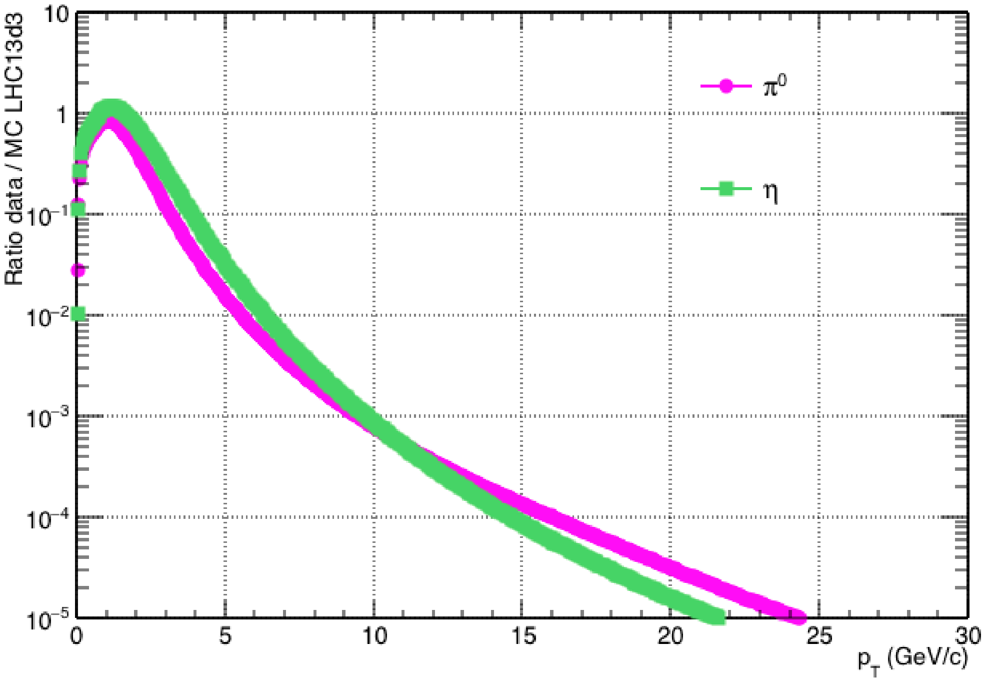

Figure 6.45: Weights for π^0 and η.

Fig. 6.46 shows the efficiency of finding pairs for the simulated data (MC2) compared to the MB efficiency (MC1). Applying the weights, the efficiency becomes compatible with the MB data, as it is expected. This comparison of MC1 and MC2 for the efficiency of finding pairs is a validation of the weights applied. It is clear that the production MC1, without weights, does not have a good statistics for high-p_{T}, justifying the requirement of a sample with π^0 and η enhancement.

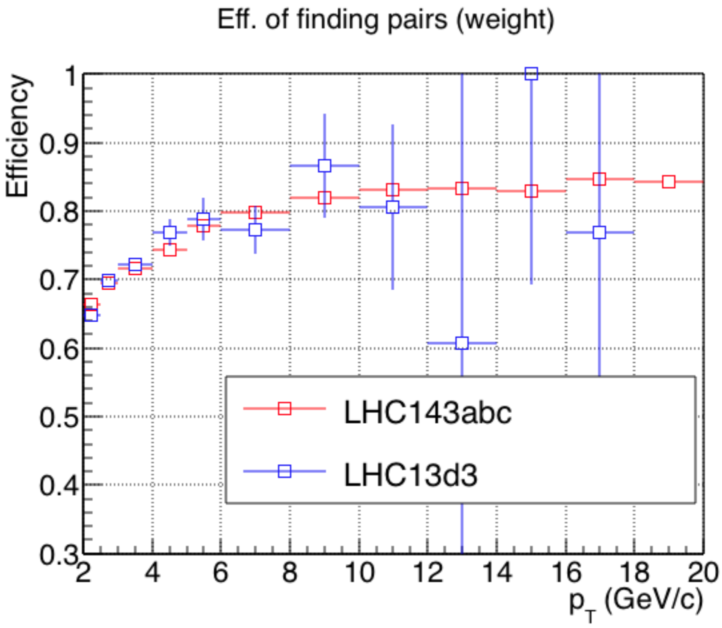

Figure 6.46: Efficiency of finding pairs with weights: Compatible with MB results (MC1).

The efficiency with weights is used to correct the electrons background. Figs. 6.47 and 6.48 show the comparison of the inclusive electrons and the background before and after applying the efficiency correction of finding pairs (top), and the inclusive electrons divided by the background, after correcting the background for the efficiency of finding pairs (bottom). From these plots, it is possible to see that the signal (inclusive minus background), in the worst case, is around 3 times the background. Then, the corrected background is subtracted from the inclusive electrons.

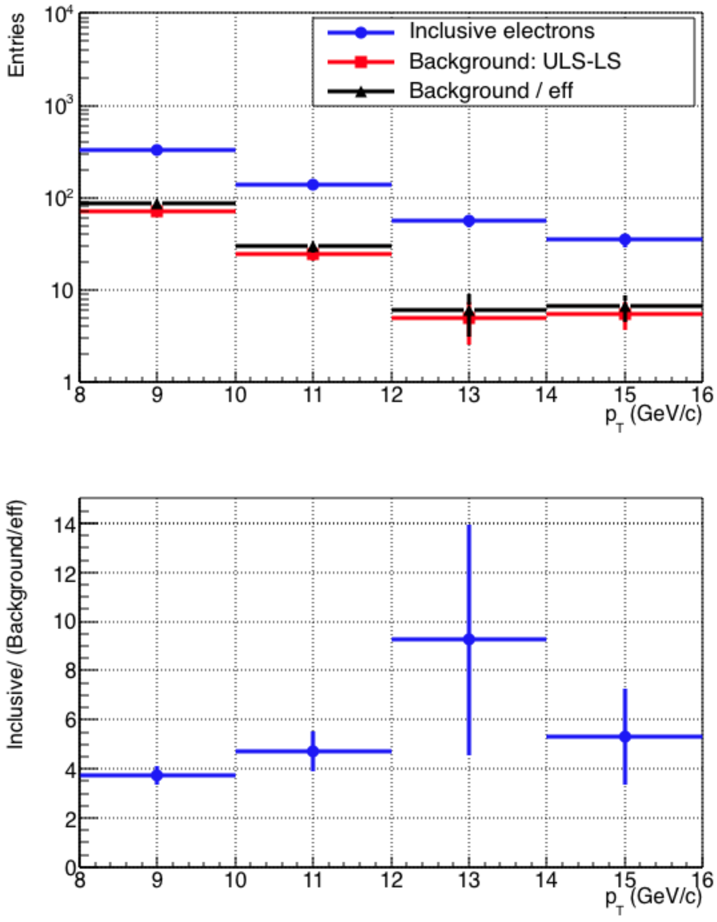

Figure 6.47: Top: inclusive electrons and the background before and after the efficiency correction. Bottom: inclusive electrons divided by the background corrected for the efficiency of finding pairs. Plots for the EGA2 (7 GeV threshold).

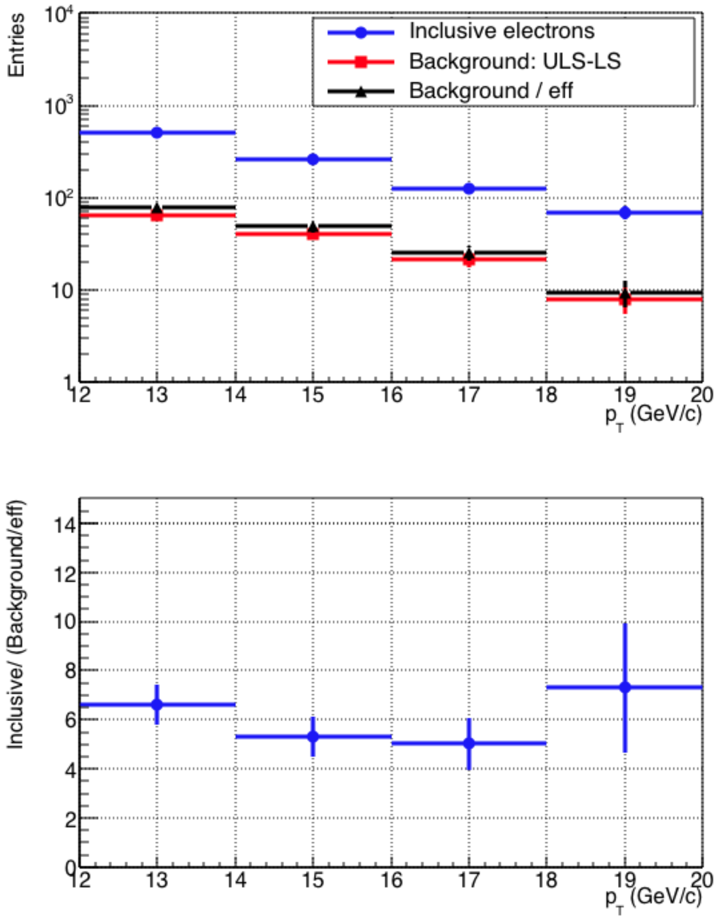

Figure 6.48: Top: inclusive electrons and the background before and after the efficiency correction. Bottom: inclusive electrons divided by the background corrected for the efficiency of finding pairs. Plots for the EGA1 (11 GeV threshold).

6.9.3 Electron reconstruction and identification efficiencies

In this section we present the efficiency correction used to obtain the final HFE spectrum. After subtracting the background from the inclusive spectrum, it is necessary to correct the spectrum for the efficiency of track reconstruction, for the efficiency of PID from TPC and EMCal and for the detectors acceptance, as it was done in the MB analysis (See Sec. 5.8.4). These efficiencies once combined is the total efficiency of electron reconstruction, which is shown in Fig. 6.52 as a function of p_T.

Unfolding corrections on the spectrum was performed using the ratio of p_{T} reconstructed and the true p_{T} from MC, as it was done in MB analysis. We have also checked the unfolding [190] using the response matrix calculated by AliCFUnfolding, available in AliRoot. This comparison is done as a validation of the simple method used in this analysis, as it was done in MB analysis.

Fig. 6.49 shows the correlation matrix between the p_{T} reconstructed and true p_{T}. We have applied the AliCFUnfolding on our result, as a method to unfolding and we have compared with our method. Fig. 6.51 and Fig. 6.50 show the comparison of the electrons spectra using each of the unfolding methods for the 7 and 11 GeV thresholds, respectively. The electrons spectra obtained in both methods are consistent.

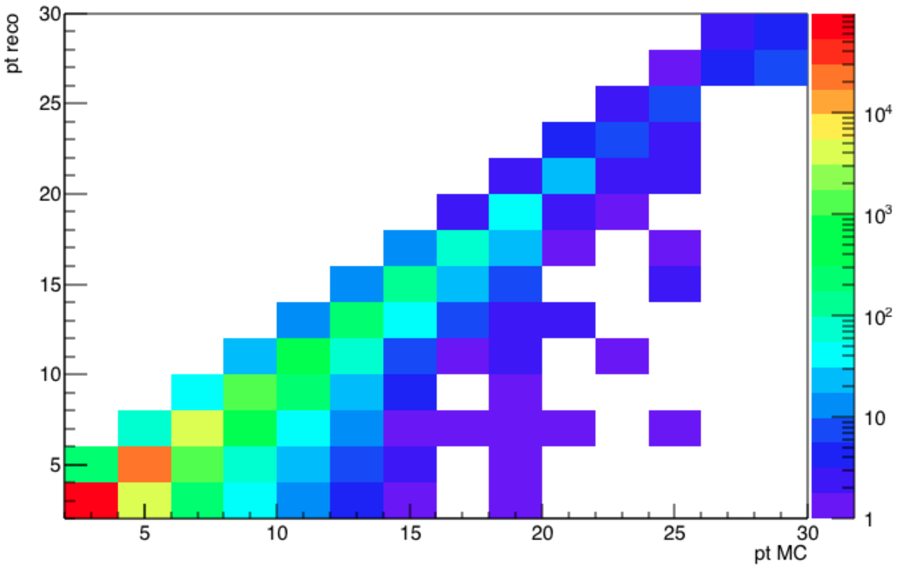

Figure 6.49: Correlation matrix between the p_T reconstructed and true p_T.

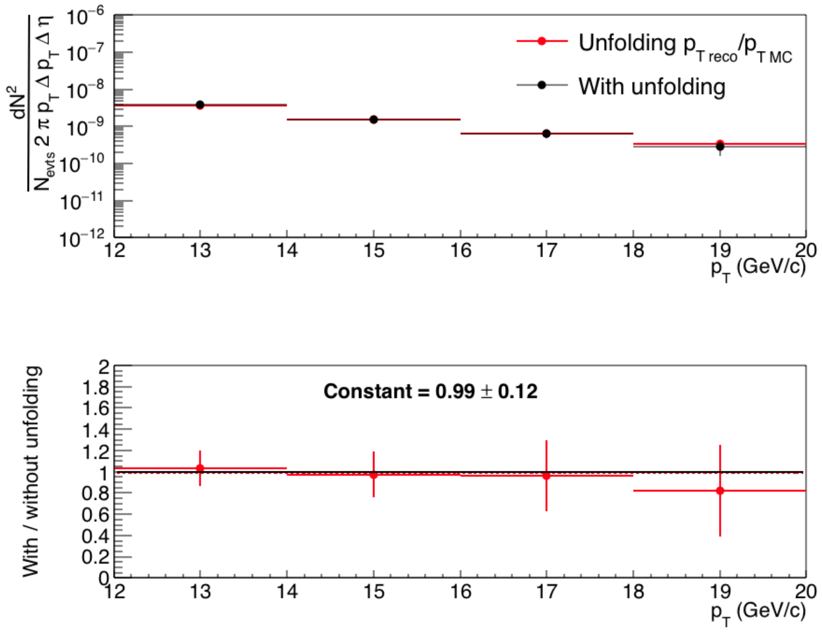

Figure 6.50: Comparison of two unfolding methods to the spectrum at 7 GeV: efficiency calculated using "p_T reconstructed over true p_T" and with unfolding using the AliCFUnfolding.

Fig. 6.53 shows the EMCal PID efficiency and Fig. 6.54 shows the TPC PID efficiency.

The EMCal PID efficiency is the ratio of the electron spectrum that passes the selection $0.8 < E/p < 1.2$ and the electrons before this selection, as in MB analysis. For $p_T > 10$ GeV/c the efficiency is around 80%, compatible with the MB analysis.

The TPC efficiency is calculated using as the numerator, the integral of the electrons

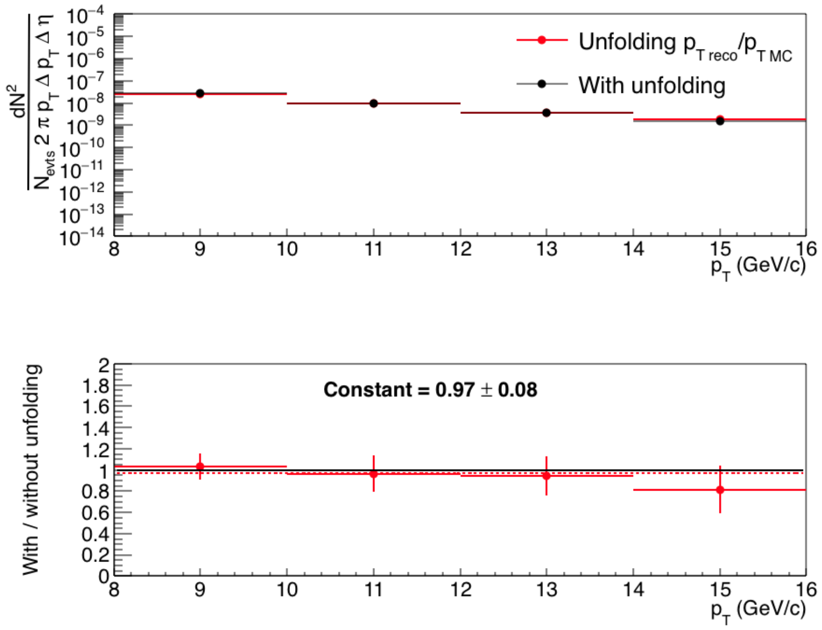

Figure 6.51: Comparison of two unfolding methods to the spectrum at 11 GeV: efficiency calculated using “p_{T} reconstructed over true p_{T}” and with unfolding using the AliCFUnfolding.

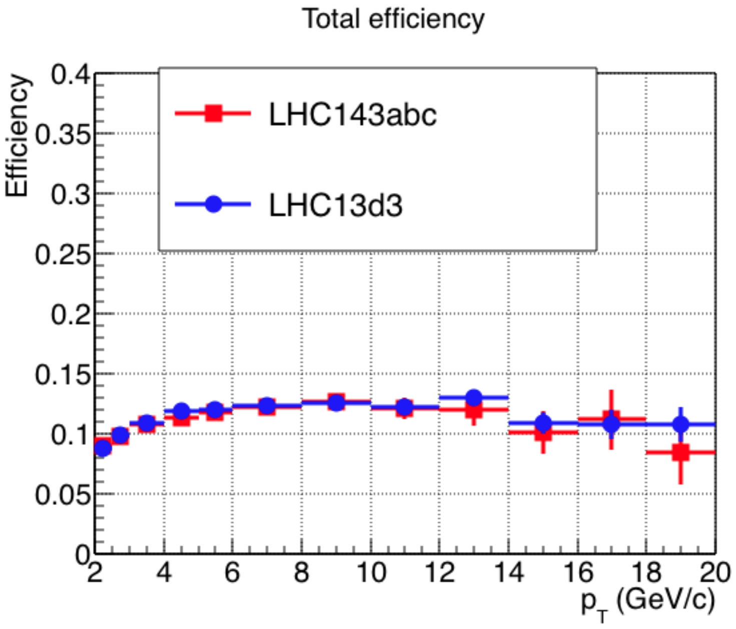

Figure 6.52: Total efficiency of finding electrons including the EMCal acceptance ($\Delta\phi = 100$ degrees and -0.6 < η <0.6).

gaussian in the range $-1 <$ TPC N$\sigma < 3$ and as the denominator, the integral in the range $-3 <$ TPC N$\sigma < 3$. Since the same cut is used as in the MB analysis, the result of the efficiency is 84%, as in the MB analysis.

Fig. 6.55 shows the EMCal track-matching efficiency already including the EMCal acceptance. As explained in the Sec. 5.8.4, the track-match efficiency, which corresponds to the tracks from TPC matched with clusters from EMCal, is calculated as the ratio of the

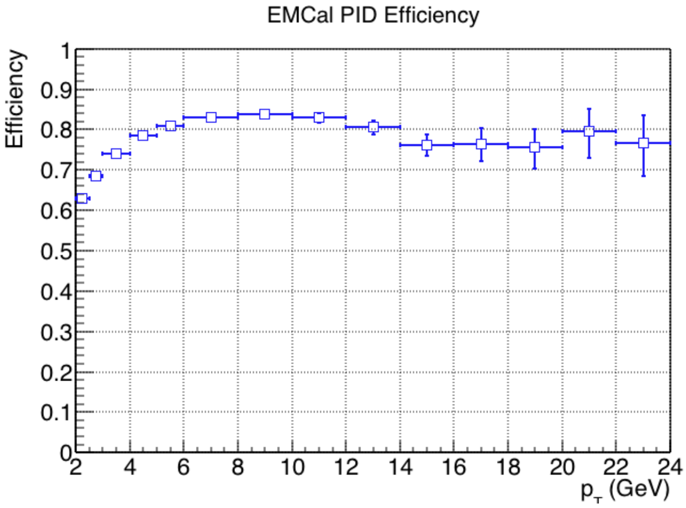

Figure 6.53: EMCal PID efficiency of finding electrons

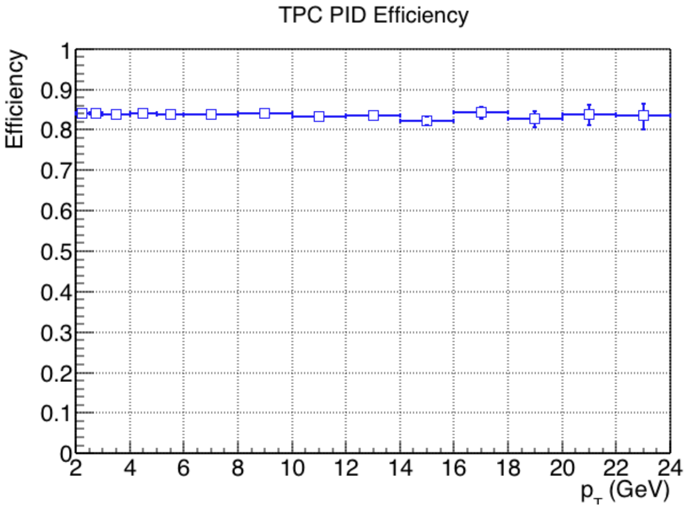

Figure 6.54: TPC PID efficiency of finding electrons

electron spectrum that passes the selection $\delta\eta < 0.05$ and $\delta\phi < 0.05$ and the electrons before this selection. $\delta\eta$ and $\delta\phi$ are the distance between the track projection on the EMCal surface and the reconstructed shower in η and ϕ, respectively. The efficiency is around 25% in the range of transverse momentum used in this analysis, as in the MB analysis.

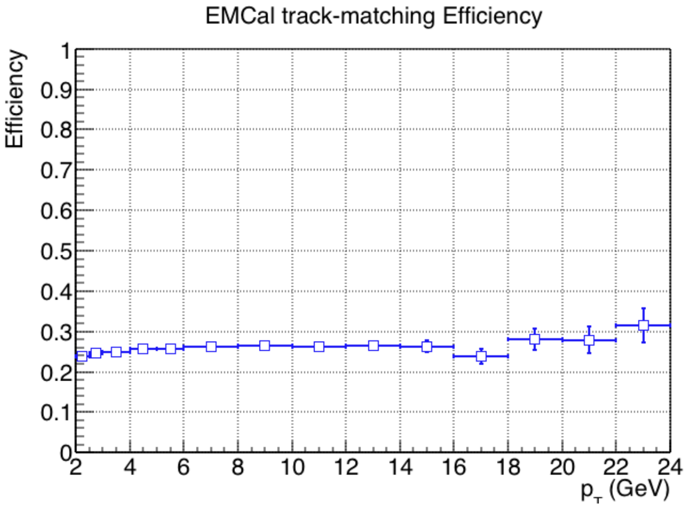

Figure 6.55: EMCal track-matching efficiency of finding electrons including the EMCal acceptance.

6.10 Trigger rejection factor

Since the trigger artificially enhances the events at high-p_T, it is necessary to correct the final spectrum by the so called rejection factor of the trigger. The rejection factor of the trigger is determined dividing the cluster energy distribution obtained in events were a trigger was used by the cluster energy distribution obtained in MB events. Then, the ratio of the curves is called turn-on curve and the ratio above the trigger threshold, which is a constant, is the rejection factor. Fig. 6.56 and 6.57 show the turn-on curve and the rejection factor values (on the top of the figures) obtained by fitting a constant above the threshold.

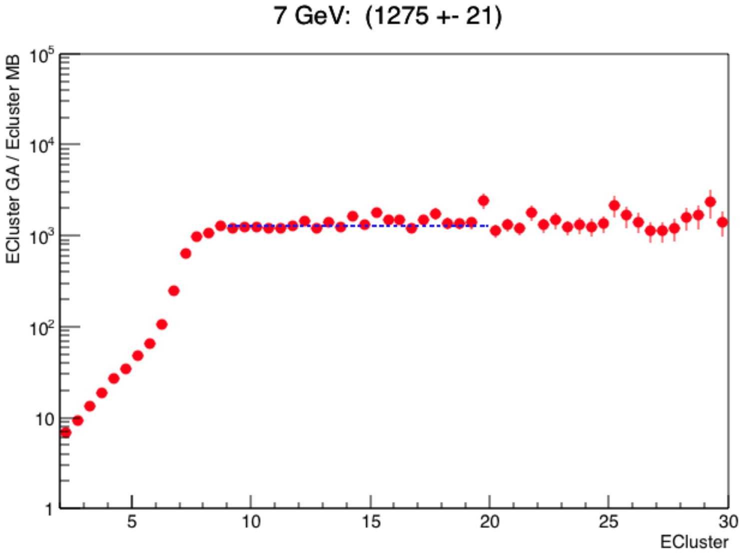

Figure 6.56: Turn-on curve for the trigger at 7 GeV using MB 13bc .

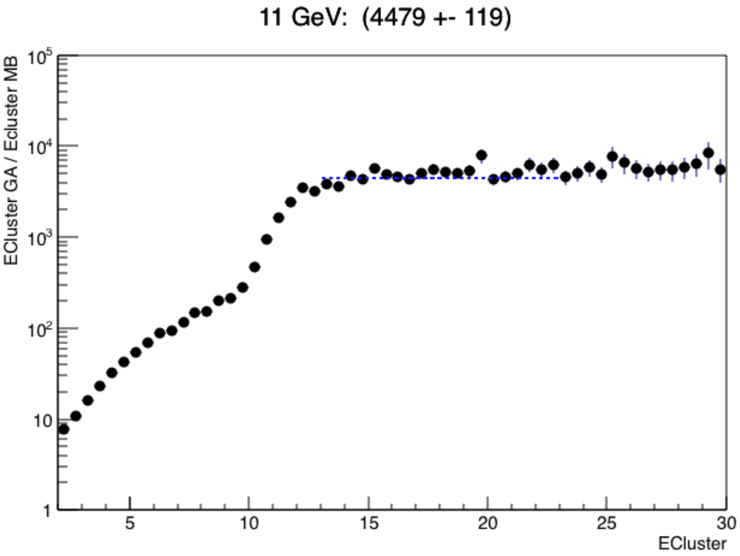

Figure 6.57: Turn-on curve for the trigger at 11 GeV using MB 13bc.

6.11 pp reference

In order to calculate the nuclear modification factor, R_{pPb} it is necessary a pp reference at the same energy of the p-Pb spectrum: $\sqrt{s} = 5.02$ TeV. It is also necessary a pp measurement in the same range as we have our spectrum: $8 \leq p_{\mathrm{T}} \leq 20$ GeV/c. The pp reference used in the MB analysis only reaches $p_{\mathrm{T}} = 12$ GeV/c, and could not be used for the full range of this analysis.

The only spectrum of heavy-flavour decay electrons in pp collisions measured in our desired p_{T} is the ATLAS results published at $\sqrt{s} = 7$ TeV [191]. In order to obtain a pp reference at $\sqrt{s} = 5.02$ TeV, we have extrapolated the ATLAS cross section using the FONLL predictions at 7 TeV and at 5.02 TeV. The procedure consists in calculating the ratio of FONLL at 7 and 5.02 TeV, for each bin of p_{T} and to use this ratios to scale the ATLAS points. The ratio values have a systematic uncertainty, propagated from each FONLL prediction. The final ATLAS points scaled has a systematic uncertainty component, which comes from the ratios, assuming them as uncorrelated.

The Fig. 6.58 shows the comparison of the invariant yield of ATLAS pp data before and after the extrapolation, together with the FONLL predictions at $\sqrt{s} = 5.02$ TeV and $\sqrt{s} =$ 7 TeV.

Tab. 6.7 shows the ATLAS points extrapolated to 5.02 TeV and the final systematic uncertainty.

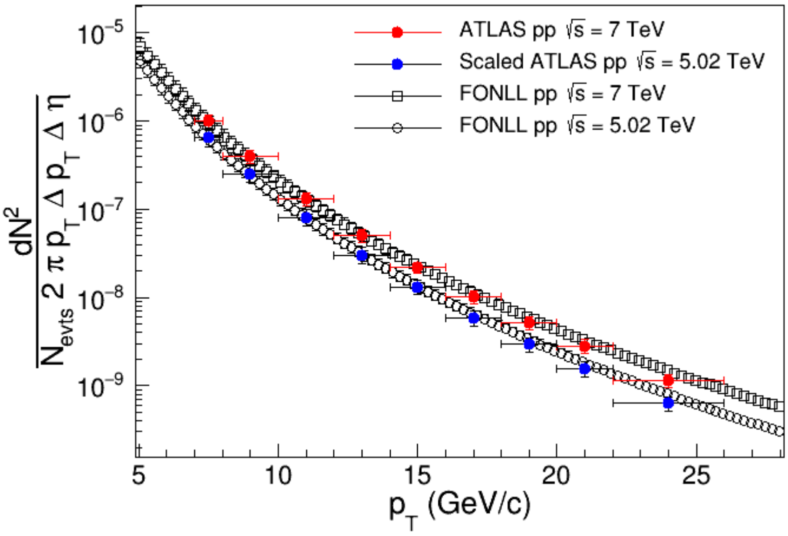

Figure 6.58: HFE invariant yield in pp collisions from ATLAS data [191] at $\sqrt{s} = 7$ TeV and the FONLL calculations [192] at $\sqrt{s} = 5.02$ TeV and $\sqrt{s} = 7$ TeV. The scaled ATLAS points was obtained using the scaling factors from FONLL predictions.

Table 6.7: ATLAS points

p_{T}	$\frac{dS}{dp_{\mathrm{T}}p_{\mathrm{T}}d\eta 2\pi}$ (mb/GeV^2)	stat	sys lower	sys higher
8-10	2.54E-07	2.87E-08	4.49E-08	4.76E-08
10-12	8.10E-08	7.82E-09	1.43E-08	1.49E-08
12-14	3.03E-08	3.64E-09	5.08E-09	5.27E-09
14-16	1.29E-08	1.15E-09	5.08E-09	2.06E-09
16-18	5.84E-09	7.59E-10	2.00E-09	1.03E-09
18-20	2.93E-09	3.40E-10	1.01E-09	1.03E-09

6.12 Invariant yield and nuclear modification factor

The spectrum of electrons from heavy-flavour hadron decays ($\mathcal{N}_{HFE}$) is obtained, similarly to the MB analysis, after subtracting the background contribution ($\mathcal{B}$) corrected for the background efficiency ($\epsilon_{\mathcal{B}}$) from the inclusive electron spectrum ($\mathcal{I}$). The result of the subtraction is corrected for the total efficiency (ϵ_T). Eq. 6.13 shows the expression for the $\mathcal{N}_{HFE}$.

$$\mathcal{N}_{HFE} = \frac{\mathcal{I} - \mathcal{B}/\epsilon_{\mathcal{B}}}{\epsilon_T} \tag{6.13}$$

The invariant differential yields of heavy flavour decay electrons ($dN^{inv}_{HFE}/dp_{\mathrm{T}}$) is given by Eq. 6.14, where the only difference, compared to MB, is the normalisation by the rejection factor $\mathcal{R}$.

$$\frac{dN^{inv}_{HFE}}{dp_{\mathrm{T}}} = \frac{d^2\mathcal{N}_{HFE}}{\mathcal{R}N_{evts}2\pi p_{\mathrm{T}}\Delta p_{\mathrm{T}}\Delta\eta} \tag{6.14}$$

Fig. 6.59 shows the invariant yield for the electrons from heavy-flavour hadrons decays. We also show in Fig. 6.59 the results obtained in the MB analysis. Fig. 6.60 shows the ratio of the spectra in the intersection region. The results for both thresholds are consistent and also consistent with the MB results, presented in Chap. 5.

N_{evts} is the number of events that passed the vertex cuts and fired the trigger. To obtain the HFE cross section, we use p-Pb cross section, $\sigma^{\mathrm{pPb}}_{\mathrm{MB}} = 2.09 \pm 0.07\ b$ [193], measured by the ALICE Collaboration. The HFE cross section is the HFE invariant yield multiplied by σ^{pPb}_{MB}.

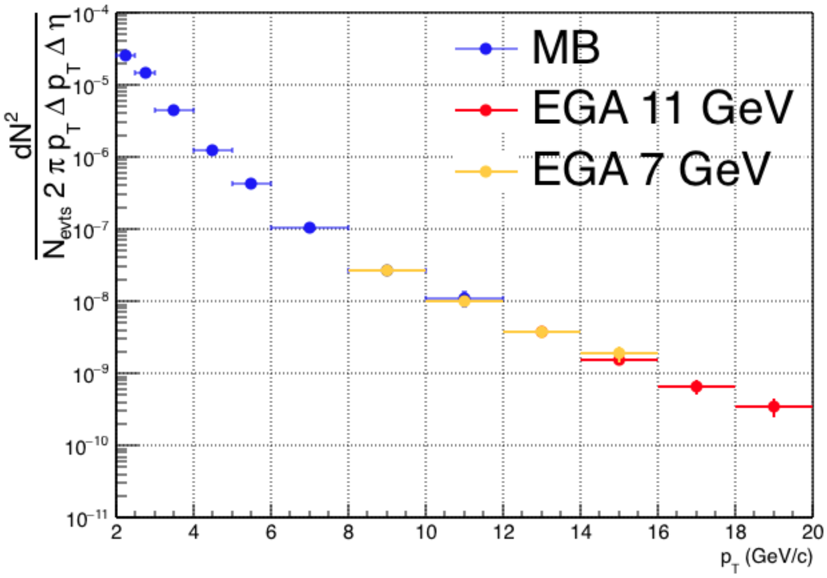

Figure 6.59: Invariant differential yields of heavy flavour decay electrons in pPb collision compared to MB results (MB results obtained using EMCal). The errors bar are the statistical ones.

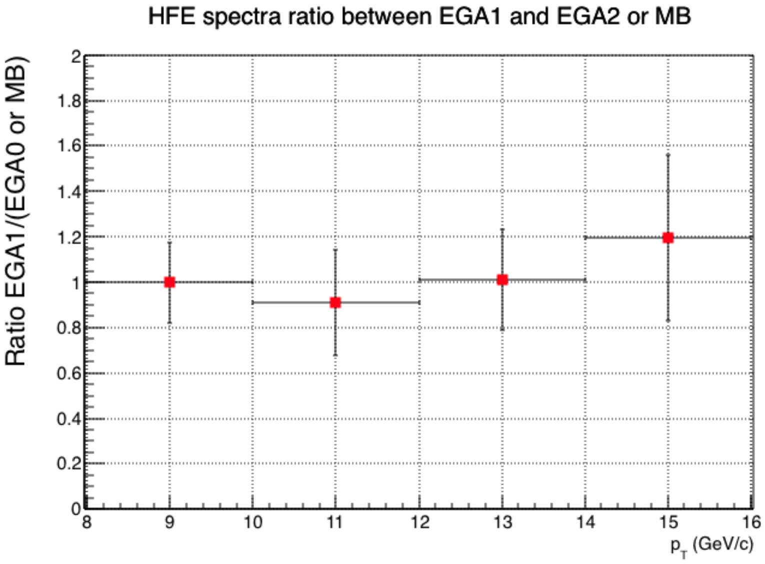

Figure 6.60: Ratio of spectra in the intersection region. Two first points are EGA at 7 GeV divide by MB and the last two points are EGA at 7 GeV divide by EGA at 11 GeV.

Fig. 6.61 shows the results compared to MB results.

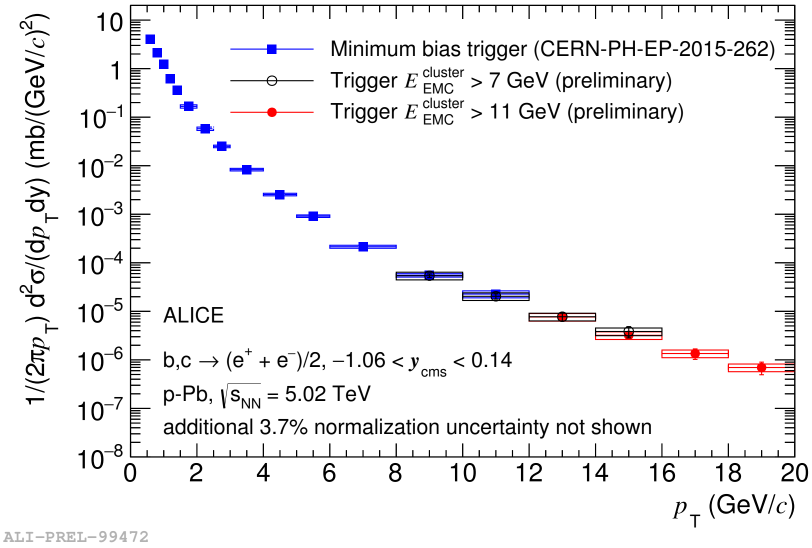

Figure 6.61: Cross section in trigger data compared with MB results.

Fig. 6.62 shows the trigger data R_{pPb} for the EGA1and EGA2, calculated using ATLAS data at 7 TeV scaled to 5.02 TeV, compared to the R_{pPb} for the EGA2 obtained using the same reference as used in the MB analysis (interpolation of pp measurements at 2.76 and 7 TeV). The results are also compared to the R_{pPb} obtained in the MB analysis and the results are all consistent. Fig. 6.63 shows only the 11 GeV threshold data, as an extension of the MB measurements. The ATLAS data was normalised by the $T_{\mathrm{AA}} = 0.0983 \pm 0.0035$. The T_{AA} is the average nuclear overlap function, obtained with the Glauber Model, as explained in Sec. 2.4.2.

The trigger data measurements are compatible with the MB measurements.

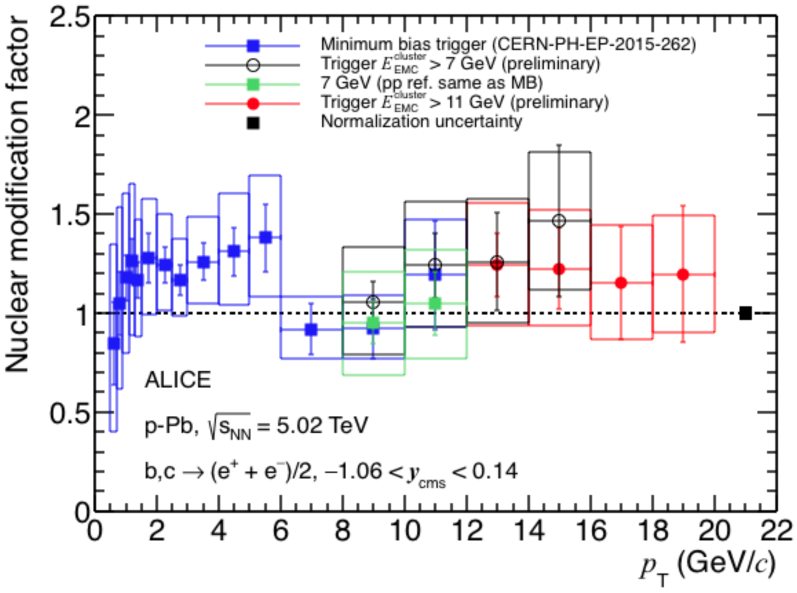

Figure 6.62: R_{pPb} in trigger data using ATLAS as reference, compared with MB results.

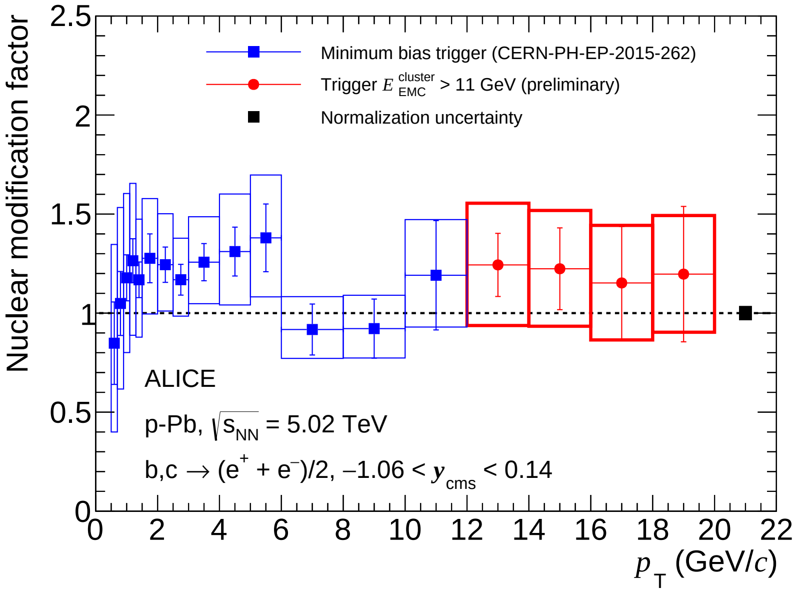

Figure 6.63: R_{pPb} in trigger data (only 11 GeV threshold) using ATLAS as reference, compared with MB results.

6.13 Evaluation of systematic uncertainty

As in the MB analysis, the systematic uncertainty was estimated using the method proposed by R. Barlow [185]. The difference in number of sigmas ($\frac{\Delta(p_{\rm T})}{\sigma_{\Delta}(p_{\rm T})}$) between the default spectrum and a spectrum obtained after a variation of a cut is used to judge if such a variation implies or not in a systematic effect.

As an example of configuration that has a systematic effect, we show in the Fig. 6.64 the comparison of two spectra. The difference in number of sigmas for two spectra and their ratio are shown in Fig. 6.65. We can see from Fig. 6.65 (left) that we have values bigger than 1. Using the ratio Fig. 6.65 (right) we can obtain the relative systematic uncertainty. In the case of the example, 3% of systematic uncertainty is observed.

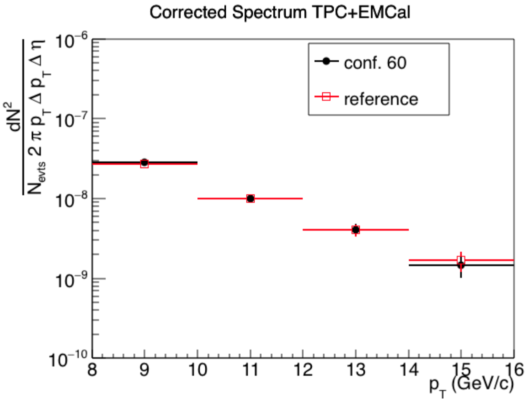

Figure 6.64: Example of a configuration that have systematic uncertainty. Comparison of reference spectrum and a spectrum obtained for a different configuration.

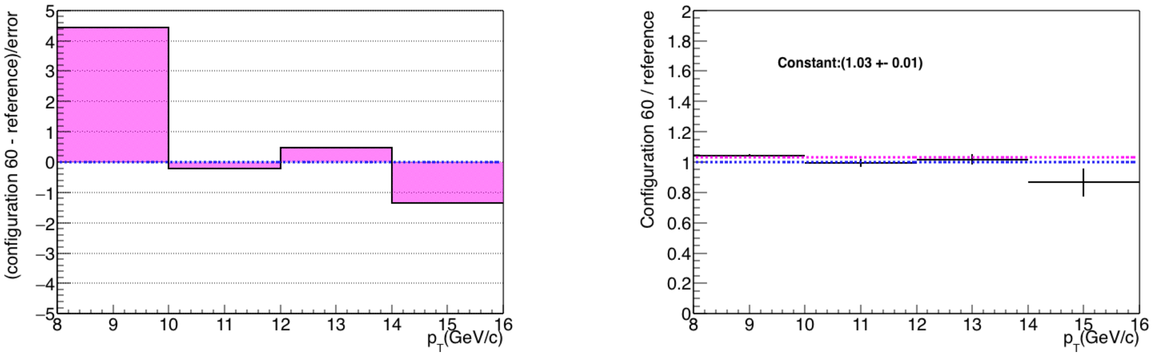

Figure 6.65: Example of a configuration that have systematic uncertainty. Left: difference in number of sigmas between reference spectrum and a spectrum obtained for a different configuration. Right: ratio between reference spectrum and a spectrum obtained for a different configuration.

To exemplify a case where we do not have any systematic effect, we show the Figs. 6.66 and 6.67. In Fig. 6.66 we show the comparison of two spectra and in Fig. 6.67, the difference in number of sigmas for the two spectra and their ratio, respectively. In this case we do not see in Fig. 6.65 (left) any value bigger than 1. Using the ratio in Fig. 6.65 (right), we also see that the ratios are compatible with one.

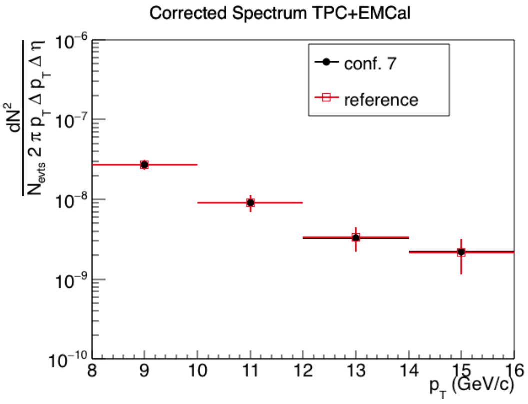

Figure 6.66: No effect example. Comparison of reference spectrum and a spectrum obtained for a different configuration.

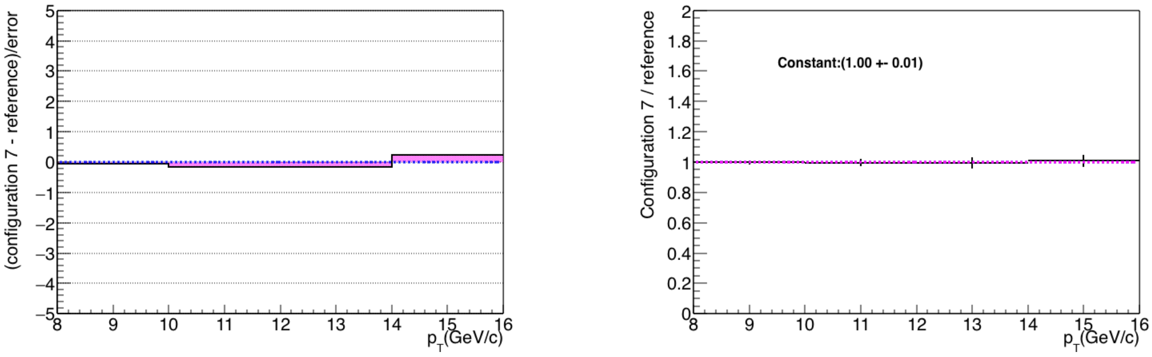

Figure 6.67: No effect example. Left: Difference in number of sigmas between reference spectrum and a spectrum obtained for a different configuration. Right: Ratio between reference spectrum and a spectrum obtained for a different configuration.

In Tab. 6.8, we summarise the systematic uncertainties found using Barlow's method. The list of the variations in each cut is shown in App. F.

Table 6.8: Variations to determine systematic effect

Signal	Systematic effect (%)
TPC PID	5
EMCal PID (E/p)	3
Shower shape M20	5
Track-selection	No effect
Track-matching	1
Non-HFE Background	**Systematic effect (%)**
Invariant mass method	3
W contribution	0.3
J/ψ and Ke3	0.06
η, π^0 weights	No effect
pseudorapidity (η) dependence	10
Normalisation	**Systematic effect (%)**
Rejection factor	12
Total	18

6.14 Final considerations of this chapter

In this chapter, we presented the analysis performed using the EMCal triggered data for the p-Pb collisions at $\sqrt{s_{\rm NN}}$ = 5.02 TeV. Two energy thresholds were available: one at 7 GeV and other at 11 GeV. We have measured electrons from heavy-flavour hadron decays in the transverse momentum range of $8 < p_{\rm T} <$16 GeV/c, using the threshold at 7 GeV and in the range $12 < p_{\rm T} <$20 GeV/c, using the threshold at 11 GeV.

The electron background was subtracted using an invariant mass method for the contributions from π^0 and η Dalitz decays and from γ conversions. The contribution from J/ψ was obtained from the cocktail method and the W contribution was obtained by POWHEG simulations. The efficiencies were determined using two different MC simulations.

The results using the triggered data extended the measurement of the MB data, up to 20 GeV and the results are consistent in the intersection range of the measurements.

The nuclear modification factor was calculated using an extrapolation of the pp measurement from ATLAS, since the ALICE pp data only reaches 12 GeV/c. The ATLAS cross section was measured at 7 TeV and we have scaled the cross section to 5.02 TeV using the FONLL predictions.

The nuclear modification factor is consistent with one in the whole measured $p_{\rm T}$ range. The results for both triggered data are consistent to each other in the intersection region and also, the results are consistent with the MB one.

Chapter 7

Discussion

In this chapter we show a brief summary of several results of open-heavy flavour obtained by LHC in p-Pb and Pb-Pb collisions. Based on the comparison between experimental data and theoretical models, we extract some of the possible explanations for the interactions of heavy-flavour with the nuclear medium and with the QGP. We comment how our measurement, which is the nuclear modification factor of the electrons from open-heavy flavour decays in p-Pb, contributes to the understanding of the heavy-flavour dynamics in p-Pb and Pb-Pb collisions.

7.1 LHC p-Pb measurements

ALICE has measured open-heavy-flavour production in p-Pb collisions at $\sqrt{s_{\rm NN}} = 5.02$ TeV in all decay channels: Hadronic decay channel, semimuonic decay channel, semielectronic decay channel and beauty contribution to inclusive semielectronic decay channel. In this section we show the results for D meson, muons at forward and backward rapidities and beauty contribution to the inclusive decay electrons.

Fig. 7.1 shows the D^0, D^+, D^{*+} and D_s^+ nuclear modification factor in p-Pb collisions at $\sqrt{s_{\rm NN}} = 5.02$ TeV. The $R_{\rm pPb}$ is consistent with unity for all the D-meson species. The average of the results are described, within uncertainties, by models including initial-state effects, as can be seen in Fig. 7.2. The model "CGC (Fujii-Watanabe)" is a model based on Colour Glass Condensate, presented in [194], where it is used an unintegrated gluon distribution at small Bjorken-x in the proton obtained by solving the Balitsky-Kovchsegov (BK) equation with running coupling correction. The model "pQCD NLO with CTEQ6M+EPS09 PDF" uses the MNR calculations for the heavy flavour production, proposed in [195], where NLO accuracy is used and the parton distribution function CTEQ6M (see Sec. 3.2.1) is used including the EPS09 [138] to take into account nuclear shadowing. The "Vitev" curve is the model presented in Sec. 3.2.4, where power corrections, momentum broadening and energy loss in the cold nuclear matter are included in the calculations [44]. The experimental data are consistent within the model calculations presented and the cold nuclear matter effects are small, since the results is consistent with one.

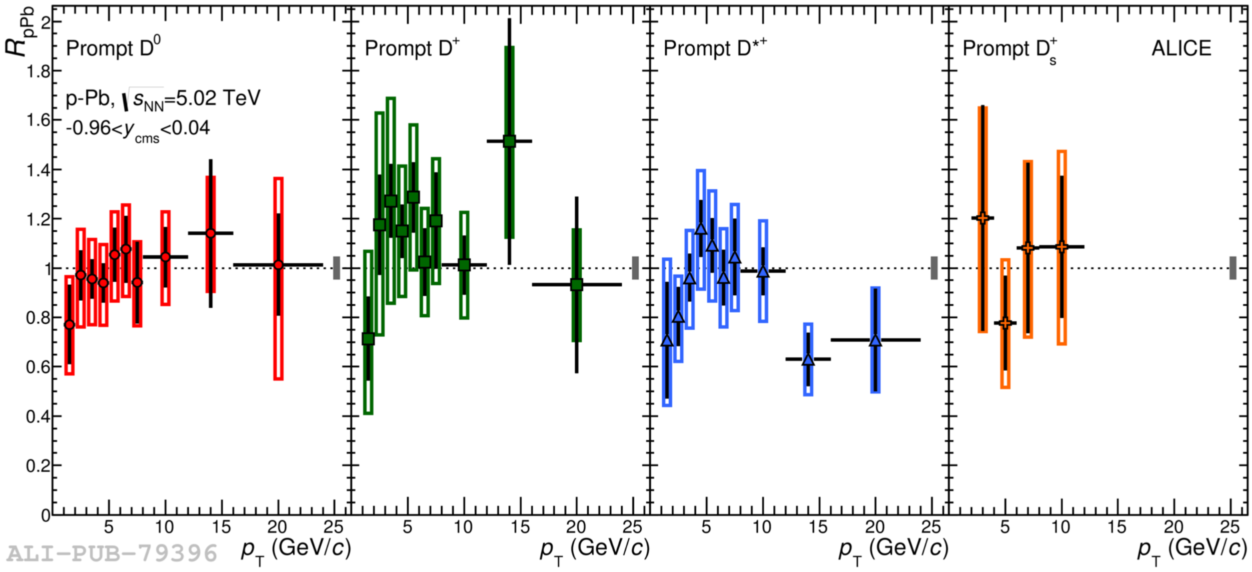

Figure 7.1: ALICE measurements of D^0, D^+, D^{*+} and D_s^+ nuclear modification factor in p-Pb collisions at $\sqrt{s_{\mathrm{NN}}} = 5.02$ TeV. Fig. from [196].

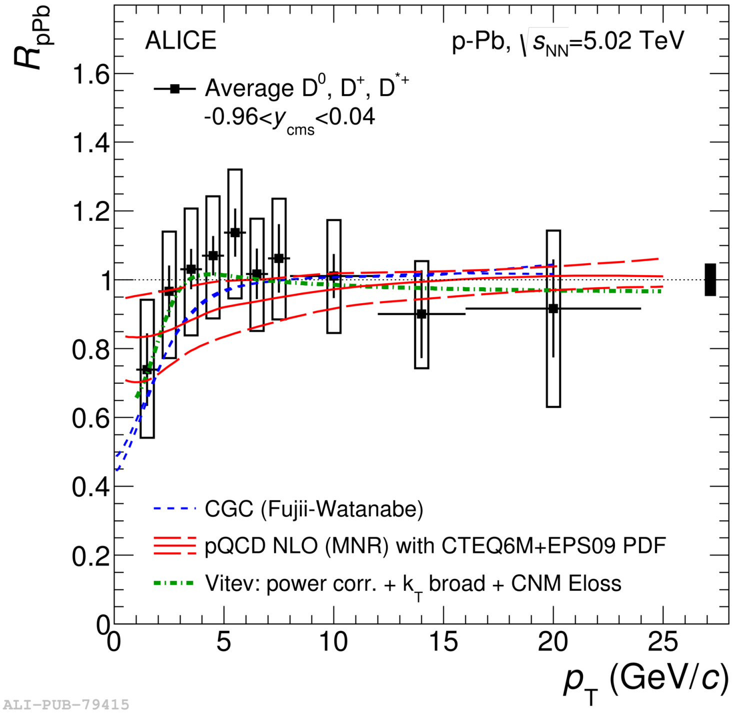

Figure 7.2: Average nuclear modification factor of D^0, D^+ and D^{*+} in p-Pb collisions at $\sqrt{s_{\mathrm{NN}}} = 5.02$ TeV. Fig. from [196].

The multiplicity dependence of the nuclear modification factor for D-meson was also measured by ALICE in p-Pb collisions and the result are shown in Fig. 7.3. The results show no multiplicity dependence and no p_{T} dependence.

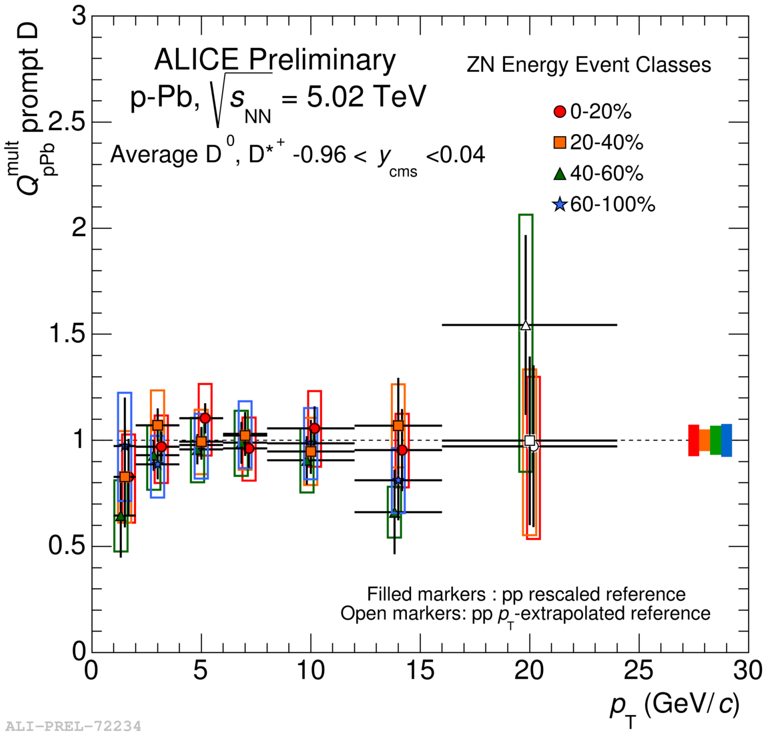

Figure 7.3: Average nuclear modification factor of D^0 and D^{*+} in p-Pb collisions at $\sqrt{s_{\rm NN}} =$ 5.02 TeV in different centrality bins. Fig. from [197].

Fig. 7.4 shows the nuclear modification factor of muons at forward[1] (left) and backward[2] (right) rapidities measured by ALICE in p-Pb collisions at $\sqrt{s_{\rm NN}} = 5.02$ TeV. The results are consistent with unity for forward rapidity and slightly larger than unity at backward rapidity for the momentum range $2 < p_{\rm T} < 4$ GeV/c.

The results are consistent with models including cold nuclear matter effects, where the model "NLO (MNR) with EPS09 PDF" [195] is the same as used for the D-meson calculations and it takes into account nuclear shadowing. The "Vitev" model is also the one presented in Sec. 3.2.4, where power corrections, momentum broadening and energy loss in the cold nuclear matter are included in the calculations [44] for the forward rapidity and incoherent multiple scatterings are considered for backward rapidity (called "Z. B. Kang" on the right plot).

---

[1] p-going side

[2] Pb-going side

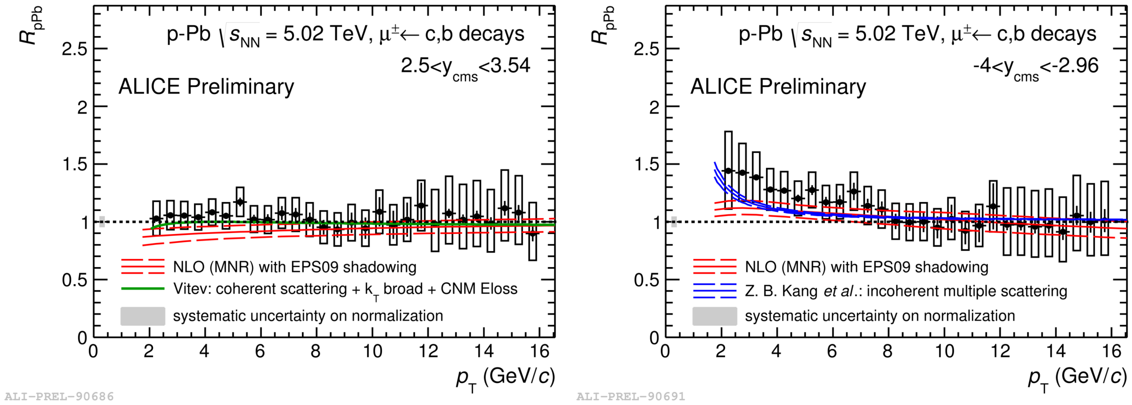

Figure 7.4: Nuclear modification factor of muons at forward (left) and backward (right) rapidities measured by ALICE in p-Pb collisions at $\sqrt{s_{\mathrm{NN}}} = 5.02$ TeV. Fig. from [197].

The measurements of the inclusive decay electrons in p-Pb collisions is the subject of this thesis and the analysis is discussed in details in the Chap. 5 and Chap. 6. Our result is shown in Fig. 7.5, where we show the nuclear modification factor of electrons from heavy-flavour hadron decays. The box represents the systematic uncertainties, which were determined using the procedure discussed in 5.10. We compare the results with four different theoretical calculations:

- *Kang et al.*: incoherent multiple scattering (model presented in Sec. 3.2.4, for the incoherent case). In this case, there is no energy loss and the propagation of the partons is governed by the momentum broadening.

- *Sharma et al.*: coherent scattering + CNM (model presented in Sec. 3.2.4, for the coherent case). The coherent scattering includes energy loss and power corrections. The CNM effects that were added in this calculation is the momentum broadening of the incoming partons, as presented in Sec. 3.2.4.

- FONLL + EPS09NLO shad. This is based on pQCD calculations (FONLL) including the nuclear shadowing (see Sec. 3.1), which is a CNM effect, present in the EPS09NLO parametrization. This model predicts that the CNM effects are small, with an R_{pPb} close to one.

- Blast wave calculation. This is a model, presented in [198], that suggests a formation of an expanding medium in p-Pb collisions, described by hydrodynamics. In this case, flow of charm and bottom are considered. This model predicts an enhancement at low p_{T}.

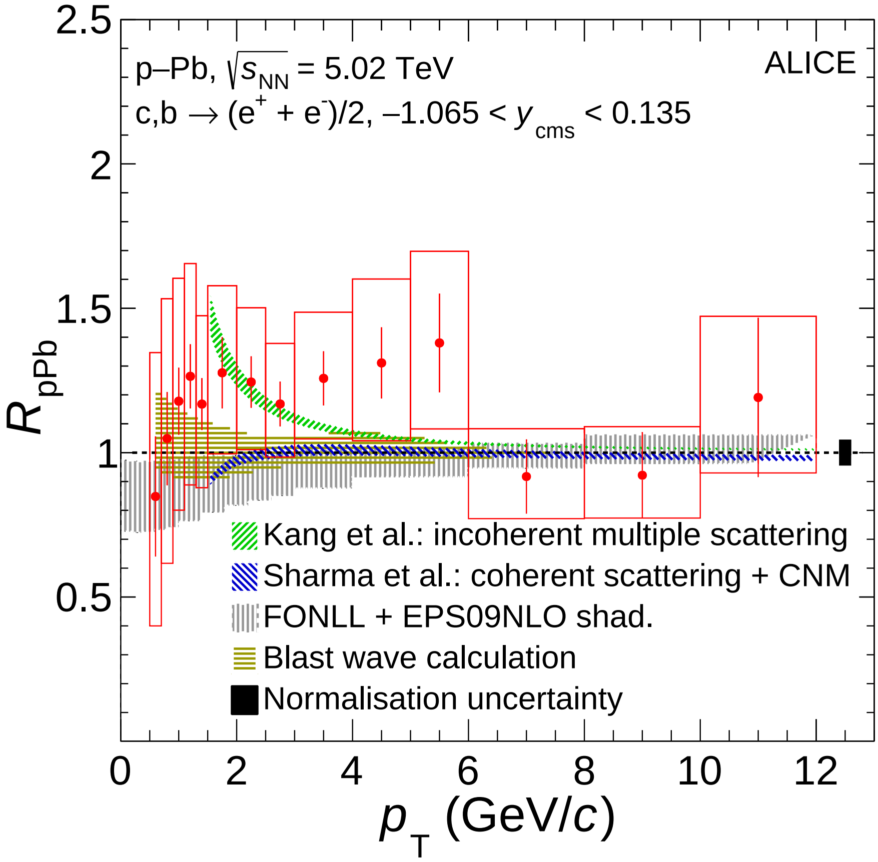

Figure 7.5: Nuclear modification factor of electrons from heavy-flavour hadron decays measured in p-Pb, as a combination of results from this analysis, using the TPC and EMCal detectors, and the results obtained by the GSI group, using the TPC and TOF detectors. This result was published in *Physics Letter B* [4].

The results of the nuclear modification factor of electrons from heavy-flavour hadron decays show a slight enhancement in the range $2 \leq p_{\mathrm{T}} \leq 6$ GeV/c, but still consistent with one, given the systematic uncertainties. For $p_{\mathrm{T}} \geq 6$ GeV/c, the results are consistent with one. The results obtained in the high p_{T} region using the EMCal trigger is compatible with one, extending the MB results (see Fig. 6.63). Given this observed shape of the R_{pPb}, we can say we have a small Cronin enhancement, which was also observed by PHENIX, as discussed in Sec. 3.2.5. However, due to the present uncertainties, the result is consistent with one and with the four presented theoretical calculations and they do not predict significant CNM effects.

This result in p-Pb is used to further understand the result obtained in Pb-Pb collisions, as will be discussed in the next section.

Fig. 7.6 shows the nuclear modification factor of electrons from beauty decays measured by ALICE in p-Pb collisions at $\sqrt{s_{\mathrm{NN}}} = 5.02$ TeV. The results are consistent with unity and, again, we can conclude that the cold nuclear matter effects are small. Comparing our result (Fig. 7.5) with the electrons from beauty, we can conclude that the electrons from charm and beauty have the same behaviour, since our measurement includes electrons from both sources (charm and beauty), and the R_{pPb} are consistent between themselves. The separation of electrons from beauty and charm allow us to investigate the mass dependence of the results.

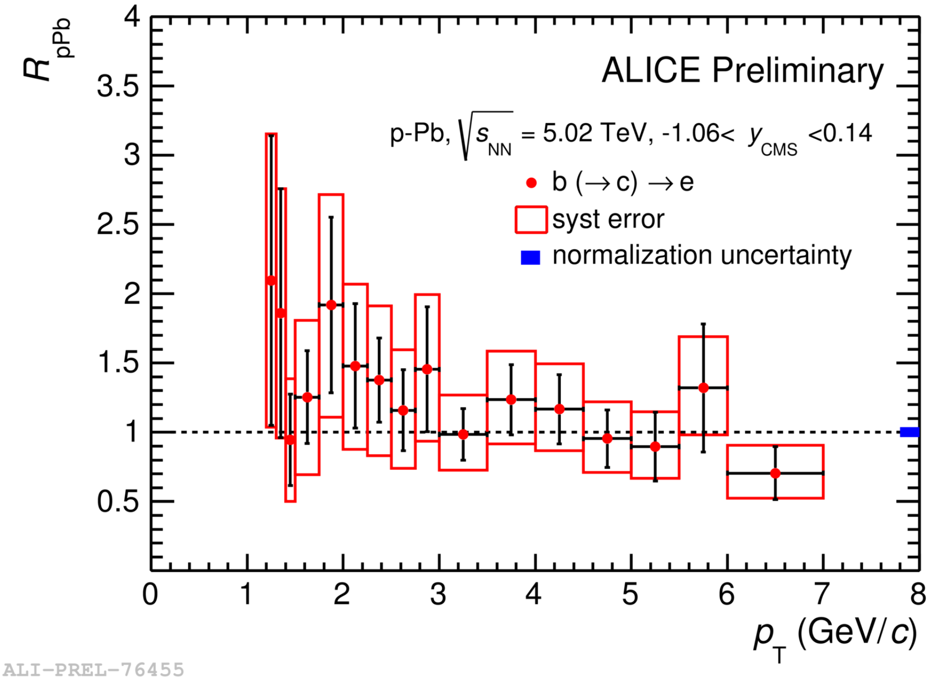

Figure 7.6: Nuclear modification factor of electrons from beauty decays measured by ALICE in p-Pb collisions at $\sqrt{s_{\mathrm{NN}}} = 5.02$ TeV [199].

The CMS collaboration has measured the production cross section of B^+, B^0 and B_s in p-Pb collisions at $\sqrt{s_{\mathrm{NN}}} = 5.02$ TeV and the results for the nuclear modification factor are shown in Fig. 7.7 [200]. The nuclear modification factor was obtained using the FONLL pQCD calculations for pp collisions scaled by the number of binary collisions and the result is consistent with one. This measurement has an intersection with our measurement in high p_{T} (the triggered data result, Fig. 6.62), and we have consistent results, showing that the cold nuclear matter effects in the high transverse momentum range are small.

In this section we have shown the results of nuclear modification factor in p-Pb collisions for several channels available to study the heavy flavour particles. Since the results are consistent with one, the present cold nuclear matter effects, which are due to the presence of the Pb nucleus in the collision, do not lead to any suppression of the heavy-flavour particles. Then, we are lead to conclude that the suppression observed in Pb-Pb collisions, which will be shown in the next section, is due to the QGP and not from the cold nuclear matter effects.

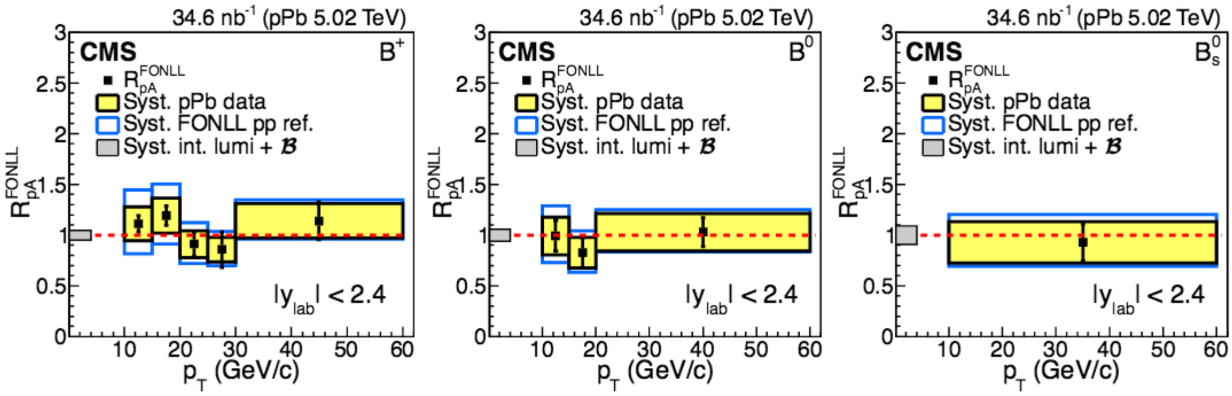

Figure 7.7: Nuclear modification factor of B^+, B^0 and B_s in p-Pb collisions at $\sqrt{s_{\mathrm{NN}}} = 5.02$ TeV measured by CMS using FONLL as pp reference. Fig. from [200].

7.2 LHC Pb-Pb measurements

In Pb-Pb collisions at $\sqrt{s_{\mathrm{NN}}} = 2.76$ TeV, the LHC results were published by ALICE and CMS. ALICE has studied the production of open heavy-flavour decays using all decay channels: hadronic decay channel, semimuonic decay channel, semielectronic decay channel and beauty contribution to inclusive semielectronic decay channel. As will be shown in the following, all the channels show an R_{AA} smaller than one, indicating a strong suppression of the particles when compared to pp collisions. Since no suppression is observed in p-Pb collisions, the suppression observed in Pb-Pb collisions is not from cold nuclear matter effects, but it is from the interactions with the QGP.

Fig. 7.8 (left) shows the ALICE measurements in Pb-Pb collisions at $\sqrt{s_{\mathrm{NN}}} = 2.76$ TeV of the R_{AA} for the average of D^0, D^+, D^{*+} compared to pp and p-Pb results. Fig. 7.8 (right) shows the comparison with light particles. A strong suppression of the R_{AA} is observed and it suggests a strong interaction of charm particles with the medium.

Fig. 7.9 shows the results of the elliptic flow of the average of the D-meson species [202], also measured by ALICE in Pb-Pb collisions, compared to results of light particles. The elliptic flow observed is higher than zero, and it is consistent with the values for light particles. It increases with decreasing centrality, as it is expected, since the v_2 occurs in non central collisions. The result is an indication that charm quarks participate in the collective motion of the medium.

Fig. 7.10 shows the D-meson R_{AA} measurement as a function of number of participants in the collision. The results are compared to $\pi^{\pm}$ (left) and non-prompt J/ψ (right) R_{AA}, suggesting the expected mass dependence of the results: $R_{\mathrm{AA}}(\pi) < R_{\mathrm{AA}}(\mathrm{D}) < \mathrm{R}_{\mathrm{AA}}(\mathrm{B})$. The results are compared to theoretical calculations presented in [203], which includes collisional and radiative energy loss and considers dynamical scattering centers in the medium. The calculations suggests a quark mass dependence of the parton energy loss, which decreases with increasing quark mass.

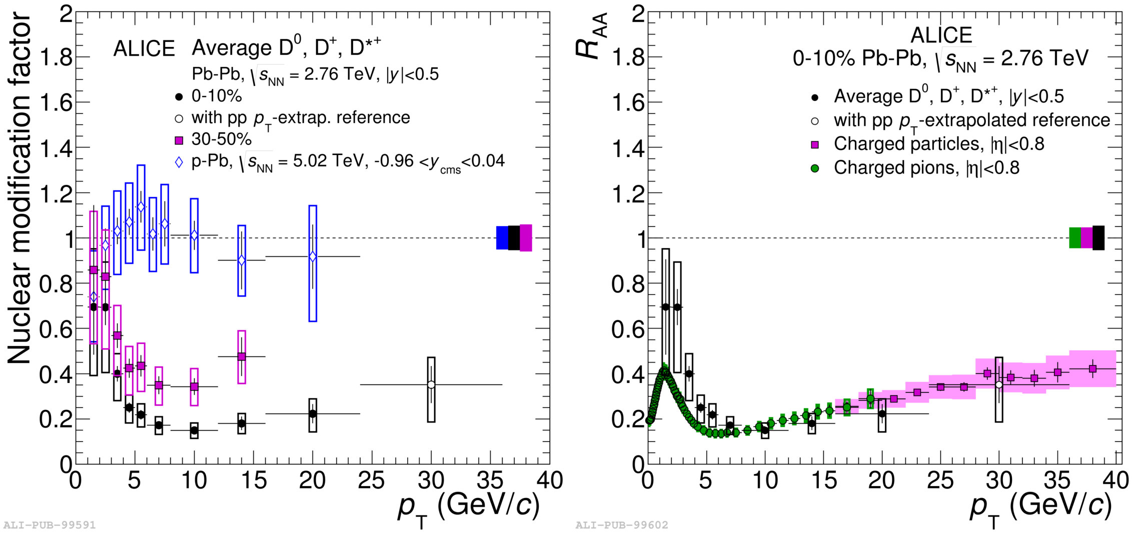

Figure 7.8: Left: R_{AA} results for the average of D^0, D^+, D^{*+} measured by ALICE in Pb-Pb collisions at $\sqrt{s_{\mathrm{NN}}} = 2.76$ TeV, compared to pp and p-Pb results. Right: D^0, D^+, D^{*+} average R_{AA} compared to light particles R_{AA}. Figs. from [201].

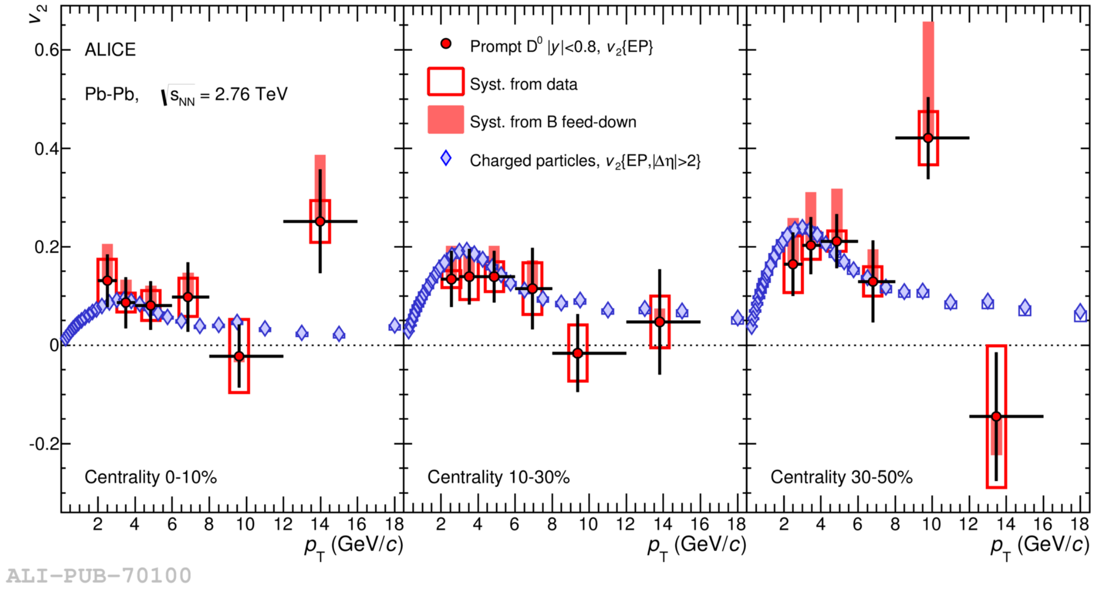

Figure 7.9: Elliptic flow results for the average of D^0, D^+, D^{*+} measured by ALICE in Pb-Pb collisions at $\sqrt{s_{\mathrm{NN}}} = 2.76$ TeV in three different centralities bins and compared to the charged particles results. Fig. from [202].

The electrons and muons from heavy flavour hadron decay were measured by ALICE in Pb-Pb collisions at $\sqrt{s_{\mathrm{NN}}} = 2.76$ TeV. The results for R_{AA} are shown in Fig. 7.11 for electrons [199] and muons [205]. Fig. 7.12 shows the results for v_2 of electrons [206] and muons [205]. The results for electrons and muons are consistent within uncertainties, showing no rapidity dependence for the open heavy-flavour production in Pb-Pb, since electrons are measured at midapidity and muons are measured at forward rapidity. Also, the results suggest a strong interaction of heavy-flavour with the medium.

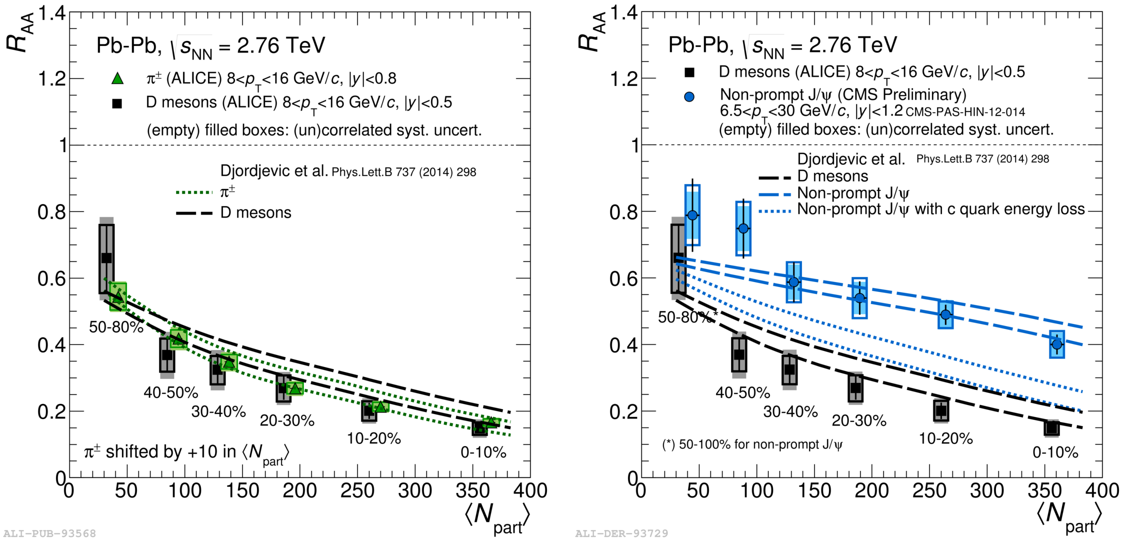

Figure 7.10: Centrality dependence of the D-meson measurements in Pb-Pb collisions, compared to $\pi^{\pm}$ (left) and non-prompt J/ψ (right). The results are compared to a theoretical calculation presented in [203]. Figs. from [204].

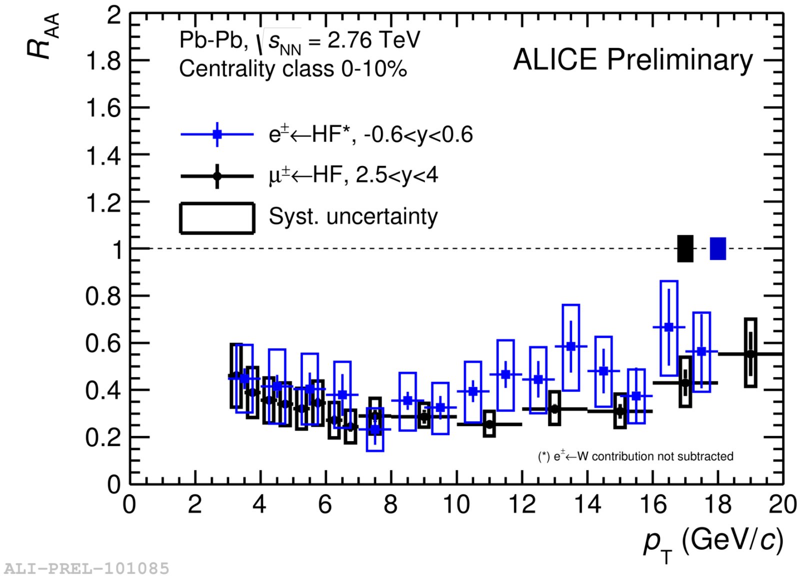

Figure 7.11: Nuclear modification factor of muons from heavy flavour hadron decays measured by ALICE in Pb-Pb collisions at $\sqrt{s_{NN}} = 2.76$TeV. The results are compared to ALICE results for electrons.

Fig. 7.13 shows the nuclear modification factor measured by ALICE for electrons from beauty hadron decays. A suppression is observed for $p_T > 3$ GeV/c.

Fig. 7.14 shows the nuclear modification factor for the prompt D^0 measured by CMS [207] and compared to ALICE results. The results are compatible within uncertainties.

Since the results in the several channels in p-Pb collisions is consistent with one, the effects from cold nuclear matter do not lead to any suppression of the particles. Then, the observed suppression in Pb-Pb collisions is due to the interactions with the QGP. To

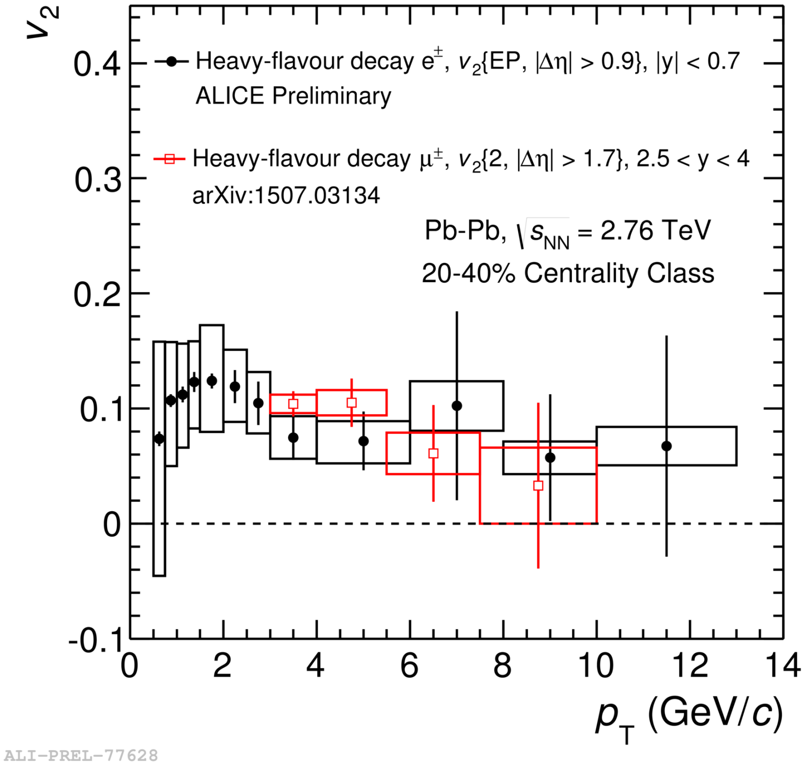

Figure 7.12: Elliptic flow of muons from heavy flavour hadron decays measured by ALICE in Pb-Pb collisions at $\sqrt{s_{NN}} = 2.76$ TeV. The results are compared to ALICE measurements of electrons from heavy-flavour hadron decays.

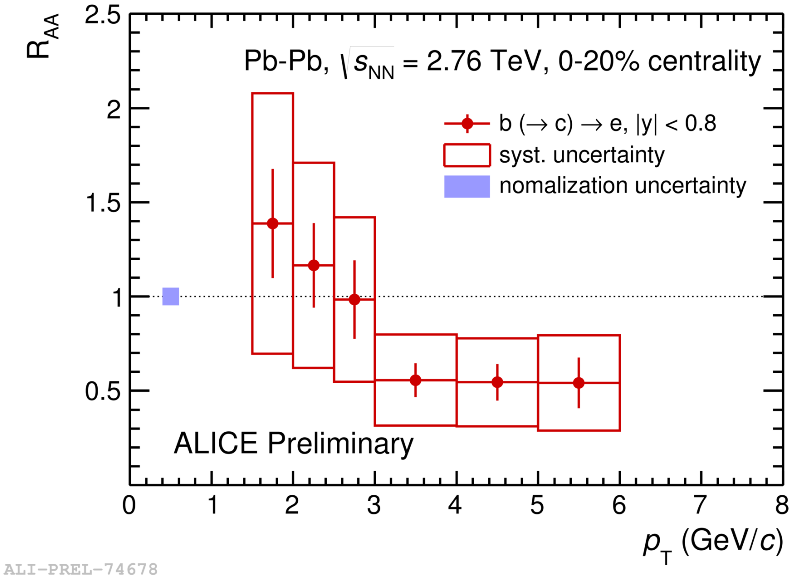

Figure 7.13: Nuclear modification factor of electrons from beauty hadron decays measured by ALICE in Pb-Pb collisions at $\sqrt{s_{NN}} = 2.76$TeV. Fig. from [199].

understand which are the interactions of the heavy-flavour with the medium, we compare the results with theoretical models and we try to extract information about the dynamics inside

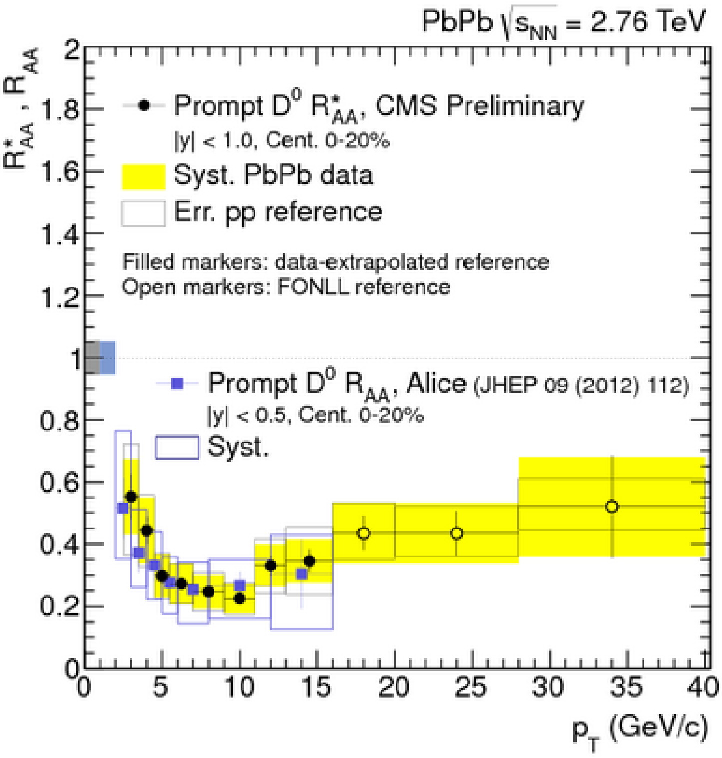

Figure 7.14: Nuclear modification factor for prompt D^0 measured by CMS in Pb-Pb collisions at $\sqrt{s_{\rm NN}} = 2.76$ TeV. Fig. from [207].

the QGP. In the next section we show the comparisons and what we can conclude with the present theoretical models available.

7.3 Comparison of results with the theoretical models for the heavy quarks interaction with the QGP

As we have commented before, in order to understand the properties of the QGP, we use theoretical calculations, with given assumptions, and we compare them to the experimental data. From the comparisons, we can extract information about the interactions of the particles with the medium. In this section we show the comparison of several models (all of them presented in Sec. 3.3) with the results ($R_{\rm AA}$ and v_2) for the D-meson and for the electrons from heavy-flavour hadron decays in Pb-Pb collisions.

Fig. 7.15 shows the preliminary results of the $R_{\rm AA}$ (top) and v_2 (bottom) of electrons from heavy-flavour hadron decays. Fig. 7.16 shows the corresponding published results for D-meson.

The models “BAMPS” and “MC@sHQ+EPOS”, shown in Fig. 7.15, do not include shadowing. As a consequence, the predictions for the low $p_{\rm T}$ is a higher $R_{\rm AA}$ than the other models (indicating less suppression or even an enhancement). Same feature is also observed for the curve “UrQMD” in Fig. 7.16. The “WHDG” also do not include shadowing, but since it starts at 3 GeV/c, we can not evaluate its shape at low $p_{\rm T}$.

The models which do not include coalescence as a hadronization mechanism presents a v_2 prediction smaller than the observed data: "POWLANG" and "BAMPS el.+rad." in Fig. 7.15 and "WHDG" in Fig. 7.16.

The "BAMPS el." can explain the HFE v_2 while it over predicts the suppression of the HFE. With the inclusion of the radiative energy loss, "BAMPS el. + rad." can predict the suppression of HFE and its calculations of v_2 is lower than the experimental data. This can be a consequence that the inclusion of the radiative process reduces the weight of collisional process and the v_2 is built mainly from collisional energy loss.

Although the "TAMU" and the "MC@sHQ" describe reasonably well the HFE R_{AA} and v_2 preliminary results, when the same models are compared to the final D-meson R_{AA} and v_2, they cannot explain the measurements.

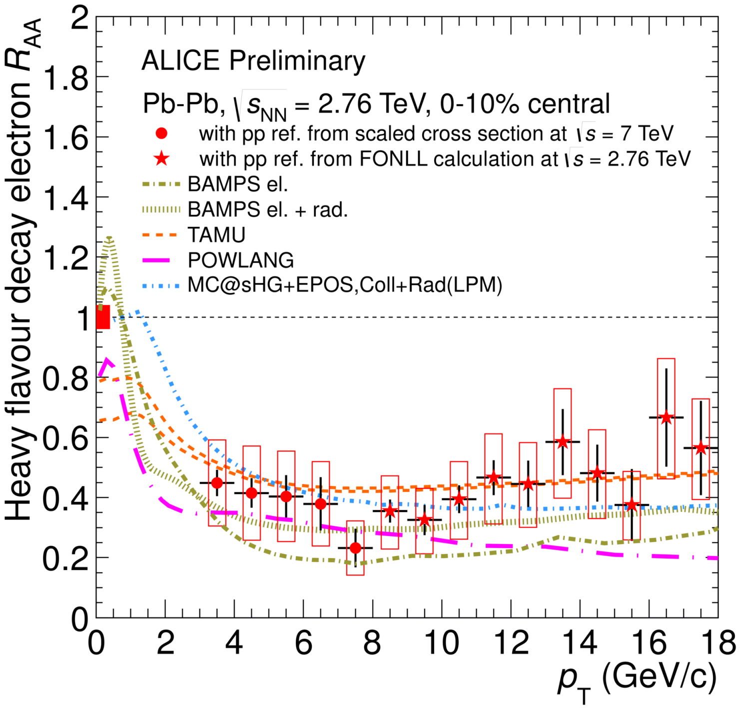

ALI-PREL-77686

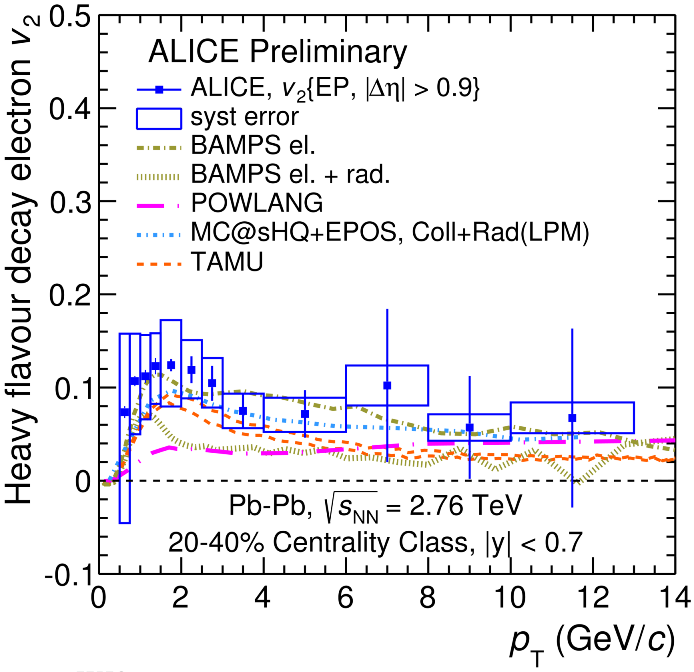

ALI-PREL-77576

Figure 7.15: Electrons from heavy-flavour hadron decays R_{AA} (top plot) and v_2 (bottom plot) measured by ALICE in Pb-Pb collisions at $\sqrt{s_{\text{NN}}} = 2.76 TeV$. Figs. from [199].

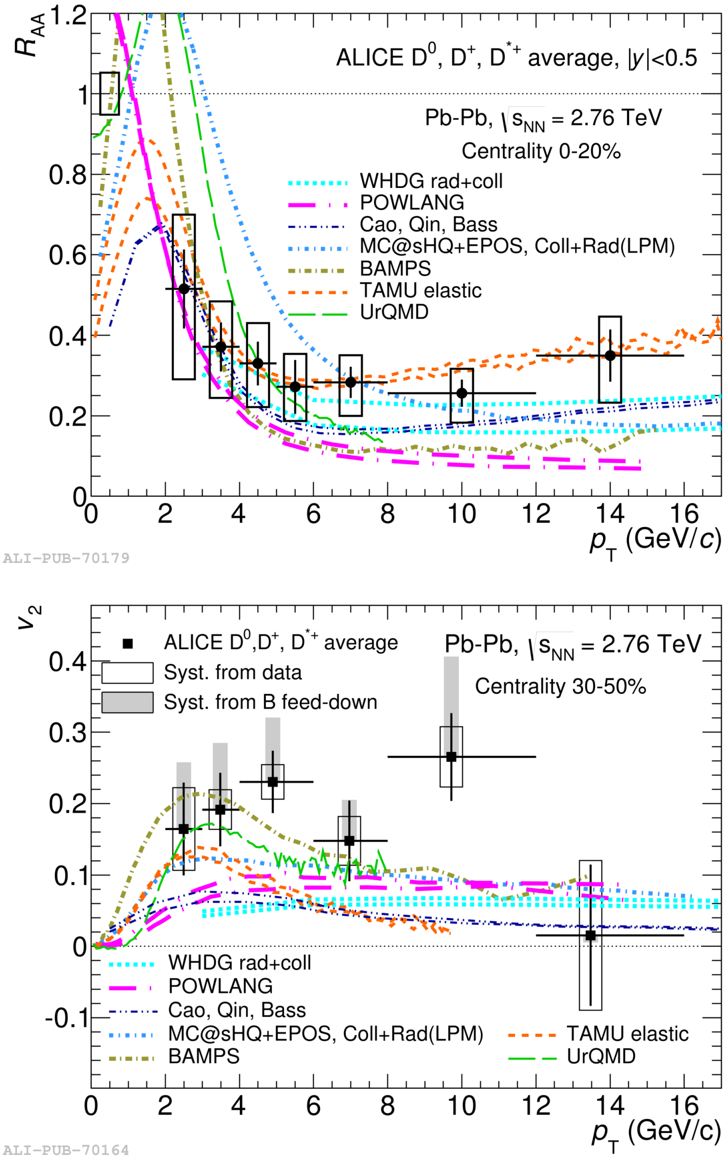

ALI-PUB-70179

ALI-PUB-70164

Figure 7.16: Average D meson R_{AA} (top plot) and v_2 (bottom plot) measured by ALICE in Pb-Pb collisions at $\sqrt{s_{\mathrm{NN}}} = 2.76 TeV$. Figs. from [202].

7.4 Comparison with RHIC data

The nuclear modification factor of D^0 in the most central Au-Au collisions at $\sqrt{s_{\mathrm{NN}}} =$ 200 GeV was measured by STAR and the results are shown in Fig. 7.17. The R_{AuAu} shows a strong suppression for $p_T > 3$ GeV/c and an enhancement around 1.5 GeV/c. Several theoretical calculations are shown in Fig. 7.17. "TAMU" is the model discussed in 3.3.6, where a Langevin approach is used to calculate heavy-quark propagation in the medium. The medium considered is described by a (2+1)-dimensional ideal hydrodynamic model and the hadronization includes both fragmentation and coalescence mechanism. "SUBATECH" is the model discussed in 3.3.4, where a BAMPS equation and HTL approach are used and the hadronization is also performed including fragmentation and coalescence. "Torino" is the model discussed in 3.3.1 (called as POWLANG in some papers), where a Langevin and a Hard Thermal Loop approach are used in a viscous medium and only fragmentation is considered as a hadronization mechanism. This model do not reproduce the peak around 1 GeV, as the TAMU and SUBATECH models. "Duke" is the model discussed in 3.3.2, where a Langevin equation with a radiative term is used to calculate the transport of the heavy-flavour in the medium. In this case, both fragmentation and coalescence are considered and the calculation are performed with and without shadowing. "LANL" is the model discussed in 3.2.4. The model that passes closer to the data is the "SUBATECH", although the same model do not explain the LHC D meson R_{AA}.

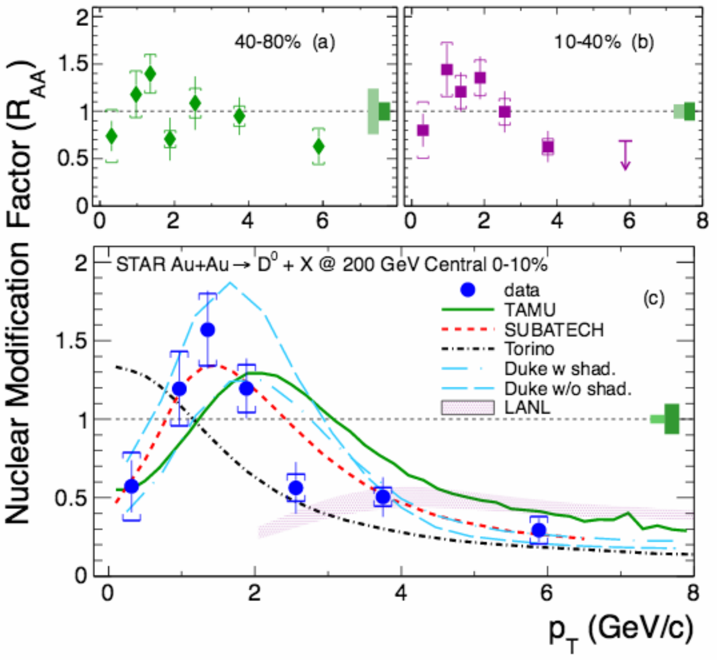

Figure 7.17: Nuclear modification factor of D^0 in the most central Au-Au collisions at $\sqrt{s_{\mathrm{NN}}}$ = 200 GeV measured by STAR in different centralities. The most central measurement are compared to several theoretical models. Fig. from [208].

Fig. 7.18 shows the PHENIX and STAR results for the HFE R_{AuAu} and v_2, also compared to theoretical models. In this case, only three models are compared to the data: “TAMU”, “MC@sHQ+EPOS2” (including only collisional energy loss) and “BAMPS” (also including only collisional energy loss). The model that is closer to both R_{AuAu} and v_2 is the “TAMU”, which also can explain the HFE results of LHC (see Fig. 7.15).

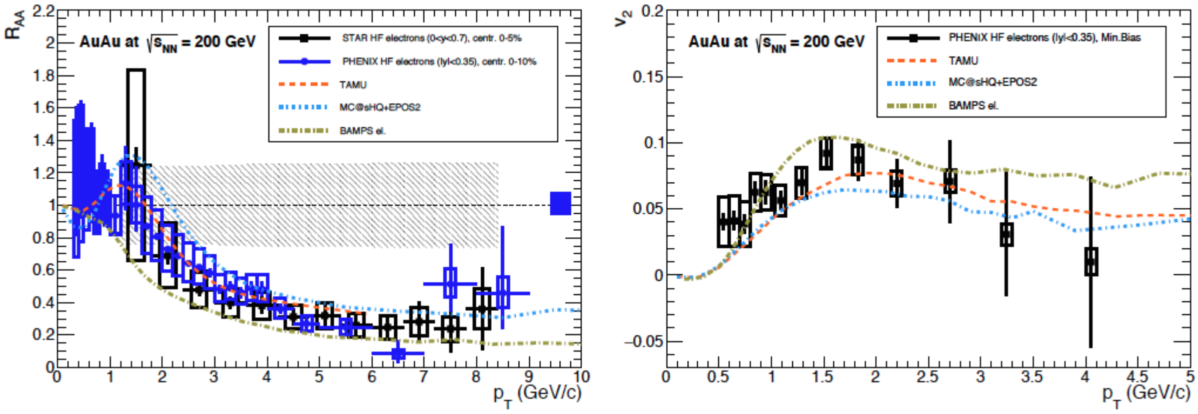

Figure 7.18: R_{AuAu} and v_2 of electrons from heavy-flavour hadron decays measured by PHENIX and STAR. Fig. from [209].

7.5 Final considerations of this chapter

The R_{AA} results for heavy-flavour particles at LHC and RHIC are smaller than one for the central collisions. The comparison of the R_{AA} and R_{pA} (or R_{dA}) allows the interpretation of the suppression observed in A-A collisions. As discussed in Chap. 3, in A-A collisions we can have effects from the formed medium and effects from the cold nuclear matter (CNM). On the other hand, in p-A collisions, since we do not expect an extended formation of a medium, the results are sensitive to CNM effects. Then, a full interpretation of results are only possible with a combination of pp, p-A and AA measurements.

The ALICE results for the R_{PbPb} of electrons from heavy-flavour at mid rapidity and muons from heavy-flavour at forward rapidity are similar (Fig. 7.11). The v_2 for electrons and muons from heavy-flavour hadron decays are also consistent within uncertainties. Since $v_2 > 0$, it indicates that heavy-flavour particles participates in the collective motion of the medium. To interpret the results of R_{PbPb} of electrons and muons from heavy-flavour hadron decays, it is necessary the R_{pPb} measurement.

The measurements of electrons from heavy-flavour hadron decays in p-Pb collisions is the contribution of this thesis, that was described in Chap. 5 and Chap. 6 and compared to models in Sec. 7.1 (see Fig. 7.5). The results of R_{pPb} are compatible with one in the whole transverse momentum range of the measurements. However, due to the large systematic uncertainty, the result is also compatible with an enhancement in the intermediate transverse momentum range: $2 \leq p_{\mathrm{T}} \leq 6$ GeV/c. We have compared the result with four theoretical models and all curves are compatible with our result. The enhancement in low p_{T} can have, as a possible explanation, the formation of an expanding medium described by hydrodynamics ("Blast wave") [198]. Since there is no suppression in p-Pb collisions, the suppression observed in Pb-Pb collisions is due to the formed medium.

In the case of muons from heavy-flavour hadron decays, ALICE has a preliminary result that shows the R_{pPb} consistent with one for the forward and backward rapidity (Fig. 7.4). Again, the suppression seen in Pb-Pb collision is due to the medium.

ALICE has also preliminaries results of the electrons from beauty in Pb-Pb and p-Pb collisions. The Pb-Pb collisions show a suppression for $p_{\mathrm{T}} > 3$ (Fig. 7.13) and since no suppression is seen in p-Pb results (Fig. 7.6), the suppression observed in Pb-Pb collisions is due to the QGP.

The R_{AA} of the average of D^0, D^+, D^{*+} (Fig. 7.8) shows a strong suppression of D-meson, which increases with the centrality. The results of R_{pPb} for the average D-meson is consistent with one, indicating that there is no CNM effects and the suppression in Pb-Pb collisions is due to the formed medium. The similar results of the R_{AA} for D-meson and light particles (Fig. 7.8) and the results of v_2 (Fig. 7.9) suggest that the heavy-particles participate in the collective motion, as the light particles.

It can be noticed that the suppression of heavy-flavour hadron decays observed in Pb-Pb collisions at LHC are due to the formation of the QGP, since the results of p-Pb collisions do not present any suppression.

Finally, we can summarise what we have learned with the measurement of this thesis and the other open heavy-flavour measurements performed by ALICE:

- The R_{pPb} results for open heavy-flavour are consistent with unity within the statistical and systematic uncertainties, indicating that CNM effects are small or even negligible. Theoretical calculations including CNM effects are close to unity and consistent with the experimental data within the uncertainties.

- The R_{AA} is smaller than one, indicating a suppression of the open heavy-flavour in A-A collisions when compared to pp collisions.

- Since no suppression is observed in p-Pb collisions, the CNM effects do not lead to suppressions in A-A collisions, and the observed suppression is due to the QGP.

- If the suppression is due to the QGP, we can extract information about the heavy-flavour interaction with the medium by comparing the experimental results with theoretical calculations.

- To understand the interactions of the particles with the QGP, we have compared the results with theoretical models. The model that can explain better the results of electrons from heavy-flavour hadron decays at RHIC and LHC is the "TAMU". This model only includes collisional energy loss and implements the notion of strongly coupled QGP for the diffusion and hadronization of heavy quarks in high-energy heavy-ion collisions (see Sec. 3.3.6). As discussed in Chap. 3, the use of pQCD assumptions implies in considering that the heavy-quarks are weakly coupled with the medium. But since experimental data shows similar suppression for light and heavy-flavours and also suggests that heavy quarks flows with the medium, they should be treated as strongly-coupled with the QGP, as in the “TAMU” model or models based on AdS/CFT. This model also considers shadowing and coalescence and these effects contribute to the predicted shape of R_{AA} and v_2. However, since this model do not fully explain the results of D meson in RHIC and in LHC, it leaves room for theoretical improvements.

Chapter 8

Conclusions

In this thesis we have presented the first measurement of electrons from heavy-flavour hadron decays in p-Pb collisions in intermediate and high transverse momentum range, up to 20 GeV/c. The electrons identification was based in the EMCal and TPC detectors of the ALICE experiment.

The background subtraction of the electrons from π^0 and η Dalitz decay and γ conversions was performed using an invariant mass method. Other background sources were estimated using POWHEG simulations and the cocktail method (explained in Sec. 5.7).

The nuclear modification factor was calculated using a pp reference: an interpolation of measurements of 2.76 TeV an 7 TeV was used in the case of MB data and in the case of the EMCal triggered data, the ATLAS 7 TeV measurements were scaled to 5.02 TeV.

The MB results of this thesis was combined with a spectrum obtained from 0.5 to 6 GeV/c using a different particle identification strategy and the results were published in Physics Letter B [4].

The obtained R_{pPb} is consistent with one [4], but given the large systematic uncertainty, the result is also consistent with an enhancement in the range $2 \leq p_{\mathrm{T}} \leq 6$ GeV/c (see Fig. 7.5). Such an enhancement was also observed at RHIC in d-Au collisions.

The results are compared with different theoretical models: "Kang et al.", where incoherent multiple scatterings are used. In this case, there is no energy loss and the propagation of the partons is governed by the momentum broadening. "Sharma et al.", where coherent scattering and cold nuclear matter effects are included in the calculations. The coherent scattering includes energy loss and power corrections. The CNM effects that were added in this calculation is the momentum broadening of the incoming partons. "FONLL + EPS09NLO shad", which is based on pQCD calculations (FONLL) including the nuclear shadowing, which is a CNM effect (EPS09NLO parametrization). This model predicts that the CNM effects are small, with an R_{pPb} close to one. "Blast wave calculation", which is a model that suggests a formation of an expanding medium in p-Pb collisions, described by hydrodynamics and in this case, flow of charm and bottom are considered. This model predicts an enhancement in low p_{T}.

All the presented models can describe our data within the uncertainties. We can also see that the theoretical predictions for CNM effects are small for $p_{\rm T} \leq 4$ GeV/c and negligible for high $p_{\rm T}$ (see Fig. 7.5).

Although a conclusion from the comparison with the models can not be drawn with the present uncertainties, this result, as a reference for the Pb-Pb results, has its role: since there is no suppression of the heavy-flavour decays electrons in p-Pb collisions, the suppression observed in Pb-Pb collisions is an effect of the interaction with the QGP.

Together with this result, other heavy-flavour measurements show that heavy-flavour particle do interact with the QGP and can even participate of the collective flow. One of the models that better explain the results of electrons from heavy-flavour hadron decay is based only in collisional energy loss of the particles in the medium, considering the heavy-quarks strongly-coupled with the QGP and the hadronization of the heavy-quarks is performed based on fragmentation and coalescence.

8.1 Outlook

To better understand the possible enhancement seen in the $R_{\rm pPb}$ in the transverse range $2 \leq p_{\rm T} \leq 6$ GeV/c, a study of the result in multiplicity classes is desired. If this enhancement is due to multiparton interactions, it would be more pronounced in the most central collisions than in peripheral ones.

The pp references used in this thesis was also a source of the systematic uncertainty in the nuclear modification factor, especially in the case where the scaling of the ATLAS data was performed using the FONLL predictions. Using the pp reference measured at the same energy as p-Pb collisions will allow a better precision in the $R_{\rm pPb}$ results.

Appendices

Appendix A

The Landau distribution

The fluctuations of the energy loss by ionization of charged particles when they traverse a thin layer of matter is known as *Landau distribution* which was theoretically described by Landau in 1944 [210]. This is a probability distribution which is similar to a gaussian with a long upper tail as shown in Fig. A.1 and this tail is due to the small number of individual collisions.

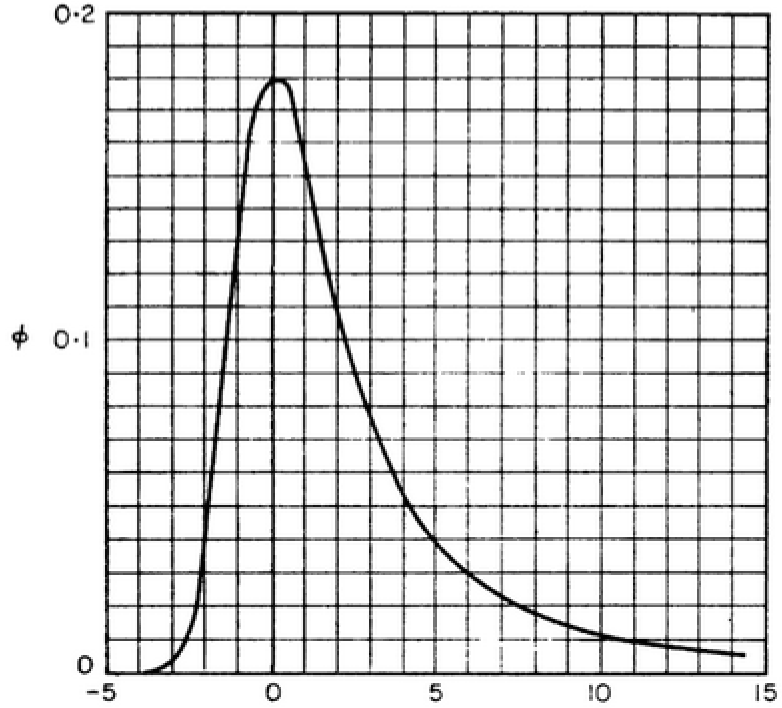

Figure A.1: The Landau distribution as proposed by Landau in his paper in 1944. The y-axis is the probability density function and the x-axis is the energy loss in arbitrary units. Fig. from [210].

Protons and pions, which usually are close to the minimum ionizing particle (MIP) when traversing the detector, produce approximately a spectra which has a Landau distribution.

The distribution is given by Eq. A.1.

$$L(x) = \frac{1}{\pi}\int_0^\infty e^{-tlog(t)-xt} sin(\pi t)dt \tag{A.1}$$

This integral can be approximated by Eq. A.2.

$$L(x) = \frac{1}{2\pi} e^{\frac{-1}{2}(x+e^{-x})} \tag{A.2}$$

We have checked in our analysis that indeed this distribution can describe the pions energy loss in the TPC detector, and this distribution was used to the TPC number of sigmas fits.

Appendix B

The Crystal Ball distribution

The Crystal Ball function is a gaussian with power low tail. This function is usually used to described process of losses in high energy physics. The Crystal Ball expression is given by Eq. B.1.

$$f_{CB}(m) = \frac{N}{\sqrt{2\pi\sigma}} \begin{cases} e^{-\frac{(m-m_0)^2}{2\sigma^2}} \text{ for } \frac{m-m_0}{\sigma} > -\alpha \\ \frac{n}{\alpha} e^{-\frac{\alpha^2}{2}} (\frac{n}{\alpha} - \alpha - \frac{m-m_0}{\sigma}) \text{ for } \frac{m-m_0}{\sigma} \leq -\alpha \end{cases} \tag{B.1}$$

The parameter α characterise the transition between the gaussian shape and the power law function. α, σ and m_0 are determined by the fit to the data and N is a normalisation parameter.

Fig. B.1 show examples of the Crystal Ball function for different values of α.

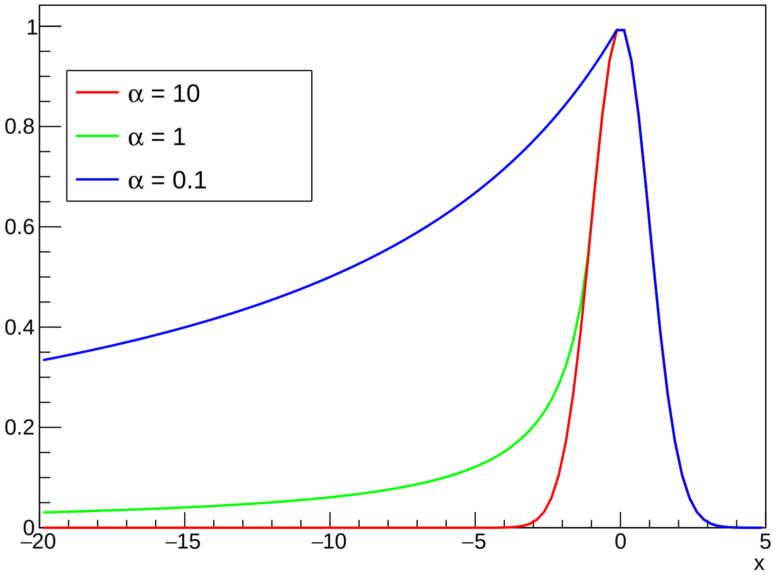

Figure B.1: Example of a Crystal Ball function $f_{CB}(x)$ for different values of α. Fig. from [211].

Appendix C

Crystal ball fits

In this appendix we show the crystal balls fits on the E/p distributions in data and MC.

The Crystal Ball fits with the quality of the fits are shown in Fig. C.1 and C.2 for data at 7 and 11 GeV thresholds respectively. Fig. C.3 and C.4 show the quality fit for MC LHC13d3 for the bins of 7 and 11 GeV thresholds respectively. Fig. C.5 and C.6 show the quality fit for MC LHC14b3abc for the bins of 7 and 11 GeV thresholds respectively.

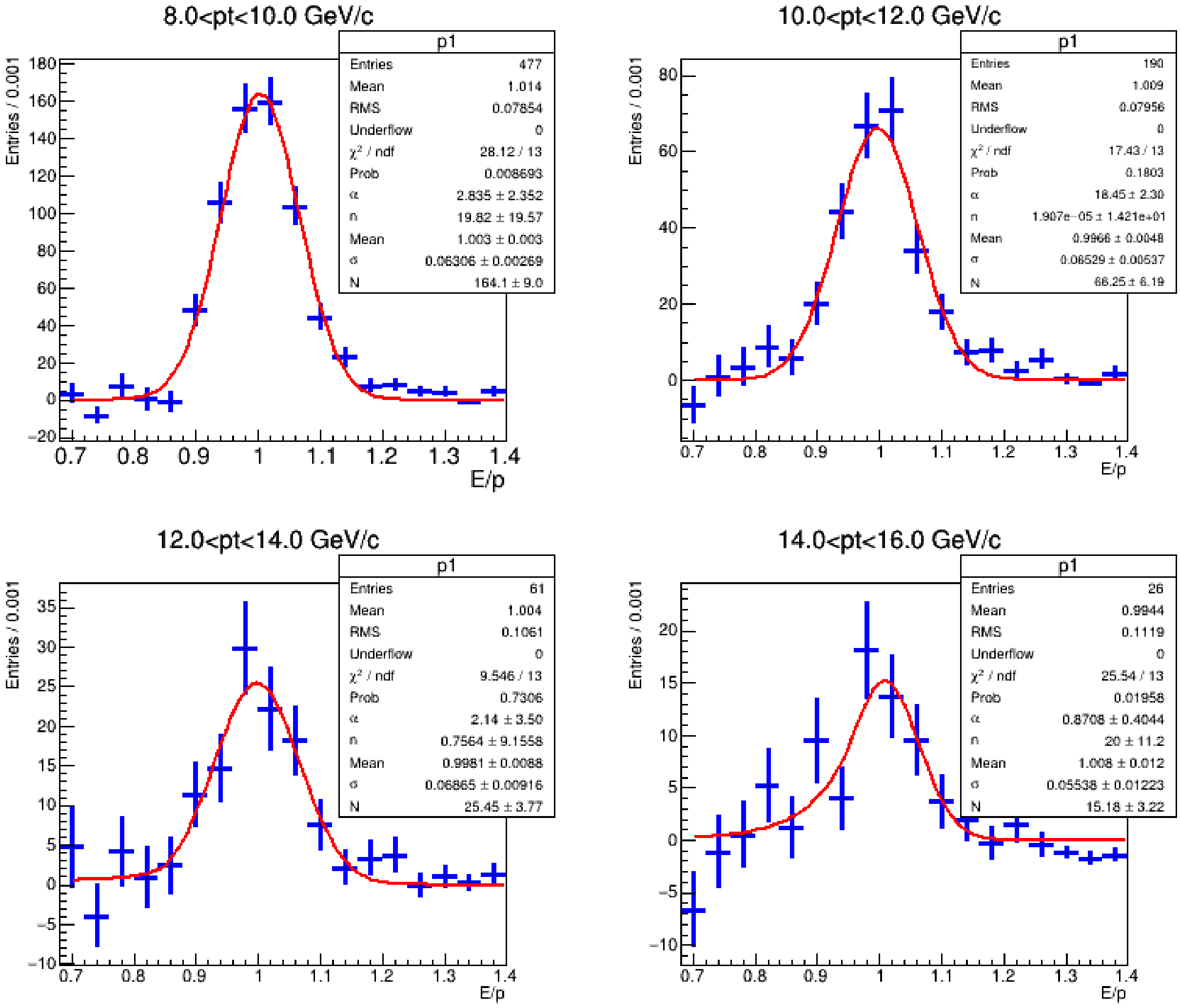

Figure C.1: Crystal ball fit in the E/p for data for the 7 GeV threshold.

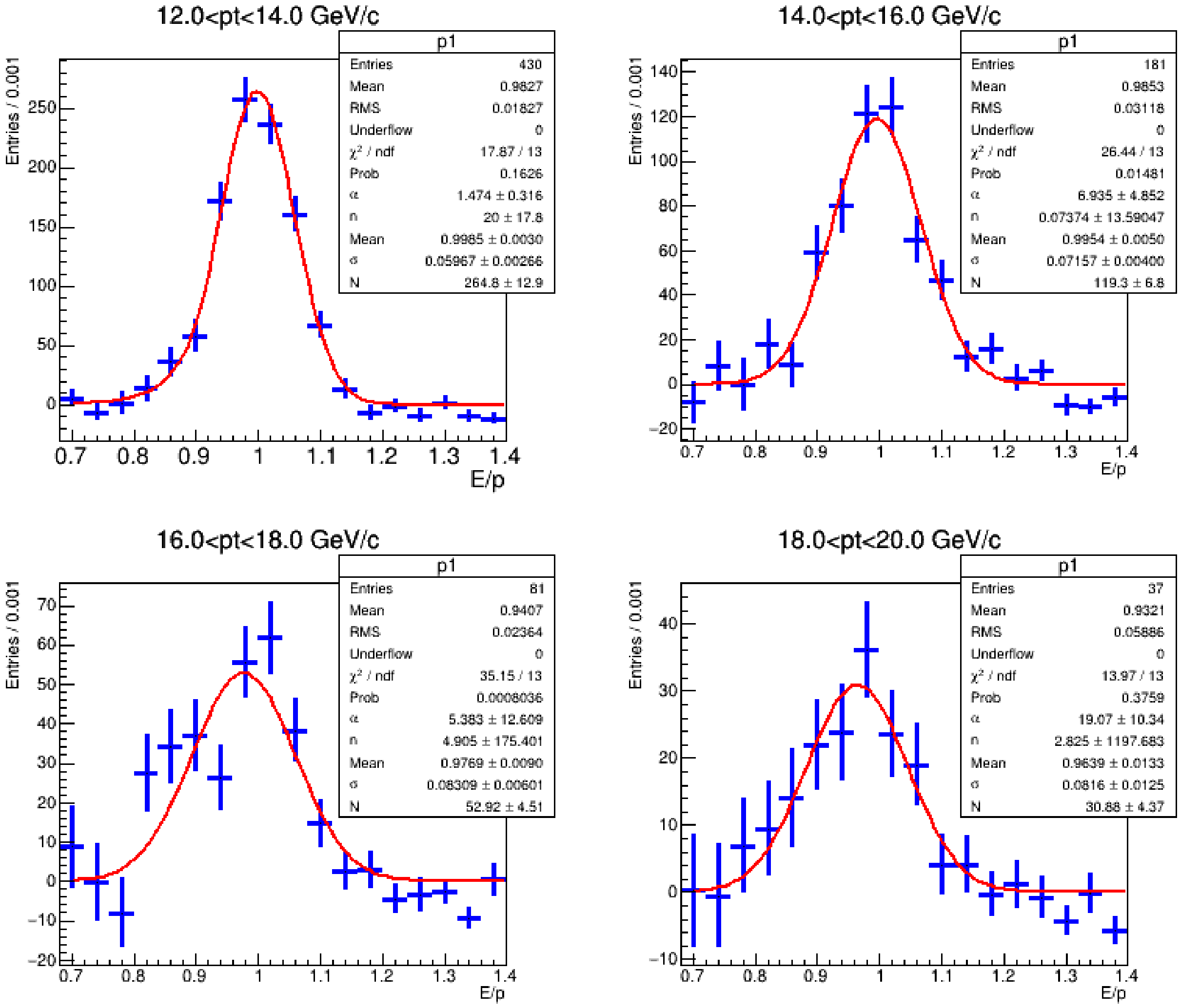

Figure C.2: Crystal ball fit in the E/p for data for the 11 GeV threshold.

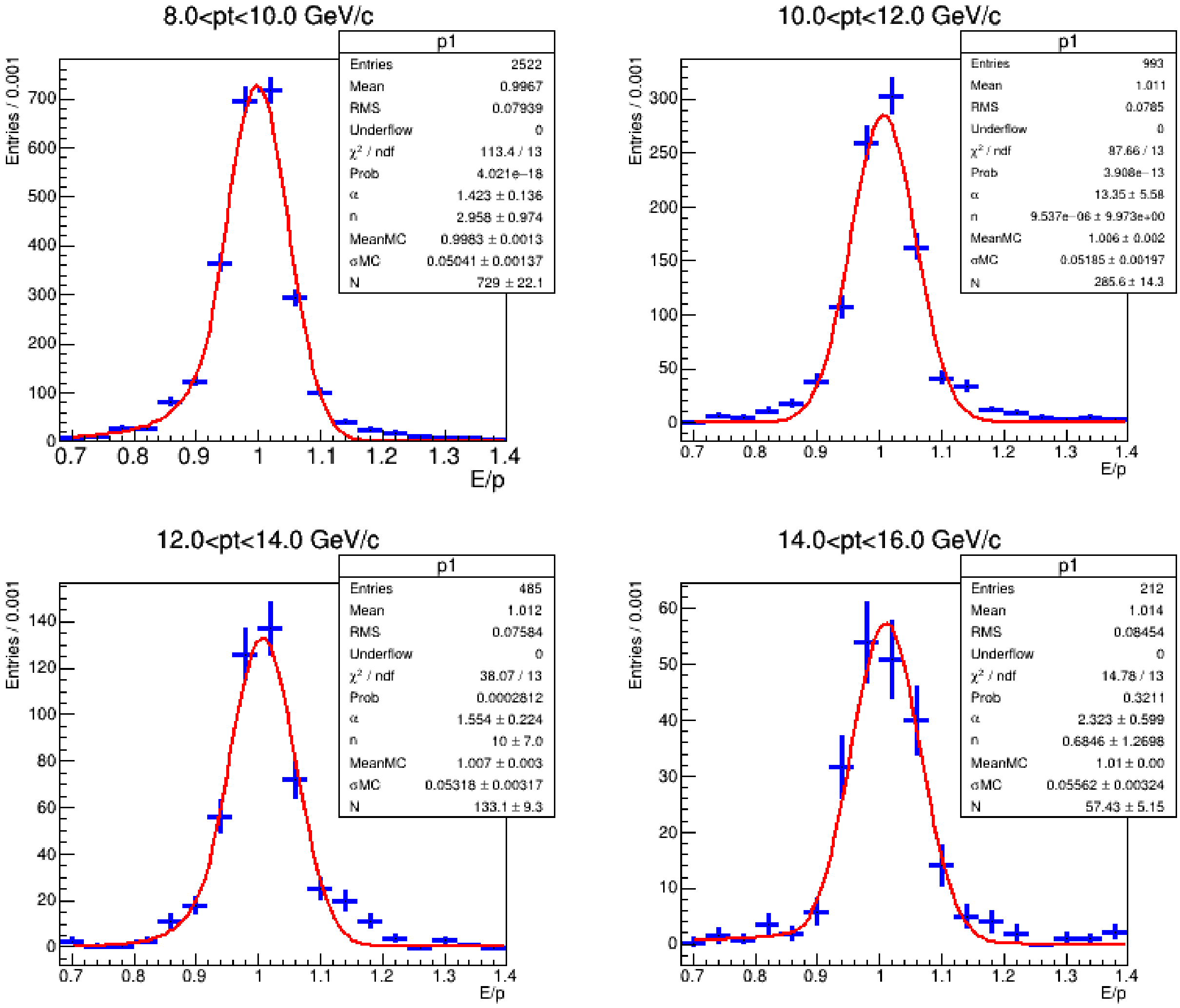

Figure C.3: Crystal ball fit in the E/p for MC LHC13d3 in the bins of 7 GeV threshold.

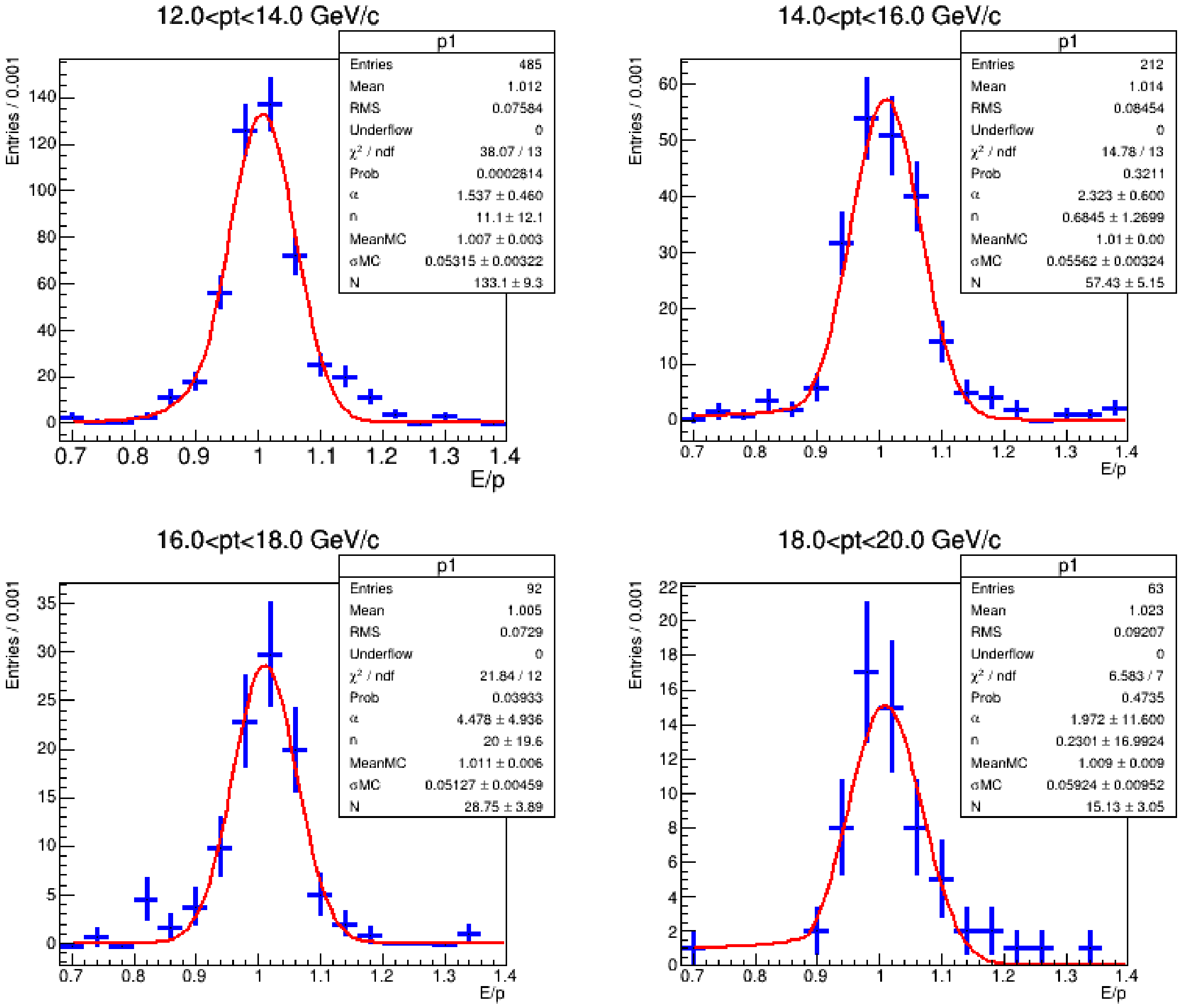

Figure C.4: Crystal ball fit in the E/p for MC LHC13d3 in the bins of 11 GeV threshold.

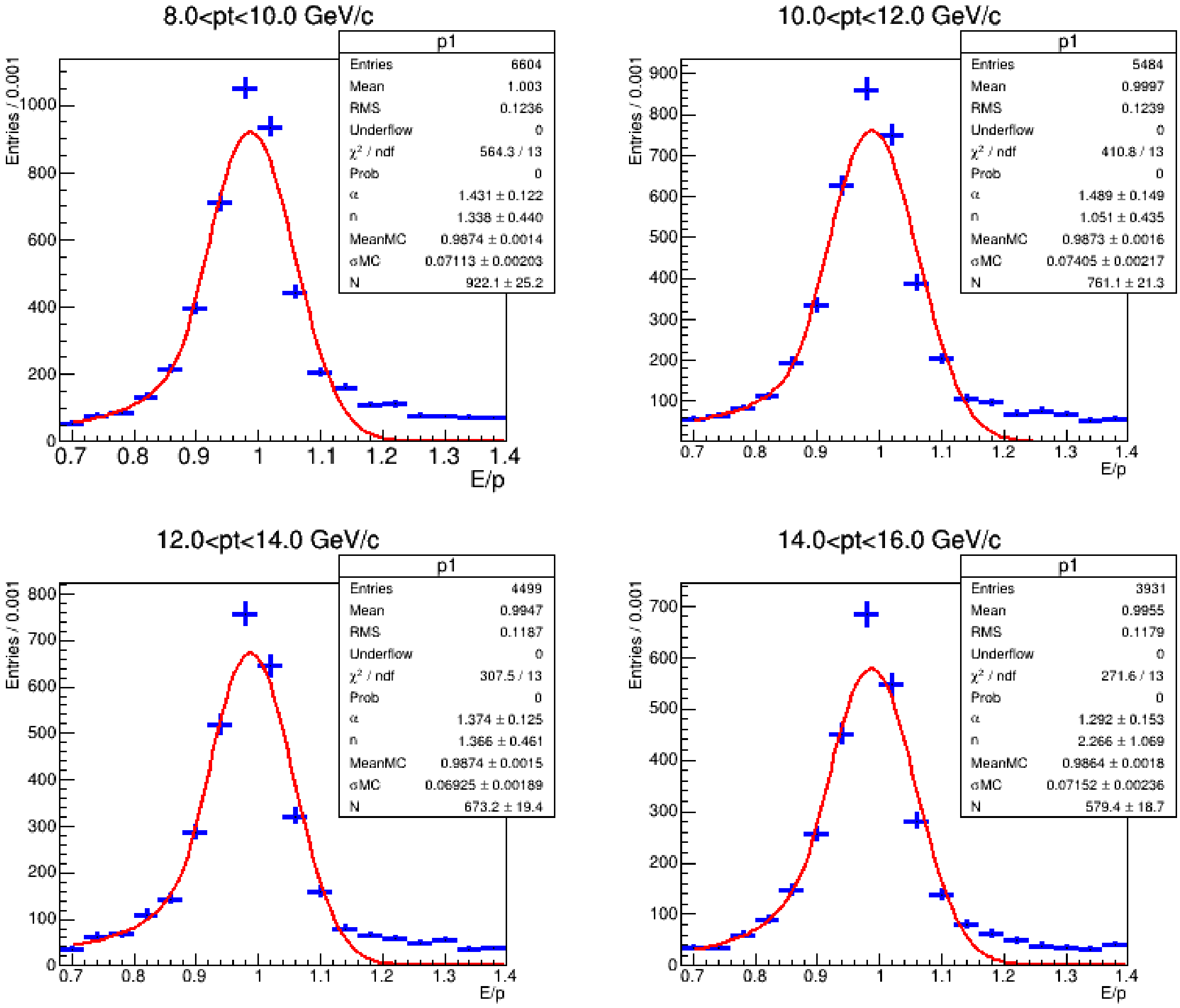

Figure C.5: Crystal ball fit in the E/p for MC LHC14b3abc in the bins of 7 GeV threshold.

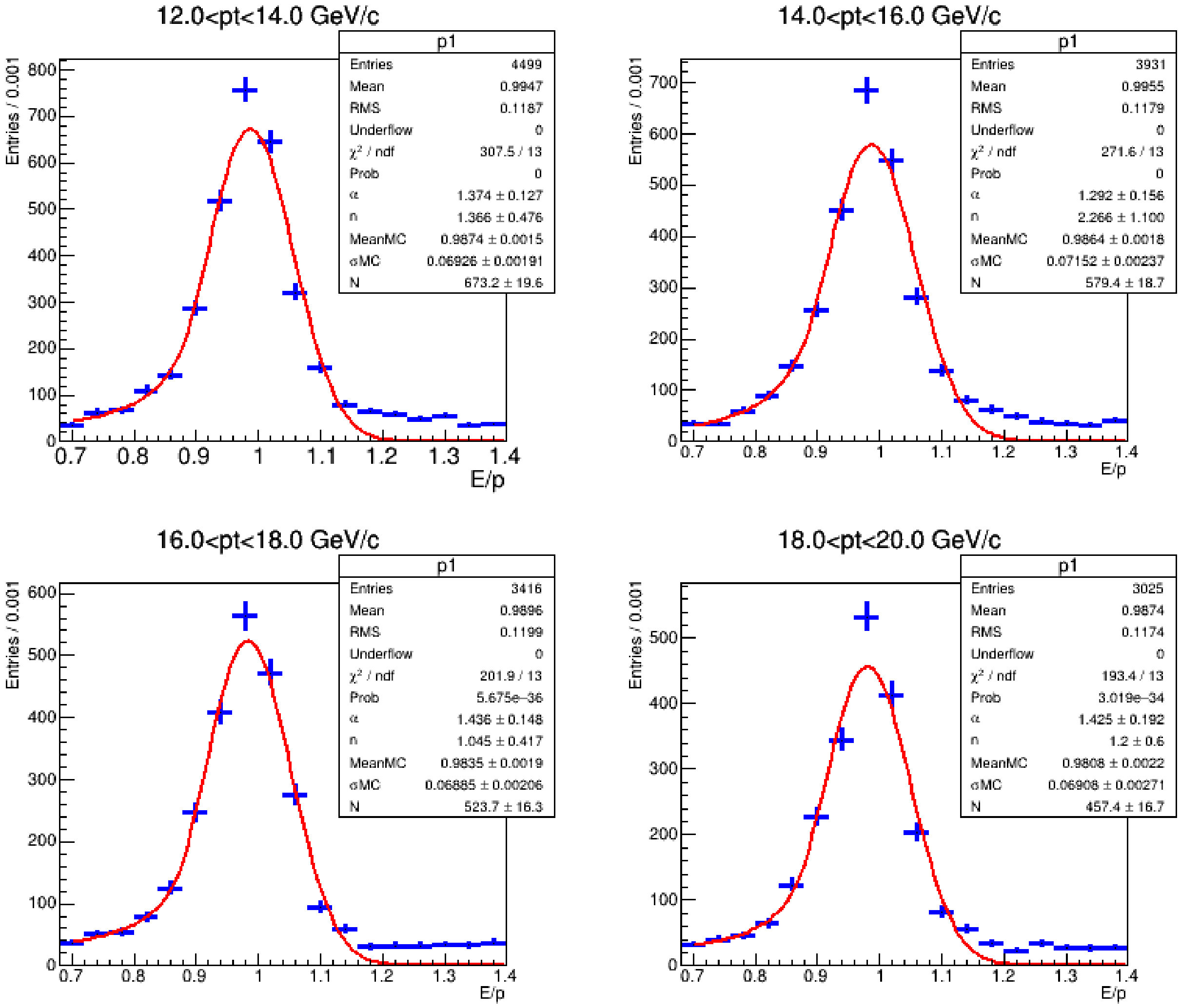

Figure C.6: Crystal ball fit in the E/p for MC LHC14b3abc in the bins of 11 GeV threshold.

Appendix D

LHC run numbers

D.1 data

In total, 26 runs were included in the analysis using: 12 runs from the period LHC13b, and 14 from LHC13c. The LHC data are organised by year and data taking. The first data taking in 2013 is called LHC13a (which was a pp collision), then the next data taking is called LHC13b and so on. The periods that corresponds to p-Pb data in MB collisions are LHC13b and LHC13c. The run numbers used in this analysis is listed below:

- LHC13b 195344 (1), 195346 (2), 195351 (3), 195389 (4), 195390 (5) 195391 (6), 195478 (7), 195479 (8), 195480 (9), 195481 (10), 195482 (11), 195483 (12).
- LHC13c 195529 (13), 195531 (14), 195566 (15), 195567 (16), 195568 (17), 195592 (18), 195593 (19), 195596 (20), 195633 (21), 195635 (22), 195644 (23), 195673 (24), 195675 (25), 195677 (26).

D.2 MC

The Monte Carlo samples used for the corrections are discussed in the following.

The MC sample used for the final result in the analysis is called LHC13d3. The runs of the Monte Carlo samples used in the analysis are listed below.

- (195389 (1), 195390 (2), 195391 (3), 195478 (4), 195479 (5), 195480 (6), 195481 (7), 195482 (8), 195483 (9), 195529 (10), 195531 (11), 195566 (12), 195567 (13), 195568 (14), 195592 (15), 195593 (16), 195633 (17), 195635 (18), 195644 (19), 195673 (20), 195675 (21), 195677 (22))

Appendix E

LHC run numbers for the EMCal trigger data

The periods LHC13d, LHC13e and LHC13f has provided data using the EMCal gamma trigger. Two thresholds of energy were used to select events with high-p_T electrons and photons: one at 7 GeV and other at 11 GeV.

The selected runs for the analysis, and data and MC are listed below.

- LHC13d: 195872(1), 195867(2), 195831(3), 195827(4), 195826(5), 195787(6), 195783(7), 195767(8), 195760(9), 195724(10).

- LHC13e: 195935(11), 195954(12), 195955(13), 195958(14), 196085(15), 196089(16), 196090(17), 196091(18), 196107(19), 196185(20), 196187(21), 196194(22), 196197(23), 196199(24), 196200(25), 196201(26), 196208(27), 196214(28), 196308(29), 196309(30), 196310(31).

- LHC13f: 197150(32), 197247(33), 197254(34), 197255(35), 197256(36), 197258(37), 197260(38), 197296(39), 197297(40), 197298(41), 197299(42), 197300(43), 197302(44), 197341(45), 197342(46), 197387(47).

Appendix F

Systematic uncertainties

F.0.1 Track selection

- Default:
    - SetMinNClustersTPC(100)
    - SetMinNClustersTPCPID(80)
    - SetMinNClustersITS(3)
- Variation:
    - SetMinNClustersTPC(90)
    - SetMinNClustersTPC(110)
    - SetMinNClustersTPCPID(70)
    - SetMinNClustersTPCPID(90)
    - SetMinNClustersITS(2)
    - SetMinNClustersITS(4)

F.0.2 E/p variations

- Default:
    - $0.8 < E/p < 1.2$
- Variations:
    - $0.76 < E/p < 1.2$
    - $0.78 < E/p < 1.2$
    - $0.82 < E/p < 1.2$
    - $0.84 < E/p < 1.2$
    - $0.85 < E/p < 1.2$
    - $0.8 < E/p < 1.3$

Shower Shape

Shower shape on EMCal, used only for the triggered data.

- Default:
  - M20 < 0.3
- Variation:
  - M20 < 0.2
  - M20 < 0.4

F.0.3 Partner variations in the invariant mass method

- Default:
  - $p_T min = 0$
  - MinNClustersTPC(80)
  - Mass cut (0.15)
  - Opening angle (no cut)
- Variations:
  - $p_{\mathrm{Tmin}} = 0.2$, $p_{\mathrm{Tmin}} = 0.3$, $p_{\mathrm{Tmin}} = 0.4$
  - MinNClustersTPC(60)
  - MinNClustersTPC(70)
  - Mass cut (0.10)
  - Mass cut (0.18)
  - Opening angle (0.1)

Bibliography

[1] J. Letessier and J. Rafelski. *Hadrons and Quark-Gluon Plasma.* Cambridge, 2000.

[2] Eds. R.C. Hwa and X.-N. Wang. Quark gluon plasma. *World Scientific Publishing*, 4(20, 21), 2010.

[3] T. Sjostrand E. Norrbin. Production and hadronization of heavy quarks. *The European Physical Journal C*, 4(20, 21), 2000.

[4] Jaroslav Adam et al. Measurement of electrons from heavy-flavour hadron decays in p-Pb collisions at $\sqrt{s_{\rm NN}} = 5.02$ TeV. *Phys. Lett.*, B754:81–93, 2016.

[5] A. D. Martin F. Halzen. Book: Quarks & Leptons: An introductory course in modern particle physics.

[6] Griffiths. Book: Introduction to Elementary Particles.

[7] B. R. Webber R. K. Ellis, W. J. Stirling. Book: Monogr. Part. Phys. Nucl. Phys. Cosmol. 8.

[8] M. Schmelling G. Dissertori, I. G. Knowles. Book: High -Energy Experiments and Theory.

[9] CTEQ Collaboaration. Book: Handbook of perturbative QCD.

[10] . `https://mbhs.edu/~jeglick/InfoCharts.html`. Accessed: 2016-01-20.

[11] Lie Groups. `https://www.math.upenn.edu/~wziller/math650/LieGroupsReps.pdf`. Accessed: 2016-02-22.

[12] Peter Skands. Introduction to QCD. In *Proceedings, Theoretical Advanced Study Institute in Elementary Particle Physics: Searching for New Physics at Small and Large Scales (TASI 2012)*, pages 341–420, 2013.

[13] Gavin P. Salam. Elements of QCD for hadron colliders. In *High-energy physics. Proceedings, 17th European School, ESHEP 2009, Bautzen, Germany, June 14-27, 2009*, 2010.

[14] Particle Data Group. `http://pdg.lbl.gov/2014/reviews/rpp2014-rev-qcd.pdf`. Accessed: 2016-02-22.

[15] Szabolcs Borsanyi, Zoltan Fodor, Christian Hoelbling, Sandor D Katz, Stefan Krieg, Claudia Ratti, and Kalman K. Szabo. Is there still any T_c mystery in lattice QCD? Results with physical masses in the continuum limit III. *JHEP*, 09:073, 2010.

[16] Peter Braun-Munzinger. Towards the quark gluon plasma. *Nucl. Phys.*, A663:183–190, 2000.

[17] Helmut Satz. The Quark-Gluon Plasma: A Short Introduction. *Nucl. Phys.*, A862-863:4–12, 2011.

[18] F. Karsch, E. Laermann, and A. Peikert. The Pressure in two flavor, (2+1)-flavor and three flavor QCD. *Phys. Lett.*, B478:447–455, 2000.

[19] Raimond Snellings. Elliptic Flow: A Brief Review. *New J. Phys.*, 13:055008, 2011.

[20] Yury Gorbunov website:. `http://www.star.bnl.gov/~gorbunov/main/node5.html`. Accessed: 2016-02-20.

[21] Andrea Dainese. Charm production and in-medium QCD energy loss in nucleus - nucleus collisions with ALICE. A performance study., 2009.

[22] Ulrich W. Heinz and Maurice Jacob. Evidence for a new state of matter: An Assessment of the results from the CERN lead beam program. 2000.

[23] F. Antinori et al. Production of strange and multistrange hadrons in nucleus nucleus collisions at the SPS. *Nucl. Phys.*, A661:130–139, 1999.

[24] E. Andersen et al. Strangeness enhancement at mid-rapidity in Pb-Pb collisions at 158-A-GeV/c. *Phys. Lett.*, B449:401–406, 1999.

[25] M. C. Abreu et al. Anomalous J/ψ suppression in Pb -Pb interactions at 158 GeV/c per nucleon. *Phys. Lett.*, B410:337–343, 1997.

[26] J. Rafelski and B. Müller. Strangeness Production in the Quark-Gluon Plasma. *Phys. Rev. Lett. 48, 1066*, 1982.

[27] T. Matsui, H. Satz. J/ψ suppression by quark-gluon plasma formation . *Physics Letters B, Volume 178, Issue 46*, 1986.

[28] G.Roland et al. Heavy-ion collisions at LHC. *Progress in Particle and Nuclear Physics*, 77(2):70–127, 2014.

[29] CERN website. `http://home.web.cern.ch/about/accelerators/super-proton-synchrotron`. Accessed: 2016-02-20.

[30] New Forms of QCD Matter Discovered at RHIC. *arXiv:nucl-th/0405013*, 2004.

[31] PHENIX Collaboration. Formation of dense partonic matter in relativistic nucleus–nucleus collisions at RHIC: Experimental evaluation by the PHENIX collaboration. *Nuclear Physics A*, 225(1):184–283, 2005.

[32] K. Nakamura et al. Review of particle physics. *J. Phys.*, G37:075021, 2010.

[33] M. B. Johnson J. W. Qiu I. Vitev, T. Goldman. Open charm tomography of cold nuclear matter. *arXiv:hep-ph/0605200*, 4(20, 21), 2006.

[34] R. Averbeck. Heavy-flavor production in heavy-ion collisions and implications for the properties of hot QCD matter. *Prog. Part. Nucl. Phys.*, 70:159–209, 2013.

[35] C. Marquet at al. Energy loss and thermalization of heavy quarks in a strongly-coupled plasma. *CERN-TH*, 4(20, 21):97–16, 2009.

[36] P. Huovinen, P. F. Kolb, Ulrich W. Heinz, P. V. Ruuskanen, and S. A. Voloshin. Radial and elliptic flow at RHIC: Further predictions. *Phys. Lett.*, B503:58–64, 2001.

[37] D. Teaney, J. Lauret, and Edward V. Shuryak. Hydro+cascade, flow, the equation of state, predictions and data. *Nucl. Phys.*, A698:479–482, 2002.

[38] P. Kovtun, Dan T. Son, and Andrei O. Starinets. Viscosity in strongly interacting quantum field theories from black hole physics. *Phys. Rev. Lett.*, 94:111601, 2005.

[39] R. J. Glauber and G. Matthiae. High-energy scattering of protons by nuclei. *Nucl. Phys.*, B21:135–157, 1970.

[40] K. J. Eskola and R. Vogt and X.-N. Wang. Nuclear overlap functions. *Int. J. Mod. Phys.*, A10:3087.

[41] Nestor Armesto. Nuclear shadowing. *J. Phys.*, G32:R367–R394, 2006.

[42] Hirotsugu Fujii, Francois Gelis, and Raju Venugopalan. Quark pair production in high energy pA collisions: General features. *Nucl. Phys.*, A780:146–174, 2006.

[43] J. W. Cronin and H. J. Frisch and M. J. Shochet and J. P. Boymond and R. Mermod et al. Production of hadrons with large transverse momentum at 200 GeV, 300 GeV, and 400 GeV. *Phys. Rev.*, D11:3105, 1975.

[44] Rishi Sharma, Ivan Vitev, and Ben-Wei Zhang. Light-cone wave function approach to open heavy flavor dynamics in QCD matter. *Phys. Rev.*, C80:054902, 2009.

[45] Zhong-Bo Kang, Ivan Vitev, Enke Wang, Hongxi Xing, and Cheng Zhang. Multiple scattering effects on heavy meson production in p+A collisions at backward rapidity. *Phys. Lett.*, B740:23–29, 2015.

[46] S. Sakai et al. Measurement of $\mathrm{R_{aa}}$ and v_2 of electrons from heavy-flavour decays in Pb-Pb collisions at $\sqrt{s} = 2.76$ with ALICE. *Nuclear Physics A*, 85(2):661c–664c, 2013.

[47] Matteo Cacciari, Mario Greco, and Paolo Nason. The P(T) spectrum in heavy flavor hadroproduction. *JHEP*, 05:007, 1998.

[48] Matteo Cacciari, Stefano Frixione, Nicolas Houdeau, Michelangelo L. Mangano, Paolo Nason, and Giovanni Ridolfi. Theoretical predictions for charm and bottom production at the LHC. *JHEP*, 10:137, 2012.

[49] B. A. Kniehl, G. Kramer, I. Schienbein, and H. Spiesberger. Inclusive B-Meson Production at the LHC in the GM-VFN Scheme. *Phys. Rev.*, D84:094026, 2011.

[50] B. A. Kniehl, G. Kramer, I. Schienbein, and H. Spiesberger. Inclusive Charmed-Meson Production at the CERN LHC. *Eur. Phys. J.*, C72:2082, 2012.

[51] Rafal Maciula and Antoni Szczurek. Open charm production at the LHC - k_t-factorization approach. *Phys. Rev.*, D87(9):094022, 2013.

[52] G. Goldhaber et al. Observation in e+ e- Annihilation of a Narrow State at 1865-MeV/c**2 Decaying to K pi and K pi pi pi. *Phys. Rev. Lett.*, 37:255–259, 1976.

[53] I. Peruzzi et al. Observation of a Narrow Charged State at 1876-MeV/c**2 Decaying to an Exotic Combination of K pi pi. *Phys. Rev. Lett.*, 37:569–571, 1976.

[54] C. Bebek et al. Evidence for New Flavor Production at the Upsilon (4S). *Phys. Rev. Lett.*, 46:84, 1981.

[55] L. J. Spencer et al. Measurement of B Meson Semileptonic Decay. *Phys. Rev. Lett.*, 47:771–774, 1981.

[56] C. Lourenco and H.K. Wahri. Heavy-flavour hadro-production from fixed-target to collider energies. *Physics Reports*, 433(3):127 – 180, 2006.

[57] Torbjorn Sjostrand, Stephen Mrenna, and Peter Z. Skands. PYTHIA 6.4 Physics and Manual. *JHEP*, 05:026, 2006.

[58] M. C. Abreu et al. Dimuon and charm production in nucleus-nucleus collisions at the CERN SPS. *Eur. Phys. J.*, C14:443–455, 2000.

[59] F. W. Busser et al. Observation of High Transverse Momentum Electrons at the CERN ISR. *Phys. Lett.*, B53:212, 1974.

[60] Nick Ellis and Anne Kernan. Heavy Quark Production at the CERN $p\bar{p}$ Collider. *Phys. Rept.*, 195:23–125, 1990.

[61] D. Acosta et al. Measurement of the J/ψ meson and $b-$hadron production cross sections in $p\bar{p}$ collisions at $\sqrt{s} = 1960$ GeV. *Phys. Rev.*, D71:032001, 2005.

[62] D. Acosta et al. Measurement of prompt charm meson production cross sections in $p\bar{p}$ collisions at $\sqrt{s} = 1.96$ TeV. *Phys. Rev. Lett.*, 91:241804, 2003.

[63] L. Adamczyk et al. Measurements of D^0 and D^* Production in $p + p$ Collisions at $\sqrt{s} = 200$ GeV. *Phys. Rev.*, D86:072013, 2012.

[64] A. Adare et al. Heavy Quark Production in $p + p$ and Energy Loss and Flow of Heavy Quarks in Au+Au Collisions at $\sqrt{s_{NN}} = 200$ GeV. *Phys. Rev.*, C84:044905, 2011.

[65] H. Agakishiev et al. High p_T non-photonic electron production in $p + p$ collisions at $\sqrt{s} = 200$ GeV. *Phys. Rev.*, D83:052006, 2011.

[66] D. J. Lange. The EvtGen particle decay simulation package. *Nucl. Instrum. Meth.*, A462:152–155, 2001.

[67] A. Adare et al. Measurement of Bottom versus Charm as a Function of Transverse Momentum with Electron-Hadron Correlations in p^+p Collisions at $\sqrt{s} = 200$ GeV. *Phys. Rev. Lett.*, 103:082002, 2009.

[68] M. M. Aggarwal et al. Measurement of the Bottom contribution to non-photonic electron production in $p + p$ collisions at $\sqrt{s}$=200 GeV. *Phys. Rev. Lett.*, 105:202301, 2010.

[69] A. Adare et al. Nuclear-Modification Factor for Open-Heavy-Flavor Production at Forward Rapidity in Cu+Cu Collisions at $\sqrt{s_{NN}} = 200$ GeV. *Phys. Rev.*, C86:024909, 2012.

[70] B. Abelev et al. Measurement of charm production at central rapidity in proton-proton collisions at $\sqrt{s} = 7$ TeV. *JHEP*, 01:128, 2012.

[71] B. A. Kniehl, G. Kramer, I. Schienbein, and H. Spiesberger. Reconciling open charm production at the Fermilab Tevatron with QCD. *Phys. Rev. Lett.*, 96:012001, 2006.

[72] Stefano Frixione and Bryan R. Webber. Matching NLO QCD computations and parton shower simulations. *JHEP*, 06:029, 2002.

[73] Stefano Frixione, Paolo Nason, and Bryan R. Webber. Matching NLO QCD and parton showers in heavy flavor production. *JHEP*, 08:007, 2003.

[74] Serguei Chatrchyan et al. Measurement of the B^0 production cross section in *pp* Collisions at $\sqrt{s} = 7$ TeV. *Phys. Rev. Lett.*, 106:252001, 2011.

[75] Vardan Khachatryan et al. Measurement of the B^+ Production Cross Section in pp Collisions at $\sqrt{s} = 7$ TeV. *Phys. Rev. Lett.*, 106:112001, 2011.

[76] Serguei Chatrchyan et al. Measurement of the Strange B Meson Production Cross Section with J/Psi ϕ Decays in *pp* Collisions at $\sqrt{s} = 7$ TeV. *Phys. Rev.*, D84:052008, 2011.

[77] R. Aaij et al. Measurement of the $B^{\pm}$ production cross-section in *pp* collisions at $\sqrt{s} = 7$ TeV. *JHEP*, 04:093, 2012.

[78] Betty Abelev et al. Measurement of prompt J/ψ and beauty hadron production cross sections at mid-rapidity in *pp* collisions at $\sqrt{s} = 7$ TeV. *JHEP*, 11:065, 2012.

[79] B. Abelev et al. . Measurement of electrons from semileptonic heavy-flavour hadron decays in pp collisions at $\sqrt{s} = 7$ TeV. *Phys. Rev.*, D86:112007, 2012.

[80] B. Abelev et al. . Measurement of electrons from semileptonic heavy-flavor hadron decays in pp collisions at $\sqrt{s} = 2.76$ TeV. *Phys. Rev.*, D91:012001, 2015.

[81] Betty Abelev et al. Measurement of electrons from beauty hadron decays in *pp* collisions at $\sqrt{s} = 7$ TeV. *Phys. Lett.*, B721:13–23, 2013.

[82] Betty Bezverkhny Abelev et al. Beauty production in pp collisions at $\sqrt{s} = 2.76$ TeV measured via semi-electronic decays. *Phys. Lett.*, B738:97–108, 2014.

[83] Betty Abelev et al. Heavy flavour decay muon production at forward rapidity in proton–proton collisions at $\sqrt{s} = 7$ TeV. *Phys. Lett.*, B708:265–275, 2012.

[84] Betty Abelev et al. Production of muons from heavy flavour decays at forward rapidity in pp and Pb-Pb collisions at $\sqrt{s_{NN}} = 2.76$ TeV. *Phys. Rev. Lett.*, 109:112301, 2012.

[85] Georges Aad et al. Measurements of the electron and muon inclusive cross-sections in proton-proton collisions at $\sqrt{s} = 7$ TeV with the ATLAS detector. *Phys. Lett.*, B707:438–458, 2012.

[86] E. Perez and E. Rizvi. The Quark and Gluon Structure of the Proton. *Rep. Prog. Phys.*, 76:046201, 2013.

[87] Alan D. Martin, R. G. Roberts, W. J. Stirling, and R. S. Thorne. MRST2001: Partons and α_s from precise deep inelastic scattering and Tevatron jet data. *Eur. Phys. J.*, C23:73–87, 2002.

[88] Pavel M. Nadolsky, Hung-Liang Lai, Qing-Hong Cao, Joey Huston, Jon Pumplin, Daniel Stump, Wu-Ki Tung, and C. P. Yuan. Implications of CTEQ global analysis for collider observables. *Phys. Rev.*, D78:013004, 2008.

[89] A. D. Martin, W. J. Stirling, R. S. Thorne, and G. Watt. Parton distributions for the LHC. *Eur. Phys. J.*, C63:189–285, 2009.

[90] A. D. Martin, W. J. Stirling, R. S. Thorne, and G. Watt. Update of parton distributions at NNLO. *Phys. Lett.*, B652:292–299, 2007.

[91] PDF website:. `http://hepdata.cedar.ac.uk/pdf/pdf3.html`. Accessed: 2016-01-20.

[92] A. Dumitru and D. E. Kharzeev and E. M. Levin and Y. Nara. Gluon Saturation in *pA* Collisions at the LHC: KLN Model Predictions For Hadron Multiplicities. *Phys. Rev.*, C85:044920, 2012.

[93] Eduardo Basso, Victor P. Goncalves, Michal Krelina, Jan Nemchik, and Roman Pasechnik. Nuclear effects in Drell-Yan pair production in high-energy *pA* collisions. 2016.

[94] Yuri L. Dokshitzer. Calculation of the Structure Functions for Deep Inelastic Scattering and e+ e- Annihilation by Perturbation Theory in Quantum Chromodynamics. *Sov. Phys. JETP*, 46:641–653, 1977. [Zh. Eksp. Teor. Fiz.73,1216(1977)].

[95] V. N. Gribov and L. N. Lipatov. Deep inelastic e p scattering in perturbation theory. *Sov. J. Nucl. Phys.*, 15:438–450, 1972. [Yad. Fiz.15,781(1972)].

[96] V. N. Gribov and L. N. Lipatov. e+ e- pair annihilation and deep inelastic e p scattering in perturbation theory. *Sov. J. Nucl. Phys.*, 15:675–684, 1972. [Yad. Fiz.15,1218(1972)].

[97] Guido Altarelli and G. Parisi. Asymptotic Freedom in Parton Language. *Nucl. Phys.*, B126:298, 1977.

[98] F. D. Aaron et al. Combined Measurement and QCD Analysis of the Inclusive e+- p Scattering Cross Sections at HERA. *JHEP*, 01:109, 2010.

[99] Alexei Prokudin. QCD Evolution Workshop: Introduction. 2012. [Int. J. Mod. Phys. Conf. Ser.20,1(2012)].

[100] Hannu Paukkunen. Nuclear PDFs in the beginning of the LHC era. *Nucl. Phys.*, A926:24–33, 2014.

[101] Michele Arneodo. Nuclear effects in structure functions. *Phys. Rept.*, 240:301–393, 1994.

[102] A. De Roeck and R. S. Thorne. Structure Functions. *Prog. Part. Nucl. Phys.*, 66:727–781, 2011.

[103] Dieter Schildknecht. Vector meson dominance. *Acta Phys. Polon.*, B37:595–608, 2006.

[104] Leo Stodolsky. Hadron-like behavior of gamma, neutrino nuclear cross-sections. *Phys. Rev. Lett.*, 18:135–137, 1967.

[105] T. H. Bauer, R. D. Spital, D. R. Yennie, and F. M. Pipkin. The Hadronic Properties of the Photon in High-Energy Interactions. *Rev. Mod. Phys.*, 50:261, 1978. [Erratum: Rev. Mod. Phys.51,407(1979)].

[106] G. Piller and Wolfram Weise. Shadowing effects in deep-inelastic lepton-nucleus scattering. *Phys. Rev.*, C42:R1834–R1837, 1990.

[107] J. Ashman et al. Measurement of the Ratios of Deep Inelastic Muon - Nucleus Cross-Sections on Various Nuclei Compared to Deuterium. *Phys. Lett.*, B202:603, 1988.

[108] J. Ashman et al. A Measurement of the ratio of the nucleon structure function in copper and deuterium. *Z. Phys.*, C57:211–218, 1993.

[109] M. Arneodo et al. Shadowing in Deep Inelastic Muon Scattering from Nuclear Targets. *Phys. Lett.*, B211:493, 1988.

[110] Nikolai N. Nikolaev and Valentin I. Zakharov. Parton Model and Deep Inelastic Scattering on Nuclei. *Phys. Lett.*, B55:397–399, 1975.

[111] J. J. Aubert et al. The ratio of the nucleon structure functions $F2_n$ for iron and deuterium. *Phys. Lett.*, B123:275, 1983.

[112] Klaus Rith. Present Status of the EMC effect. In *51st International School of Subnuclear Physics: Reflections on the next step for LHC (ISSP 2013) Erice, Italy, June 24-July 3, 2013*, 2014.

[113] Koichi Saito and Toshihiro Uchiyama. Effect of the Fermi Motion on Nuclear Structure Functions and the Emc Effect. *Z. Phys.*, A322:299, 1985.

[114] Alberto Accardi et al. Hard probes in heavy ion collisions at the lhc: pdfs, shadowing and pa collisions. In *3rd Workshop on Hard Probes in Heavy Ion Collisions: 3rd Plenary Meeting Geneva, Switzerland, October 7-11, 2002*, 2004.

[115] J.W. Cronin et al. Production of hadrons with large transverse momentum at 200 and 300 GeV. *Physical Review Letters*, 31(23), 1973.

[116] Ming Shao for the STAR Collaboration. Cronin effect at RHIC. 2013.

[117] R. Hwa, C. B. Yang. Scaling distributions of quarks, mesons, and protons for all pT energy and centrality. *Physics Review C 67, 064902*, 2003.

[118] J. Qiu, I. Vitev. Resumed QCD Power Corrections to Nuclear Shadowing. *PRL 93, 262301*, 2004.

[119] L. D. Landau and I. Y. Pomeranchuk. EMISSION OF UPSILON QUANTA DURING THE COLLISION OF FAST pi-MESONS WITH NUCLENS. 1953.

[120] Arkady B. Migdal. Bremsstrahlung and pair production in condensed media at high-energies. *Phys. Rev.*, 103:1811–1820, 1956.

[121] Rishi Sharma and Ivan Vitev. High transverse momentum quarkonium production and dissociation in heavy ion collisions. *Phys. Rev.*, C87(4):044905, 2013.

[122] A. Adare et al. Cold-nuclear-matter effects on heavy-quark production in d+Au collisions at $\sqrt{s_{NN}} = 200$ GeV. *Phys. Rev. Lett.*, 109(24):242301, 2012.

[123] W. M. Alberico, A. Beraudo, A. De Pace, A. Molinari, M. Monteno, M. Nardi, and F. Prino. Heavy-flavour spectra in high energy nucleus-nucleus collisions. *Eur. Phys. J.*, C71:1666, 2011.

[124] W. M. Alberico, A. Beraudo, A. De Pace, A. Molinari, M. Monteno, M. Nardi, F. Prino, and M. Sitta. Heavy flavors in AA collisions: production, transport and final spectra. *Eur. Phys. J.*, C73:2481, 2013.

[125] Shanshan Cao, Guang-You Qin, and Steffen A. Bass. Energy loss, hadronization and hadronic interactions of heavy flavors in relativistic heavy-ion collisions. *Phys. Rev.*, C92(2):024907, 2015.

[126] Jan Uphoff, Oliver Fochler, Zhe Xu, and Carsten Greiner. Elastic and radiative heavy quark interactions in ultra-relativistic heavy-ion collisions. *J. Phys.*, G42(11):115106, 2015.

[127] Jan Uphoff, Oliver Fochler, Zhe Xu, and Carsten Greiner. Elliptic Flow and Energy Loss of Heavy Quarks in Ultra-Relativistic heavy Ion Collisions. *Phys. Rev.*, C84:024908, 2011.

[128] Jan Uphoff, Oliver Fochler, Zhe Xu, and Carsten Greiner. Open Heavy Flavor in Pb+Pb Collisions at $\sqrt{s} = 2.76$ TeV within a Transport Model. *Phys. Lett.*, B717:430–435, 2012.

[129] Marlene Nahrgang, Joerg Aichelin, Pol Bernard Gossiaux, and Klaus Werner. Azimuthal correlations of heavy quarks in Pb + Pb collisions at $\sqrt{s} = 2.76$ TeV at the CERN Large Hadron Collider. *Phys. Rev.*, C90(2):024907, 2014.

[130] Simon Wicks, William Horowitz, Magdalena Djordjevic, and Miklos Gyulassy. Elastic, inelastic, and path length fluctuations in jet tomography. *Nucl. Phys.*, A784:426–442, 2007.

[131] Min He, Rainer J. Fries, and Ralf Rapp. Heavy-Quark Diffusion and Hadronization in Quark-Gluon Plasma. *Phys. Rev.*, C86:014903, 2012.

[132] Min He, Rainer J. Fries, and Ralf Rapp. Heavy Flavor at the Large Hadron Collider in a Strong Coupling Approach. *Phys. Lett.*, B735:445–450, 2014.

[133] Thomas Lang, Hendrik van Hees, Jan Steinheimer, Gabriele Inghirami, and Marcus Bleicher. Heavy quark transport in heavy ion collisions at energies available at the BNL Relativistic Heavy Ion Collider and at the CERN Large Hadron Collider within the UrQMD hybrid model. *Phys. Rev.*, C93(1):014901, 2016.

[134] Thomas Lang, Hendrik van Hees, Jan Steinheimer, and Marcus Bleicher. Elliptic flow and nuclear modification factors of D-mesons at FAIR in a Hybrid-Langevin approach. 2013.

[135] Thomas Lang, Hendrik van Hees, Jan Steinheimer, and Marcus Bleicher. Dileptons from correlated D- and $\bar{\mathrm{D}}$-meson decays in the invariant mass range of the QGP thermal radiation using the UrQMD hybrid model. 2013.

[136] Stefano Frixione, Paolo Nason, and Giovanni Ridolfi. The POWHEG-hvq manual version 1.0. 2007.

[137] Nan Su. A brief overview of hard-thermal-loop perturbation theory. *Commun. Theor. Phys.*, 57:409, 2012.

[138] K. J. Eskola and H. Paukkunen and C. A. Salgado. EPS09: A new generation of NLO and LO nuclear parton distribution functions. *JHEP*, 0904:065, 2009.

[139] C. Peterson, D. Schlatter, I. Schmitt, and Peter M. Zerwas. Scaling Violations in Inclusive e+ e- Annihilation Spectra. *Phys. Rev.*, D27:105, 1983.

[140] Shanshan Cao, Guang-You Qin, and Steffen A. Bass. Heavy-quark dynamics and hadronization in ultrarelativistic heavy-ion collisions: Collisional versus radiative energy loss. *Phys. Rev.*, C88:044907, 2013.

[141] Huichao Song and Ulrich W. Heinz. Suppression of elliptic flow in a minimally viscous quark-gluon plasma. *Phys. Lett.*, B658:279–283, 2008.

[142] Zhi Qiu, Chun Shen, and Ulrich Heinz. Hydrodynamic elliptic and triangular flow in Pb-Pb collisions at $\sqrt{s} = 2.76\mathrm{ATeV}$. *Phys. Lett.*, B707:151–155, 2012.

[143] Huichao Song and Ulrich W. Heinz. Causal viscous hydrodynamics in 2+1 dimensions for relativistic heavy-ion collisions. *Phys. Rev.*, C77:064901, 2008.

[144] Dmitri Kharzeev, Eugene Levin, and Marzia Nardi. QCD saturation and deuteron nucleus collisions. *Nucl. Phys.*, A730:448–459, 2004. [Erratum: Nucl. Phys.A743,329(2004)].

[145] F. Carvalho, F. O. Duraes, F. S. Navarra, and S. Szpigel. Charm and longitudinal structure functions with the KLN model. *Phys. Rev.*, C79:035211, 2009.

[146] Fred Cooper and Graham Frye. Comment on the Single Particle Distribution in the Hydrodynamic and Statistical Thermodynamic Models of Multiparticle Production. *Phys. Rev.*, D10:186, 1974.

[147] S. A. Bass et al. Microscopic models for ultrarelativistic heavy ion collisions. *Prog. Part. Nucl. Phys.*, 41:255–369, 1998. [Prog. Part. Nucl. Phys.41,225(1998)].

[148] W. Horowitz. private communication.

[149] J. F. Gunion and G. Bertsch. HADRONIZATION BY COLOR BREMSSTRAHLUNG. *Phys. Rev.*, D25:746, 1982.

[150] Yuri L. Dokshitzer and D. E. Kharzeev. Heavy quark colorimetry of QCD matter. *Phys. Lett.*, B519:199–206, 2001.

[151] S. Albino, B. A. Kniehl, and G. Kramer. AKK Update: Improvements from New Theoretical Input and Experimental Data. *Nucl. Phys.*, B803:42–104, 2008.

[152] P. B. Gossiaux and J. Aichelin. Towards an understanding of the RHIC single electron data. *Phys. Rev.*, C78:014904, 2008.

[153] K. Werner, Iu. Karpenko, T. Pierog, M. Bleicher, and K. Mikhailov. Event-by-Event Simulation of the Three-Dimensional Hydrodynamic Evolution from Flux Tube Initial Conditions in Ultrarelativistic Heavy Ion Collisions. *Phys. Rev.*, C82:044904, 2010.

[154] K. Werner, Iu. Karpenko, M. Bleicher, T. Pierog, and S. Porteboeuf-Houssais. Jets, Bulk Matter, and their Interaction in Heavy Ion Collisions at Several TeV. *Phys. Rev.*, C85:064907, 2012.

[155] P. B. Gossiaux, R. Bierkandt, and J. Aichelin. Tomography of a quark gluon plasma at RHIC and LHC energies. *Phys. Rev.*, C79:044906, 2009.

[156] Beat Hahn, D. G. Ravenhall, and Robert Hofstadter. High-Energy Electron Scattering and the Charge Distributions of Selected Nuclei. *Phys. Rev.*, 101:1131–1142, 1956.

[157] Leo P. Kadanoff. *Statistical Physics: Statics, Dynamics and Renormalization.* World Scientific, 2002. 0-511-01944-0.

[158] L. Ravagli and R. Rapp. Quark Coalescence based on a Transport Equation. *Phys. Lett.*, B655:126–131, 2007.

[159] Peter F. Kolb and Ulrich W. Heinz. Hydrodynamic description of ultrarelativistic heavy ion collisions. 2003.

[160] M. Bleicher et al. Relativistic hadron hadron collisions in the ultrarelativistic quantum molecular dynamics model. *J. Phys.*, G25:1859–1896, 1999.

[161] Hannah Petersen, Jan Steinheimer, Gerhard Burau, Marcus Bleicher, and Horst Stocker. A Fully Integrated Transport Approach to Heavy Ion Reactions with an Intermediate Hydrodynamic Stage. *Phys. Rev.*, C78:044901, 2008.

[162] R. C. Myers and S. E. Vazquez. Quark Soup al dente: Applied Superstring Theory. *Class. Quant. Grav.*, 25:114008, 2008.

[163] V. Jahnke. private communication.

[164] Jorge Casalderrey-Solana, Hong Liu, David Mateos, Krishna Rajagopal, and Urs Achim Wiedemann. Gauge/String Duality, Hot QCD and Heavy Ion Collisions. 2011.

[165] W. A. Horowitz. Heavy Quark Production and Energy Loss. *Nucl. Phys.*, A904-905:186c–193c, 2013.

[166] B. I. Abelev et al. Transverse momentum and centrality dependence of high-p_T non-photonic electron suppression in Au+Au collisions at $\sqrt{s_{NN}} = 200\,\text{GeV}$. *Phys. Rev. Lett.*, 98:192301, 2007. [Erratum: Phys. Rev. Lett.106,159902(2011)].

[167] Magdalena Djordjevic, Miklos Gyulassy, Ramona Vogt, and Simon Wicks. Influence of bottom quark jet quenching on single electron tomography of Au + Au. *Phys. Lett.*, B632:81–86, 2006.

[168] Nestor Armesto, Matteo Cacciari, Andrea Dainese, Carlos A. Salgado, and Urs Achim Wiedemann. How sensitive are high-p(T) electron spectra at RHIC to heavy quark energy loss? *Phys. Lett.*, B637:362–366, 2006.

[169] R. Baier, Yuri L. Dokshitzer, Alfred H. Mueller, S. Peigne, and D. Schiff. Radiative energy loss and p(T) broadening of high-energy partons in nuclei. *Nucl. Phys.*, B484:265–282, 1997.

[170] A. Adare et al. System-size dependence of open-heavy-flavor production in nucleus-nucleus collisions at $\sqrt{s_{_{NN}}}$=200 GeV. *Phys. Rev.*, C90(3):034903, 2014.

[171] Andrea Beraudo. Dynamics of heavy flavor quarks in high energy nuclear collisions. *Nucl. Phys.*, A931:145–154, 2014.

[172] K. Aamodt et al. . The ALICE experiment at the CERN LHC. *JINST*, 3:S08002, 2008.

[173] U. Abeysekara et al. ALICE EMCal Physics Performance Report. 2010.

[174] EMCal Offline Documentation. `http://svn.cern.ch/guest/AliRoot/trunk/EMCAL/doc/EMCALDocumentation.pdf`. Accessed: 2016-02-20.

[175] G. Bourdaud. private communication.

[176] P. Cortese et al. ALICE: Physics performance report, volume I. *J. Phys.*, G30:1517–1763, 2004.

[177] ROOT website. `https://root.cern.ch`. Accessed: 2016-01-20.

[178] P. Billoir. Track Fitting With Multiple Scattering: A New Method. *Nucl. Instrum. Meth.*, A225:352, 1984.

[179] P Cortese et al. ALICE: Physics performance report, volume II. *J. Phys.*, G32:1295–2040, 2006.

[180] A. Adare et al. Detailed measurement of the e^+e^- pair continuum in $p+p$ and Au+Au collisions at $\sqrt{s_{NN}} = 200$ GeV and implications for direct photon production. *Phys. Rev.*, C81:034911, 2010.

[181] L. Adamczyk et al. Di-electron spectrum at mid-rapidity in $p+p$ collisions at $\sqrt{s} = 200$ GeV. *Phys. Rev.*, C86:024906, 2012.

[182] R. Averbeck. private communication.

[183] G. D'Agostini. A Multidimensional unfolding method based on Bayes' theorem. *Nucl. Instrum. Meth.*, A362:487–498, 1995.

[184] J. Wagner. private communication.

[185] Roger Barlow. Systematic errors: Facts and fictions. In *Advanced statistical techniques in particle physics. Proceedings, Conference, Durham, UK, March 18-22, 2002*, pages 134–144, 2002.

[186] T. C. Awes, F. E. Obenshain, F. Plasil, S. Saini, S. P. Sorensen, and G. R. Young. A Simple method of shower localization and identification in laterally segmented calorimeters. *Nucl. Instrum. Meth.*, A311:130–138, 1992.

[187] D. J. Fegan. gamma/hadron separation at TeV energies. *J. Phys.*, G23:1013–1060, 1997.

[188] Carlo Oleari. The POWHEG-BOX. *Nucl. Phys. Proc. Suppl.*, 205-206:36–41, 2010.

[189] S. Sakai. private communication.

[190] Jan Fiete. Measurement of the Charged-Particle Multiplicity in Proton–Proton Collisions with the ALICE Detector, 2009.

[191] G. Aad et al. Measurements of the electron and muon inclusive cross-sections in proton-proton collisions at $\sqrt{s} = 7$ TeV with the ATLAS detector. *Phys. Lett.*, B707:438, 2012.

[192] M. Cacciari and M. Greco and P. Nason. The p_{T} spectrum in heavy flavor hadroproduction. *JHEP*, 9805:007, 1998.

[193] B. Abelev et al. . Measurement of visible cross sections in proton-lead collisions at $\sqrt{s_{\mathrm{NN}}} = 5.02$ TeV in van der Meer scans with the ALICE detector. *JINST*, 9:P11003, 2014.

[194] Hirotsugu Fujii and Kazuhiro Watanabe. Heavy quark pair production in high energy pA collisions: Open heavy flavors. *Nucl. Phys.*, A920:78–93, 2013.

[195] Michelangelo L. Mangano, Paolo Nason, and Giovanni Ridolfi. Heavy quark correlations in hadron collisions at next-to-leading order. *Nucl. Phys.*, B373:295–345, 1992.

[196] Betty Bezverkhny Abelev et al. Measurement of prompt D-meson production in $p-Pb$ collisions at $\sqrt{s_{NN}} = 5.02$ TeV. *Phys. Rev. Lett.*, 113(23):232301, 2014.

[197] Jeremy Wilkinson. Measurements of heavy-flavour production in p-Pb collisions with ALICE. In *25th International Conference on Ultra-Relativistic Nucleus-Nucleus Collisions (Quark Matter 2015) Kobe, Japan, September 27-October 3, 2015*, 2015.

[198] A. M. Sickles. Possible evidence for radial flow of heavy mesons in d+Au collisions. *Phys. Lett.*, B731:51, 2014.

[199] Shingo Sakai. Measurements of heavy-flavour decay leptons with ALICE. *EPJ Web Conf.*, 95:04058, 2015.

[200] V. Khachatryan et al. Study of B meson production in pPb collisions at $\sqrt{s_{NN}} = 5.02$ TeV. 2015.

[201] Jaroslav Adam et al. Transverse momentum dependence of D-meson production in Pb-Pb collisions at $\sqrt{s_{\rm NN}} = 2.76$ TeV. 2015.

[202] Betty Bezverkhny Abelev et al. Azimuthal anisotropy of D meson production in Pb-Pb collisions at $\sqrt{s_{\rm NN}} = 2.76$ TeV. *Phys. Rev.*, C90(3):034904, 2014.

[203] Magdalena Djordjevic, Marko Djordjevic, and Bojana Blagojevic. RHIC and LHC jet suppression in non-central collisions. *Phys. Lett.*, B737:298–302, 2014.

[204] Jaroslav Adam et al. Centrality dependence of high-p$_T$ D meson suppression in Pb-Pb collisions at $\sqrt{s_{\rm NN}} = 2.76$ TeV. *JHEP*, 11:205, 2015.

[205] Jaroslav Adam et al. Elliptic flow of muons from heavy-flavour hadron decays at forward rapidity in Pb–Pb collisions at $\sqrt{s_{\rm NN}} = 2.76$ TeV. *Phys. Lett.*, B753:41–56, 2016.

[206] Andrea Dubla. Measurements of heavy-flavour production and azimuthal anisotropy in Pb–Pb collisions with the ALICE detector. In *Proceedings, 2nd Conference on Large Hadron Collider Physics Conference (LHCP 2014)*, 2014.

[207] CMS Collaboration. Nuclear Modification Factor of prompt D^0 in PbPb Collisions at $\sqrt{s_{\rm NN}} = 2.76$ TeV. 2015.

[208] L. Adamczyk et al. Observation of D^0 Meson Nuclear Modifications in Au+Au Collisions at $\sqrt{s_{NN}} = 200$ GeV. *Phys. Rev. Lett.*, 113(14):142301, 2014.

[209] A. Andronic et al. Heavy-flavour and quarkonium production in the LHC era: from proton-proton to heavy-ion collisions. *Eur. Phys. J.*, C76(3):107, 2016.

[210] L. Landau. On the energy loss of fast particles by ionization. *J. Phys.(USSR)*, 8:201–205, 1944.

[211] H. Zanoli. private communication.